THESIS FOR THE DEGREE OF DOCTOR OF PHILOSOPHY

Design and Control of Electrically Excited Synchronous Machines for Vehicle Applications

JUNFEI TANG

Division of Electric Power Engineering
Department of Electrical Engineering
CHALMERS UNIVERSITY OF TECHNOLOGY
Gothenburg, Sweden 2021

Design and Control of Electrically Excited Synchronous Machines for Vehicle Applications

JUNFEI TANG

ISBN: 978-91-7905-466-3

Doktorsavhandlingar vid Chalmers tekniska högskola

Ny series nr 4933

ISSN 0346-718X

Division of Electric Power Engineering

Department of Electrical Engineering

Chalmers University of Technology

SE-412 79 Gothenburg

Sweden

Telephone +46 (0)31-772 1000

Chalmers Library, Reproservice

Gothenburg, Sweden 2021

Design and Control of Electrically Excited Synchronous Machines for Vehicle Applications

JUNFEI TANG

Department of Electrical Engineering

Chalmers University of Technology

Abstract

Electrically excited synchronous machines (EESMs) are becoming an alternative to permanent magnet synchronous machines (PMSMs) in electric vehicles (EVs). This mainly attributes to the zero usage of rare-earth materials, as well as the ability to achieve high starting torque, the effectiveness to do field weakening and the flexibility to adjust power factor provided by EESMs. Furthermore, in case of converter failure at high speed, safety can be improved by shutting down the field current in EESMs.

The purpose of this study is to investigate the potential application of EESMs in EVs. To achieve this aim, several topics are covered in this study. These topics are studied to confront the challenges before EESMs could become prevalent and to maximumly use the advantages of EESMs for EV applications. In control strategies, the challenge is to properly adjust the combination of stator and field currents so that high power factor and minimum copper losses can be achieved. To tackle this, control strategies are proposed so that reactive power consumption and total copper losses are minimized. With the proposed strategies, the output power is maximized along the torque-speed envelope and high efficiency in field-weakening is achieved. In dynamic current control, due to the magnetic couplings between field winding and stator winding, a current rise in one winding would induce an electromagnetic force (EMF) in the other. This introduces disturbances in dynamic current control. In this study, a current control algorithm is proposed to cancel the induced EMF and the disturbances are mitigated. In machine design, high starting torque and effective field weakening are expected to be achieved in the same EESM design. To realize this, some criteria need to be satisfied. These criteria are derived and integrated into the design procedure including multi-objective optimizations. A 48 V EESM is prototyped during the study. In experimental verification, a torque density of 10 N·m/L is achieved including cooling jacket. In field excitation, a contactless excitation technology is adopted, which leads to inaccessibility of the field winding. To realize precise control of field current in a closed loop, an estimation method of field current is proposed. Based on the estimation, closed-loop field current control is established. The field current reference is tracked within an error of 2% in experimental verifications. The cost of an EESM drive increases because of the additional converter used for field excitation. A technique is proposed in which the switching harmonics are extracted for field excitation. With this technique, both stator and field windings can be powered using only one inverter.

From all the challenges tackled in this study, it can be concluded that the application of EESMs in EVs is feasible.

Index Terms: Electrically excited synchronous machines, electric vehicles, electric machine modeling, electric machine design, electric machine control, brushless excitation.

Acknowledgement

I would like to take the opportunity here to thank all of those that have had positive impact of this work.

Firstly, I would like to express my gratitude to my main supervisor Yujing Liu for his continuous support during the work. His enthusiastic spirits have encouraged me to explore the areas that I enjoyed. His knowledge and experience as well as his innovative thinking have improved my understanding of engineering and research. Further, I would like to thank my co-supervisor Stefan Lundberg for his vital support in both theorical analysis and practical implementations. His conscientious attitude, meticulous thinking and extensive experience to tackle challenges are impressive. I would like to thank my examiner Ola Carlson, especially for his guidance in study planning and his feedbacks of this thesis work.

I am grateful for all the supports from the division. Special thanks go to Luca Boscaglia for his excellence in thermal analysis, Xiaoliang Huang for his help with drive systems, Jian Zhan for his guidance in machine design and help in machine assembly, Daniel Pehrman for his tutorials in all aspects of engineering, Georgios Mademlis for the discussions we have and the enjoyment of sparks in the lab together, Chih-Han Kuo for his professional assistance in digital processor programing, Felix Mannerhagen for his advices and help in mechanical work, Robert Karlsson for his advices with circuit design and many other collogues in our electric power engineering division.

This project is financially supported by the Swedish Energy Agency and the European Commission. I appreciate the support of this study from them, the advices from the reference group and the discussions with the collogues from Lund in collaboration.

Finally, I would like to thank my family who give me essential support to pursue my doctoral study.

Junfei Tang

Gothenburg, Sweden

January 2021

List of Abbreviations

ADC	Analogue to Digital Converter
BEV	Battery Electric Vehicle
CNG	Compressed Natural Gas
DAC	Digital to Analogue Converter
DSP	Digital Signal Processor
EESM	Electrically Excited Synchronous Machine
EV	Electric Vehicle
FEM	Finite Element Method
GHG	Green-House Gas
IM	Induction Machine
PHEV	Plug-in Hybrid Electric Vehicle
PMSM	Permanent Magnet Synchronous Machine
PWM	Pulse Width Modulation
RMS	Root Mean Square
SynRM	Synchronous Reluctance Machine
SVM	Space Vector Modulation
WPT	Wireless Power Transfer

List of Symbols

A, a	Phase A
B, b	Phase B
C, c	Phase C; Capacitance
d	Direct-Axis, duty cycle
E, e	EMF; Error in dynamic control
f	Field
h	Heat transfer coefficient
i	Current
J	Current density
L	Apparent Inductance; Length
l	Incremental inductance
M	Mutual inductance
m	Number of phases
N	Number of turns
P	Active power
p	Instantaneous active power; Number of pole pairs
Q	Reactive power; Total number of slots
q	Instantaneous reactive power; Number of slots per pole per phase; Quadrature-axis
S	Apparent power
s	Instantaneous apparent power
t	Time
u	Voltage
x	Electrical quantity in general

α	α-axis
β	β-axis
γ	γ-axis
ε	Error between successive iterations
ψ	Flux linkage
λ	Thermal conductivity

Contents

Chapter 1

Introduction

1.1 Background

Electric Vehicles (EVs) have become a fast-growing area in recent years due to an increase of environmental concerns from society. Lifecycle analysis of EVs has shown that even powered by the most carbon-intensive electricity in Europe, the greenhouse emission (GHG) from an EV is still lower than that from a conventional diesel vehicle [1]. Besides, as the grid starts to accept more renewable electricity, the climate impact caused by EVs will be even lower. A comparison of GHG emissions per km pursued in [2] is shown in Figure 1-1. A reduction in GHG emissions is demonstrated with an increasing degree of electrification. Therefore, the electrification of vehicles has shown an undisputed approach to a sustainable society in the future. Consequently, from the data collected in [3] , the global electric car sales surpassed 1 million vehicles in 2017, and 2 million vehicles in 2019, as shown in Figure 1-2. Moreover, to keep consistent with the Paris Declaration, the stock of EVs need to achieve over 110 million by 2030 [4].

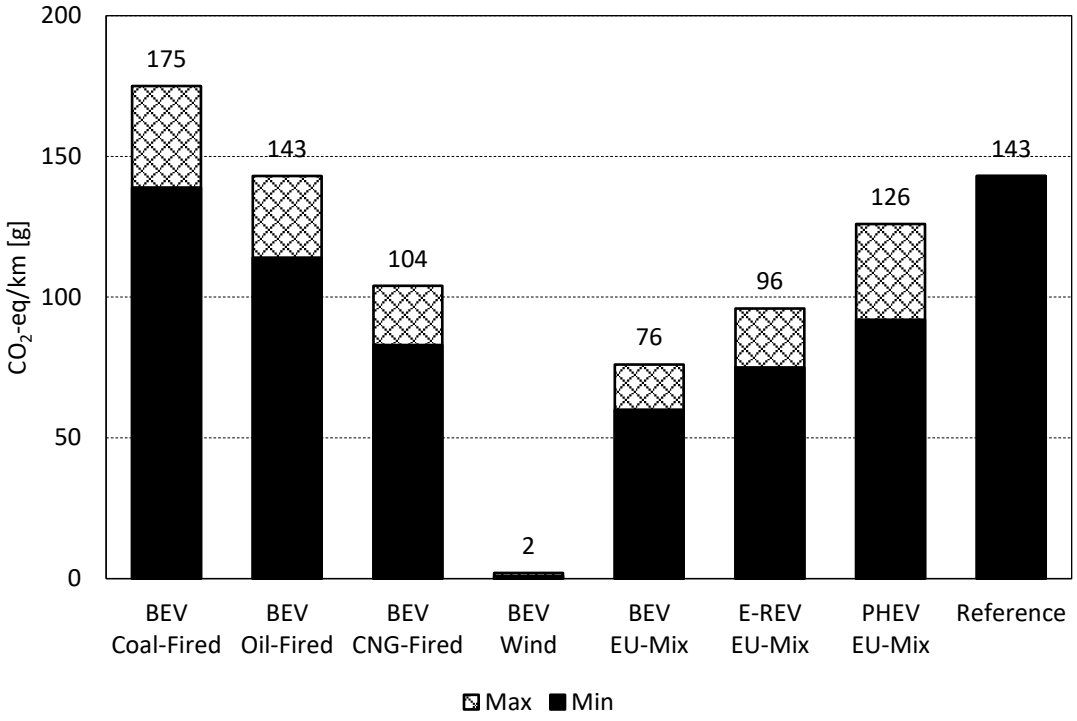

Figure 1-1 Comparison of GHG emissions per km. The data for the figure is from [2].

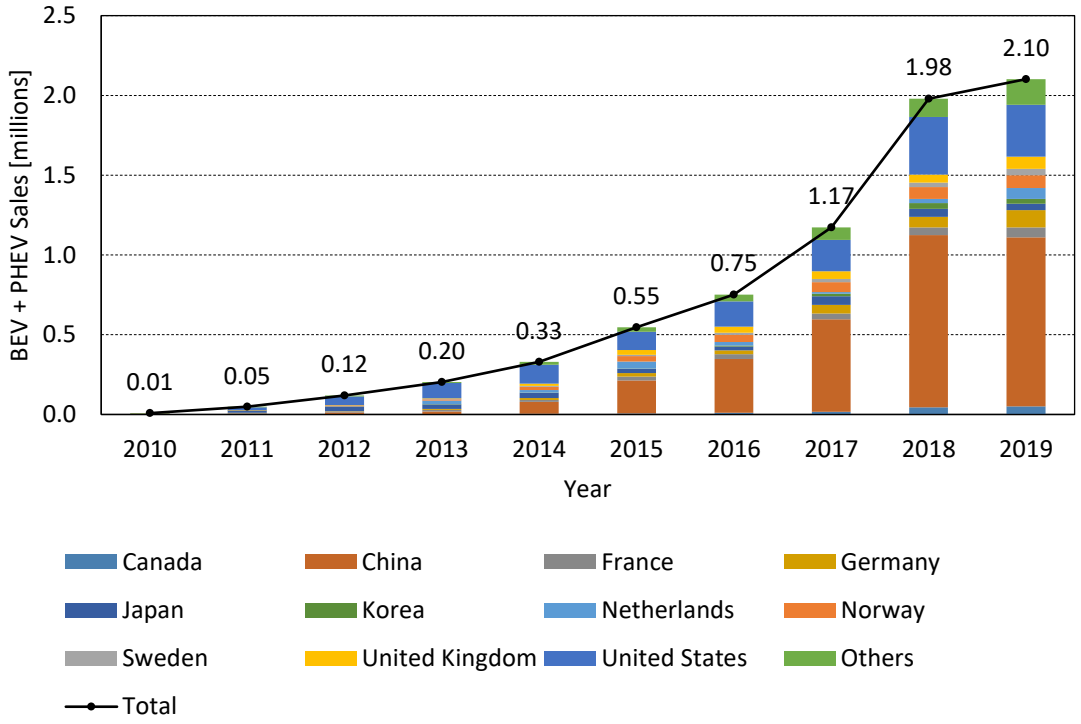

Figure 1-2 Fast growing of the global electric car sales, 2010-2019. The data for the figure is from [3].

1.1.1 Rare-Earth Electric Machines in EV Applications

Electric machines are one of the key components in EVs. To achieve a compact design, rare-earth materials are widely used nowadays. The application of rare-earth materials in electric vehicles start to prevail since Toyota Prius, equipped with permanent magnet synchronous machines (PMSMs), was launched in 1997 [5]. Rare-earth materials, especially Neodymium Iron Boron (NdFeB), allow a strong magnetic field to be generated from a small volume, and this significantly increases torque and power densities of electric machines. A comparison between rare-earth-free material ferrite and rare-earth material NdFeB is made in Figure 1-3, with the data from [5] [6] [7]. As can be seen, the maximum energy product $(B \cdot H)_{\max}$ [8] [9] of NdFeB is generally seven times higher than that of ferrite, which means NdFeB shows a prominent advantage with respect to rare-earth-free magnet materials [5]. However, regarding the application of rare-earth material in electric vehicles, more concerns have been raised in various areas, from market imbalance, environmental and performance perspectives.

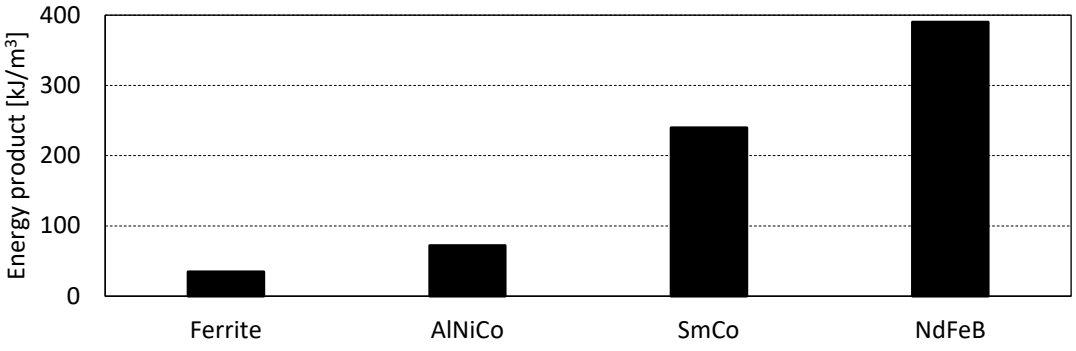

Figure 1-3 Comparison of typical maximum energy products between ferrite and rare-earth magnets. The data for the figure is from [6] [7].

A. Imbalance between Demand and Supply

In general, the rare-earth material used in an electric machine is less than 5% by mass, but more than 70% by material cost and 25% of material related greenhouse gas emission [10] [5]. If the electrification of vehicles follows the same approach as before, a tremendous amount of rare-earth material needs to be consumed. According to the estimation in [11], the demand of NdFeB magnet in EV will become 14 times higher in 2020 compared to that in 2015. However, the growth of NdFeB magnet production will be less than 100% during the same time interval [12]. Therefore, the production capacity seems not able to keep pace with the demand increment and there becomes a huge gap between the demand and supply.

B. Environmental Risk

It has been widely recognized that the extraction and refinement process of rare-earth oxides are the sources of serious pollution [10] [5]. The research from automotive industry agrees with this and suggests that NdFeB magnets may be, per unit mass, more damaging than other materials commonly used in electric machines. The production of NdFeB permanent magnets is a relatively complicated process, which mainly includes smelting, casting, milling, sintering, forming, electroplating, and magnetization. And among all the processes, smelting, casting, sintering and electroplating consume huge amount of electric energy, and generate a large amount of waste slag and waste gas at the same time, which cause great challenges to the environment. In addition, electroplating is a significant source of water pollution, which requires an extremely complicated wastewater treatment system. Furthermore, the recycling of NdFeB has been investigated but until now there are still concerns relating to the quality and repeatability of such recycled magnetic materials [13].

C. Performance and Safety Risk

As the temperature goes higher, rare-earth magnets risk demagnetization. Once the rare-earth magnets are demagnetized, the torque output capability will reduce dramatically. Furthermore, the magnetic flux cannot be shut down even in fault conditions. This can lead to high faulty current, and it is extremely dangerous when a fault happens at high speed operation since the strong magnetic flux will induce high voltages in the stator windings.

1.1.2 Trend to Develop Rare-Earth-Free Electrical Machines

Due to the reasons illustrated above, a tendency has appeared to develop rare–earth–free machines. Following this stream, induction machines (IMs) and electrically excited synchronous machines (EESMs) have become popular candidates. A comparison of the rotors of an IM, a PMSM and an EESM is shown in Figure 1-4. As shown in (a), aluminum or copper bars are commonly applied in the rotor of an IM, in which the field current is induced by the flux created by the stator winding. Then the field current from the rotor excites the machine. Since the field current originates from the stator side, power factor is usually low for IM. An interior PMSM rotor is shown in (b), where rare earth magnets are placed in the rotor. The magnets generate the magnetic flux in the machine without any electric current, which gives low losses in the rotor. An EESM rotor is shown in (c), which employs copper windings instead of rare-earth magnets to generate the magnetic flux, and it shows advantages in the following aspects:

- EESMs are free of rare earth material and therefore is more environmentally friendly with lower cost, easier to produce and easier to recycle.

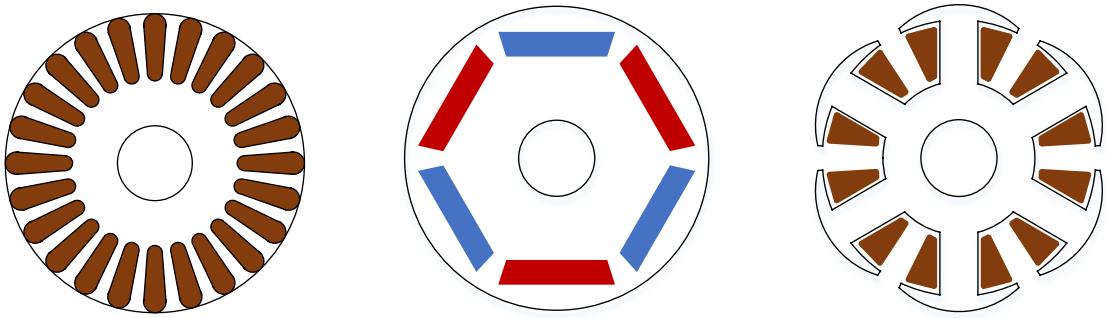

(a) IM. (b) PMSM. (c) EESM.

Figure 1-4 Comparison of rotors of IM, PMSM and EESM.

- Due to the flexible field excitation provided by EESMs, high torque at low speed can be achieved with high field current, and good field weakening at high speed can be achieved by reducing field current.
- In fault conditions at high speed, the EMF in stator winding can be removed by shutting down the field current in EESM rotor. In this way, the harmful overvoltage for insulation and inverter can be avoided.
- Finally, the flexibility of flux also brings a new strategy of sensorless control, which is to inject high-frequency signal on the field current, and the rotor angle information can be extracted from the harmonics in the stator currents.

1.1.3 State of Art for EESM in EV Applications

A. Machine Design

In traction applications, the machine is expected to achieve high starting torque, high power factor in field weakening and high efficiency. Previous studies regarding the design of traction EESM systems are presented in [14], [15], [16] and [17]. The focus is to design and optimize rotor shape so that efficiency and torque production capability are improved.

B. Field Excitation

In terms of sending power to the field winding, high-frequency brushless excitation, which transfers power with no mechanical contact, becomes interesting and is studied in [14] [15]

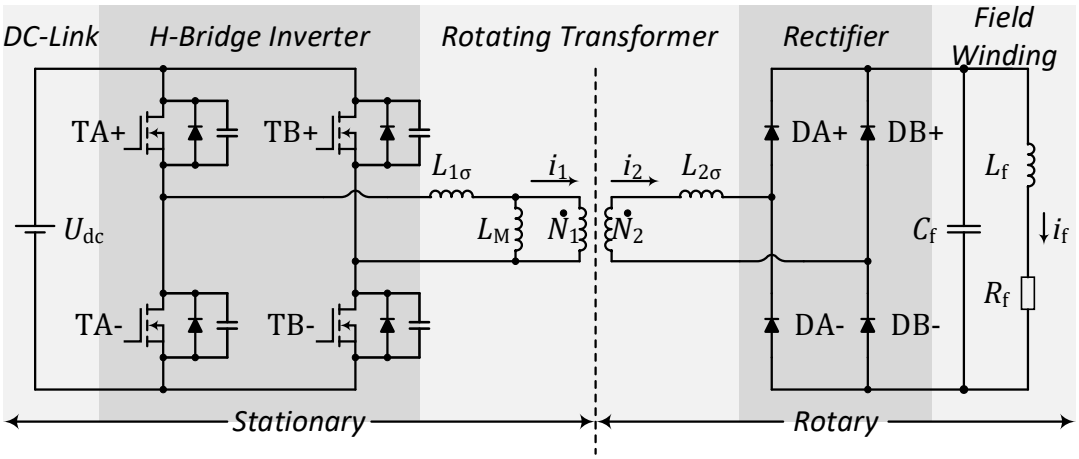

Figure 1-5 Schematic of wireless excitation system dynamic model.

[17] [18] [19] [20] [21] and [22]. Friction losses are reduced due to the avoidance of brushes and slip rings. Efforts to clear the dust, to replace the brushes and to maintain the sliprings are not needed any more. A general schematic of the high-frequency brushless excitation system is shown in Figure 1-5. A rotating transformer is introduced between the power supply and the field winding. The primary side stands still and receives power from an H-bridge inverter under phase-shift control. Through an airgap the power is transmitted to the secondary side. The secondary side rotates together with the rotor. A diode rectifier converts power from AC to DC again and power flows to the field winding.

Some early studies have explored this area. In [14] [15], the design and control of the brushless excitation system are described. A PCB winding is employed to withstand centrifugal force. A fill factor of around 35% is achieved. In [23], a compact high-frequency brushless excitation system is designed and tested with a standalone EESM. The output capacitance of the switch and the leakage inductance of the transformer are used to achieve Zero-Voltage Switching (ZVS). The system efficiency reaches 97.6%. In [18], a geometry optimization is performed to achieve the minimum volume of the transformer. It is concluded that radial-flux excitation gives higher efficiency to the system compared with the axial-flux excitation. In [19], interleaved windings and resonant compensation are introduced. The overall design parameters, including the rotating transformer geometries and the capacitance for compensation, are optimized. It is confirmed that significant improvement of power transfer capability is achieved. In [20], the transformer is fit inside the space of the stator end turns, and SiC diodes are employed. The transformer core and the windings are constructed from high-temperature-rated material so that the components can survive in the high temperature environment. These studies have proved that a compact design of high-frequency brushless excitation system is applicable in EESM drive systems.

Apart from inductive power transfer, capacitive power transfer technology is proposed in EESM field excitation as well [17]. However, the capacitive coupling requires a small airgap with a large area. In order to achieve this, five rotary plates are sandwiched between six stationary plates with 100 mm as the diameter and 115 μm as the airgap. Consequently, reliability issues due to mechanical vibrations become a concern. In addition, the frequency needed is at MHz range (500 kHz – 2.0 MHz in [17]) which brings EMI issues as well. Therefore, this is currently not the mainstream of the study.

C. Machine Control

Different strategies to determine current references are proposed by introducing a magnetic equivalent circuit model or a dynamic equivalent core losses resistance, in order to improve the efficiency including both iron core losses and copper losses [24] [25]. The strategy to minimize the total copper loss including both the stator side and the rotor side is proposed to improve efficiency [26]. Control of power factor is also under consideration to decide current references [27]. In previous studies, the focus is mainly to minimize the losses. However, due to complicated operation situations for traction motors, losses may not be the only quantity to minimize, and various strategies therefore need to be investigated.

Sensorless control of EESM is of great interest as well. In [28] and [29], sensorless control by high-frequency signal injection to the field winding of EESM through brush and slipring is implemented. The advantage of this mechanism is that it is independent from the saliency of the machine. Besides, an inverter-integrated rotor for sensorless control is studied in [30]. In [31], an excitation machine is mounted on the shaft of the EESM, which acts as a sensor for

the rotor position detection of the EESM. Nevertheless, high-frequency signal injection with the high-frequency brushless exciter is claimed to be a huge challenge and has not been solved yet.

1.2 Aim and Scope

The purpose of this study is to investigate the potential of EESM application with high-frequency brushless exciter in EVs. The scope of this study is to tackle some key challenges of EESMs, mainly in aspects of control, design and excitation, which are summarized as follows.

1.2.1 Characteristics Study and Control Strategy

The flexibility of field current in EESMs indicates the possibility to achieve high power factor and the complexity of control strategy to minimize copper losses. Therefore, it is essential to figure out (1) in which condition can high power factor be achieved and (2) in which condition can the total copper loss be minimized.

Moreover, the torque-speed envelope of the machine would be influenced when the field current is adjusted. The torque-speed envelope is decided by the maximum available torque at each speed of the machine, which indicates the maximum starting torque and maximum electromagnetic power of the machine. Thus, it is important to comprehend the impacts on torque-speed envelope in case of different field current levels, especially (1) how would unity power factor be achieved in field-weakening part of the torque-speed envelope so that a maximum electromagnetic power can be achieved, and (2) how would stator and field currents be assigned most properly so that a maximum torque can be achieved.

Furthermore, inside the torque-speed envelope, the adjustable field current in EESM means easier field-weakening at high speed since there is no need to inject high amount of negative d-axis stator current to cancel the rotor flux. This further means lower losses at high speed and consequently higher efficiency compared to PMSM. Hence it is of interest to comprehend the impacts on distribution of efficiency in torque-speed maps when different strategies of controlling stator and field currents are followed.

1.2.2 Machine Dynamic Control

In machine dynamic control, the field-oriented control (FOC) is a mature technology. In FOC structure, (1) current references are calculated based on the torque request, and then (2) the current references are followed by regulating the terminal voltages. To have the FOC structure in EESM dynamic control, the field current is introduced as the third degree of control freedom. Therefore, in EESM dynamic control, one challenge is to determine the current references effectively with three degrees of control freedom. In addition, due to the magnetic coupling between stator and field windings, an EMF spike will be induced in the stator winding when there is a field current rise and vice versa. This EMF spike is proportional to the derivative of current rise and it is a disturbance in EESM current control which does not exist in PMSM current control since the PMSM field excitation is always fixed. Thus, another challenge is to compensate for the EMF disturbances due to the magnetic coupling in dynamic current control.

1.2.3 Machine Design

In traction applications, it is preferable to have high starting torque at low speed and effective field-weakening at high speed. This is a contradiction in PMSM design, since to achieve high starting torque, a high rotor flux is needed whereas a high rotor flux leads to difficulties of

field-weakening at high speed. Therefore, a trade-off of rotor flux always needs to be made in PMSM design. However, this is not a problem for EESM due to the flexibility to adjust field current. Thus, the possibility to achieve both high starting torque and good field-weakening in the same machine design is the key advantage for the application of EESMs.

Nevertheless, the design criteria to maximize this advantage have not been studied yet, specifically (1) following which criterion can starting torque achieve the maximum, (2) following which criterion can electromagnetic power achieve the maximum at high speed. Furthermore, since machine design is a multi-objective problem, another challenge is to integrate both criteria into a systematic design procedure with other optimization objectives, such as to minimize iron-core loss while to have high starting torque.

1.2.4 High-Frequency Brushless Field Excitation

As an alternative to excitation through brushes and sliprings, friction can be reduced when high-frequency brushless excitation is adopted. However, with brushless excitation, the field current becomes physically inaccessible. Consequently, it becomes difficult to feedback control the field current in a closed loop. To solve this problem, it is essential to explore the possibility to estimate the field current from the stationary side of the excitation system.

Another challenge of EESM in traction applications is that, compared to PMSM and IM, the field excitation of EESM requires an H-bridge converter in addition to the three-phase inverter which powers the stator winding. This indicates an extra cost for EESM drives. Hence it is of interest to explore the possibility of using one inverter to power both stator and field windings simultaneously.

1.3 Contributions

Contributions of this study cover the following aspects: characteristics study, machine control, machine design and high-frequency brushless field excitation.

1.3.1 Characteristics Study and Control Strategy

Power factor contours in dq current plane are proposed in this study to comprehend in which condition can high power factor be achieved. Areas with different levels of power factor can be identified with these power factor contours. The most special power factor contour is the one that defines unity power factor. This contour can be used to determine whether the maximum electromagnetic power can be achieved along the torque-speed envelope.

Visualization of machine characteristics with isosurfaces in 3D space is proposed in this study. The traditional illustration using characteristic curves in the dq-plane for PMSM analysis becomes not intuitive in EESM since the field current is introduced as the third degree of control freedom. To improve the visualization in EESM control strategy analysis, the field current is illustrated as an f-axis perpendicular to the dq-plane. Then a 3D space is established, and the characteristic curves in the dq-plane are extended to iso-surfaces in this 3D space. In this 3D space, the current limit is visualized as an oblique elliptic cylinder and unity power factor is visualized as a purple oblique elliptical cone. Copper loss minimization can be illustrated as the copper loss isosurface and the torque isosurface pushing against each other.

To achieve the best performance of the machine, control strategies are studied to find the most proper combination of stator and field currents. Considering saturation of the iron-core, an iterative method is proposed to find the optimum solution of current reference in torque-speed map. Flexible penalty factors are introduced for stator current and field current

separately. Relations between d-axis, q-axis and field currents are derived for different control strategies to achieve different optimization targets. The shape of the torque-speed envelope is decided by the maximum level of field current. Inside the envelope, the distributions of efficiency, power factor and terminal voltage are decided by different control strategies. Relative contents are included in Article VIII of the publication list in Section 1.3.5.

1.3.2 Machine Dynamic Control

In this study, an algorithm is proposed to determine current references by taking torque gradients. This is to tackle the increased complexity of current reference determination in the FOC structure due to the third degree of control freedom introduced by the field current. The move of current reference vector follows the direction of torque gradients so that the torque built by the current references catches the torque request swiftly. When the current limit or voltage limit is reached, extra constraints are introduced. Consequently, the move of current reference vector is redirected following the limits. Therefore, the algorithm also works in the torque boosting and field weakening conditions.

To deal with the disturbances due to the magnetic mutual coupling between stator and field windings, a compensation technique is proposed in dynamic current control. With this technique, an extra voltage component is added into the output of the controller which cancels the induced EMF due to the magnetic mutual coupling. Consequently, the disturbances due to mutual coupling are mitigated. Relative contents are included in Article III of the publication list in Section 1.3.5.

1.3.3 Machine Design

In this study, design criteria are proposed to maximize the starting torque and peak electromagnetic power of EESMs. This is to make use of the flexibility to adjust field current in EESMs. Following these design criteria, a multi-objective machine design procedure is proposed. Pareto Frontier is used to identify the optimal solution. With this procedure, a high peak torque is achieved whereas the losses are kept low. Relative contents are included in Article II of the publication list in Section 1.3.5.

1.3.4 High-Frequency Brushless Field Excitation

To avoid mechanical losses and maintenance, high-frequency brushless excitation is used in this study. A simplified but effective dynamic model of high-frequency brushless excitation system is developed [32]. Based on the model, some key characteristics of the system are studied. Relative contents are included in Article V of the publication list in Section 1.3.5.

Due to that the field winding is inaccessible using high-frequency brushless excitation, to have feedback control of field current in closed-loop, a dynamic estimation method is proposed. An observer is established using the duty cycle of the H-bridge inverter as the input and the dc-link input current as the correction. The algorithm is validated in simulations and experiments. A closed-loop field current control is built by using the estimation of the observer. Relative contents are included in Article I of the publication list in Section 1.3.5.

In this study, a technique is proposed to make use of the common mode switching harmonics of the stator inverter for field excitation [33]. With this technique, it is sufficient to use only one inverter to power both the stator and field windings. To realize this, an extraction circuit is built to form resonance at switching frequency. The rotating transformer and the rectifier are kept the same as those in the conventional solution of brushless excitation. Relative

contents are included in Article XI of the publication list in Section 1.3.5. The harmonic analysis can be applied to mitigate zero-sequence power flow in emulation of traction motors [34]. Relative contents are included in Article XII of the publication list in Section 1.3.5.

1.3.5 List of Publications

I J. Tang, Y. Liu and S. Lundberg, "Estimation Algorithm for Current and Temperature of Field Winding in Electrically Excited Synchronous Machines With High-Frequency Brushless Exciters," in *IEEE Transactions on Power Electronics*, vol. 36, no. 3, pp. 3512-3523, March 2021, doi: 10.1109/TPEL.2020.3017139.

II J. Tang and Y. Liu, "Design of Electrically Excited Synchronous Machines to Achieve Unity Power Factor in Field Weakening for Long-Haul Electric Trucks," 2020 International Conference on Electrical Machines (ICEM), Gothenburg, 2020, pp. 422-428, doi: 10.1109/ICEM49940.2020.9270755.

III J. Tang and Y. Liu, "Dynamic Current Control to Compensate for Magnetic Mutual Coupling in Electrically Excited Synchronous Machines," 2020 International Conference on Electrical Machines (ICEM), Gothenburg, 2020, pp. 1779-1785, doi: 10.1109/ICEM49940.2020.9270842.

IV G. Mademlis, Y. Liu, J. Tang, L. Boscaglia and N. Sharma, "Performance Evaluation of Electrically Excited Synchronous Machine compared to PMSM for High-Power Traction Drives," 2020 International Conference on Electrical Machines (ICEM), Gothenburg, 2020, pp. 1793-1799, doi: 10.1109/ICEM49940.2020.9270852.

V J. Tang, Y. Liu and N. Sharma, "Modeling and Experimental Verification of High-Frequency Inductive Brushless Exciter for Electrically Excited Synchronous Machines," in IEEE Transactions on Industry Applications, vol. 55, no. 5, pp. 4613-4623, Sept.-Oct. 2019, doi: 10.1109/TIA.2019.2921259.

VI J. Tang and Y. Liu, "Design and Experimental Verification of a 48 V 20 kW Electrically Excited Synchronous Machine for Mild Hybrid Vehicles," 2018 XIII International Conference on Electrical Machines (ICEM), Alexandroupoli, 2018, pp. 649-655, doi: 10.1109/ICELMACH.2018.8507259.

VII J. Tang, Y. Liu, Y. Rastogi, N. Sharma and T. Shukla, "Study of Voltage Spikes and Temperature Rise in Power Module Based Integrated Converter for 48 V 20 kW Electrically Excited Synchronous Machines," 2018 IEEE Applied Power Electronics Conference and Exposition (APEC), San Antonio, TX, 2018, pp. 210-217, doi: 10.1109/APEC.2018.8341011.

VIII J. Tang and Y. Liu, "Comparison of copper loss minimization and field current minimization for Electrically Excited Synchronous Motor in mild hybrid drives," 2017 19th European Conference on Power Electronics and Applications (EPE'17 ECCE Europe), Warsaw, 2017, pp. P.1-P.10, doi: 10.23919/EPE17ECCEEurope.2017.8099352.

IX Y. Liu, D. Pehrman, O. Lykartsis, J. Tang and T. Liu, "High frequency exciter of electrically excited synchronous motors for vehicle applications," 2016 XXII International Conference on Electrical Machines (ICEM), Lausanne, 2016, pp. 378-383, doi: 10.1109/ICELMACH.2016.7732554.

X J. Tang, S. Lundberg, F. Marra and Y. Liu, "Sensorless control of a PMSM with a transmission system including shunt branches," 2016 XXII International Conference on Electrical Machines (ICEM), Lausanne, 2016, pp. 1160-1166, doi: 10.1109/ICELMACH.2016.7732671.

XI J. Tang, D. Pehrman, G. Mademlis and Y. Liu, "Common Mode Power Control of Three-Phase Inverter for Auxiliary Load without Access to Neutral Point (Submitted on 2021-02-20)," IEEE Transactions on Power Electronics.

XII G. Mademlis, N. Sharma, Y. Liu and J. Tang, "Zero-Sequence Current Reduction Technique for Electrical Machine Emulators with DC-Coupling by Regulating the SVM Zero States (Submitted on 2021-02-23)," IEEE Transactions on Industrial Electronics.

Chapter 2

Machine Modeling

In this chapter, modeling of electrical and thermal parts of an EESM is presented. The model is used for the analysis of machine characteristics, machine design and machine control in the coming chapters. Electrical modeling can be done in stationary frame and then transformed to rotary frame using abc-αβγ transformation (Park) [35] and αβγ-dqo transformation (Clarke) [36]. These relative contents are attached in Appendix A. The transformation adopted in this study is amplitude-invariant. In this chapter, modeling starts directly in dq-frame.

2.1 Electrical Dynamics

In dynamic control of the machine, an accurate model of the electrical dynamics is required, whereas the accuracy of efficiency calculation is not the focus. Hence the current consumption due to iron-core losses can be neglected in this section. The terminal voltages $\boldsymbol{u}$, currents $\boldsymbol{i}$, and flux linkages $\boldsymbol{\psi}$ follow

$$\boldsymbol{u} = \boldsymbol{R}\boldsymbol{i} + \boldsymbol{\omega}\boldsymbol{\psi} + \frac{d\boldsymbol{\psi}}{dt} \tag{2-1}$$

where the vectors consist of d-axis, q-axis and field quantities

$$\boldsymbol{u} = \begin{bmatrix} u_\mathrm{d} \\ u_\mathrm{q} \\ u_\mathrm{f} \end{bmatrix} \quad , \quad \boldsymbol{i} = \begin{bmatrix} i_\mathrm{d} \\ i_\mathrm{q} \\ i_\mathrm{f} \end{bmatrix} \quad , \quad \boldsymbol{\psi} = \begin{bmatrix} \psi_\mathrm{d} \\ \psi_\mathrm{q} \\ \psi_\mathrm{f} \end{bmatrix} \tag{2-2}$$

the resistance matrix $\boldsymbol{R}$ consists of stator resistance R_s and field resistance R_f, and the speed matrix $\boldsymbol{\omega}$ consists of rotation speed ω_r

$$\boldsymbol{R} = \begin{bmatrix} R_\mathrm{s} & 0 & 0 \\ 0 & R_\mathrm{s} & 0 \\ 0 & 0 & R_\mathrm{f} \end{bmatrix} \quad , \quad \boldsymbol{\omega} = \begin{bmatrix} 0 & -\omega_\mathrm{r} & 0 \\ \omega_\mathrm{r} & 0 & 0 \\ 0 & 0 & 0 \end{bmatrix} \tag{2-3}$$

The differential of flux linkages can be expressed by incremental inductances and currents

$$d\boldsymbol{\psi} = \boldsymbol{l}d\boldsymbol{i} \tag{2-4}$$

where $\boldsymbol{l}$ is the incremental inductance matrix which is the Jacobian of the flux linkage matrix

$$\boldsymbol{l} = \begin{bmatrix} l_\mathrm{dd} & l_\mathrm{dq} & l_\mathrm{df} \\ l_\mathrm{qd} & l_\mathrm{qq} & l_\mathrm{qf} \\ l_\mathrm{fd} & l_\mathrm{fq} & l_\mathrm{ff} \end{bmatrix} = \begin{bmatrix} \partial\psi_\mathrm{d}/\partial i_\mathrm{d} & \partial\psi_\mathrm{d}/\partial i_\mathrm{q} & \partial\psi_\mathrm{d}/\partial i_\mathrm{f} \\ \partial\psi_\mathrm{q}/\partial i_\mathrm{d} & \partial\psi_\mathrm{q}/\partial i_\mathrm{q} & \partial\psi_\mathrm{q}/\partial i_\mathrm{f} \\ \partial\psi_\mathrm{f}/\partial i_\mathrm{d} & \partial\psi_\mathrm{f}/\partial i_\mathrm{q} & \partial\psi_\mathrm{f}/\partial i_\mathrm{f} \end{bmatrix} \tag{2-5}$$

The incremental inductance matrix can be decomposed into two parts, the self-inductance part and the mutual inductance part

$$\boldsymbol{l} = \boldsymbol{l}_\mathbf{self} + \boldsymbol{l}_\mathbf{mutual} \tag{2-6}$$

where

$$\boldsymbol{l}_{\mathbf{self}} = \begin{bmatrix} l_{\mathrm{dd}} & 0 & 0 \\ 0 & l_{\mathrm{qq}} & 0 \\ 0 & 0 & l_{\mathrm{ff}} \end{bmatrix} \quad , \quad \boldsymbol{l}_{\mathbf{mutual}} = \begin{bmatrix} 0 & l_{\mathrm{dq}} & l_{\mathrm{df}} \\ l_{\mathrm{qd}} & 0 & l_{\mathrm{qf}} \\ l_{\mathrm{fd}} & l_{\mathrm{fq}} & 0 \end{bmatrix} \tag{2-7}$$

Usually the mutual inductances between d- and q-axis are much smaller than other elements. Hence sometimes an approximation can be made

$$\boldsymbol{l} \approx \begin{bmatrix} l_{\mathrm{dd}} & 0 & l_{\mathrm{df}} \\ 0 & l_{\mathrm{qq}} & 0 \\ l_{\mathrm{fd}} & 0 & l_{\mathrm{ff}} \end{bmatrix} = \begin{bmatrix} l_{\mathrm{d}} & 0 & l_{\mathrm{m}} \\ 0 & l_{\mathrm{q}} & 0 \\ \frac{3}{2} l_{\mathrm{m}} & 0 & l_{\mathrm{f}} \end{bmatrix} \tag{2-8}$$

The factor 3/2 appears in the matrix due to the amplitude-invariant transformation, which is explained in Appendix A. In case of no saturation, the inductances are constant. Otherwise, the values are variables. With the definition in (2-5), (2-1) can be reformulated and current derivatives can be calculated

$$\boldsymbol{u} = \boldsymbol{R}\boldsymbol{i} + \boldsymbol{\omega}\boldsymbol{\psi} + \boldsymbol{l}\frac{d\boldsymbol{i}}{dt} \quad \Rightarrow \quad \frac{d\boldsymbol{i}}{dt} = \boldsymbol{l}^{-1}(\boldsymbol{u} - \boldsymbol{R}\boldsymbol{i} - \boldsymbol{\omega}\boldsymbol{\psi}) \tag{2-9}$$

The schematic diagram of the dynamic model can be illustrated in Figure 2-1. The inputs of the model are terminal voltages and rotation speed, while the outputs are terminal currents and electromagnetic torque as shown in (a). The current derivatives are calculated by using (2-9) and then the currents are obtained by integrating current derivatives as shown in (b) and (c). The flux linkages are interpolated using the maps obtained from finite element method (FEM) analysis. The inductance map is calculated from the flux linkage maps using (2-5). The flux linkages can also be described using apparent inductances

$$\boldsymbol{\psi} = \boldsymbol{L}\boldsymbol{i} \tag{2-10}$$

where $\boldsymbol{L}$ is the apparent inductance matrix, which can be calculated as

$$\boldsymbol{L} = \begin{bmatrix} L_{\mathrm{dd}} & L_{\mathrm{dq}} & L_{\mathrm{df}} \\ L_{\mathrm{qd}} & L_{\mathrm{qq}} & L_{\mathrm{qf}} \\ L_{\mathrm{fd}} & L_{\mathrm{fq}} & L_{\mathrm{ff}} \end{bmatrix} = \begin{bmatrix} \frac{\int l_{\mathrm{dd}} \cdot di_{\mathrm{d}}}{i_{\mathrm{d}}} & \frac{\int l_{\mathrm{dq}} \cdot di_{\mathrm{q}}}{i_{\mathrm{q}}} & \frac{\int l_{\mathrm{df}} \cdot di_{\mathrm{f}}}{i_{\mathrm{f}}} \\ \frac{\int l_{\mathrm{qd}} \cdot di_{\mathrm{d}}}{i_{\mathrm{d}}} & \frac{\int l_{\mathrm{qq}} \cdot di_{\mathrm{q}}}{i_{\mathrm{q}}} & \frac{\int l_{\mathrm{qf}} \cdot di_{\mathrm{f}}}{i_{\mathrm{f}}} \\ \frac{\int l_{\mathrm{fd}} \cdot di_{\mathrm{d}}}{i_{\mathrm{d}}} & \frac{\int l_{\mathrm{fq}} \cdot di_{\mathrm{q}}}{i_{\mathrm{q}}} & \frac{\int l_{\mathrm{ff}} \cdot di_{\mathrm{f}}}{i_{\mathrm{f}}} \end{bmatrix} \tag{2-11}$$

Similar to (2-8), an approximation can be made to apparent inductances

$$\boldsymbol{L} \approx \begin{bmatrix} L_{\mathrm{dd}} & 0 & L_{\mathrm{df}} \\ 0 & L_{\mathrm{qq}} & 0 \\ L_{\mathrm{fd}} & 0 & L_{\mathrm{ff}} \end{bmatrix} = \begin{bmatrix} L_{\mathrm{d}} & 0 & L_{\mathrm{m}} \\ 0 & L_{\mathrm{q}} & 0 \\ \frac{3}{2} L_{\mathrm{m}} & 0 & L_{\mathrm{f}} \end{bmatrix} \tag{2-12}$$

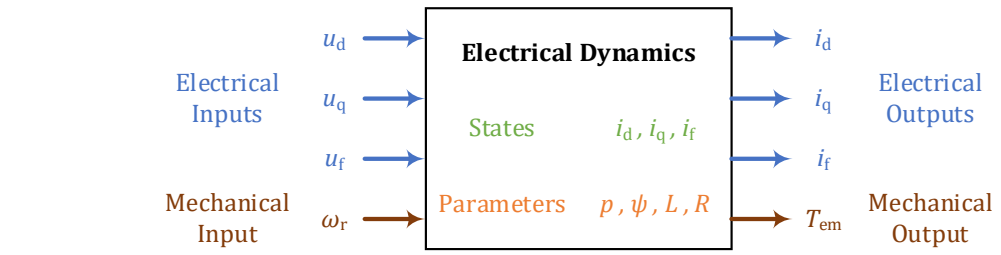

(a) Inputs, outputs, states and parameters of electrical dynamic model.

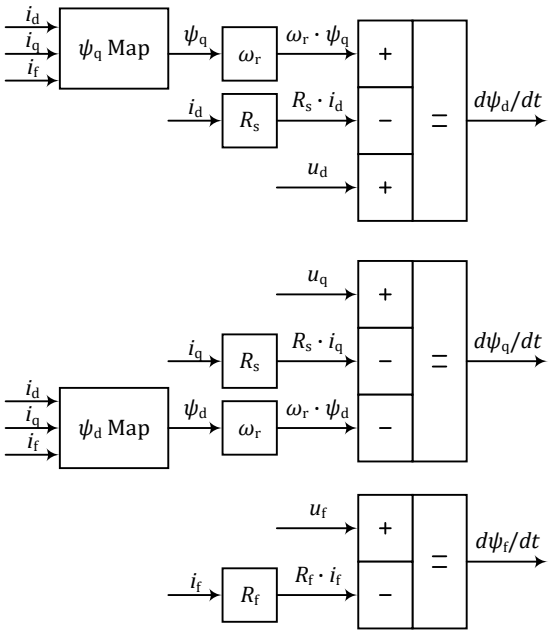

(b) Determination of flux linkage derivatives.

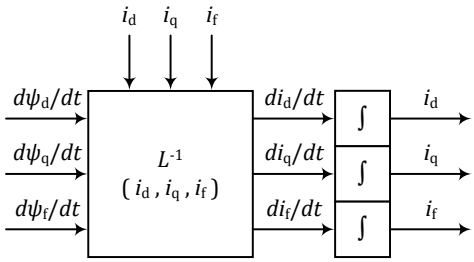

(c) Determination of currents.

Figure 2-1 Schematic diagram of EESM dynamic model.

In case of $L_\mathrm{d} = L_\mathrm{q}$, the machine is named as non-salient. Otherwise, it is salient. The difference and ratio in between can be used to describe the saliency

$$L_\Delta = L_\mathrm{d} - L_\mathrm{q} \quad , \quad k_\mathrm{dq} = \frac{L_\mathrm{d}}{L_\mathrm{q}} \tag{2-13}$$

With the apparent inductances defined, (2-9) can be formulated as

$$\frac{d\boldsymbol{i}}{dt} = \boldsymbol{l}^{-1}(\boldsymbol{u} - \boldsymbol{R}\boldsymbol{i} - \boldsymbol{\omega}\boldsymbol{L}\boldsymbol{i}) \tag{2-14}$$

Then the model can be structured into state space format

$$\begin{aligned} \frac{d\boldsymbol{i}}{dt} &= \boldsymbol{A}\ \boldsymbol{i} + \boldsymbol{B}\ \boldsymbol{u} \\ \boldsymbol{i} &= \boldsymbol{C}\ \boldsymbol{i} + \boldsymbol{D}\ \boldsymbol{u} \end{aligned} \tag{2-15}$$

where

$$\begin{aligned} \boldsymbol{A} &= -\boldsymbol{l}^{-1}(\boldsymbol{R} + \boldsymbol{\omega}\boldsymbol{L}) & \boldsymbol{B} &= \boldsymbol{l}^{-1} \\ \boldsymbol{C} &= \boldsymbol{I} & \boldsymbol{D} &= \boldsymbol{O} \end{aligned} \tag{2-16}$$

2.2 Instantaneous Power

According to the instantaneous power theory [37], the instantaneous stator power can be calculated by voltages and currents at the stator terminal

$$\vec{s}_\mathrm{s} = \frac{3}{2} \cdot \vec{u}_\mathrm{s} \cdot \vec{\imath}_\mathrm{s}^{*} \quad \Rightarrow \quad \begin{cases} p_\mathrm{s} & = & \mathrm{Re}\{\vec{s}_\mathrm{s}\} & = & \frac{3}{2} \cdot \left(u_\mathrm{d} \cdot i_\mathrm{d} + u_\mathrm{q} \cdot i_\mathrm{q}\right) \\ q_\mathrm{s} & = & \mathrm{Im}\{\vec{s}_\mathrm{s}\} & = & \frac{3}{2} \cdot \left(u_\mathrm{q} \cdot i_\mathrm{d} - u_\mathrm{d} \cdot i_\mathrm{q}\right) \\ s_\mathrm{s} & = & \left\|\vec{s}_\mathrm{s}\right\| & = & \frac{3}{2} \cdot \|\vec{u}_\mathrm{s}\| \cdot \|\vec{\imath}_\mathrm{s}\| \end{cases} \tag{2-17}$$

The basics of instantaneous power theory are introduced in Appendix B. The instantaneous power due to the interaction between EMFs and currents are

$$\vec{s}_\mathrm{em} = \frac{3}{2} \cdot \vec{e}_\mathrm{s} \cdot \vec{\imath}_\mathrm{s}^{*} \quad \Rightarrow \quad \begin{cases} p_\mathrm{em} & = & \mathrm{Re}\{\vec{s}_\mathrm{em}\} & = & \frac{3}{2} \cdot \left(e_\mathrm{d} \cdot i_\mathrm{d} + e_\mathrm{q} \cdot i_\mathrm{q}\right) \\ q_\mathrm{em} & = & \mathrm{Im}\{\vec{s}_\mathrm{em}\} & = & \frac{3}{2} \cdot \left(e_\mathrm{q} \cdot i_\mathrm{d} - e_\mathrm{d} \cdot i_\mathrm{q}\right) \\ s_\mathrm{em} & = & \|\vec{s}_\mathrm{em}\| & = & \frac{3}{2} \cdot \|\vec{e}_\mathrm{s}\| \cdot \|\vec{\imath}_\mathrm{s}\| \end{cases} \tag{2-18}$$

where

$$e_\mathrm{d} = -\omega_\mathrm{r} \cdot \psi_\mathrm{q} \quad , \quad e_\mathrm{q} = \omega_\mathrm{r} \cdot \psi_\mathrm{d} \tag{2-19}$$

and p_em is the electromagnetic power produced by the machine. Due to resistive losses, $p_\mathrm{s} > p_\mathrm{em}$ while $q_\mathrm{s} = q_\mathrm{em}$. With the apparent inductances introduced in (2-11), the power can also be expressed in quadratic form as

$$p_\mathrm{em} = \frac{3}{2} \cdot \omega_\mathrm{r} \cdot \boldsymbol{i}^\mathrm{T} \boldsymbol{K}_\mathbf{P} \boldsymbol{i} \quad , \quad q_\mathrm{em} = \frac{3}{2} \cdot \omega_\mathrm{r} \cdot \boldsymbol{i}^\mathrm{T} \boldsymbol{K}_\mathbf{Q} \boldsymbol{i} \tag{2-20}$$

where

$$\boldsymbol{K}_\mathbf{P} = \begin{bmatrix} -L_\mathrm{qd} & \frac{L_\mathrm{dd} - L_\mathrm{qq}}{2} & -\frac{L_\mathrm{qf}}{2} \\ \frac{L_\mathrm{dd} - L_\mathrm{qq}}{2} & L_\mathrm{dq} & \frac{L_\mathrm{df}}{2} \\ -\frac{L_\mathrm{qf}}{2} & \frac{L_\mathrm{df}}{2} & 0 \end{bmatrix} \quad , \quad \boldsymbol{K}_\mathbf{Q} = \begin{bmatrix} L_\mathrm{dd} & \frac{L_\mathrm{dq} + L_\mathrm{qd}}{2} & \frac{L_\mathrm{df}}{2} \\ \frac{L_\mathrm{dq} + L_\mathrm{qd}}{2} & L_\mathrm{qq} & \frac{L_\mathrm{qf}}{2} \\ \frac{L_\mathrm{df}}{2} & \frac{L_\mathrm{qf}}{2} & 0 \end{bmatrix} \tag{2-21}$$

Neglecting the couplings between d- and q-axis, (2-21) becomes

$$\boldsymbol{K}_\mathbf{P} = \begin{bmatrix} 0 & \frac{L_\mathrm{d} - L_\mathrm{q}}{2} & 0 \\ \frac{L_\mathrm{d} - L_\mathrm{q}}{2} & 0 & \frac{L_\mathrm{m}}{2} \\ 0 & \frac{L_\mathrm{m}}{2} & 0 \end{bmatrix} \quad , \quad \boldsymbol{K}_\mathbf{Q} = \begin{bmatrix} L_\mathrm{d} & 0 & \frac{L_\mathrm{m}}{2} \\ 0 & L_\mathrm{q} & 0 \\ \frac{L_\mathrm{m}}{2} & 0 & 0 \end{bmatrix} \tag{2-22}$$

2.3 Electromagnetic Torque

The instantaneous electromagnetic torque can be derived from the electromagnetic power

$$T_{\mathrm{em}} = \frac{p_{\mathrm{em}}}{\Omega_{\mathrm{r}}} = \frac{3}{2} \cdot p \cdot \left(\psi_{\mathrm{d}} \cdot i_{\mathrm{q}} - \psi_{\mathrm{q}} \cdot i_{\mathrm{d}}\right) \tag{2-23}$$

where Ω_{r} is the mechanical speed and p is the number of pole pairs. With the apparent inductances, the torque can also be formulated as

$$T_{\mathrm{em}} = \frac{3}{2} \cdot p \cdot \boldsymbol{i}^{\mathrm{T}} \boldsymbol{K}_{\mathbf{P}} \boldsymbol{i} \tag{2-24}$$

In case of constant d- and q-axis inductances and neglecting coupling between d- and q-axis,

$$T_{\mathrm{em}} = \frac{3}{2} \cdot p \cdot \left[L_{\mathrm{m}} \cdot i_{\mathrm{f}} + \left(L_{\mathrm{d}} - L_{\mathrm{q}}\right) \cdot i_{\mathrm{d}}\right] \cdot i_{\mathrm{q}} \tag{2-25}$$

As can be seen, T_{em} consists of two components, a synchronous torque component, which is due to the interaction between field excitation and q-axis current, and a reluctance torque component, which is due to the difference between d- and q-axis inductances

$$T_{\mathrm{syn}} = \frac{3}{2} \cdot p \cdot L_{\mathrm{m}} \cdot i_{\mathrm{f}} \cdot i_{\mathrm{q}} \quad , \quad T_{\mathrm{rel}} = \frac{3}{2} \cdot p \cdot \left(L_{\mathrm{d}} - L_{\mathrm{q}}\right) \cdot i_{\mathrm{d}} \cdot i_{\mathrm{q}} \tag{2-26}$$

For a non-salient EESM, the reluctance torque component is zero.

2.4 Copper Losses

The total copper loss p_{Cu} consists of stator copper loss $p_{\mathrm{Cu.s}}$ and field copper loss $p_{\mathrm{Cu.f}}$

$$p_{\mathrm{Cu}} = p_{\mathrm{Cu.s}} + p_{\mathrm{Cu.f}} \tag{2-27}$$

The stator copper loss is

$$p_{\mathrm{Cu.s}} = \left(i_{\mathrm{a}}^2 + i_{\mathrm{b}}^2 + i_{\mathrm{c}}^2\right) \cdot R_{\mathrm{s}} = \frac{3}{2} \cdot \left(i_{\mathrm{d}}^2 + i_{\mathrm{q}}^2\right) \cdot R_{\mathrm{s}} = \frac{3}{2} \cdot i_{\mathrm{s}}^2 \cdot R_{\mathrm{s}} \tag{2-28}$$

where i_{s} is the amplitude of the stator phase current, while the field copper loss is

$$p_{\mathrm{Cu.f}} = i_{\mathrm{f}}^2 \cdot R_{\mathrm{f}} \tag{2-29}$$

The copper loss can also be expressed in quadratic form as

$$p_{\mathrm{Cu}} = \boldsymbol{i}^{\mathrm{T}} \boldsymbol{K}_{\mathbf{R}} \boldsymbol{i} \tag{2-30}$$

where

$$\boldsymbol{K}_{\mathbf{R}} = \begin{bmatrix} 3R_{\mathrm{s}}/2 & 0 & 0 \\ 0 & 3R_{\mathrm{s}}/2 & 0 \\ 0 & 0 & R_{\mathrm{f}} \end{bmatrix} \tag{2-31}$$

2.5 Iron-Core Losses

The iron-core loss p_{Fe} of lamination steel is modeled as the sum of hysteresis loss $p_{\mathrm{Fe.h}}$, classical eddy current loss $p_{\mathrm{Fe.c}}$ and excess eddy current loss $p_{\mathrm{Fe.e}}$ [38]

$$p_{\mathrm{Fe}} = p_{\mathrm{Fe.h}} + p_{\mathrm{Fe.c}} + p_{\mathrm{Fe.e}} \tag{2-32}$$

where

$$p_{\mathrm{Fe.h}} = k_{\mathrm{h}} \cdot f \cdot B_{\mathrm{m}}^2 \cdot M \quad , \quad p_{\mathrm{Fe.c}} = k_{\mathrm{c}} \cdot f^2 \cdot B_{\mathrm{m}}^2 \cdot M \quad , \quad p_{\mathrm{Fe.e}} = k_{\mathrm{e}} \cdot f^{1.5} \cdot B_{\mathrm{m}}^{1.5} \cdot M \tag{2-33}$$

where k_{h}, k_{c}, k_{e} are coefficients of hysteresis loss, classical eddy current loss, excess eddy current loss, f is frequency, B_{m} is the flux density amplitude and M is the mass of the lamination steel. The values of k_{h} and k_{c} for commonly used lamination steels in automotive machines are shown in Table 2-1, whereas the values of k_{e} of these materials are negligible.

Table 2-1 Iron-Core loss parameters

Lamination Grade	$\boldsymbol{\rho_{\mathrm{m}}}$	$\boldsymbol{k_{\mathrm{h}}}$	$\boldsymbol{k_{\mathrm{c}}}$
	$\mathbf{kg/m^3}$	$\mathbf{W/m^3}$	$\mathbf{W/m^3}$
SURA M235-35A	7600	204.5	0.3239
SURA M250-35A	7600	219.3	0.3446
B35AV1500	7650	130.7	0.3279
B35AV1900	7650	156.2	0.5543

Therefore, it is applicable to only consider $p_{\mathrm{Fe.h}}$ and $p_{\mathrm{Fe.c}}$, which means

$$p_{\mathrm{Fe}} \propto B_{\mathrm{m}}^2 \cdot M \tag{2-34}$$

Considering only fundamental component of B_{m}, the iron-core loss at a frequency f_2 can be scaled from the iron-core loss at another frequency f_1, i.e.

$$\frac{p_{\mathrm{Fe.2}}}{p_{\mathrm{Fe.1}}} = \frac{k_{\mathrm{h}} \cdot f_2 \cdot B_{\mathrm{m}}^2 \cdot M + k_{\mathrm{c}} \cdot f_2^2 \cdot B_{\mathrm{m}}^2 \cdot M}{k_{\mathrm{h}} \cdot f_1 \cdot B_{\mathrm{m}}^2 \cdot M + k_{\mathrm{c}} \cdot f_1^2 \cdot B_{\mathrm{m}}^2 \cdot M} = \frac{k_{\mathrm{h}} \cdot f_2 + k_{\mathrm{c}} \cdot f_2^2}{k_{\mathrm{h}} \cdot f_1 + k_{\mathrm{c}} \cdot f_1^2} \tag{2-35}$$

To model the iron-core loss more accurately, additional losses due to rotational fields and sheet cutting can be considered as well [39]. The corrected iron-core loss $p_{\mathrm{Fe.cor}}$ becomes

$$p_{\mathrm{Fe.cor}} = p_{\mathrm{Fe}} \cdot k_{\mathrm{rot}} \cdot k_{\mathrm{cut}} \tag{2-36}$$

where k_{rot} is the rotation correction factor and k_{cut} is the sheet cutting correction factor. From the results in [39], the range of k_{rot} are 1.04 – 1.06 for machines in MW range whereas around 1.02 for machines in kW range. For a strip width thinner than 30 mm, k_{cut} is positive, whereas k_{cut} is negative for a strip width wider than 30 mm. For instance, k_{cut} is around 1.02 with a strip width of 10 mm.

In dynamic modeling, an iron-core loss map p_{Fe} as a function of i_{d}, i_{q} and i_{f} can be calculated in FEM at a base speed. Then interpolation and scaling are applied based on (2-36) to find the instantaneous iron-core loss

$$p_{\mathrm{Fe}}\left(i_{\mathrm{d}}, i_{\mathrm{q}}, i_{\mathrm{f}}, f\right) = \frac{k_{\mathrm{h}} \cdot f + k_{\mathrm{c}} \cdot f^2}{k_{\mathrm{h}} \cdot f_{\mathrm{base}} + k_{\mathrm{c}} \cdot f_{\mathrm{base}}^2} \cdot p_{\mathrm{Fe.base}}\left(i_{\mathrm{d}}, i_{\mathrm{q}}, i_{\mathrm{f}}\right) \tag{2-37}$$

2.6 Steady State Model Considering Iron-Core Current Consumption

In this thesis, the lower-case letters e, u and i are used to describe instantaneous quantities, whereas upper-case letters E, U and I are used to describe steady state quantities. The steady state model can be obtained by setting $\frac{d\boldsymbol{i}}{dt} = 0$ in (2-1)

$$\boldsymbol{U} = \boldsymbol{R}\boldsymbol{I} + \boldsymbol{\omega}\boldsymbol{\psi} \tag{2-38}$$

This equation is true in general. However, especially in machine design, when a higher accuracy of efficiency calculation is required, the voltage drop across the end winding inductance and the additional current consumption due to the iron-core losses need to be included. To implement this, the end winding inductance is represented separately, and an iron-core loss branch is added in parallel to the electromagnetic branch as shown in Figure 2-2. The flux linkage used to calculate the terminal voltage in (2-38) consists of the electromagnetic part obtained from FEM and the end winding part

$$\psi_{\mathrm{d}} = \psi_{\mathrm{d.em}} + L_{\mathrm{d.end}} \cdot I_{\mathrm{d}} \quad , \quad \psi_{\mathrm{q}} = \psi_{\mathrm{q.em}} + L_{\mathrm{q.end}} \cdot I_{\mathrm{q}} \tag{2-39}$$

The terminal current used in (2-38) consists of the components going through the electromagnetic branch and the iron-core loss branch

$$I_{\mathrm{d}} = I_{\mathrm{d.em}} - I_{\mathrm{d.Fe}} \quad , \quad I_{\mathrm{q}} = I_{\mathrm{q.em}} + I_{\mathrm{q.Fe}} \tag{2-40}$$

The iron-core loss branch current consumption can be calculated as

$$I_{\mathrm{d.Fe}} = \frac{P_{\mathrm{d.Fe}}}{\omega_{\mathrm{r}} \cdot \psi_{\mathrm{q.em}}} \quad , \quad I_{\mathrm{q.Fe}} = \frac{P_{\mathrm{q.Fe}}}{\omega_{\mathrm{r}} \cdot \psi_{\mathrm{d.em}}} \tag{2-41}$$

where $P_{\mathrm{d.Fe}}$ and $P_{\mathrm{q.Fe}}$ are the iron-core losses in d- and q-axis respectively

$$P_{\mathrm{d.Fe}} = \frac{\psi_{\mathrm{q.em}}^2}{\psi_{\mathrm{d.em}}^2 + \psi_{\mathrm{q.em}}^2} \cdot P_{\mathrm{Fe}} \quad , \quad P_{\mathrm{q.Fe}} = \frac{\psi_{\mathrm{d.em}}^2}{\psi_{\mathrm{d.em}}^2 + \psi_{\mathrm{q.em}}^2} \cdot P_{\mathrm{Fe}} \tag{2-42}$$

From (2-41) and (2-42), the equivalent resistance in iron-core branch can be calculated as

$$R_{\mathrm{Fe}} = \frac{P_{\mathrm{d.Fe}}}{I_{\mathrm{d.Fe}}^2} = \frac{P_{\mathrm{q.Fe}}}{I_{\mathrm{q.Fe}}^2} = \omega_{\mathrm{r}}^2 \cdot \frac{\psi_{\mathrm{d.em}}^2 + \psi_{\mathrm{q.em}}^2}{P_{\mathrm{Fe}}} \tag{2-43}$$

In (2-43) when both $\psi_{\mathrm{d.em}}$ and $\psi_{\mathrm{q.em}}$ are close to zero, P_{Fe} is also close to zero. In this case, R_{Fe} can be interpolated from the points around it. It should be pointed out that, (2-41) and (2-42) are intermediate steps to achieve (2-43). In practical implementations, R_{Fe} is firstly calculated by using (2-43). Then $I_{\mathrm{d.Fe}}$ and $I_{\mathrm{q.Fe}}$ are calculated as

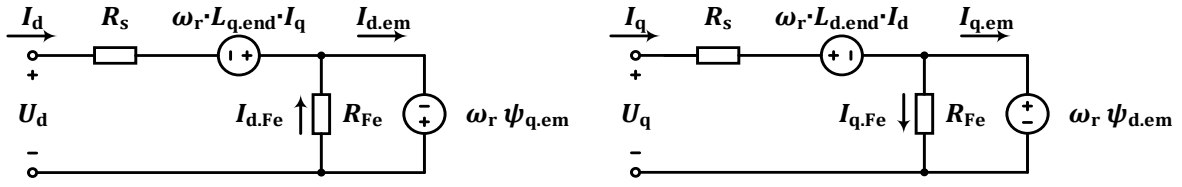

(a) Circuit in d-axis. (b) Circuit in q-axis.

Figure 2-2 Circuit diagram of EESM steady state model.

$$I_{\mathrm{d.Fe}} = \frac{\omega_{\mathrm{r}} \cdot \psi_{\mathrm{q.em}}}{R_{\mathrm{Fe}}} \quad , \quad I_{\mathrm{q.Fe}} = \frac{\omega_{\mathrm{r}} \cdot \psi_{\mathrm{d.em}}}{R_{\mathrm{Fe}}} \tag{2-44}$$

The electromagnetic torque is calculated by only considering the electromagnetic branch

$$T_{\mathrm{em}} = \frac{3}{2} \cdot p \cdot \left(\psi_{\mathrm{d.em}} \cdot I_{\mathrm{q.em}} - \psi_{\mathrm{q.em}} \cdot I_{\mathrm{d.em}}\right) \tag{2-45}$$

2.7 Efficiency

Neglecting stray and mechanical losses, the efficiency of EESM can be formulated as

$$\eta = \frac{p_{\mathrm{out}}}{p_{\mathrm{in}}} \times 100\% = \frac{p_{\mathrm{em}}}{p_{\mathrm{em}} + p_{\mathrm{Cu}} + p_{\mathrm{Fe}}} \times 100\% \tag{2-46}$$

In steady state, if mechanical losses P_{mechloss} and stray losses $P_{\mathrm{strayloss}}$ are considered, then the efficiency of the machine can be formulated as

$$\eta = \frac{P_{\mathrm{out}}}{P_{\mathrm{in}}} \times 100\% = \frac{P_{\mathrm{em}} - P_{\mathrm{mechloss}}}{P_{\mathrm{em}} + P_{\mathrm{Cu}} + P_{\mathrm{Fe}} + P_{\mathrm{strayloss}}} \times 100\% \tag{2-47}$$

P_{mechloss} and $P_{\mathrm{strayloss}}$ in steady state operation can usually be estimated as [40]

$$P_{\mathrm{mechloss}} \approx P_{\mathrm{nom}} \cdot \frac{f^2}{f_{\mathrm{nom}}^2} \cdot 0.5\% \tag{2-48}$$

$$P_{\mathrm{strayloss}} \approx P_{\mathrm{nom}} \cdot \left(\frac{I_{\mathrm{s}}}{I_{\mathrm{s\cdot nom}}}\right)^2 \cdot \frac{f}{f_{\mathrm{nom}}} \cdot 0.5\% \tag{2-49}$$

where P_{nom} is the nominal power, f_{nom} is the nominal frequency and $I_{\mathrm{s\cdot nom}}$ is the nominal stator current.

2.8 Power Factor

In instantaneous power theory, the instantaneous power factor (PF) can be calculated as [37]

$$PF = \frac{p_{\mathrm{s}}}{s_{\mathrm{s}}} = \frac{p_{\mathrm{s}}}{\sqrt{p_{\mathrm{s}}^2 + q_{\mathrm{s}}^2}} \tag{2-50}$$

Another approach is to determine power factor by the angle difference between the voltage and current vectors

$$PF = \cos \varphi_{\mathrm{PF}} = \cos(\theta_{\mathrm{u}} - \theta_{\mathrm{i}}) \tag{2-51}$$

where θ_{u} is the voltage vector angle, θ_{i} is the current vector angle and φ_{PF} is the power factor angle. In terms of a converter-driven machine, the inverter output voltage contains switching harmonics. In this case, the amount of reactive power is not only decided by the machine, but also decided by the switching actions of the inverter. To evaluate the machine performance, displacement power factor (DPF) is use. DPF is defined as the power factor considering only the fundamental voltage and current components

$$DPF = \frac{p_{\mathrm{s(1)}}}{s_{\mathrm{s(1)}}} = p_{\mathrm{s(1)}} / \sqrt{p_{\mathrm{s(1)}}^2 + q_{\mathrm{s(1)}}^2} = \cos \varphi_{\mathrm{PF(1)}} = \cos\left(\theta_{u(1)} - \theta_{i(1)}\right) \tag{2-52}$$

In terms of experimental validation of the machine performance in this study, DPF is used.

2.9 Thermal Modeling

To assist the design and analysis of the machine, a thermal model is needed to estimate the thermal condition of the machine at different operation points. The schematics of the machine radial cross-section in terms of thermal modeling are shown in Figure 2-3. The stator structure is shown in (a). The copper winding in stator slot is simplied as an area of copper in the center, surrounded by an equivalent material with equivalent thermal conductivity [41] [42]. The winding together with the equivalent material is further enclosed by the stator iron. The stator iron is attached to an aluminum cooling jacket with an interface gap in the between. Inside the aluminum cooling jacket, there is a coolent channel, through which water flows to take the heat away. The stator iron has an interface with airgap as well in which convection occurs. The rotor structure is simplier, as shown in (b). The winding-slot structure is the same as the stator side and the rotor iron has an interface with airgap. Wedge in both cases are considered not as thermal conductive material.

With this simplified structure, a lumped parameter model is built. Heat transfer mechanisms are firstly presented, based on which the lumped parameter model is built. The consideration of adiabatic process to characterize peak operation of the machine is presented as well.

2.9.1 Conductive Heat Transfer

Conduction is the heat transfer through homogeneous and opaque solid and it originates from the difference in temperature between the warm and the cold part of the solid [43]. The conductive heat transfer P can be calculated by

$$P = \frac{T_1 - T_2}{R_{\text{th.cond}}} \tag{2-53}$$

where T_1 is the temperature at Point 1, T_2 is the temperature at Point 2 and $R_{\text{th.cond}}$ is the conductive thermal resistance. $R_{\text{th.cond}}$ can be calculated as

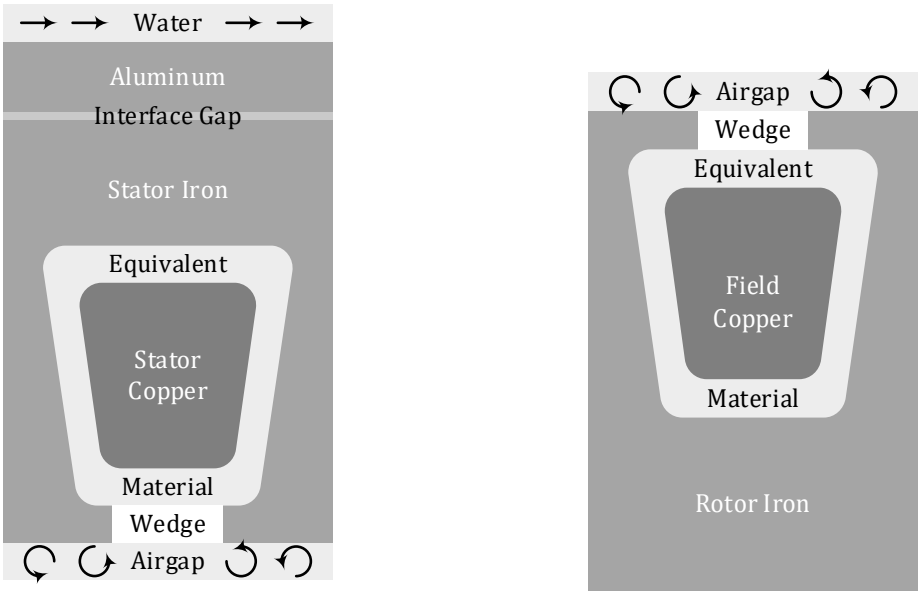

(a) Stator. (b) Rotor.

Figure 2-3 Schematics of machine structure in terms of thermal modeling.

$$R_{\text{th.cond}} = \int_0^L \frac{1}{\lambda \cdot A(l)} \cdot dl \tag{2-54}$$

where λ is the thermal conductivity of the solid in W/(m·K) and A is the cross-section as a function of distance l.

In EESM, thermal conduction happens between different parts of the iron-core, from copper winding to the iron-core, and from the stator iron to the aluminum cooling jacket. The first is simple since the geometry is known and lamination iron is the only material. The latter two are complicated and are explained as follows.

A. Conduction between Copper Winding and Iron Core

The slot-winding structure involves several different materials. In terms of the winding insulations, there are mainly three: the surface varnish of the strands, the impregnated vanish and the slot insulation [44]. For low-voltage AC machines (rated voltage lower than 1 kV), a thickness of 0.2-0.3 mm is usually reserved for slot insulation. In order to simplify the calculation, an equivalent slot thermal conductivity λ_{eq} is proposed in [45] [46] [41] [42]

$$\lambda_{\text{eq}} = 0.2425 \cdot [(1 - k_{\text{fill}}) \cdot A_{\text{slot}} \cdot L_{\text{core}}]^{-0.427} \tag{2-55}$$

where k_{fill} is the fill factor, i.e. the copper area divided by the slot cross-section area, A_{slot} is the slot cross-section area, L_{core} is the length of the iron-core. Figure 2-4 shows the curve of the equivalent slot thermal conductivity with respect to $(1 - k_{\text{fill}}) \cdot A_{\text{slot}} \cdot L_{\text{core}}$.

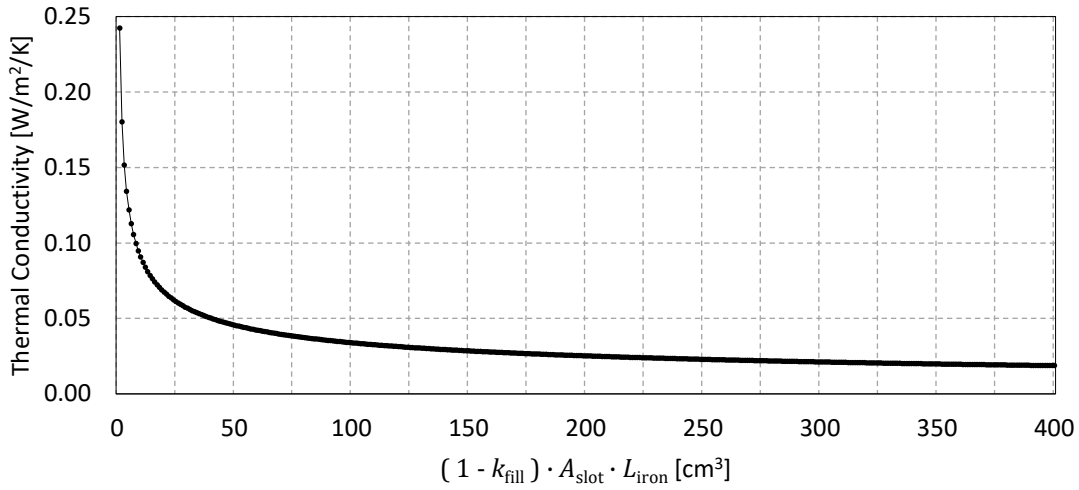

Figure 2-4 Equivalent slot thermal conductivity.

B. Conduction between Stator Iron Core and Aluminum Cooling Jacket

From the study in [45] [46], the interface gap between the stator iron core and aluminum cooling jacket is related to the imperfections along the touching surfaces. The imperfection is a complex function of material hardness, interface pressure, surface smoothness, and so forth. From an engineering perspective, one simple way to model the thermal contact is to utilize an average interference airgap. From the data presented in [46], the average interference airgap varies from 0.01 mm to 0.08 mm. And it is concluded that the thickness of average interference airgap is strongly influenced by the assembly process. Therefore, in this study, 0.05 mm is taken as the initial value to do the modeling.

2.9.2 Convective Heat Transfer

Convection is the type of heat transfer that occurs between different parts of fluid with temperature differences, or between the fluid and the wall licked by the fluid itself [47]. Several dimensionless numbers are for frequent use in convective heat transfer analysis, and they are summarized in Table 2-2.

Table 2-2 Dimensionless numbers of frequent use

Name	Symbol	Meaning	Expression
Reynolds Number	Re	The ratio of inertial forces to viscous forces within a fluid	$\frac{\rho \cdot v \cdot l}{\mu}$
Nusselt Number	Nu	The ratio of convective to conductive heat transfer at a boundary in a fluid	$\frac{h \cdot d}{\lambda}$
Prandtl Number	Pr	The ratio of momentum diffusivity to thermal diffusivity	$\frac{c_\mathrm{p} \cdot \mu}{\lambda}$

The flow of a fluid can be classified as laminal flow, i.e. smooth flow, and turbulent flow, i.e. distorted flow. The schematics of laminal flow and turbulent flow are shown in Figure 2-5. In order to determine whether a flow is laminal or turbulent, the *Reynolds number*, which is the ratio between inertia force and viscous force, needs to be calculated

$$Re = \frac{\rho \cdot v \cdot l}{\mu} \tag{2-56}$$

where the density of the fluid ρ is in kg/m^3, the velocity of the fluid v is in m/s, the characteristic length l, i.e. the hydraulic diameter, is in m, the dynamic viscosity of the fluid μ is in kg/m·s and the kinematic viscosity of the fluid ν is in m^2/s. In terms of the flow in airgap, the hydraulic diameter is twice of the annular airgap thickness [48]. For a Re below 2000, the viscous force is dominated and the flow is certainly laminar, whereas for a Re above 3000, the inertia force is dominated and the flow is certainly turbulent [47].

(a) Laminar flow. (b) Turbulent flow.

Figure 2-5 Schematics of laminar flow and turbulent flow.

The convective heat transfer can be calculated by temperature difference and thermal resistance as well

$$P = \frac{T_1 - T_2}{R_{\mathrm{th\cdot conv}}} \tag{2-57}$$

and the convective thermal resistance $R_{\mathrm{th\cdot conv}}$ can be calculated as

$$R_{\mathrm{th\cdot conv}} = \frac{1}{h \cdot A} \tag{2-58}$$

where the convection heat transfer coefficient h is in W/(m²·K). Further, h can be calculated as

$$h = \frac{\lambda \cdot Nu}{l} \tag{2-59}$$

where the thermal conductivity of the fluid λ is in W/(m·K), and the characteristic surface length l, i.e. the hydraulic diameter, is in m. Nu is the *Nusselt number*, which represents the ratio of convective to conductive heat transfer at a boundary in the fluid

$$Nu = \frac{h \cdot L}{\lambda} \tag{2-60}$$

And in order to determine Nu, the *Prandtl Number*, Pr, is sometimes necessary, which is defined as the ratio of momentum diffusivity to thermal diffusivity

$$Pr = \frac{c_\mathrm{p} \cdot \mu}{\lambda} \tag{2-61}$$

A low value of Pr , $Pr \ll 1$, means a domination of thermal diffusivity, whereas in case of a large Pr, $Pr \gg 1$, means a domination of momentum diffusivity.

A. Convection Thermal Resistance Between Coolant and Cooling Channels

In order to calculate h to characterize the convection between coolant and cooling channels, one approach is provided by [49], where the *Nusselt Number* can be calculated as

$$Nu = \frac{f}{8} \cdot \frac{(Re - 1000) \cdot Pr}{1 + 12.7 \cdot \left(\frac{f}{8}\right)^{\frac{1}{2}} \cdot \left(Pr^{\frac{2}{3}} - 1\right)} \tag{2-62}$$

where f is the friction factor and if the wall is smooth, then it can be approximated as

$$f = \frac{1}{(0.79 \cdot \ln Re - 1.64)^2} \tag{2-63}$$

and then, the heat transfer factor is calculated as in (2-59) where the characteristic surface length is the channel diameter.

B. Convection Thermal Resistance Between Iron-Core and Airgap

To calculate the heat transfer coefficient at the airgap, the type of airflow in the airgap has to be determined [48]. The Taylor number indicates the relative effects of inertial forces and viscosity for an annulus with rotation of one or more of the cylindrical surfaces. The Taylor number based on mean annulus radius $r_m = \frac{r_a + r_b}{2}$ is defined as

$$Ta_m = \frac{\Omega_a \cdot {r_m}^{0.5} \cdot (r_b - r_a)^{1.5}}{\nu} \tag{2-64}$$

where r_a and r_b are the inner and outer annulus radius respectively. Please be aware that ν is the Greek letter “nu” instead of the English letter “v”, and it is the kinematic viscosity of the fluid in m²/s. The critical speed based on Taylor’s solution can be determined as

$$\Omega_{\mathrm{cr}} = \pi^2 \cdot \nu \cdot \sqrt{\frac{r_a + r_b}{2 \cdot S \cdot (r_b - r_a)^3 \cdot {r_a}^2 \cdot \left(1 - \frac{\Omega_{\mathrm{b}}}{\Omega_{\mathrm{a}}} \cdot \frac{{r_b}^2}{{r_a}^2}\right) \cdot \left(1 - \frac{\Omega_{\mathrm{b}}}{\Omega_{\mathrm{a}}}\right)}} \tag{2-65}$$

where Ω_{a} is the speed of the inner cylindrical surface, Ω_{b} is the speed of the outer cylindrical surface, and

$$S = 0.0571 \left[\frac{1 + \frac{\Omega_{\mathrm{b}}}{\Omega_{\mathrm{a}}}}{1 - \frac{\Omega_{\mathrm{b}}}{\Omega_{\mathrm{a}}}} + 0.652 \left(1 - \frac{r_b}{r_a}\right)\right] + 0.00056 \left[\frac{1 + \frac{\Omega_{\mathrm{b}}}{\Omega_{\mathrm{a}}}}{1 - \frac{\Omega_{\mathrm{b}}}{\Omega_{\mathrm{a}}}} + 0.652 \left(1 - \frac{r_b}{r_a}\right)\right]^{-1} \tag{2-66}$$

In case of outer stator, i.e. $\Omega_{\mathrm{b}} = 0$, and a narrow gap, i.e. $r_a \approx r_b$, then (2-65) becomes

$$\Omega_{\mathrm{cr}} = \pi^2 \cdot \nu \cdot \sqrt{\frac{1}{S \cdot (r_b - r_a)^3 \cdot r_m}} \tag{2-67}$$

Hence (2-66) becomes

$$S = 0.0571 + 0.00056 = 0.05766 \tag{2-68}$$

together with the assumption of a stationary outer cylinder, the critical speed gives a corresponding critical Taylor number $Ta_{m.cr}$ as

$$Ta_{m.cr} = \frac{\pi^2}{\sqrt{S}} = \sqrt{1697} = 41.19 \tag{2-69}$$

In case of a Taylor number smaller than $Ta_{m.cr}$, the air flow in the airgap remains a Couette flow, whereas in case of a Taylor number greater than $Ta_{m.cr}$, Taylor vortices can form. The critical speed in (2-67) in this case becomes

$$\Omega_{\mathrm{cr}} = \frac{41.19 \cdot \nu}{\sqrt{(r_b - r_a)^3 \cdot r_m}} \tag{2-70}$$

For a larger airgap size, i.e. when $r_a \approx r_b$ is not valid, the value of $Ta_{m.cr}$ needs to be corrected accordingly. However, for the sack of convenience, in order to use the same pricewise function to determine Nu for all geometries, a geometric factor can be defined to correct Ta_m instead of $Ta_{m.cr}$

$$F_g = \frac{\pi^2}{41.19 \cdot \sqrt{S}} \cdot \left(\frac{r_b + r_a}{2 \cdot r_a}\right) \tag{2-71}$$

In case $r_a \approx r_b$ is valid, $F_g = 1$. Then according to [50] [51] [52] [48], the *Nusselt Number* can be determined by the same pricewise function

$$Nu = \begin{cases} 2 \cdot \left(\frac{r_b}{r_a} - 1\right) / \ln\left(\frac{r_b}{r_a}\right) & \left(\frac{Ta_m}{F_g}\right)^2 < 1.7 \times 10^3 \\ 0.128 \cdot \left(\frac{Ta_m}{F_g}\right)^{0.734} & 1.7 \times 10^3 < \left(\frac{Ta_m}{F_g}\right)^2 < 10^4 \\ 0.409 \cdot \left(\frac{Ta_m}{F_g}\right)^{0.482} & 10^4 < \left(\frac{Ta_m}{F_g}\right)^2 < 10^7 \end{cases} \quad (2\text{-}72)$$

Then based on the definition of Nu, the heat transfer coefficient can be calculated as

$$h = \frac{\lambda \cdot Nu}{L} = \frac{\lambda \cdot Nu}{r_b - r_a} \quad (2\text{-}73)$$

2.9.3 Thermal Capacitance

In case thermal dynamics is of interest, thermal capacitance needs to be introduced. The thermal capacitance of each structure can be expressed as the multiplication of specific heat of the material and the mass, and the mass is the product of mass density and the volume

$$C_{\text{th}} = c \cdot m = c \cdot \rho_{\text{m}} \cdot Volume = c \cdot \rho_{\text{m}} \cdot Area \cdot Length \quad (2\text{-}74)$$

where ρ_{m} is the mass density and c is the specific heat of the material.

2.9.4 Lumped Parameter Model

Based on the schematics of structure shown in Figure 2-3, and the theories introduced in previous sections, a simplified lumped parameter thermal model can be formulated as shown in Figure 2-6. The stator windings and the field winding are the sources of heat, and they are denoted as Node 1 and 2 in the figure. The heat then flows to the iron core through the material with equivalent thermal conductivity as introduced in (2-55). The heat from the rotor is dissipated to the airgap and further to the stator iron core with the convection mechanism. The heat in stator then goes to the aluminum jacket through the average interface gap of 0.05 mm. Finally, the heat is taken away by the coolant in the form of convection.

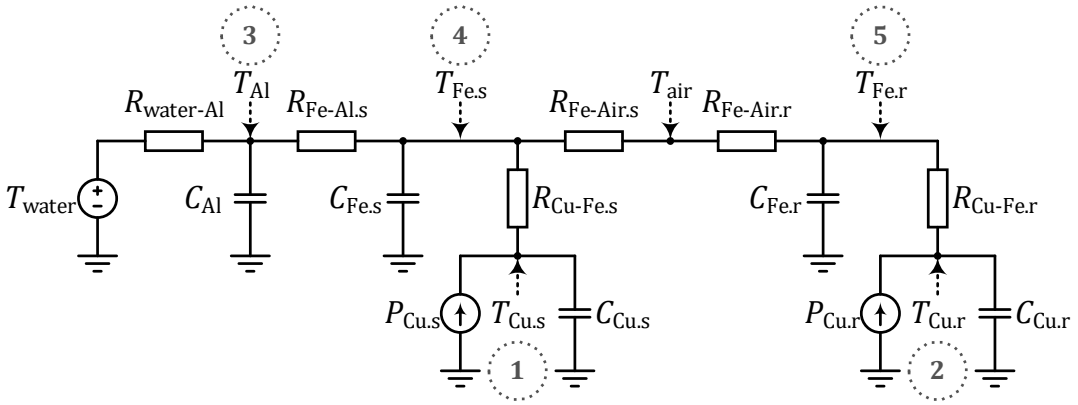

Figure 2-6 Schematic of a simplified lumped parameter thermal model for EESM.

2.9.5 Adiabatic Process

Adiabatic process is to study the temperature rise before any cooling mechanism takes effect. This study is performed to verify the peak operation of traction electric motors for 30 s [53]. The copper loss can be expressed as

$$P_{\mathrm{Cu}} = I^2 \cdot R = I^2 \cdot \rho_{\mathrm{r}} \cdot \frac{l}{A} = I \cdot J \cdot \rho_{\mathrm{r}} \cdot l \tag{2-75}$$

in J/s. With (2-74), the copper thermal capacitance is expressed as

$$C_{\mathrm{th}} = c \cdot \rho_{\mathrm{m}} \cdot A_{\mathrm{Cu}} \cdot l_{\mathrm{Cu}} \tag{2-76}$$

where A_{Cu} is the cross-section area of copper wire and l_{Cu} is the length of copper wire. Based on these, it becomes possible to calculate the temperature derivative when copper heats up itself

$$\frac{dT}{dt} = \frac{P_{\mathrm{Cu}}}{C_{\mathrm{th.Cu}}} = \frac{I \cdot J \cdot \rho_{\mathrm{r}} \cdot l_{\mathrm{Cu}}}{c_{\mathrm{Cu}} \cdot \rho_{\mathrm{m}} \cdot l_{\mathrm{Cu}} \cdot A_{\mathrm{Cu}}} = J^2 \cdot \frac{\rho_{\mathrm{r}}}{c_{\mathrm{Cu}} \cdot \rho_{\mathrm{m}}} \tag{2-77}$$

With the parameters of copper, $\rho_{\mathrm{r}} = 1.72 \times 10^{-8}\ [\Omega \cdot \mathrm{m}]$, $c_{\mathrm{Cu}} = 3.9 \times 10^{2}\ [\mathrm{J/(kg \cdot K)}]$ and $\rho_{\mathrm{m}} = 8.96 \times 10^{3}\ [\mathrm{kg/m^3}]$ into the formula, then

$$\frac{dT}{dt} = 4.92 \times 10^{-3} \cdot J^2 \tag{2-78}$$

with the current density J in A/mm^2. It should be pointed out that, in case of AC current, the current density here should be the root mean square (RMS) value. The temperature rise derivative of adiabatic process of copper in K/s is shown in Figure 2-7.

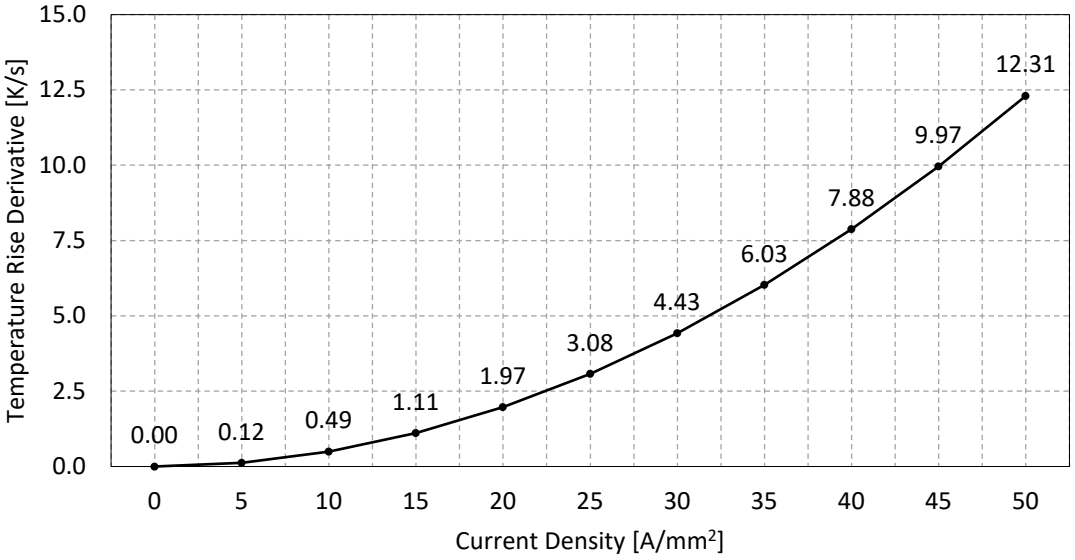

Figure 2-7 Temperature rise derivative during adiabatic process.

Chapter 3

Machine Performance in Steady State

In this chapter, the steady-state performance of EESM is discussed. This includes the characteristic curves in the dq-plane, the characteristic surfaces in three-dimensional space of d-, q- and field coordinates and torque-speed characteristics.

3.1 Characteristic Curves in the DQ-Plane

To describe the machine characteristics, the vectors in the dq-plane are presented in Figure 3-1, where θ_i is the *current vector angle*, θ_u is the *voltage vector angle*, φ_PF is the *power factor angle* and δ is the *load angle* (*power angle*). The current and voltage vector angles are defined with respect to the d-axis. The EMF vector is at the q-axis. The power factor angle is defined as the difference between the current and voltage angles, while the load angle (power angle) is defined as the difference between the voltage angle and the back-EMF

$$\varphi_\mathrm{PF} = \theta_\mathrm{u} - \theta_\mathrm{i} \quad , \quad \delta = \theta_\mathrm{u} - \frac{\pi}{2} \tag{3-1}$$

Hence, these angles follow

$$\theta_\mathrm{i} + \varphi_\mathrm{PF} = \theta_\mathrm{u} = \delta + \frac{\pi}{2} \tag{3-2}$$

The d- and q-axis current components can be expressed in polar form as

$$i_\mathrm{d} = i_\mathrm{s} \cdot \cos\theta_\mathrm{i} \quad , \quad i_\mathrm{q} = i_\mathrm{s} \cdot \sin\theta_\mathrm{i} \tag{3-3}$$

so as the d- and q-axis voltage components

$$u_\mathrm{d} = u_\mathrm{s} \cdot \cos\theta_\mathrm{u} \quad , \quad u_\mathrm{q} = u_\mathrm{s} \cdot \sin\theta_\mathrm{u} \tag{3-4}$$

Here the vectors presented in Figure 3-1 and the relation described in (3-1) (3-2) (3-3) and (3-4) are instantaneous. They are also valid in steady state.

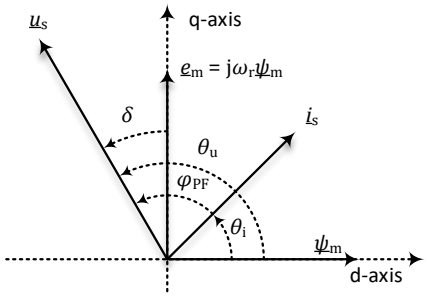

Figure 3-1 Angles in EESM dq-plane.

3.1.1 Current Limit Circle and Voltage Limit Ellipse

A. Current Limit Circle

The stator current is limited by the current output capability of the power electronic converter and the cross-section of the copper conductors of the machine winding. A maximum current amplitude $I_{\mathrm{s.max}}$ is decided by these two aspects for the operation of the machine

$$i_{\mathrm{d}}^2 + i_{\mathrm{q}}^2 = i_{\mathrm{s}}^2 \leq I_{\mathrm{s.max}}^2 \tag{3-5}$$

The current limit can be illustrated as a circle with a radius of $I_{\mathrm{s.max}}$ in Figure 3-2.

B. Voltage Limit Ellipse

Similarly, the stator voltage is limited by the voltage output capability of the power electronic converter and the insulation level of the machine winding. A maximum voltage amplitude $U_{\mathrm{s.max}}$ is decided by these two aspects for the operation of the machine

$$u_{\mathrm{d}}^2 + u_{\mathrm{q}}^2 = u_{\mathrm{s}}^2 \leq U_{\mathrm{s.max}}^2 \tag{3-6}$$

With third harmonic injection or with space vector modulation (SVM)

$$U_{\mathrm{s.max}} = \frac{U_{\mathrm{dc}}}{\sqrt{3}} \tag{3-7}$$

In steady state, assuming the resistive voltage drops are negligible, then the voltage limit criterion (3-6) can be described as

$$\psi_{\mathrm{d}}^2 + \psi_{\mathrm{q}}^2 = \frac{U_{\mathrm{s}}^2}{\omega_{\mathrm{r}}^2} \leq \frac{U_{\mathrm{s.max}}^2}{\omega_{\mathrm{r}}^2} \tag{3-8}$$

To describe (3-8) with apparent inductances, it becomes

$$(L_{\mathrm{d}} \cdot I_{\mathrm{d}} + L_{\mathrm{m}} \cdot I_{\mathrm{f}})^2 + \left(L_{\mathrm{q}} \cdot I_{\mathrm{q}}\right)^2 = \frac{U_{\mathrm{s}}^2}{\omega_{\mathrm{r}}^2} \leq \frac{U_{\mathrm{s.max}}^2}{\omega_{\mathrm{r}}^2} \tag{3-9}$$

which can be further formulated as an ellipse in Figure 3-2

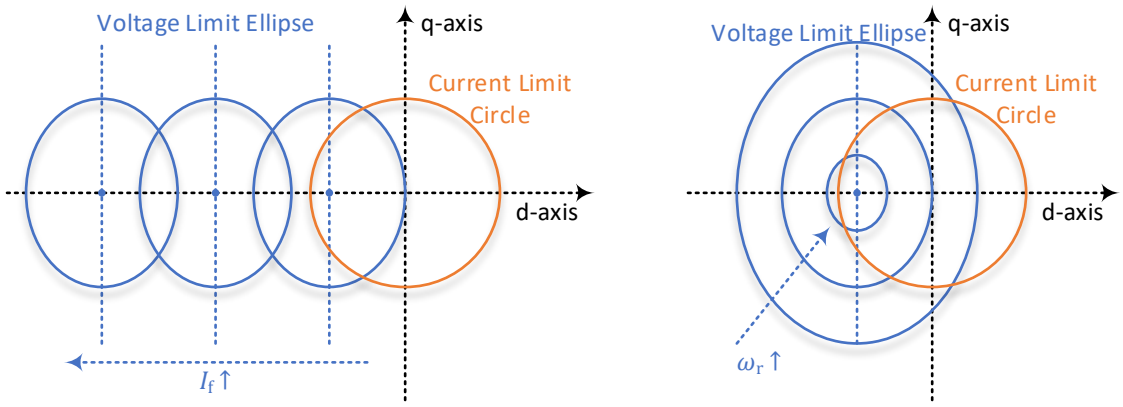

(a) Increase of field current. (b) Increase of speed.

Figure 3-2 Current limit circle and voltage limit ellipse of EESM in the dq-plane.

$$\frac{(I_\mathrm{d}+I_\mathrm{ch})^2}{a^2}+\frac{I_\mathrm{q}^2}{b^2}\leq 1 \tag{3-10}$$

where a is the major semi-axis, b is the minor semi-axis and $(-I_\mathrm{ch}\,,0)$ is the ellipse center

$$a^2=\left(\frac{U_\mathrm{s.max}}{\omega_\mathrm{r}\cdot L_\mathrm{d}}\right)^2 \quad , \quad b^2=\left(\frac{U_\mathrm{s.max}}{\omega_\mathrm{r}\cdot L_\mathrm{q}}\right)^2 \quad , \quad I_\mathrm{ch}=\frac{L_\mathrm{m}}{L_\mathrm{d}}I_\mathrm{f} \tag{3-11}$$

The eccentricity of the ellipse is determined by the saliency ratio of the machine

$$e=\sqrt{1-\frac{b^2}{a^2}}=\sqrt{1-\frac{L_\mathrm{d}^2}{L_\mathrm{q}^2}}=\sqrt{1-k_\mathrm{dq}^2} \tag{3-12}$$

In PMSM studies, a *characteristic current* is usually defined as $\frac{\psi_\mathrm{m}}{L_\mathrm{d}}$ [54] [55], and similarly here for EESM studies, a *characteristic current* can be defined as $I_\mathrm{ch}=\frac{L_\mathrm{m}}{L_\mathrm{d}}I_\mathrm{f}$, which decides the center of the voltage limit ellipse. The center of the ellipse $(-I_\mathrm{ch}\,,0)$ shifts as the field current changes as illustrated in Figure 3-2 (a). Additionally, as the speed ω_r increases, a and b decrease which means a collapse of the ellipse to its center as illustrated in Figure 3-2 (b).

At low speed, the current limit circle is inside the voltage limit ellipse. As the speed goes higher, the voltage limit ellipse collapses and starts to intersect the current limit circle. In case of $I_\mathrm{ch}>I_\mathrm{s}$, the voltage limit ellipse will detach the current limit circle at high speed, whereas in case of $I_\mathrm{ch}<I_\mathrm{s}$, the voltage limit ellipse will become totally inside the current limit circle. However, no matter how the ellipse collapses or shifts, the eccentricity remains the same.

C. Intersection

It is the common area of the current limit circle and the voltage limit ellipse that defines the possible operation area on the dq-plane. Therefore, the intersection of the two defines the case when the maximum apparent power is reached. When the intersection occurs, the speed ω_r can be solved from (3-9) and it can be expressed by d- and q-axis current components in polar form

$$\begin{aligned}\omega_\mathrm{r}&=\frac{U_\mathrm{s.max}}{\sqrt{(L_\mathrm{d}\cdot I_\mathrm{d}+L_\mathrm{m}\cdot I_\mathrm{f})^2+\left(L_\mathrm{q}\cdot I_\mathrm{q}\right)^2}}\\&=\frac{U_\mathrm{s.max}}{\sqrt{(L_\mathrm{d}\cdot I_\mathrm{s.max}\cdot\cos\theta_\mathrm{I}+L_\mathrm{m}\cdot I_\mathrm{f})^2+\left(L_\mathrm{q}\cdot I_\mathrm{s.max}\cdot\sin\theta_\mathrm{I}\right)^2}}\end{aligned} \tag{3-13}$$

The speeds when tangential intersection occurs can be found out by

$$\frac{d\omega_\mathrm{r}}{d\theta_\mathrm{I}}=0 \quad \Rightarrow \quad L_\mathrm{m}\cdot I_\mathrm{f}\cdot L_\mathrm{d}\cdot I_\mathrm{s.max}\cdot\sin\theta_\mathrm{I}+\frac{L_\mathrm{d}^2-L_\mathrm{q}^2}{2}\cdot {I_\mathrm{s.max}}^2\cdot\sin 2\theta_\mathrm{I}=0 \tag{3-14}$$

The solutions at $\theta_\mathrm{I}=0°$ and $180°$ are always available

$$\omega_\mathrm{r}(\theta_\mathrm{I}=0°)=\frac{U_\mathrm{s}}{L_\mathrm{m}\cdot I_\mathrm{f}+L_\mathrm{d}\cdot I_\mathrm{s}} \quad , \quad \omega_\mathrm{r}(\theta_\mathrm{I}=180°)=\frac{U_\mathrm{s}}{|L_\mathrm{m}\cdot I_\mathrm{f}-L_\mathrm{d}\cdot I_\mathrm{s}|} \tag{3-15}$$

Obviously $\omega_{\mathrm{r}}(\theta_{\mathrm{I}}=180°)$ is the maximum speed among all intersection situations, which depends on the field current

$$\omega_{\mathrm{r.max}}=\omega_{\mathrm{r}}(\theta_{\mathrm{I}}=180°)=\begin{cases}\dfrac{U_{\mathrm{s}}}{L_{\mathrm{m}}\cdot I_{\mathrm{f}}-L_{\mathrm{d}}\cdot I_{\mathrm{s}}} & \text{if} \quad I_{\mathrm{f}}>\dfrac{L_{\mathrm{d}}}{L_{\mathrm{m}}}I_{\mathrm{s}} \\ \infty & \text{if} \quad I_{\mathrm{f}}=\dfrac{L_{\mathrm{d}}}{L_{\mathrm{m}}}I_{\mathrm{s}} \\ \dfrac{U_{\mathrm{s}}}{L_{\mathrm{d}}\cdot I_{\mathrm{s}}-L_{\mathrm{m}}\cdot I_{\mathrm{f}}} & \text{if} \quad I_{\mathrm{f}}<\dfrac{L_{\mathrm{d}}}{L_{\mathrm{m}}}I_{\mathrm{s}}\end{cases} \tag{3-16}$$

3.1.2 Electromagnetic Torque

The electromagnetic torque can be illustrated as contours in the dq-plane. Together with the voltage limit ellipse and the current limit circle, it becomes intuitive to know how much torque is reachable within the voltage and current limits. From the torque formula (2-25), the q-axis current can be solved as

$$I_{\mathrm{q}}=\frac{2}{3\cdot p}\cdot\frac{T_{\mathrm{em}}}{\psi_{\mathrm{m}}+\left(L_{\mathrm{d}}-L_{\mathrm{q}}\right)\cdot I_{\mathrm{d}}} \tag{3-17}$$

which means I_{q} along the torque contour can be expressed as a hyperbola

$$I_{\mathrm{q}}=\frac{k_1}{I_{\mathrm{d}}+k_2} \tag{3-18}$$

where

$$k_1=\frac{2}{3\cdot p}\cdot\frac{T_{\mathrm{em}}}{L_{\mathrm{d}}-L_{\mathrm{q}}} \quad , \quad k_2=\frac{L_{\mathrm{m}}}{L_{\mathrm{d}}-L_{\mathrm{q}}}\cdot I_{\mathrm{f}} \tag{3-19}$$

The contours in case of $L_{\mathrm{d}}>L_{\mathrm{q}}$, $L_{\mathrm{d}}=L_{\mathrm{q}}$ and $L_{\mathrm{d}}<L_{\mathrm{q}}$ are illustrated in Figure 3-3 (a), (b) and (c) respectively. In (a) where $L_{\mathrm{d}}>L_{\mathrm{q}}$, as L_{Δ} decreases, the asymptotic line of the hyperbola moves towards positive infinity, and once L_{Δ} decreases to zero, plot (a) becomes plot (b). Similar tendency applies for (c) where $L_{\mathrm{d}}<L_{\mathrm{q}}$.

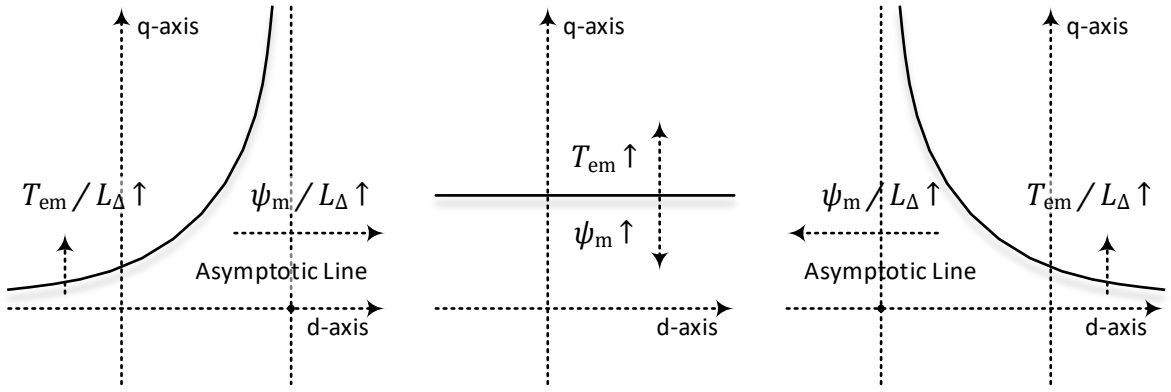

(a) $L_{\mathrm{d}}<L_{\mathrm{q}}$. (b) $L_{\mathrm{d}}=L_{\mathrm{q}}$. (c) $L_{\mathrm{d}}>L_{\mathrm{q}}$.

Figure 3-3 Equal torque hyperbola of EESM in the dq-plane.

3.1.3 Unity Power Factor Ellipse

One advantage of EESM is that the field current can be adjusted to improve the power factor. Hence it becomes essential to know where the unity power operation points locate in the dq-plane. The condition of unity power factor, $\cos \varphi_{\mathrm{PF}} = 1$, can be achieved by setting Q_{s} to zero. Neglecting the resistive voltage drops, it yields

$$Q_{\mathrm{s}} = \frac{3}{2} \cdot \left(U_{\mathrm{q}} \cdot I_{\mathrm{d}} - U_{\mathrm{d}} \cdot I_{\mathrm{q}} \right) = 0 \quad \Rightarrow \quad \psi_{\mathrm{d}} \cdot I_{\mathrm{d}} + \psi_{\mathrm{q}} \cdot I_{\mathrm{q}} = 0 \tag{3-20}$$

To describe the equation with apparent inductances, it becomes

$$L_{\mathrm{d}} \cdot I_{\mathrm{d}}^2 + L_{\mathrm{q}} \cdot I_{\mathrm{q}}^2 + L_{\mathrm{m}} \cdot I_{\mathrm{f}} \cdot I_{\mathrm{d}} = 0 \tag{3-21}$$

Since I_{f} is non-negative, to achieve unity power factor, I_{d} must be negative. Additionally, with a fixed I_{f}, (3-21) can be further reformulated into an equation of ellipse

$$\frac{(I_{\mathrm{d}} + a)^2}{a^2} + \frac{{I_{\mathrm{q}}}^2}{b^2} = 1 \tag{3-22}$$

where a is the major semi-axis, b is the minor semi-axis and $(-a, 0)$ is the ellipse center

$$a^2 = \frac{1}{4} \cdot \frac{L_{\mathrm{m}}^2}{L_{\mathrm{d}}^2} \cdot I_{\mathrm{f}}^2 \quad , \quad b^2 = \frac{1}{4} \cdot \frac{L_{\mathrm{m}}^2}{L_{\mathrm{d}} \cdot L_{\mathrm{q}}} \cdot I_{\mathrm{f}}^2 \tag{3-23}$$

As shown in Figure 3-4 (a), the unity power factor ellipse expands and shrinks as the field current increases and decreases. The eccentricity of the ellipse is decided by the saliency ratio of the machine as well

$$e = \sqrt{1 - \frac{b^2}{a^2}} = \sqrt{1 - \frac{L_{\mathrm{d}}}{L_{\mathrm{q}}}} = \sqrt{1 - k_{\mathrm{dq}}} \tag{3-24}$$

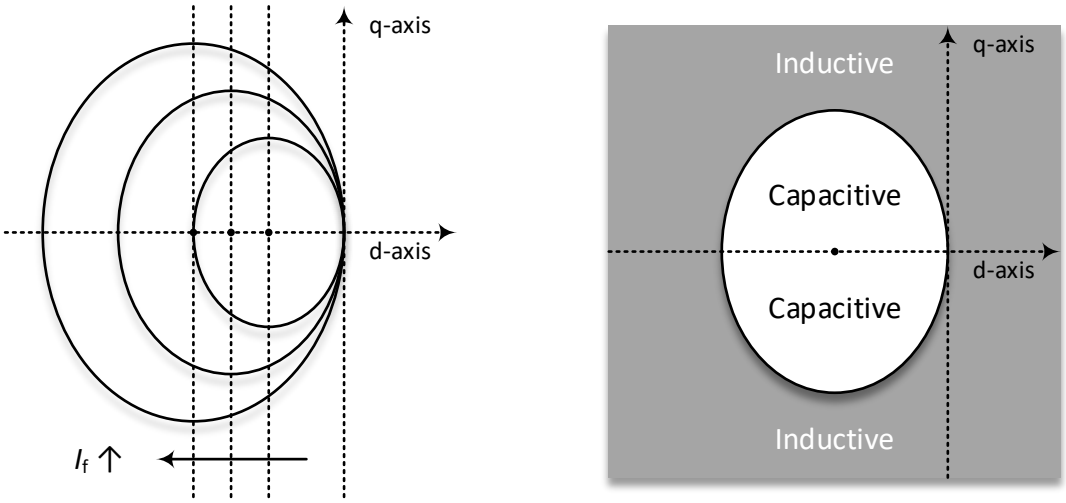

(a) Increase of field current. (b) Capacitive and inductive area.

Figure 3-4 Unity power factor ellipse of EESM in the dq-plane ($L_{\mathrm{d}} > L_{\mathrm{q}}$).

When the current vector locates at the unity power factor ellipse, the EESM operates at unit power factor. As can be noticed by comparing (3-11) and (3-23), several conclusions can be drawn as follows.

- The center of the voltage limit ellipse is twice further away than the center of the unit power factor ellipse to the origin. In other words, the unity power factor ellipse crosses the center of the voltage limit ellipse.
- In case of $I_{\mathrm{d.0}} > I_{\mathrm{s}}$, the unity power factor ellipse intersects the current limit circle.
- Inside the unity power factor ellipse, the operation is capacitive, whereas outside is inductive, as shown in Figure 3-4 (b).

3.1.4 Equal Power Factor Ellipse

Furthermore, equal power factor contours can be derived. According to (2-17) and (2-50)

$$\tan\varphi_{\mathrm{PF}} = \frac{Q_{\mathrm{s}}}{P_{\mathrm{s}}} = \frac{L_{\mathrm{d}} \cdot I_{\mathrm{d}}^2 + L_{\mathrm{q}} \cdot I_{\mathrm{q}}^2 + L_{\mathrm{m}} \cdot I_{\mathrm{f}} \cdot I_{\mathrm{d}}}{\left(L_{\mathrm{d}} - L_{\mathrm{q}}\right) \cdot I_{\mathrm{d}} \cdot I_{\mathrm{q}} + L_{\mathrm{m}} \cdot I_{\mathrm{f}} \cdot I_{\mathrm{q}}} \tag{3-25}$$

In polar form, (3-25) becomes,

$$I_{\mathrm{s}} = \frac{L_{\mathrm{m}} \cdot I_{\mathrm{f}} \cdot (\cos\theta_{\mathrm{I}} - \sin\theta_{\mathrm{I}} \cdot \tan\varphi_{\mathrm{PF}})}{\frac{L_{\mathrm{d}} - L_{\mathrm{q}}}{2} \cdot \sin 2\theta_{\mathrm{I}} \cdot \tan\varphi_{\mathrm{PF}} - L_{\mathrm{d}} \cdot \cos^2\theta_{\mathrm{I}} - L_{\mathrm{q}} \cdot \sin^2\theta_{\mathrm{I}}} \tag{3-26}$$

The power factor ellipse with PF = 0.8, 0.9 and 1.0 for both inductive and capacitive cases, and in cases of $L_{\mathrm{d}} > L_{\mathrm{q}}$, $L_{\mathrm{d}} = L_{\mathrm{q}}$ and $L_{\mathrm{d}} < L_{\mathrm{q}}$ are shown in Figure 3-5. For unity power factor, $\tan\varphi_{\mathrm{PF}} = 0$, and (3-26) becomes (3-21). Specially, at $\theta_{\mathrm{I}} = 0$, (3-26) becomes

$$I_{\mathrm{s}} = -\frac{L_{\mathrm{m}} \cdot I_{\mathrm{f}}}{L_{\mathrm{d}}} \tag{3-27}$$

This means all equal power factor ellipses come across the center of the voltage ellipse.

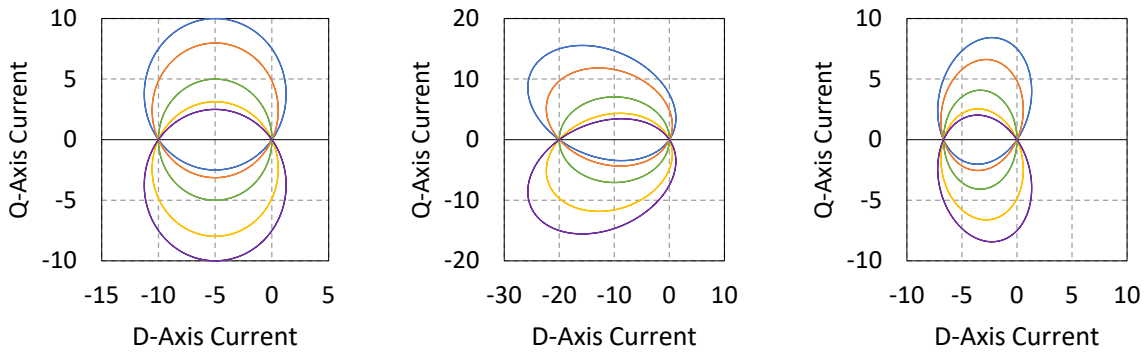

(a) $L_{\mathrm{d}} = 10$ [mH], $L_{\mathrm{q}} = 10$ [mH]. (b) $L_{\mathrm{d}} = 5$ [mH], $L_{\mathrm{q}} = 10$ [mH]. (c) $L_{\mathrm{d}} = 15$ [mH], $L_{\mathrm{q}} = 10$ [mH].

cos(φ_{PF}) = -0.8 cos(φ_{PF}) = -0.9 cos(φ_{PF}) = 1.0 cos(φ_{PF}) = 0.9 cos(φ_{PF}) = 0.8

Figure 3-5 Equal power factor ellipse (negative power factor means inductive operation, $L_{\mathrm{m}} I_{\mathrm{f}} = 0.1$ [Wb]).

3.2 Characteristic Surfaces in 3D Space

From the control perspective, the field current is the third degree of freedom in addition to d- and q-axis currents. Geometrically, the field current can be illustrated in an axis vertical to the dq-plane. Then the dq-plane together with the field current axis form a 3D space.

The isosurfaces of current limit, voltage limit, torque, and unity power factor of an 48 V EESM are shown in Figure 3-6 and Figure 3-7. The design and test of the 48 V EESM are described in Chapter 5. In Figure 3-6, the current limit at 500 A can be visualized as an oblique elliptic cylinder in red, while the voltage limit at 6000 rpm is shown as the blue isosurface. The torque isosurface at 30 N·m is in green. In Figure 3-7, the purple oblique elliptical cone is the power factor isosurface at unity. The opening of the cone enlarges as field current increases. The capacitive space is inside the cone while the inductive space is outside of the cone. The copper loss isosurface can be derived from (2-30)

$$\frac{I_\mathrm{d}^2}{a^2}+\frac{I_\mathrm{q}^2}{b^2}+\frac{I_\mathrm{f}^2}{c^2}=1 \tag{3-28}$$

which can be shown as the orange ellipsoid in Figure 3-7. Since usually R_f is much larger than R_s in traction motors, the semi-axes follow

$$a=b=\sqrt{\frac{2}{3}\frac{P_\mathrm{Cu}}{R_\mathrm{s}}}\gg\sqrt{\frac{P_\mathrm{Cu}}{R_\mathrm{f}}}=c \tag{3-29}$$

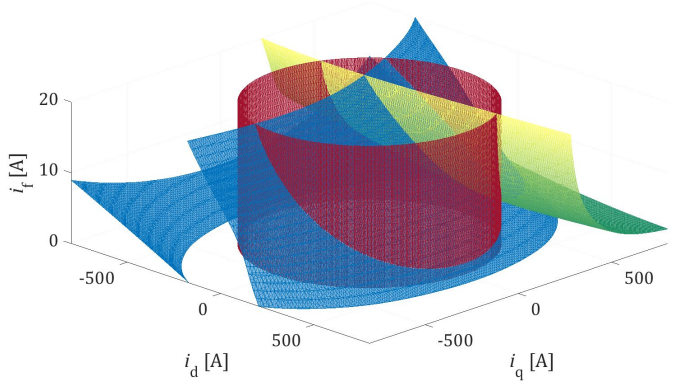

Figure 3-6 Isosurfaces of $T_\mathrm{em}=30\ \mathrm{N\cdot m}$, $i_\mathrm{s}=500\ \mathrm{A}$, $u_\mathrm{s}=\frac{48}{\sqrt{3}}\ \mathrm{V}$ in a 48 V EESM.

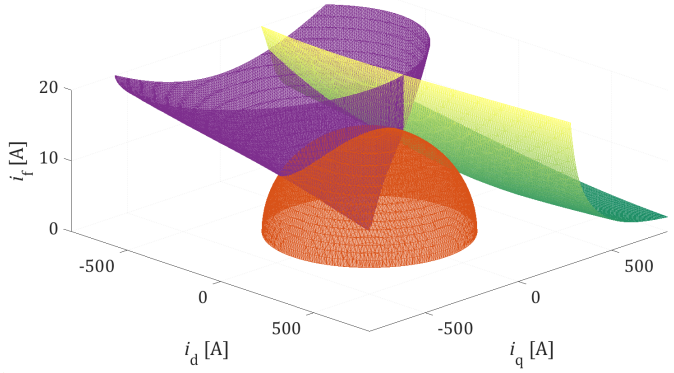

Figure 3-7 Isosurfaces of $T_\mathrm{em}=15\ \mathrm{N\cdot m}$, $P_\mathrm{Cu}=1\ \mathrm{kW}$, $PF=1.0$ in a 48 V EESM.

3.3 Steady-State Performance within Voltage and Current Limits

In control of steady-state performance, the independent variables are the d-axis, q-axis and field currents. The cost function can be formulated in quadratic format

$$f = \boldsymbol{i}^{\mathrm{T}} \boldsymbol{K}_{\mathbf{I}} \boldsymbol{i} \tag{3-30}$$

where $\boldsymbol{K}_{\mathbf{I}}$ depends on the optimization scenario. The current control optimization can be formulated as a least square problem (LSP), in which the squares of the currents are to be minimized. In this case, $\boldsymbol{K}_{\mathbf{I}}$ is diagonal

$$\boldsymbol{K}_{\mathbf{I}} = \begin{bmatrix} k_{\mathrm{d}} & 0 & 0 \\ 0 & k_{\mathrm{q}} & 0 \\ 0 & 0 & k_{\mathrm{f}} \end{bmatrix} \tag{3-31}$$

in which, k_{d}, k_{q} and k_{f} are the penalty coefficients added for i_{d}, i_{q} and i_{f} respectively. The constraint is identical among all scenarios, to achieve a certain amount of torque

$$\boldsymbol{i}^{\mathrm{T}} \boldsymbol{K}_{\mathbf{P}} \boldsymbol{i} = \frac{2}{3} \frac{T_{\mathrm{em.ref}}}{p} \tag{3-32}$$

In this chapter, copper loss minimization is the focus. However, the framework introduced here can be universally applied. A general case is introduced initially, followed by a few special cases.

3.3.1 General Case

The coefficients k_{d}, k_{q} and k_{f} are free to choose in this case. A Lagrange multiplier is applied

$$\Lambda = \boldsymbol{i}^{\mathrm{T}} \boldsymbol{K}_{\mathbf{Cu}} \boldsymbol{i} + \lambda \left(\boldsymbol{i}^{\mathrm{T}} \boldsymbol{K}_{\mathbf{T}} \boldsymbol{i} - \frac{2}{3} \frac{T_{\mathrm{em.ref}}}{p} \right) \tag{3-33}$$

To get the solutions, set

$$\frac{\partial \Lambda}{\partial I_{\mathrm{d}}} = \frac{\partial \Lambda}{\partial I_{\mathrm{q}}} = \frac{\partial \Lambda}{\partial I_{\mathrm{f}}} = 0 \tag{3-34}$$

This gives

$$I_{\mathrm{d}} = c_{\mathrm{d}} \cdot I_{\mathrm{f}} \quad , \quad I_{\mathrm{q}} = c_{\mathrm{q}} \cdot I_{\mathrm{f}} \quad , \quad I_{\mathrm{f}} = I_{\mathrm{s}} / \sqrt{c_{\mathrm{d}}^2 + c_{\mathrm{q}}^2} \tag{3-35}$$

where c_{d} and c_{q} are two coefficients

$$c_{\mathrm{d}} = \frac{k_{\mathrm{f}}}{k_{\mathrm{d}}} \cdot \frac{L_{\mathrm{d}} - L_{\mathrm{q}}}{L_{\mathrm{m}}} \quad , \quad c_{\mathrm{q}} = \sqrt{\left(\frac{k_{\mathrm{f}}}{k_{\mathrm{d}}} \cdot \frac{L_{\mathrm{d}} - L_{\mathrm{q}}}{L_{\mathrm{m}}} \right) \cdot \left(\frac{k_{\mathrm{f}}}{k_{\mathrm{q}}} \cdot \frac{L_{\mathrm{d}} - L_{\mathrm{q}}}{L_{\mathrm{m}}} \right) + \frac{k_{\mathrm{f}}}{k_{\mathrm{q}}}} \tag{3-36}$$

With the derived c_{d} and c_{q}, the torque can be formulated as

$$T_{\mathrm{em}} = \frac{3}{2} \cdot p \cdot c_{\mathrm{q}} \cdot \left[L_{\mathrm{m}} + c_{\mathrm{d}} \cdot \left(L_{\mathrm{d}} - L_{\mathrm{q}} \right) \right] \cdot I_{\mathrm{f}}^2 \tag{3-37}$$

As can be noticed, I_{d}, I_{q}, I_{f} and $\sqrt{T_{\mathrm{em}}}$ are proportional to each other, so as the voltages,

$$I_{\mathrm{d}} \propto I_{\mathrm{q}} \propto I_{\mathrm{f}} \propto \sqrt{T_{\mathrm{em}}} \quad , \quad U_{\mathrm{d}} \propto U_{\mathrm{q}} \propto U_{\mathrm{f}} \tag{3-38}$$

which means providing the iron-core is unsaturated, the current angle is constant

$$\theta = \tan^{-1}\frac{i_{\mathrm{q}}}{i_{\mathrm{d}}} = \tan^{-1}\frac{c_{\mathrm{q}}}{c_{\mathrm{d}}} = constant \tag{3-39}$$

This indicates that copper losses are proportional to the torque

$$P_{\mathrm{Cu}} \propto P_{\mathrm{Cu\cdot s}} \propto P_{\mathrm{Cu\cdot r}} \propto I_{\mathrm{f}}^2 \propto T_{\mathrm{em.ref}} \tag{3-40}$$

3.3.2 Special Case: Copper Loss Minimization

In this case

$$\boldsymbol{K}_{\mathbf{I}} = \boldsymbol{K}_{\mathbf{R}} \tag{3-41}$$

To obtain the solution in this case, according to (3-36), c_{d} and c_{q} become

$$c_{\mathrm{d}} = \frac{2}{3}\cdot\frac{R_{\mathrm{f}}}{R_{\mathrm{s}}}\cdot\frac{L_{\mathrm{d}} - L_{\mathrm{q}}}{L_{\mathrm{m}}} \quad , \quad c_{\mathrm{q}} = \sqrt{\left(\frac{2}{3}\cdot\frac{R_{\mathrm{f}}}{R_{\mathrm{s}}}\cdot\frac{L_{\mathrm{d}} - L_{\mathrm{q}}}{L_{\mathrm{m}}}\right)^2 + \frac{2}{3}\cdot\frac{R_{\mathrm{f}}}{R_{\mathrm{s}}}} \tag{3-42}$$

which decide the ratio between d-axis, q-axis and field currents. Additionally, in this case

$$P_{\mathrm{Cu.s}} = \frac{3}{2}\cdot\left(I_{\mathrm{d}}^2 + I_{\mathrm{q}}^2\right)\cdot R_{\mathrm{s}} = 3\cdot c_{\mathrm{d}}^2\cdot R_{\mathrm{s}}\cdot I_{\mathrm{f}}^2 + P_{\mathrm{Cu.f}} > P_{\mathrm{Cu.f}} \tag{3-43}$$

3.3.3 Special Case: Maximum Torque Per Stator Ampere (Stator MTPA)

This is to achieve the maximum torque with a fixed amount of field current, also denoted as stator MTPA. Setting

$$\frac{\partial \Lambda}{\partial I_{\mathrm{d}}} = \frac{\partial \Lambda}{\partial I_{\mathrm{q}}} = 0 \tag{3-44}$$

and taking i_{f} as a constant gives

$$I_{\mathrm{q}} = \sqrt{\frac{k_{\mathrm{d}}}{k_{\mathrm{q}}}}\cdot\sqrt{I_{\mathrm{d}}^2 + \frac{L_{\mathrm{m}}}{L_{\mathrm{d}} - L_{\mathrm{q}}}\cdot I_{\mathrm{f}}\cdot I_{\mathrm{d}}} \tag{3-45}$$

In addition, the current angle in polar form can be achieved by

$$\left(\frac{k_{\mathrm{d}}}{k_{\mathrm{q}}} + 1\right)\cdot I_{\mathrm{s}}^2\cdot\cos^2\theta + \frac{k_{\mathrm{d}}}{k_{\mathrm{q}}}\cdot\frac{L_{\mathrm{m}}\cdot I_{\mathrm{f}}}{L_{\mathrm{d}} - L_{\mathrm{q}}}\cdot I_{\mathrm{s}}\cdot\cos\theta - I_{\mathrm{s}}^2 = 0 \tag{3-46}$$

which can be solved as

$$\cos\theta = \frac{-b + \sqrt{b^2 - 4\cdot a\cdot c}}{2\cdot a} \tag{3-47}$$

where

$$a = \left(\frac{k_\mathrm{d}}{k_\mathrm{q}} + 1\right) \cdot I_\mathrm{s}^2 \quad , \quad b = \frac{k_\mathrm{d}}{k_\mathrm{q}} \cdot \frac{L_\mathrm{m}}{L_\mathrm{d} - L_\mathrm{q}} \cdot i_\mathrm{f} \cdot I_\mathrm{s} \quad , \quad c = -I_\mathrm{s}^2 \tag{3-48}$$

In case of $k_\mathrm{d} = k_\mathrm{q}$, the solution becomes

$$\cos\theta = \frac{-L_\mathrm{m} \cdot I_\mathrm{f} + \sqrt{(L_\mathrm{m} \cdot I_\mathrm{f})^2 + 8 \cdot \left(L_\mathrm{d} - L_\mathrm{q}\right)^2 \cdot I_\mathrm{s}^2}}{4 \cdot \left(L_\mathrm{d} - L_\mathrm{q}\right) \cdot I_\mathrm{s}} \tag{3-49}$$

A comparison between stator MTPA and copper loss minimization is presented in Figure 3-8. The set of I_d, I_q and I_f obtained from total copper loss minimization all at once, is the same as, to obtain I_f from total copper loss minimization and then to obtain I_d and I_q from MTPA with such I_f. In the 3D space, the solution of MTPA at different levels of field current forms a surface whereas the solution of copper loss minimization forms a line.

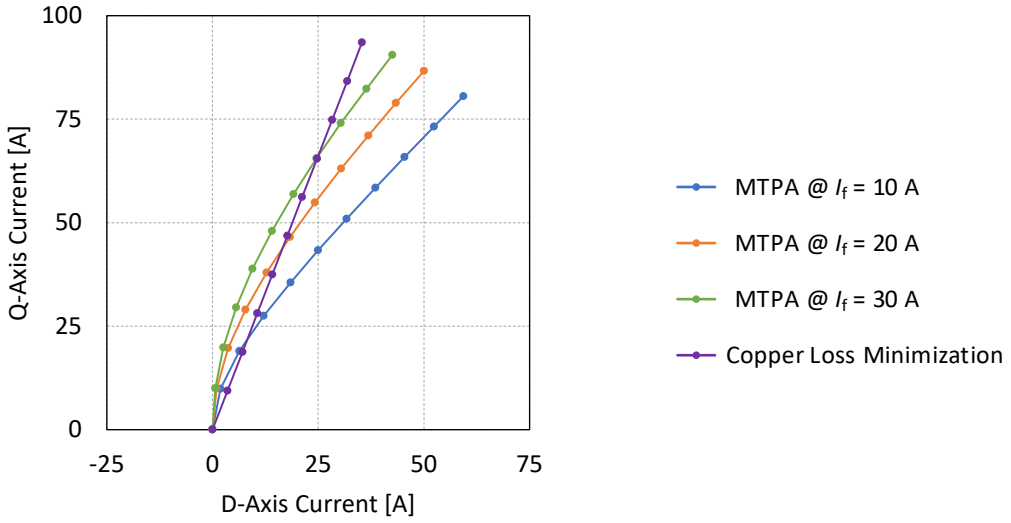

Figure 3-8 Comparison of MTPA and copper loss minimization ($L_\mathrm{d} = 15$ [mH], $L_\mathrm{q} = 10$ [mH], $L_\mathrm{m} = 10$ [mH]).

3.3.4 Special Case: Maximum Torque Per Field Ampere (Field MTPA)

This is to achieve a certain torque with a minimum amount of field current. There are two situations. If the torque required can be achieved by purely reluctance torque, then

$$i_\mathrm{f} = 0 \quad , \quad \theta_\mathrm{I} = \begin{cases} 45° & L_\mathrm{d} > L_\mathrm{q} \\ 135° & L_\mathrm{d} < L_\mathrm{q} \end{cases} \tag{3-50}$$

If the maximum pure reluctance torque is not high enough, then field current is needed,

$$i_\mathrm{f} > 0 \quad , \quad i_\mathrm{s} = I_\mathrm{s.max} \tag{3-51}$$

To minimize the field current, MTPA of stator current needs to be applied. Hence the solution in (3-49) can be applied in this case

$$\cos\theta_\mathrm{I} = \frac{-L_\mathrm{m} \cdot I_\mathrm{f} + \sqrt{(L_\mathrm{m} \cdot I_\mathrm{f})^2 + 8 \cdot \left(L_\mathrm{d} - L_\mathrm{q}\right)^2 \cdot I_\mathrm{s.max}^2}}{4 \cdot \left(L_\mathrm{d} - L_\mathrm{q}\right) \cdot I_\mathrm{s.max}} \tag{3-52}$$

3.3.5 Special Case: Zero D-Axis Current

Zero d-axis current is a special case that simplifies the control from three degrees of control freedom to two degrees. In this case, the penalty factor of d-axis current goes to infinity. According to the general solution, the ratio between the q-axis and field currents becomes

$$\frac{i_\mathrm{q}}{i_\mathrm{f}} = \lim_{k_\mathrm{d}\to\infty} c_\mathrm{q} = \sqrt{k_\mathrm{f}/k_\mathrm{q}} \tag{3-53}$$

Providing the total copper loss is to be minimized, the paneities of q-axis and field currents can be set as

$$k_\mathrm{q} = \frac{3}{2}\cdot R_\mathrm{s} \quad , \quad k_\mathrm{f} = R_\mathrm{f} \tag{3-54}$$

In this case, the stator copper loss equals field copper loss

$$\frac{3}{2}\cdot i_\mathrm{q}^2 \cdot R_\mathrm{s} = P_\mathrm{Cu.s} = P_\mathrm{Cu.f} = i_\mathrm{f}^2 \cdot R_\mathrm{f} \tag{3-55}$$

and the stator current is proportional to the field current

$$i_\mathrm{q} \propto i_\mathrm{f} \propto \sqrt{T_\mathrm{em}} \tag{3-56}$$

Furthermore, with the minimized total copper loss, the power factor angle φ follows

$$\tan\varphi_\mathrm{PF} = \frac{\boldsymbol{i}^\mathrm{T}\boldsymbol{K_Q}\boldsymbol{i}}{\boldsymbol{i}^\mathrm{T}\boldsymbol{K_P}\boldsymbol{i}} = \frac{L_\mathrm{q}}{L_\mathrm{m}}\cdot\frac{i_\mathrm{q}}{i_\mathrm{f}} = \frac{L_\mathrm{q}}{L_\mathrm{m}}\cdot\sqrt{\frac{2}{3}\cdot\frac{R_\mathrm{f}}{R_\mathrm{s}}} \tag{3-57}$$

which is constant providing the iron core is not saturated.

3.3.6 Special Case: Unity Power Factor

The *unity power factor* (UPF) control is applied to fully utilize the power capability of the inverter. Let unity power factor be an additional constraint

$$\Lambda = \boldsymbol{i}^\mathrm{T}\boldsymbol{K_I}\boldsymbol{i} + \lambda_1\cdot\left(\boldsymbol{i}^\mathrm{T}\boldsymbol{K_P}\boldsymbol{i} - \frac{2}{3}\frac{T_\mathrm{em.ref}}{p}\right) + \lambda_2\cdot\left(\boldsymbol{i}^\mathrm{T}\boldsymbol{K_Q}\boldsymbol{i} - 0\right) \tag{3-58}$$

This results in a polynomial exceeding fourth degree, and a complete analytical solution is therefore not possible. However, some other characteristics can be derived for UPF control. In UPF condition, the voltage vector angle equals the current vector angle

$$Q = \frac{3}{2}\cdot\left(U_\mathrm{q}\cdot I_\mathrm{d} - U_\mathrm{d}\cdot I_\mathrm{q}\right) = 0 \quad \Rightarrow \quad \tan\theta_\mathrm{U} = \frac{U_\mathrm{q}}{U_\mathrm{d}} = \frac{I_\mathrm{q}}{I_\mathrm{d}} = \tan\theta_\mathrm{I} \tag{3-59}$$

In case of $L_\mathrm{d} = L_\mathrm{q}$, the vector of reactance voltage drop is perpendicular to the current vector. Since the addition of reactance voltage drop and EMF gives the terminal voltage, these three vectors form a right triangle as shown in Figure 3-9 (a). Hence the voltage vector is always along the circle which diameter is defined by the back-EMF. Similarly for the case $L_\mathrm{d} > L_\mathrm{q}$, the voltage vector is at the ellipse which major-axis is defined by the back-EMF, as shown in Figure 3-9 (b). When the current vector amplitude I_s or angle θ_I changes, the field current should be adjusted accordingly using (3-21)

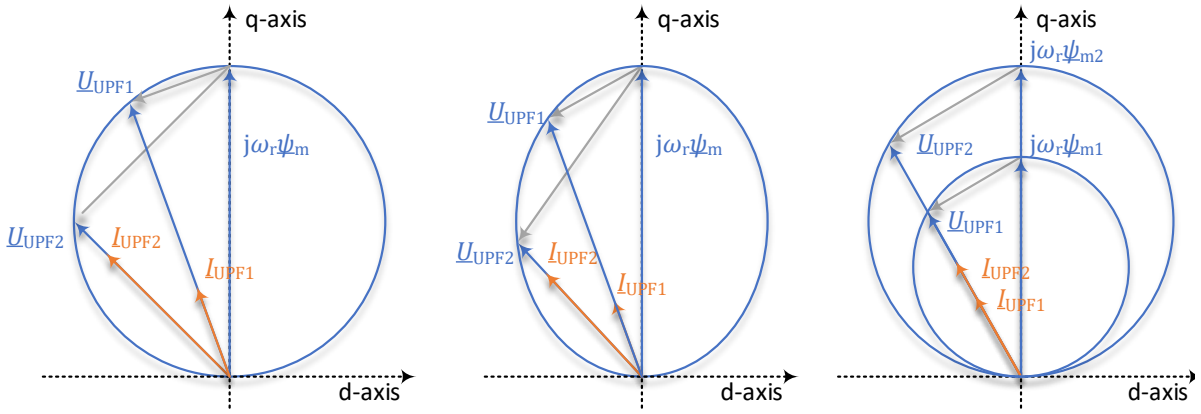

(a) $L_{\mathrm{d}} = L_{\mathrm{q}}$. (b) $L_{\mathrm{d}} > L_{\mathrm{q}}$. (c) Active power increase.

Figure 3-9 Vector diagram in unity power factor control.

$$I_{\mathrm{d}} = I_{\mathrm{s}} \cdot \cos\theta_{\mathrm{I}} \quad , \quad I_{\mathrm{d}} = I_{\mathrm{s}} \cdot \sin\theta_{\mathrm{I}} \quad , \quad I_{\mathrm{f}} = -\frac{L_{\mathrm{d}} \cdot I_{\mathrm{d}}^2 + L_{\mathrm{q}} \cdot I_{\mathrm{q}}^2}{L_{\mathrm{m}} \cdot I_{\mathrm{d}}} \tag{3-60}$$

In addition, following (3-59), the active power in UPF can be described as

$$P = \frac{3}{2} \cdot \left(U_{\mathrm{d}} \cdot I_{\mathrm{d}} + U_{\mathrm{q}} \cdot I_{\mathrm{q}}\right) = \frac{3}{2} \cdot U_{\mathrm{d}} \cdot I_{\mathrm{d}} \cdot (1 + \tan^2\theta_{\mathrm{I}}) \tag{3-61}$$

This indicates that, to increase the active power P by a factor of k at a certain θ_{I}, then U_{d} and I_{d} shall increase by a factor of $\sqrt{k}$. Hence the vector diagrams before and after a power increase form homothetic (similar) triangles as shown in Figure 3-9 (c).

3.4 Steady-State Performance at Voltage or Current Limits

In traction applications, the constraints are the current and voltage limits

$$I_{\mathrm{s}} \le I_{\mathrm{s.max}} \quad , \quad 0 \le I_{\mathrm{f}} \le I_{\mathrm{f.max}} \quad , \quad U_{\mathrm{s}} \le U_{\mathrm{s.max}} \tag{3-62}$$

The limits, the unity power facor ellipse and torque contour can be illustrated in the dq-plane as shown in Figure 3-10. The current vector can only be placed in the common area within the current and voltage limits shown as the green area.

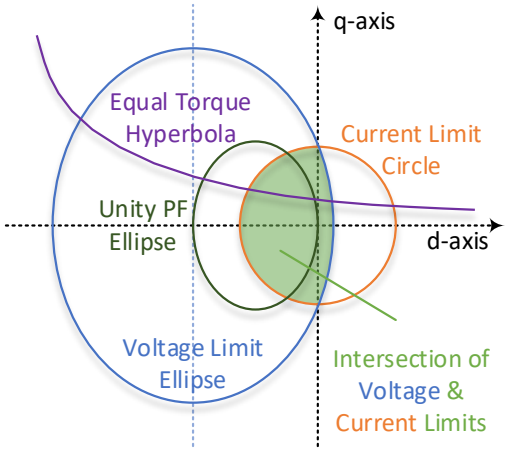

Figure 3-10 Schematic diagram of current limit circle, voltage limit ellipse, equal torque hyperbola and unity power factor ellipse in the dq-plane.

3.4.1 Torque-Speed Envelope

Along the torque-speed envelope, the machine outputs the maximum torque at any specific speed. This is equivalent to solving $\max_{\boldsymbol{i}}\{\boldsymbol{i}^{\mathrm{T}}\boldsymbol{K}_{\mathbf{P}}\boldsymbol{i}\}$ with the constraints introduced in (3-72). The torque-speed envelope is composed by the operation points with the highest torque at each speed. The torque-speed envelope can be divided into three sections as shown by the schematic in Figure 3-11 and the corresponding power-speed is presented in Figure 3-12.

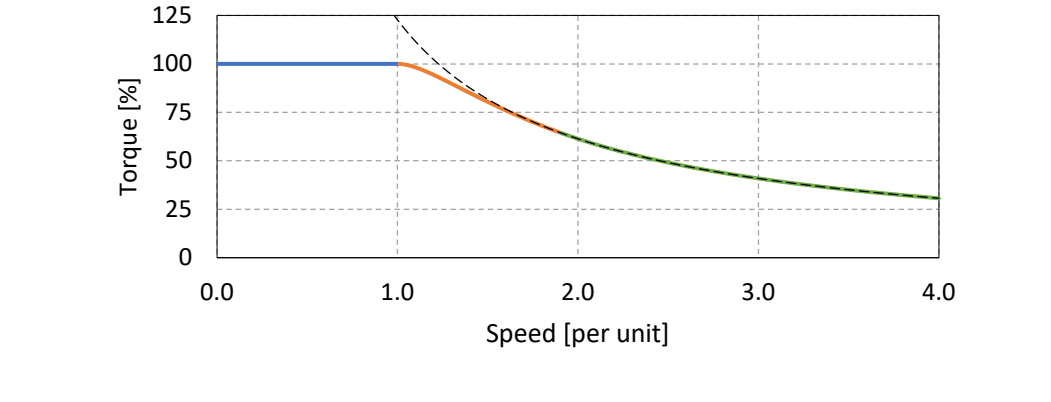

Figure 3-11 Schematic diagram of torque-speed curve.

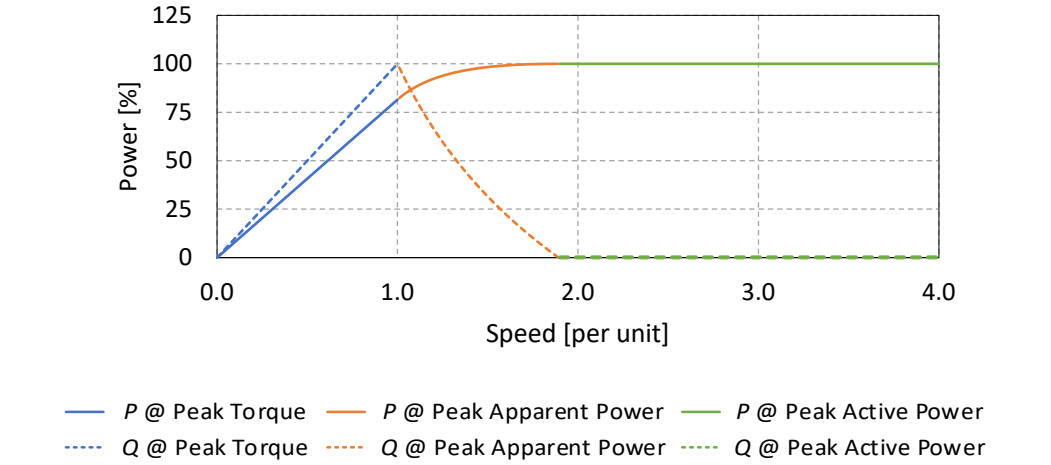

Figure 3-12 Schematic diagram of power-speed curve.

A. Section 1 (Low Speed): Peak Torque

At low speed when the back-EMF is below the voltage limit, to maximize the torque, the stator and field currents are at the limits

$$I_{\mathrm{s}} = I_{\mathrm{s.max}} \quad , \quad I_{\mathrm{f}} = I_{\mathrm{f.max}} \tag{3-63}$$

This is the stator MTPA problem solved in Section 3.3.3. Recall the solution (3-49), the current angle here is

$$\cos\theta_1 = \frac{-\psi_{\mathrm{m.max}} + \sqrt{\psi_{\mathrm{m\cdot max}}^2 + 8\cdot\left(L_{\mathrm{d}} - L_{\mathrm{q}}\right)^2 \cdot I_{\mathrm{s\cdot max}}^2}}{4\cdot\left(L_{\mathrm{d}} - L_{\mathrm{q}}\right)\cdot I_{\mathrm{s.max}}} = \cos\theta_{\mathrm{MTPA}} \tag{3-64}$$

where $\psi_{\mathrm{m.max}}$ is the maximum mutual flux linkage

$$\psi_{\mathrm{m.max}} = L_{\mathrm{m}} \cdot I_{\mathrm{f.max}} \tag{3-65}$$

The corresponding torque can be calculated as

$$T_{\mathrm{em}} = \frac{3}{2} \cdot p \cdot \left(\psi_{\mathrm{m\cdot max}} \cdot I_{\mathrm{s.max}} \cdot \sin\theta_{\mathrm{I}} + \frac{L_{\mathrm{d}} - L_{\mathrm{q}}}{2} \cdot I_{\mathrm{s.max}}^2 \cdot \sin 2\theta_{\mathrm{I}} \right) \tag{3-66}$$

This is valid until the terminal voltage hits the voltage limit. According to (3-72), this solution is valid when

$$\omega_{\mathrm{r}} \le \omega_{\mathrm{r\cdot MTPA}} = \frac{U_{\mathrm{s.max}}}{\sqrt{(L_{\mathrm{d}} \cdot I_{\mathrm{d}} + \psi_{\mathrm{m.max}})^2 + \left(L_{\mathrm{q}} \cdot I_{\mathrm{q}}\right)^2}} \tag{3-67}$$

where $\omega_{\mathrm{r\cdot MTPA}}$ is the critical speed that distinguishes the peak torque section and the peak apparent power section. In the dq-plane, this is when the stator voltage limit ellipse cuts the stator current limit circle at the MTPA operation point.

B. Section 2 (Medium Speed): Peak Apparent Power

After ω_{r} reaches $\omega_{\mathrm{r,1}}$, the operation point in the dq-plane moves along the stator current limit circle in the anti-clockwise direction. In this case, the operation point is located at the intersect of the current limit circle and the voltage limit ellipse

$$I_{\mathrm{s}} = I_{\mathrm{s.max}} \quad , \quad I_{\mathrm{f}} = I_{\mathrm{f.max}} \quad , \quad U_{\mathrm{s}} = U_{\mathrm{s.max}} \tag{3-68}$$

With (3-72), the stator current angle of intersection point can be solved as

$$\cos\theta_2 = \frac{-b + \sqrt{b^2 - 4 \cdot a \cdot c}}{2 \cdot a} \tag{3-69}$$

where

$$a = \frac{L_{\mathrm{d}}^2 - L_{\mathrm{q}}^2}{2} \cdot I_{\mathrm{s\cdot max}} \quad , \quad b = L_{\mathrm{d}} \cdot \psi_{\mathrm{m\cdot max}} \quad , \quad c = \frac{\psi_{\mathrm{m.max}}^2 + L_{\mathrm{q}}^2 \cdot I_{\mathrm{s\cdot max}}^2 - \frac{U_{\mathrm{s\cdot max}}^2}{\omega_{\mathrm{r}}^2}}{2} \tag{3-70}$$

In case unity power factor ellipse intersects the current limit ellipse, i.e.

$$I_{\mathrm{ch.max}} = \frac{L_{\mathrm{m}}}{L_{\mathrm{d}}} \cdot I_{\mathrm{f.max}} \ge I_{\mathrm{s.max}} \tag{3-71}$$

then this section is valid until the operation point moves to the unity power factor point where the current angle is

$$\cos\theta_2 = \frac{-\psi_{\mathrm{m\cdot max}} + \sqrt{\psi_{\mathrm{m\cdot max}}^2 - 4 \cdot \left(L_{\mathrm{d}} - L_{\mathrm{q}}\right) \cdot L_{\mathrm{q}} \cdot I_{\mathrm{s\cdot max}}^2}}{2 \cdot \left(L_{\mathrm{d}} - L_{\mathrm{q}}\right) \cdot I_{\mathrm{s\cdot max}}} = \cos\theta_{\mathrm{UPF}} \tag{3-72}$$

This further gives the speed range of this section

$$\omega_{\mathrm{r\cdot MTPA}} \le \omega_{\mathrm{r}} \le \omega_{\mathrm{r\cdot UPF}} = \frac{U_{\mathrm{s\cdot max}}}{\sqrt{(L_{\mathrm{d}} I_{\mathrm{s\cdot max}} \cos\theta_2 + \psi_{\mathrm{m\cdot max}})^2 + \left(L_{\mathrm{q}} I_{\mathrm{s\cdot max}} \cos\theta_2\right)^2}} \tag{3-73}$$

C. *Section 3 (High Speed): Peak Active Power (Unity Power Factor)*

After unity power factor is reached, in order to maintain the maximum torque, power factor should be kept at unity. This is done by shrinking the field current so that the current limit circle, the voltage limit ellipse and the unity power factor ellipse intersect at the same point. In this case

$$I_{\mathrm{s}} = I_{\mathrm{s.max}} \quad , \quad U_{\mathrm{s}} = U_{\mathrm{s.max}} \quad , \quad \boldsymbol{i}^{\mathrm{T}}\boldsymbol{K}_{\mathbf{Q}}\boldsymbol{i} = 0 \tag{3-74}$$

This gives

$$\tan\theta_3 = \frac{i_{\mathrm{q}}}{i_{\mathrm{d}}} = -\frac{U_{\mathrm{s.max}}}{\omega_{\mathrm{r}} \cdot L_{\mathrm{q}} \cdot I_{\mathrm{s.max}}} \quad , \quad I_{\mathrm{f}} = -\frac{L_{\mathrm{d}} \cdot i_{\mathrm{d}}^2 + L_{\mathrm{q}} \cdot i_{\mathrm{q}}^2}{L_{\mathrm{m}} \cdot i_{\mathrm{d}}} \tag{3-75}$$

As speed increases, the characteristic current i_{ch} gradually shifts towards the current limit $I_{\mathrm{s.max}}$ to keep unity power factor. This means that the operation points along this section are all at peak active power, since current, voltage and power factor are all at maximum. Hence

$$T_{\mathrm{em}} = \frac{3}{2} \cdot p \cdot \frac{U_{\mathrm{s.max}} \cdot I_{\mathrm{s.max}}}{\omega_{\mathrm{r}}} \propto \frac{1}{\omega_{\mathrm{r}}} \tag{3-76}$$

D. *Current Vector Loci*

The field current and dq-plane currents along the envelope shown in Figure 3-11 are presented in Figure 3-13. The field current decreases in the section of peak active power whereas the stator current amplitude keeps the same in all three sections. The current vector stays at the MTPA point in the section of peak torque, but moves anti-clockwise in sections of peak apparent power and peak active power. It should be point out that, due to the voltage and current constraints, the combinations of d- and q-axis current components and the field current are unique along the envelope. However, inside the envelope, there are multiple solutions.

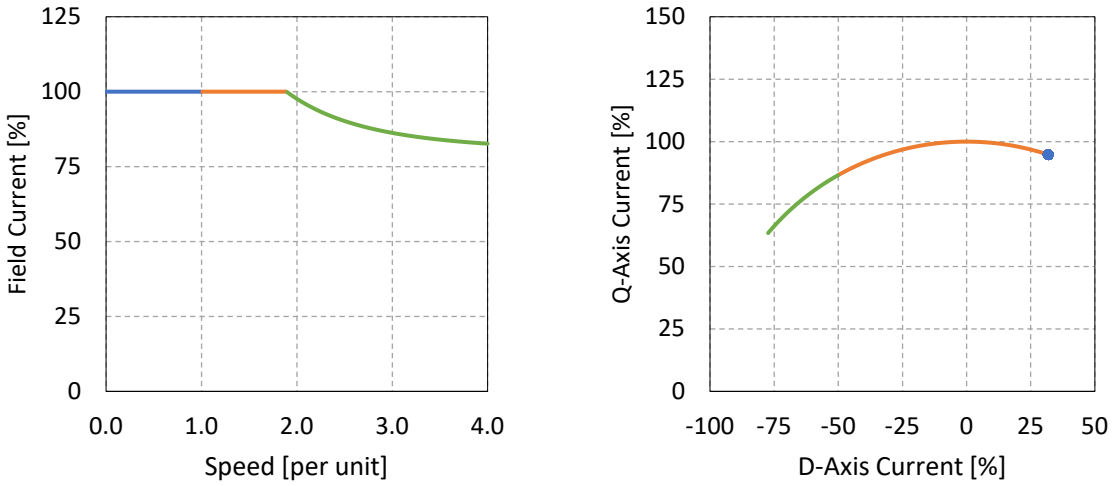

(a) Field current. (b) D- and q-axis currents.

Peak Torque — Peak Apparent Power — Peak Active Power

Figure 3-13 Schematic diagram of d-axis, q-axis and field currents.

3.4.2 Torque-Boosting Area

Within the torque-speed envelope, the strategy of copper loss minimization can be applied. In case of

$$I_{\mathrm{f.max}} = I_{\mathrm{s.max}} / \sqrt{c_{\mathrm{d}}^2 + c_{\mathrm{q}}^2} \tag{3-77}$$

total copper loss minimization can be followed from zero torque until the peak torque. However, in case of

$$I_{\mathrm{f.max}} > I_{\mathrm{s.max}} / \sqrt{c_{\mathrm{d}}^2 + c_{\mathrm{q}}^2} \tag{3-78}$$

when the stator current reaches the limit, the field current is still beneath the limit. This gives a torque-boosting area by increasing field current from $I_{\mathrm{s.max}} / \sqrt{c_{\mathrm{d}}^2 + c_{\mathrm{q}}^2}$ until $I_{\mathrm{f.max}}$, while at the same time, $I_{\mathrm{s}} = I_{\mathrm{s.max}}$. In contrast, in case of

$$I_{\mathrm{f.max}} < I_{\mathrm{s.max}} / \sqrt{c_{\mathrm{d}}^2 + c_{\mathrm{q}}^2} \tag{3-79}$$

when the field current reaches the limit, the stator current is still beneath the limit. This gives a torque-boosting area by increasing stator current from $I_{\mathrm{s.max}}$ until $I_{\mathrm{f.max}} \cdot \sqrt{c_{\mathrm{d}}^2 + c_{\mathrm{q}}^2}$, while at the same time, $I_{\mathrm{f}} = I_{\mathrm{f.max}}$.

3.4.3 Field-Weakening Area

When the speed of the machine increases, the back-EMF increases. If the voltage reaches the limit, the machine enters the field weakening area. Hence

$$\Lambda = \boldsymbol{i}^{\mathrm{T}} \boldsymbol{K}_{\mathbf{I}} \boldsymbol{i} + \lambda_1 \cdot \left(\boldsymbol{i}^{\mathrm{T}} \boldsymbol{K}_{\mathbf{T}} \boldsymbol{i} - \frac{2}{3} \frac{T_{\mathrm{em.ref}}}{p} \right) + \lambda_2 \cdot (U_{\mathrm{s}} - U_{\mathrm{s.max}}) \tag{3-80}$$

This results in polynomials exceeding fourth degree, and a complete analytical solution is therefore not possible [56]. However, the boundary between the normal operation area and the field weakening area can be solved. Apply

$$I_{\mathrm{d}} = c_{\mathrm{d}} \cdot I_{\mathrm{f}} \quad , \quad I_{\mathrm{q}} = c_{\mathrm{q}} \cdot I_{\mathrm{f}} \quad , \quad U_{\mathrm{s}} = U_{\mathrm{s.max}} \tag{3-81}$$

and this gives

$$\omega_{\mathrm{r}} = \frac{1}{\sqrt{(c_{\mathrm{d}} \cdot L_{\mathrm{d}} + L_{\mathrm{m}})^2 + \left(c_{\mathrm{q}} \cdot L_{\mathrm{q}}\right)^2}} \cdot \frac{U_{\mathrm{s.max}}}{I_{\mathrm{f}}} \tag{3-82}$$

According to the torque equation (3-37), along the boundary, the torque is inversely proportional to the square of speed

$$T_{\mathrm{em}} = \frac{3}{2} \cdot p \cdot \frac{U_{\mathrm{s.max}}^2}{\omega_{\mathrm{r}}^2} \cdot \frac{c_{\mathrm{q}} \cdot \left[L_{\mathrm{m}} + c_{\mathrm{d}} \cdot \left(L_{\mathrm{d}} - L_{\mathrm{q}} \right) \right]}{(c_{\mathrm{d}} \cdot L_{\mathrm{d}} + L_{\mathrm{m}})^2 + \left(c_{\mathrm{q}} \cdot L_{\mathrm{q}}\right)^2} \propto \frac{U_{\mathrm{s.max}}^2}{\omega_{\mathrm{r}}^2} \tag{3-83}$$

3.5 Solution Considering Saturation

When the iron-core of a machine saturates, the inductance value decreases with an increase of current. In this case, a numerical method needs to be established so that the effects of saturations are considered in the optimization process. In this section, the FEM calculation results of a machine are used to describe the performance of a 48 V EESM for mild-hybrid vehicles. The design of the machine is presented in Chapter 5. After the non-linear characteristics of machine is presented, the algorithm is introduced. Then the performance of the machine is illustrated with different coefficients introduced to cost functions.

3.5.1 Non-Linear Characteristics of Machine

In this section, the non-linear characteristics of machine, including flux linkages, inductances, electromagnetic torque, power factor and iron-core losses are presented. These characteristics are obtained from FEM analysis.

A. Flux Linkages

The d- and q-axis flux linkage maps of the machine at different levels of field current are shown in Figure 3-14 and Figure 3-15 respectively. The circle shows the current limit of 500 A as the amplitude. As field current increases, the ψ_{d} and ψ_{q} contours on the dq-plane moves towards left horizontally whereas the shape of the contours remain the same. It is therefore possible to calculate ψ_{d} and ψ_{q} once at zero field current level and then shift the origin of the plane to the right to get the flux linkage values when a field current is introduced. In other words, the d-axis current and the field current can be transformed from each other to get the values of ψ_{d} and ψ_{q}. Additionally, the d-axis current influences ψ_{q} and the q-axis current influences ψ_{d}. In addition, the field current gives an impact on ψ_{q} as well. This indicates the magnetic coupling between d- and q-axis flux paths.

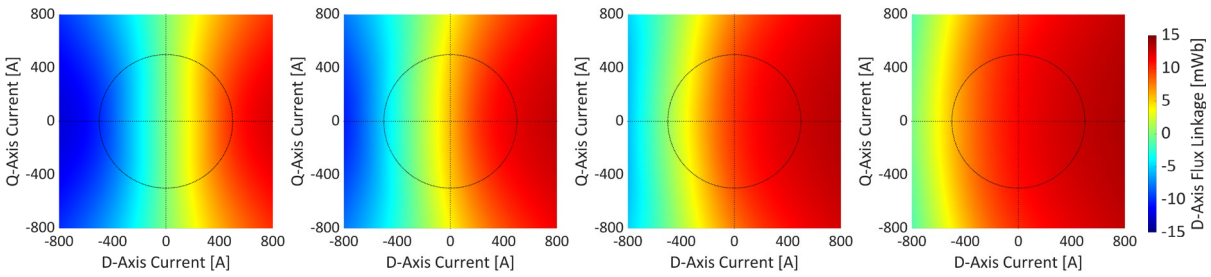

(a) $I_{\mathrm{f}} = 0$ A. (b) $I_{\mathrm{f}} = 5$ A. (c) $I_{\mathrm{f}} = 10$ A. (d) $I_{\mathrm{f}} = 15$ A.

Figure 3-14 D-axis flux linkage ψ_{d} at different field current levels in a 48 V EESM.

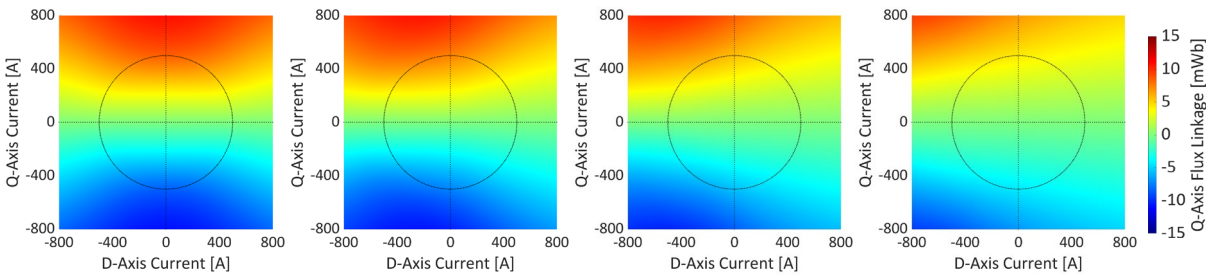

(a) $I_{\mathrm{f}} = 0$ A. (b) $I_{\mathrm{f}} = 5$ A. (c) $I_{\mathrm{f}} = 10$ A. (d) $I_{\mathrm{f}} = 15$ A.

Figure 3-15 Q-axis flux linkage ψ_{q} at different field current levels in a 48 V EESM.

B. *Inductances*

The d- and q-axis inductance maps of the machine are shown in Figure 3-16 and Figure 3-17 respectively. As can be noticed, when the field current increases, the inductances decrease. This can be seen more obviously in Figure 3-18 where the d-axis, q-axis and mutual incremental inductances at $I_\mathrm{d} = 0$ and $I_\mathrm{q} = 0$ are compared. The d-axis inductance decreases more than the q-axis inductance does since the d-axis flux path can be directly saturated by the field current whereas the q-axis flux path is only partly affected by field current due to cross-saturation, e.g. in the rotor pole shoe and the stator yoke. As a result, $L_\mathrm{d} > L_\mathrm{q}$ at lower field current whereas $L_\mathrm{d} < L_\mathrm{q}$ at high field current.

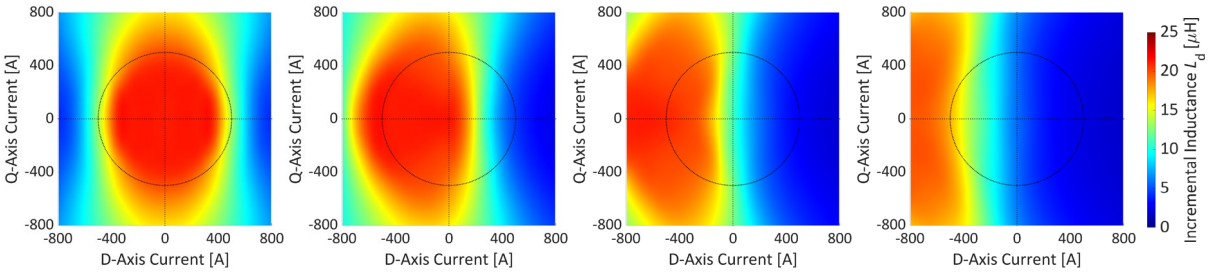

(a) $I_\mathrm{f} = 0$ A. (b) $I_\mathrm{f} = 5$ A. (c) $I_\mathrm{f} = 10$ A. (d) $I_\mathrm{f} = 15$ A.

Figure 3-16 D-axis incremental inductance at different field current levels in a 48 V EESM.

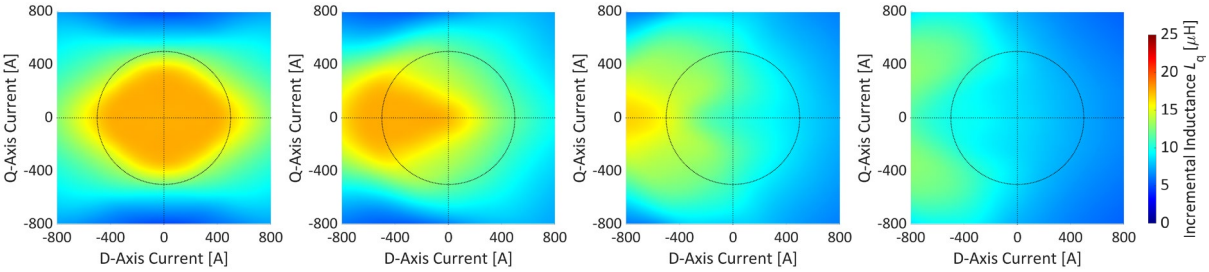

(a) $I_\mathrm{f} = 0$ A. (b) $I_\mathrm{f} = 5$ A. (c) $I_\mathrm{f} = 10$ A. (d) $I_\mathrm{f} = 15$ A.

Figure 3-17 Q-axis incremental inductance at different field current levels in a 48 V EESM.

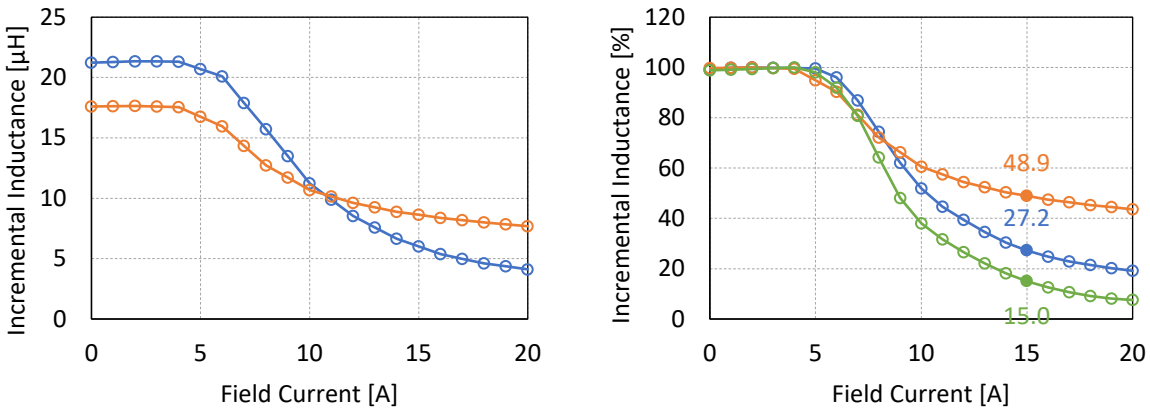

(a) Incremental inductances in μH. (b) Incremental inductances in percentage.

Figure 3-18 Comparison of d-axis, q-axis and mutual incremental inductances at $I_\mathrm{d} = 0$ & $I_\mathrm{q} = 0$.

C. *Electromagnetic Torque*

The electromagnetic torque is calculated using (2-23) and the map is shown in Figure 3-19. In the figure, the MTPA curves are perpendicular to the torque contours shown as the black dots. At zero field current, the torque generated by the machine is purely reluctance torque. In this case, the MTPA curves locate at ±45 deg and ±135 deg as shown in (a). The torque component due to field current appears in (b), (c) and (d). It is interesting to notice that the MTPA curve firstly turn to the first quadrant at low field current level as shown in (b) and then to the second quadrant as field current goes higher as shown in (d). This is due to the salience flip in inductances presented in Figure 3-16, Figure 3-17 and Figure 3-18. As presented in Figure 3-3, the asymptotic line of the torque contour locates on the left plane when $L_\mathrm{d} > L_\mathrm{q}$ which is the case in Figure 3-19 (b), whereas it locates on the right plane when $L_\mathrm{d} > L_\mathrm{q}$ which is the case in Figure 3-19 (d). The case shown in Figure 3-19 (c) is the intermediate case when $L_\mathrm{d} \approx L_\mathrm{q}$ and the MTPA curve follows the q-axis.

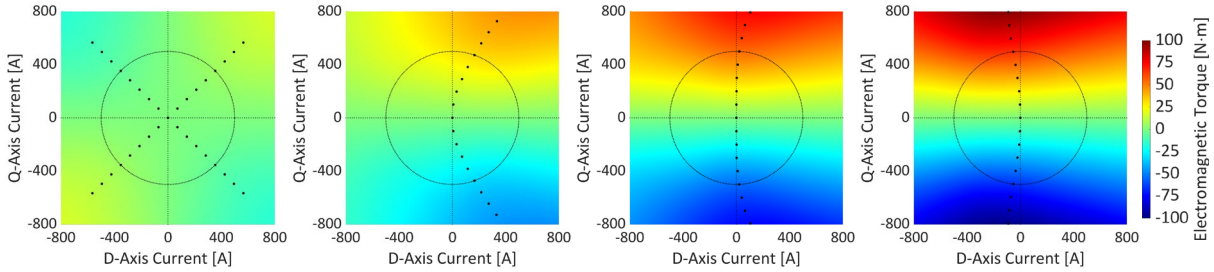

(a) $I_\mathrm{f} = 0$ A. (b) $I_\mathrm{f} = 5$ A. (c) $I_\mathrm{f} = 10$ A. (d) $I_\mathrm{f} = 15$ A.

Figure 3-19 Electromagnetic torque T_em at different field current levels in a 48 V EESM.

D. *Power Factor*

The power factor is calculated and shown in Figure 3-20. Resistive voltage drops are neglected here, so that the shape of the curves is independent from the speed. The positive values in the plot indicate motor operation whereas the negative values indicate generator operation. The high power factor area forms an ellipse as introduced in (3-22) and (3-23), and the shape of the curves is consistent with that in Figure 3-4 and Figure 3-5. The area inside the unity power factor ellipse is capacitive whereas the area outside is inductive. The unity power factor ellipse intersects the d-axis at two points. One is the origin and the other is at $(-i_\mathrm{ch}, 0)$. As can be noticed, as the field current increases, i_ch increases as well, and the area with high power factor expends consequently.

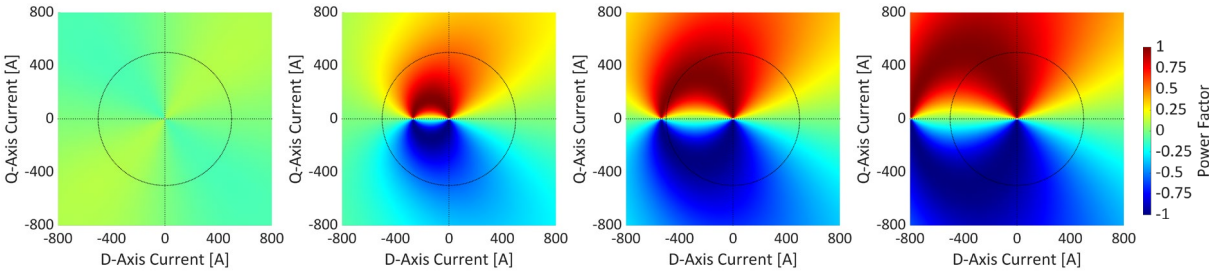

(a) $I_\mathrm{f} = 0$ A. (b) $I_\mathrm{f} = 5$ A. (c) $I_\mathrm{f} = 10$ A. (c) $I_\mathrm{f} = 15$ A.

Figure 3-20 Power factor (resistive voltage drops neglected) at different field current levels in a 48 V EESM.

3.5.2 Iterative Algorithm

An iteration algorithm for copper loss minimization with the flux linkage maps from FEM analysis is shown in Figure 3-21. The algorithm starts with a set of initial values, and then a parameter sweep is applied to I_s, θ_I and I_f around the initial values so that a 3D matrix of I_s, θ_I and I_f is generated. The sweep is performed with a range of k. k can be from 50% to 150% in the beginning. Thereafter, the d- and q-axis flux linkages corresponding to each combination of I_s, θ_I and I_f are interpolated using the flux linkage maps. After that, the corresponding torques and voltages are calculated, and the 3D matrix is filtered so that the remaining combinations of I_s, θ_I and I_f fulfill all the criteria of current, voltage and torque limits. In the end, a cost function is applied. The cost function in the figure is the copper loss as an example, but it can also be the total loss or the field current, and so forth. Then the combination of I_s, θ_I and I_f with a minimum cost is the solution obtained in this iteration. At the same time, an error ε is calculated by comparing the I_s, θ_I and I_f obtained from this iteration and the ones from the previous iteration. If ε is small enough, then the parameter sweep in the next iteration will be carried out in a smaller range so that the resolution can be improved. Then a new iteration starts with the I_s, θ_I and I_f obtained in the previous iteration. The iteration loop will continue until the searching range k becomes small enough, i.e. when the improvement of resolution by starting a new iteration is negligible. At this point, the results from the last iteration are considered as the optimal solution.

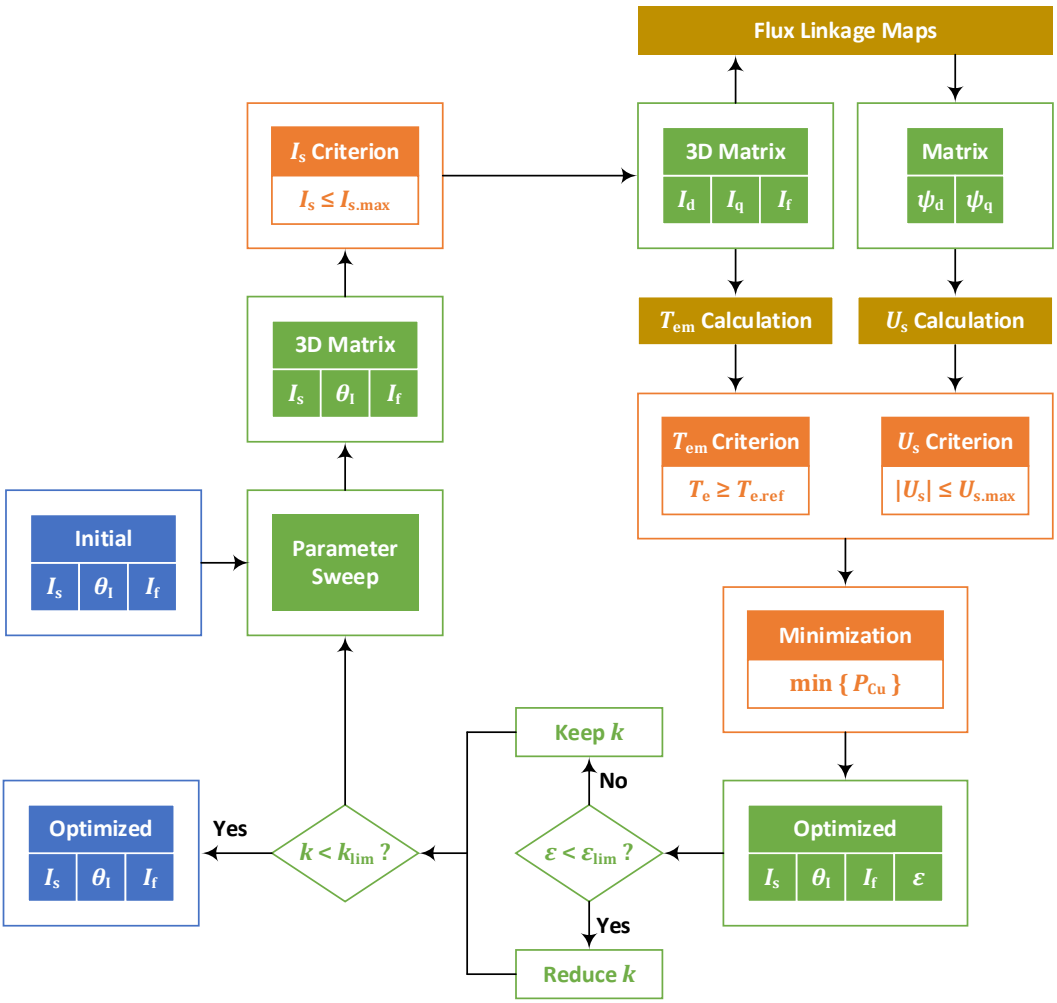

Figure 3-21 Iteration algorithm considering iron-core saturation.

3.5.3 Copper Loss Minimization

Geometrically, copper loss minimization can be illustrated as to find the point of tangency of the copper loss isosurface and the torque isosurface. The torque isosurfaces at 10, 20 and 30 N·m with the corresponding copper loss isosurfaces in tangency are shown in Figure 3-22. The two isosurfaces are illustrated as pushing against each other. A growing copper loss isosurface pushes the torque isosurface away to a higher torque level.

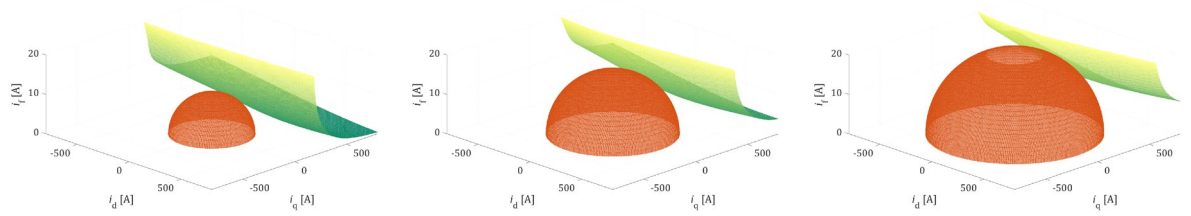

(a) $T_{\mathrm{em}} = 10\ \mathrm{N \cdot m}$, $P_{\mathrm{Cu}} = 530\ \mathrm{W}$. (b) $T_{\mathrm{em}} = 20\ \mathrm{N \cdot m}$, $P_{\mathrm{Cu}} = 1250\ \mathrm{W}$. (c) $T_{\mathrm{em}} = 30\ \mathrm{N \cdot m}$, $P_{\mathrm{Cu}} = 2230\ \mathrm{W}$.

Figure 3-22 Isosurfaces of torque and the total copper loss in tangency using the FEM data of a 48 V EESM.

The trajectories of the stator MTPA at different field current levels and the solutions given by total copper loss minimization are compared in Figure 3-23. The stator MTPA trajectory goes to the first quadrant at low field current level and then goes to the second quadrant at high field current level. This is due to the saturation of iron core in d-axis flux path as field current grows. The flip of saliency influences the torque contour in dq-frame and therefore influences the stator MTPA trajectory.

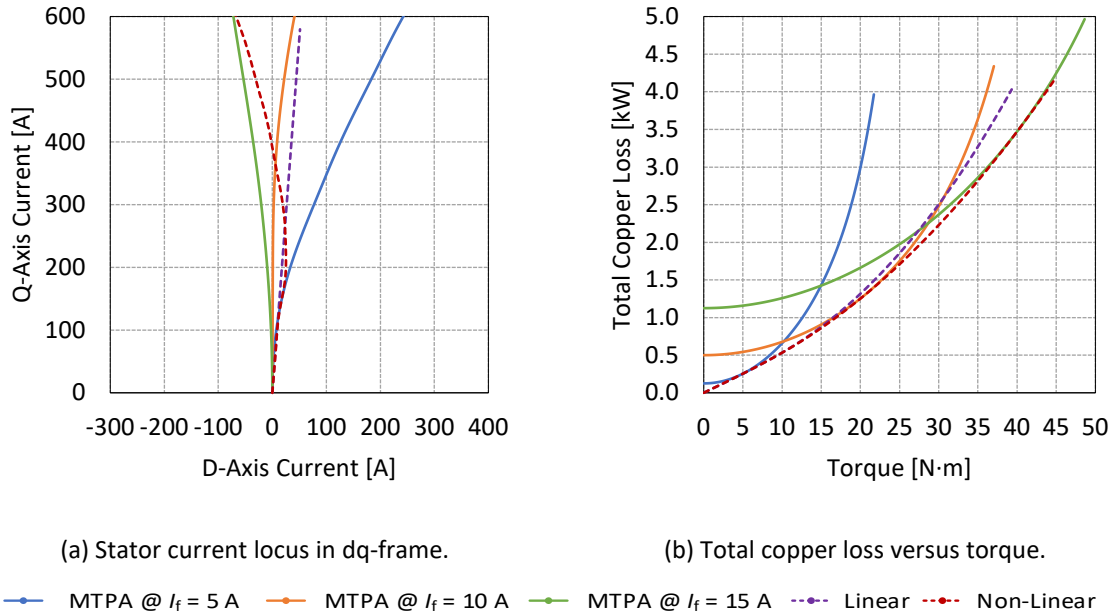

(a) Stator current locus in dq-frame. (b) Total copper loss versus torque.

Figure 3-23 Comparisons of stator MTPA at different levels of field current and total copper loss minimization considering linear or non-linear magnetic properties using the FEM data of a 48 V EESM.

The trajectory denoted as “Linear” shows the solutions of total copper loss minimization considering linear magnetic characteristics, i.e. taking non-saturated inductance values. The ratio between d- and q-axis currents is decided by the proportionality in (3-38). The trajectory denoted as “Non-Linear” shows the solutions considering non-linear magnetic characteristics, i.e. taking saturated inductance values as currents increase. The “Non-Linear” trajectory intersects different stator MTPA loci at different field current levels.

The amount of total copper losses versus torque is compared in Figure 3-23 (b). All torque values are determined considering saturation despite of whether the solutions of currents are obtained with or without considering saturation. As can be notices, the “Non-Linear” curve is the envelop covering all the MTPA curves from the bottom. The tangency points in (b) are corresponding to the intersections in (a). The “Linear” curve coincides with the “Non-Linear” curve at lower torque level. However, when the torque level goes higher, field current grows, and the iron core becomes saturated. Consequently, the two curves deviate from each other.

The solutions of two and three degrees of control freedom are compared in Figure 3-23. In the two-degree case, only I_q and I_f are free to control while I_d is set to zero. Due to (3-57), to achieve minimum copper losses in the 48 V machine, the ratio between q-axis current and field current is 28.87. This ratio is verified by comparing (a) and (b) in Figure 3-23.

Additionally, the solutions determined by considering linear and non-linear magnetic properties are compared. Again, all torque values are determined considering saturation. At low torque level, the difference between all cases is minor. As the torque level increases, the linear and non-linear curves start to deviate, and the difference in between is more significant than the difference due to different degrees of control freedom. This is due to the minor deviation between the locus of copper loss minimization and the q-axis as shown in Figure 3-23 (a).

In the non-linear case, more stator current but less field current is requested. This is due to the decrease of mutual inductance as the growing field current saturates the iron core. After the iron core is saturated, increasing field current does not provide sufficient increment of flux as before, so it becomes more effective in torque production by adding more stator current instead. This applies for both two and three degrees of control freedom cases.

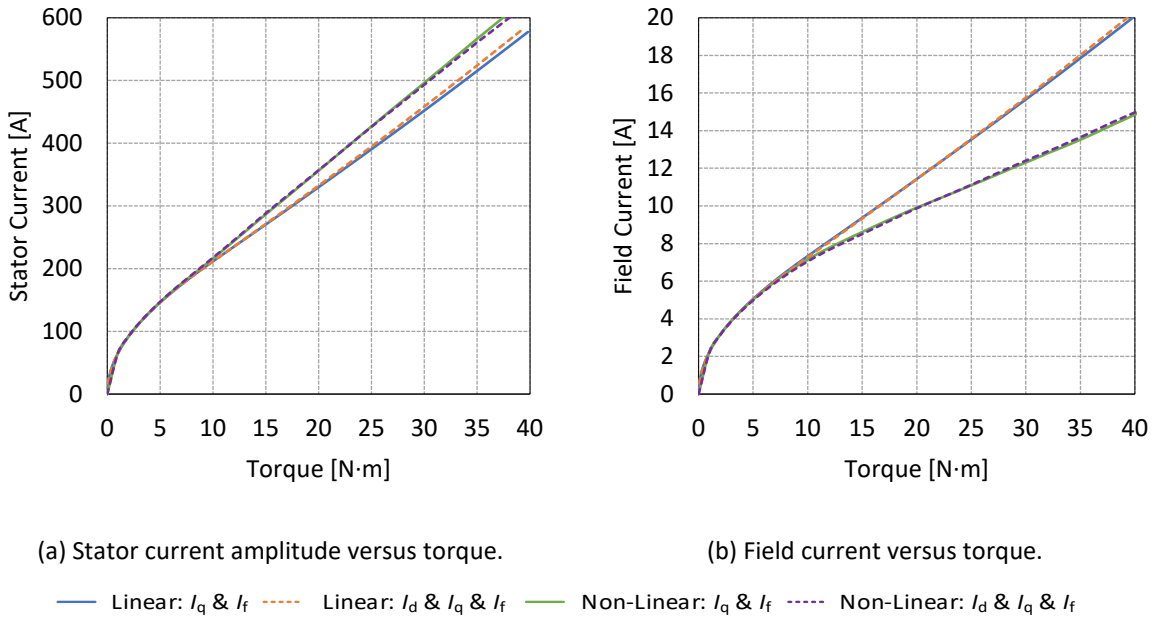

(a) Stator current amplitude versus torque.

(b) Field current versus torque.

Figure 3-24 Copper loss minimization with two degrees of control freedom, i.e. I_q & I_f, and three degrees of control freedom, i.e. I_d & I_q & I_f using the FEM data of a 48 V EESM.

3.5.4 Torque-Speed Map

The torque-speed map can be obtained with different choices of penalty factors k_d, k_q and k_f. The performance is presented from Figure 3-25 to Figure 3-29. The penalty factor for stator current increases by 10 times from case (a) to case (b), and by 10 times again from case (b) to case (c). The strategy of copper loss minimization is configured in case (b). With a variation of penalty factors, the balance of stator current and field current is adjusted. The differences in between show a significant impact from penalty factors on machine performance.

A. Torque-Boosting Area

The stator current amplitude and the field current are shown in Figure 3-25 and Figure 3-26 respectively. As can be noticed, along the envelop, the solution is unique, irrespective of the selection of penalty factors. However, inside the envelop, as the penalty factors for stator current increases, a lower stator current is consumed to achieve the same torque. For instance, in Figure 3-25 (a), the maximum stator current of 500 A is consumed for torque higher than 20 N·m whereas in (c), the maximum stator current of 500 A is only used at

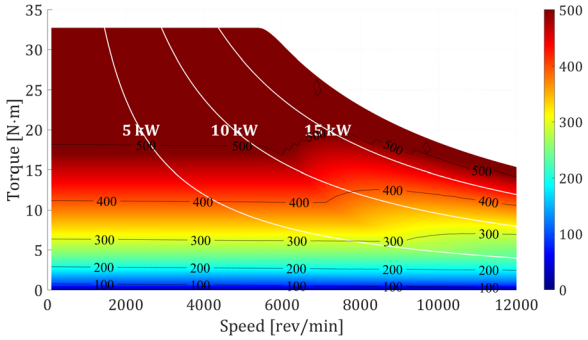

(a) $k_\mathrm{d} = k_\mathrm{q} = 0.15 \cdot R_\mathrm{s}$ and $k_\mathrm{f} = R_\mathrm{f}$.

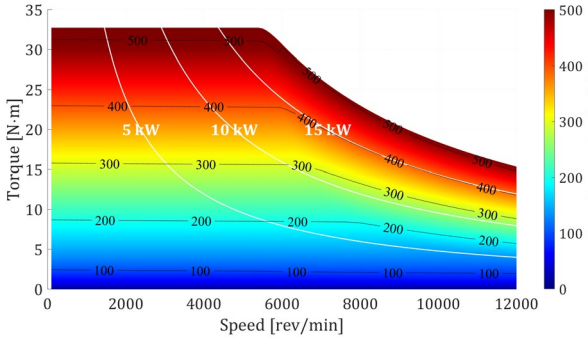

(b) $k_\mathrm{d} = k_\mathrm{q} = 1.5 \cdot R_\mathrm{s}$ and $k_\mathrm{f} = R_\mathrm{f}$.

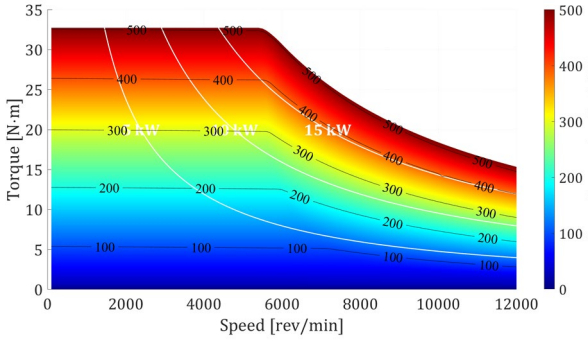

(c) $k_\mathrm{d} = k_\mathrm{q} = 15 \cdot R_\mathrm{s}$ and $k_\mathrm{f} = R_\mathrm{f}$.

Figure 3-25 Stator current amplitude maps with different penalty factors for stator currents using the FEM data of a 48 V EESM.

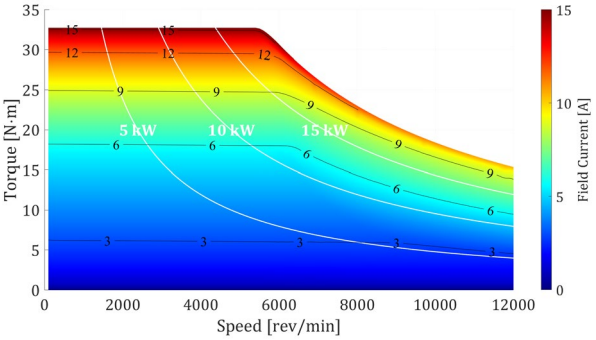

(a) $k_\mathrm{d} = k_\mathrm{q} = 0.15 \cdot R_\mathrm{s}$ and $k_\mathrm{f} = R_\mathrm{f}$.

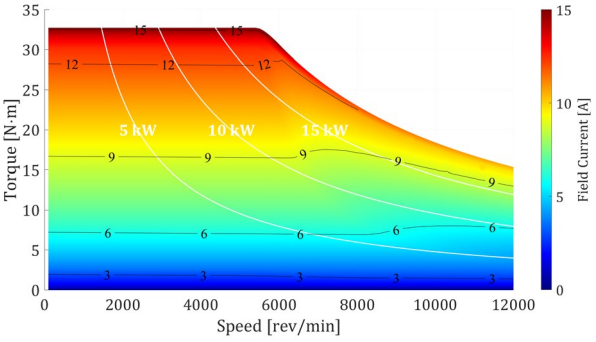

(b) $k_\mathrm{d} = k_\mathrm{q} = 1.5 \cdot R_\mathrm{s}$ and $k_\mathrm{f} = R_\mathrm{f}$.

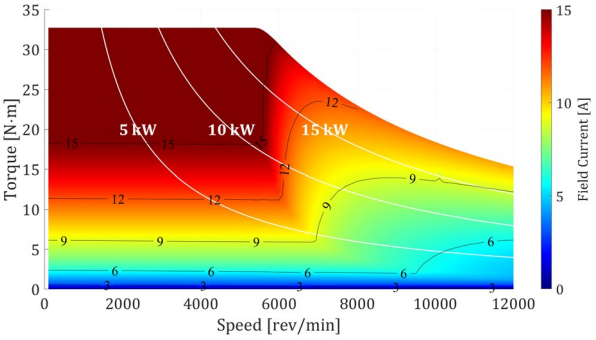

(c) $k_\mathrm{d} = k_\mathrm{q} = 15 \cdot R_\mathrm{s}$ and $k_\mathrm{f} = R_\mathrm{f}$.

Figure 3-26 Field current maps with different penalty factors for stator currents using the FEM data of a 48 V EESM.

maximum torque. Similarly for field current, in Figure 3-26 (c), the maximum field current of 15 A is consumed for torque higher than 20 N·m whereas in (a), the maximum field current of 15 A is only used at maximum torque. The torque-boosting area can be clearly seen, especially in Figure 3-25 (a) and Figure 3-26 (c), where approximately half of the torque range is covered by the maximum level of current.

The torque boosting area can also be illustrated considering different levels of stator and field current limits, as shown in Figure 3-27. The field current is limited to 15 A while the stator current is limited to 300 A, 500 A and 700 A respectively. In the 300 A and the 500 A cases, the stator current and field current increase simultaneously as torque increases. After the stator current reaches the limit, the increase of torque relies totally on the increase of field current. Consequently, field current increases dramatically thereafter. In contrast, in the 700 A case, the field current reaches the limit before stator current. The increase of torque relies totally on the increase of stator current instead. For all the three cases, before any limit is reached, the curves overlap each other which indicates that the solutions are identical.

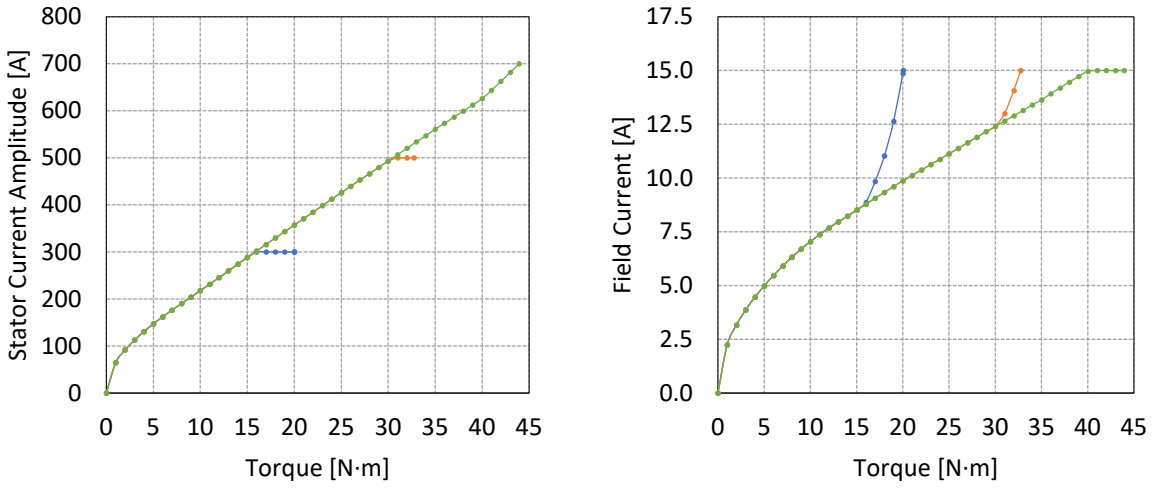

(a) Stator current amplitude versus torque.

(b) Field current versus torque.

Figure 3-27 Relationship of current and torque in with different stator current limits using the FEM data of a 48 V EESM ($k_\mathrm{d} = k_\mathrm{q} = 1.5 \cdot R_\mathrm{s}$ and $k_\mathrm{f} = R_\mathrm{f}$).

B. Field Weakening Area

The stator voltage amplitude is shown in Figure 3-28. A more significant discrepancy can be detected between (b) and (c) compared with between (a) and (b). The boundary between field weakening area and the normal area is steeper in (c). This means the field weakening area in (c) is larger. The difference is mainly attributed to the significantly higher level of field current in case (c) as shown in Figure 3-26. A higher field current results in a higher back-EMF. Hence the voltage limit is reached at a lower speed, which agrees with (3-35), (3-36) and (3-82). The steeper boundary can also be explained using (3-83), which can be formulated as

$$T_\mathrm{em} = \frac{3}{2} \cdot p \cdot U_\mathrm{s.max}^2 \cdot \frac{k_\mathrm{fw}}{\omega_\mathrm{r}^2} \quad , \quad k_\mathrm{fw} = \frac{c_\mathrm{q} \cdot \left[L_\mathrm{m} + c_\mathrm{d} \cdot \left(L_\mathrm{d} - L_\mathrm{q}\right)\right]}{\left(c_\mathrm{d} \cdot L_\mathrm{d} + L_\mathrm{m}\right)^2 + \left(c_\mathrm{q} \cdot L_\mathrm{q}\right)^2} \tag{3-84}$$

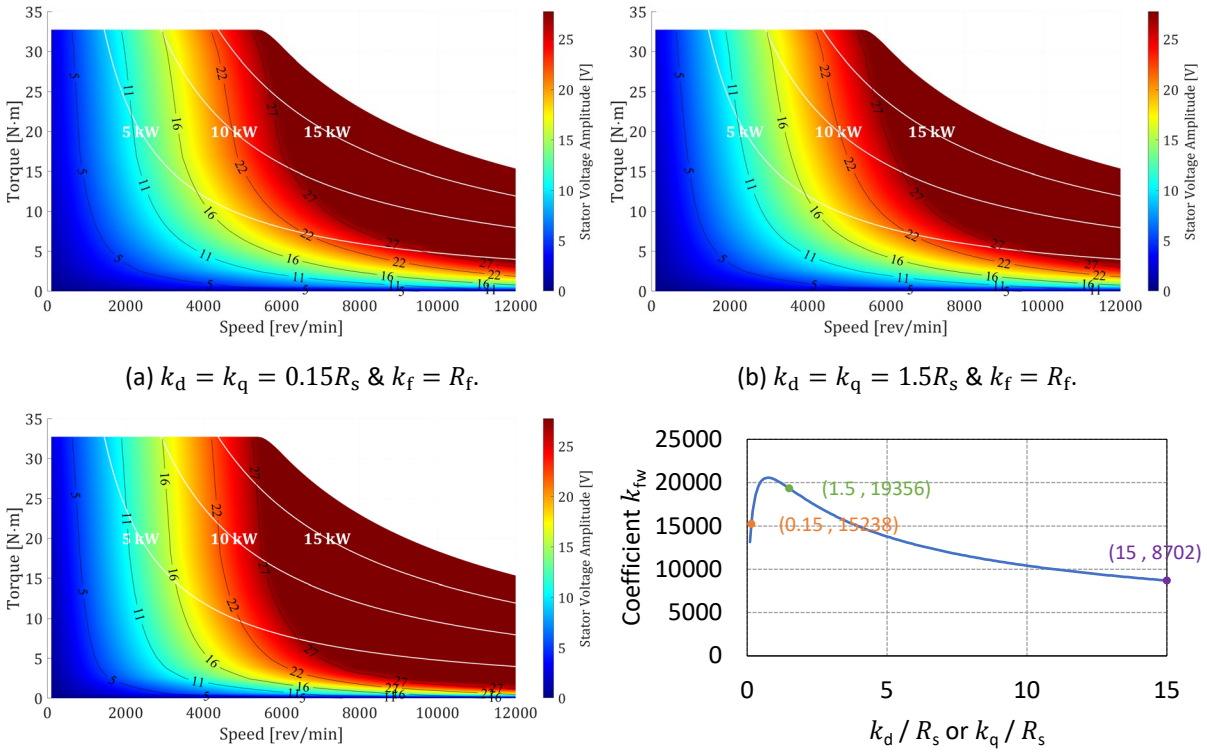

(a) $k_d = k_q = 0.15R_s$ & $k_f = R_f$.

(b) $k_d = k_q = 1.5R_s$ & $k_f = R_f$.

(c) $k_d = k_q = 15R_s$ & $k_f = R_f$.

(d) k_{fw} versus different k_d or k_q while $k_f = R_f$.

Figure 3-28 Stator voltage amplitude maps with different penalty factors for stator currents using the FEM data of a 48 V EESM.

The profile of k_{fw} is presented in Figure 3-28 (d) using the non-saturated values of inductances. As can be noticed, the coefficient k_{fw} firstly increases and then decreases with an increasing k_d or k_q. The value of k_{fw} becomes much lower in $k_d = k_q = 15R_s$ than in $k_d = k_q = 1.5R_s$. Consequently, this leads to a steeper boundary.

C. Efficiency

The efficiency is shown in Figure 3-29. The iron-core losses are scaled from the FEM calculations at the base speed of 4500 rpm. The mechanical loss and the stray loss are estimated by scaling from the peak power and the base speed [40]. As can be noticed from the figure, the highest maximum efficiency and the largest high-efficiency area are achieved in case (b), in which the total copper loss is minimized. Additionally, as can be noticed by comparing (a) and (c), the increase of stator current deteriorates efficiency more significantly than the increase of field current does.

D. Power Factor

The power factor is shown in Figure 3-30. The power factor in (a) ranges from 0.5 to 1.0, whereas the power factor in (b) and (c) is generally above 0.9. This reveals the improvement of power factor due to a higher level of field current. This agrees with (3-22) where a larger area of high power factor can be achieved with a higher level of field current. Furthermore, the power factor is higher in field weakening area. This is due to the fact that, in field weakening, the current angle increases, and the d-axis current increases in the negative direction. According to Figure 3-20, a negative d-axis current yields a lower reactive power and consequently a higher power factor.

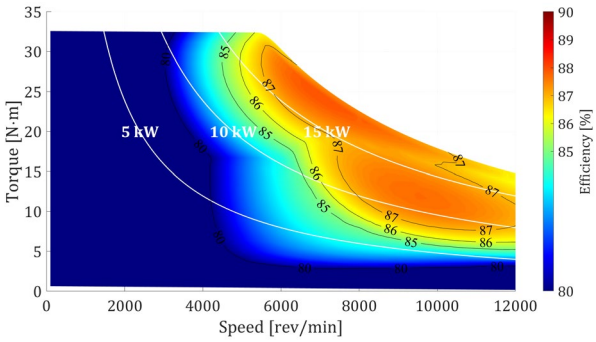

(a) $k_{\mathrm{d}} = k_{\mathrm{q}} = 0.15 \cdot R_{\mathrm{s}}$ and $k_{\mathrm{f}} = R_{\mathrm{f}}$.

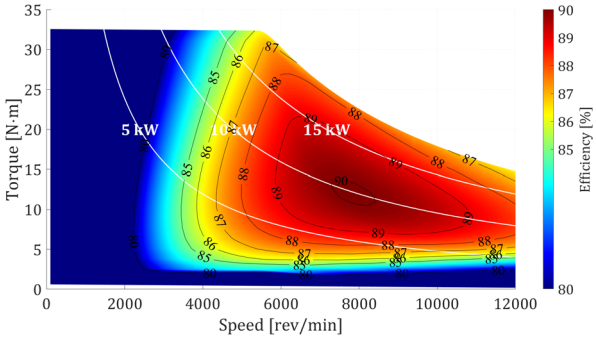

(b) $k_{\mathrm{d}} = k_{\mathrm{q}} = 1.5 \cdot R_{\mathrm{s}}$ and $k_{\mathrm{f}} = R_{\mathrm{f}}$.

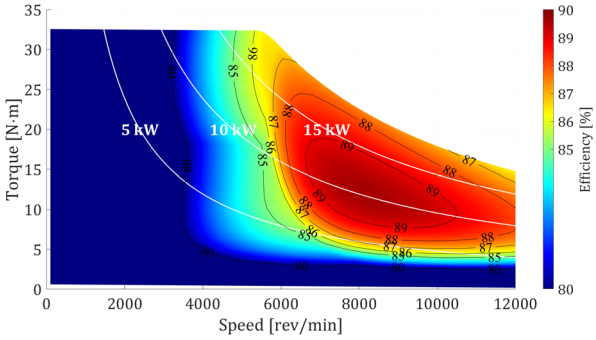

(c) $k_{\mathrm{d}} = k_{\mathrm{q}} = 15 \cdot R_{\mathrm{s}}$ and $k_{\mathrm{f}} = R_{\mathrm{f}}$.

Figure 3-30 Efficiency maps with different penalty factors for stator currents using the FEM data of a 48 V EESM.

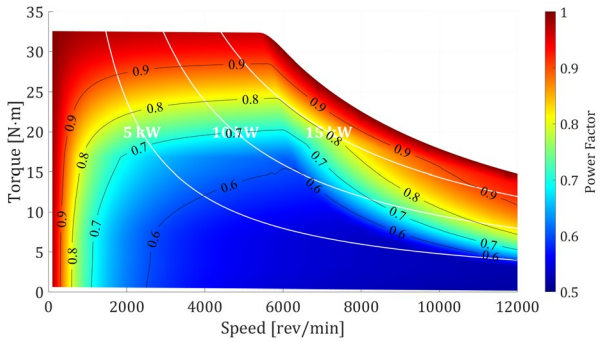

(a) $k_{\mathrm{d}} = k_{\mathrm{q}} = 0.15 \cdot R_{\mathrm{s}}$ and $k_{\mathrm{f}} = R_{\mathrm{f}}$.

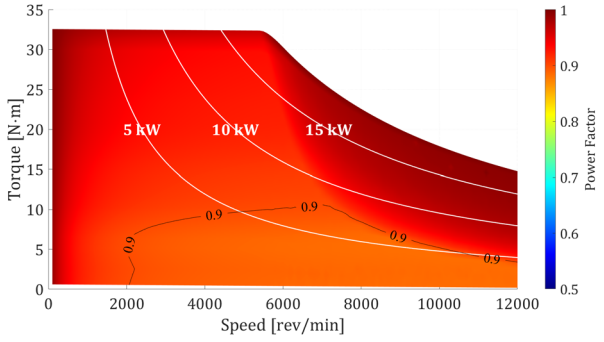

(b) $k_{\mathrm{d}} = k_{\mathrm{q}} = 1.5 \cdot R_{\mathrm{s}}$ and $k_{\mathrm{f}} = R_{\mathrm{f}}$.

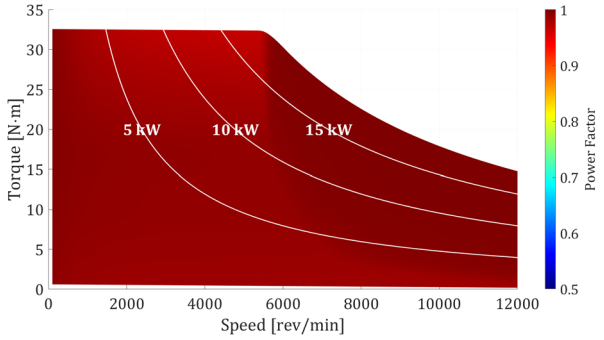

(c) $k_{\mathrm{d}} = k_{\mathrm{q}} = 15 \cdot R_{\mathrm{s}}$ and $k_{\mathrm{f}} = R_{\mathrm{f}}$.

Figure 3-29 Power factor maps with different penalty factors for stator currents using the FEM data of a 48 V EESM.

3.5.5 Torque-Speed Envelope

The envelope of the prototype is illustrated in Figure 3-31 (a) and the current vector projected to dq-plane is presented in Figure 3-31 (b). The solutions can be described in three sections, peak torque at low speed, peak apparent power at medium speed and peak active power at high speed. These are consistent to the ones shown in Figure 3-11. As has been pointed out, the solutions along the envelope are unique, regardless of how the penalty factors are selected.

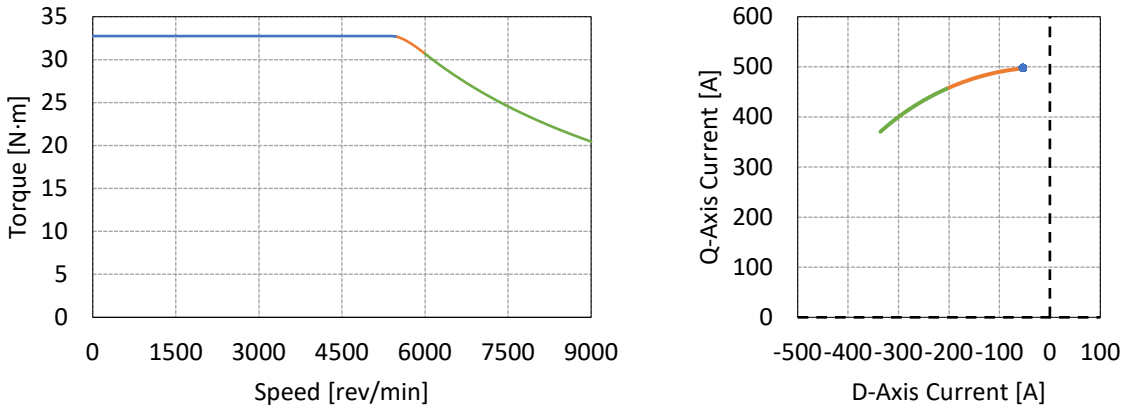

(a) Torque-Speed boundary.

(b) Stator current locus in the dq-plane.

Figure 3-31 Envelope of the torque-speed map using the FEM data of a 48 V EESM.

Chapter 4

Machine Dynamic Control

In this chapter, the study of EESM dynamic control is presented. The dynamic control is developed in the structure of field-oriented control (FOC), where the current references are determined from torque request at a given speed and the voltages are regulated so that the current follow the current references. Hence this chapter consists of two parts, dynamic current reference determination and dynamic current control.

4.1 Dynamic Current Reference Determination

Due to the third degree of control freedom introduced by field current, the dynamic current reference determination for EESM is more complicated than that for PMSM. In this section, gradients of torque versus copper losses are introduced to assist the determination.

4.1.1 Cost Function

The total copper loss can be decomposed into three parts

$$P_{\mathrm{Cu}} = P_{\mathrm{Cu.d}} + P_{\mathrm{Cu.q}} + P_{\mathrm{Cu.f}} \tag{4-1}$$

where

$$P_{\mathrm{Cu.d}} = \frac{3}{2} \cdot R_{\mathrm{s}} \cdot i_{\mathrm{d}}^2 \quad , \quad P_{\mathrm{Cu.q}} = \frac{3}{2} \cdot R_{\mathrm{s}} \cdot i_{\mathrm{q}}^2 \quad , \quad P_{\mathrm{Cu.f}} = R_{\mathrm{f}} \cdot i_{\mathrm{f}}^2 \tag{4-2}$$

To generalize solution, if P_{Cu} is not the target to be minimized, then weights can be introduced to the copper loss of each axis individually and a cost function can be defined as

$$P_{\mathrm{cost}} = P_{\mathrm{cost.d}} + P_{\mathrm{cost.q}} + P_{\mathrm{cost.f}} \tag{4-3}$$

where

$$P_{\mathrm{cost.d}} = k_{\mathrm{cost.d}} \cdot P_{\mathrm{Cu.d}} \quad , \quad P_{\mathrm{cost.q}} = k_{\mathrm{cost.q}} \cdot P_{\mathrm{Cu.q}} \quad , \quad P_{\mathrm{cost.f}} = k_{\mathrm{cost.f}} \cdot P_{\mathrm{Cu.f}} \tag{4-4}$$

4.1.2 Global Current Coordinate System

A set of equivalent currents can be defined, named as global currents

$$i_{\mathrm{cost.d}} = i_{\mathrm{d}} \sqrt{\frac{3}{2} k_{\mathrm{cost.d}} R_{\mathrm{s}}} \quad , \quad i_{\mathrm{cost.q}} = i_{\mathrm{q}} \sqrt{\frac{3}{2} k_{\mathrm{cost.q}} R_{\mathrm{s}}} \quad , \quad i_{\mathrm{cost.f}} = i_{\mathrm{f}} \sqrt{k_{\mathrm{cost.f}} R_{\mathrm{f}}} \tag{4-5}$$

With the global current defined, the costs can be formulated as

$$P_{\mathrm{cost.d}} = i_{\mathrm{cost.d}}^2 \quad , \quad P_{\mathrm{cost.q}} = i_{\mathrm{cost.q}}^2 \quad , \quad P_{\mathrm{Cu.f}} = i_{\mathrm{cost.f}}^2 \tag{4-6}$$

4.1.3 Gradients of Electromagnetic Torque

Since the torque T_{em} is a function of real currents, T_{em} should also be a function of global currents. Therefore, the torque can be presented as a scaler field in the coordinate system of global currents. From the scaler field, the gradient of torque in the global current coordinate system can be defined, which establishes a vector field. The gradient at each point in the coordinate system is a vector represented by the components along each axis

$$\nabla T_{\mathrm{em.cost}} = \left[\frac{\partial T_{\mathrm{em}}}{\partial i_{\mathrm{cost.d}}} \quad \frac{\partial T_{\mathrm{em}}}{\partial i_{\mathrm{cost.q}}} \quad \frac{\partial T_{\mathrm{em}}}{\partial i_{\mathrm{cost.f}}}\right]^{\mathrm{T}} \tag{4-7}$$

4.1.4 Decomposition of Current Vector

In the global current coordinate system, a tangential plane can be defined at the tip of any current vector $\boldsymbol{i}$. The normal direction of such tangential plane is defined by the torque gradient at $\boldsymbol{i}$. Let $\boldsymbol{n}$ be the unit vector in the normal direction. Moving the current vector in the direction of $\boldsymbol{n}$, the torque tends to increase the most. Moving the current vector in the direction perpendicular to $\boldsymbol{n}$, the copper loss is changed while the torque tends not to change. The vectors are presented in Figure 4-1.

With this tangential plane introduced, $\boldsymbol{i}$ can be decomposed orthogonally, a normal component $\boldsymbol{i}_n$ penetrating the tangential plane and a tangential component $\boldsymbol{i}_t$ along the tangential plane

$$\boldsymbol{i} = \boldsymbol{i}_n + \boldsymbol{i}_t \quad \& \quad \langle \boldsymbol{i}_n , \boldsymbol{i}_t \rangle = 0 \tag{4-8}$$

where

$$\boldsymbol{i}_n = \langle \boldsymbol{i} , \boldsymbol{n} \rangle \cdot \boldsymbol{n} \quad \& \quad \boldsymbol{i}_t = \boldsymbol{i} - \boldsymbol{i}_n \tag{4-9}$$

Let $\boldsymbol{t}$ be the unit vector in the direction of $\boldsymbol{i}_t$. Then the inner product of $\boldsymbol{n}$ and $\boldsymbol{t}$ gives zero

$$\langle \boldsymbol{n} , \boldsymbol{t} \rangle = 0 \tag{4-10}$$

The length of the tangential component $\|\boldsymbol{i}_t\|$ represents the amount of cost that can be possibly reduced. When the minimum cost is achieved, the current vector $\boldsymbol{i}$ is perpendicular to the torque contour, which means $\boldsymbol{i} = \boldsymbol{i}_n$ and $\boldsymbol{i}_t = \boldsymbol{0}$. Hence to reduce the cost means to reduce $\|\boldsymbol{i}_t\|$.

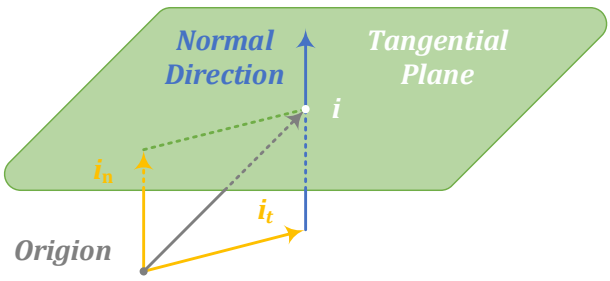

Figure 4-1 Decomposition of current vector in dynamic current reference determination.

4.1.5 Move of Current Vector

When a torque request is sent to the current reference determination algorithm, the algorithm starts to move the current vector to achieve the torque request while minimize the cost. The move of the current reference $d\boldsymbol{i}$ can also be decomposed into normal and tangential directions as well

$$d\boldsymbol{i} = d\boldsymbol{i}_n + d\boldsymbol{i}_t \quad \& \quad \langle d\boldsymbol{i}_n \, , d\boldsymbol{i}_t \rangle = 0 \tag{4-11}$$

where $d\boldsymbol{i}_n$ is the move to penetrate the torque contour in the normal direction $\boldsymbol{n}$, while $d\boldsymbol{i}_t$ is the move to slide along the torque contour in the tangential direction $\boldsymbol{t}$.

As for $d\boldsymbol{i}_n$, the length of $d\boldsymbol{i}_n$ should be proportional to the difference between the torque request $T_{\mathrm{em.req}}$ and the torque reference $T_{\mathrm{em.ref}}$ at the current stage. As for $d\boldsymbol{i}_t$, the current reference vector needs to move against the direction of $\boldsymbol{i}_t$ to reduce $\|\boldsymbol{i}_t\|$. Hence

$$d\boldsymbol{i}_n = k_n \cdot \frac{T_{\mathrm{em.req}} - T_{\mathrm{em.ref}}}{\psi_{\mathrm{m}}} \cdot \boldsymbol{n} \quad \& \quad d\boldsymbol{i}_t = -k_t \cdot \boldsymbol{i}_t \tag{4-12}$$

where k_n and k_t are relaxing factors.

4.1.6 Determination with Current Limits

When the current limit is reached, if the move of current vector tends to break the limit, then a cancellation vector $d\boldsymbol{i}_{\mathrm{cancel.i}}$ needs to be defined to keep the current vector within the limit

$$d\boldsymbol{i}_{\mathrm{lim}} = d\boldsymbol{i} - d\boldsymbol{i}_{\mathrm{cancel.i}} \tag{4-13}$$

where

$$d\boldsymbol{i}_{\mathrm{cancel.i}} = [i_{\mathrm{d.cancel}} \quad i_{\mathrm{q.cancel}} \quad i_{\mathrm{f.cancel}}]^{\mathrm{T}} \tag{4-14}$$

The stator current limit and the field current limit need to be considered separately. When the stator current limit is reached, the move of current vector will break the limit if it consists of an extending normal component, i.e.

$$\langle d\boldsymbol{i} \, , \boldsymbol{i}_{\mathrm{dq.unit}} \rangle > 0 \tag{4-15}$$

where $\boldsymbol{i}_{\mathrm{dq.unit}}$ is the unit vector of $\boldsymbol{i}_{\mathrm{dq}}$ and $\boldsymbol{i}_{\mathrm{dq}}$ is the projection of $\boldsymbol{i}$ to the dq-plane

$$\boldsymbol{i}_{\mathrm{dq.unit}} = \boldsymbol{i}_{\mathrm{dq}} / \left\| \boldsymbol{i}_{\mathrm{dq}} \right\| \quad , \quad \boldsymbol{i}_{\mathrm{dq}} = [i_{\mathrm{d}} \quad i_{\mathrm{q}}]^{\mathrm{T}} \tag{4-16}$$

If this is the case, then the normal component of the move needs to be cancelled, while the tangential component can be kept

$$d\boldsymbol{i}_{\mathrm{dq.cancel}} = d\boldsymbol{i}_{\mathrm{dq.normal}} = \langle d\boldsymbol{i} \, , \boldsymbol{i}_{\mathrm{dq.unit}} \rangle \cdot \boldsymbol{i}_{\mathrm{dq.unit}} \tag{4-17}$$

Otherwise

$$d\boldsymbol{i}_{\mathrm{dq.cancel}} = [0 \quad 0]^{\mathrm{T}} \tag{4-18}$$

When the field current limit is reached, if it still tends to increase, i.e.

$$di_{\mathrm{f}} > 0 \tag{4-19}$$

then this increase of field current needs to be cancelled

$$di_{\text{f.cancel}} = di_{\text{f.normal}} \tag{4-20}$$

Otherwise

$$di_{\text{f.cancel}} = 0 \tag{4-21}$$

The decomposition of current vector can be illustrated in Figure 4-2 (a).

4.1.7 Determination with Voltage Limits

The change in voltage $d\boldsymbol{u}$ can be calculated from $d\boldsymbol{i}$

$$\boldsymbol{u} = \boldsymbol{R}\boldsymbol{i} + \boldsymbol{\omega}\boldsymbol{\psi} = \boldsymbol{R}\boldsymbol{i} + \boldsymbol{\omega}\boldsymbol{L}\boldsymbol{i} \quad \Rightarrow \quad d\boldsymbol{u} = \boldsymbol{R}d\boldsymbol{i} + \boldsymbol{\omega}d\boldsymbol{\psi} = (\boldsymbol{R} + \boldsymbol{\omega}\boldsymbol{l})d\boldsymbol{i} \tag{4-22}$$

in which

$$d\boldsymbol{u}_{\text{dq}} = [du_{\text{d}} \quad du_{\text{q}}]^{\text{T}} \tag{4-23}$$

Then the voltages in the dq-plane can be illustrated in Figure 4-2 (b). The outer orange circle represents the voltage limit, whereas the inner blue circle represents the safe area for placing steady state voltage references. The yellow annulus in between represents the margin for dynamic current control. The voltage limit algorithm is activated when the voltage vector contacts the voltage limit reference circle, i.e. the blue circle and tries to enter the margin, i.e. the yellow annulus.

When the voltage vector is along the blue circle, it will break the limit if it consists of a normal component

$$d\boldsymbol{u}_{\text{dq.normal}} = \langle d\boldsymbol{u}_{\text{dq}}, \boldsymbol{u}_{\text{dq.unit}} \rangle \cdot \boldsymbol{u}_{\text{dq.unit}} > 0 \tag{4-24}$$

where

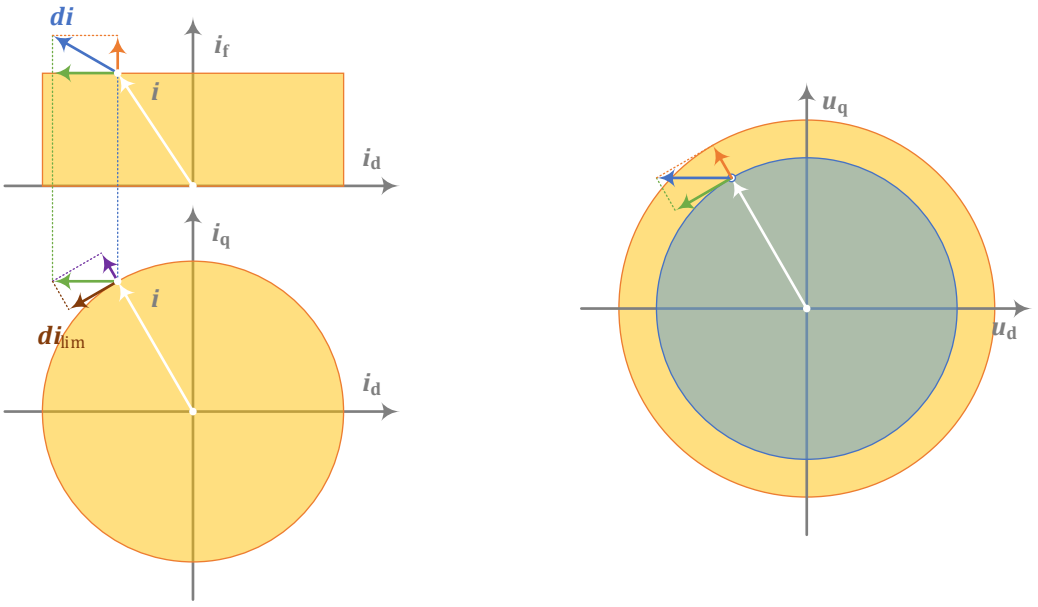

(a) Decomposition of current vector move. (b) Decomposition of voltage vector move.

Figure 4-2 Decomposition of vector move in dynamic current reference determination.

$$\boldsymbol{u}_{\mathrm{dq.unit}} = \frac{\boldsymbol{u}_{\mathrm{dq}}}{\left\|\boldsymbol{u}_{\mathrm{dq}}\right\|} \tag{4-25}$$

Then the normal component $d\boldsymbol{u}_{\mathrm{dq.normal}}$ trying to break the limit should be cancelled whereas the tangential component can be kept

$$d\boldsymbol{u}_{\mathrm{dq.cancel}} = d\boldsymbol{u}_{\mathrm{dq.normal}} \tag{4-26}$$

When the speed rises, and the voltage vector already enters the yellow annulus margin

$$\left\|\boldsymbol{u}_{\mathrm{dq}}\right\| > u_{\mathrm{s.max}} \tag{4-27}$$

then a move of voltage component is needed to bring the vector back to inside the circle

$$d\boldsymbol{u}_{\mathrm{dq.back}} = \left(\left\|\boldsymbol{u}_{\mathrm{dq}}\right\| - u_{\mathrm{s.max}}\right) \cdot \boldsymbol{u}_{\mathrm{dq.unit}} \tag{4-28}$$

Otherwise

$$d\boldsymbol{u}_{\mathrm{dq.back}} = 0 \tag{4-29}$$

Hence the

$$d\boldsymbol{u}_{\mathrm{dq.cancel}} = d\boldsymbol{u}_{\mathrm{dq.normal}} + d\boldsymbol{u}_{\mathrm{dq.back}} \tag{4-30}$$

If the voltage is inside the reference limit circle, i.e. the blue circle, then the voltage limit algorithm is not activated

$$d\boldsymbol{u}_{\mathrm{dq.cancel}} = 0 \tag{4-31}$$

The field voltage is usually designed higher than the amount that is required in steady state in order to guarantee fast response in dynamic performance. Hence, in steady state, the field voltage would never exceed the limit. The voltage limit comes into picture only in dq-frame

$$du_{\mathrm{f.cancel}} = 0 \tag{4-32}$$

Then the canceling voltage vector is converted to canceling current vector

$$d\boldsymbol{i}_{\mathrm{cancel.u}} = (\boldsymbol{R} + \boldsymbol{\omega l})^{-1} d\boldsymbol{u}_{\mathrm{cancel}} \tag{4-33}$$

where

$$d\boldsymbol{u}_{\mathrm{cancel}} = [du_{\mathrm{d.cancel}} \quad du_{\mathrm{q.cancel}} \quad du_{\mathrm{f.cancel}}]^{\mathrm{T}} \tag{4-34}$$

Hence considering both current and voltage limit, the limited move of current vector is

$$d\boldsymbol{i}_{\mathrm{lim}} = d\boldsymbol{i} - d\boldsymbol{i}_{\mathrm{cancel.u}} \tag{4-35}$$

4.1.8 Evaluation

A. Machine and Converter

An 800 V 250 kW EESM for electric trucks is designed with the assistance of finite element method (FEM) analysis. The details of the design are introduced in Chapter 5. The parameters of the machine are listed in Table 4-1.

Table 4-1 Parameters of an 800 V 250 kW EESM

Parameter	Symbol	Value	Unit
Lamination outer diameter	D_{STA}	270	mm
Lamination stack length	L_{STK}	360	mm
Peak torque	$T_{\mathrm{em.max}}$	800	N·m
Peak power	$P_{\mathrm{em.max}}$	250	kW
Maximum stator current amplitude	$I_{\mathrm{s.amp.max}}$	450	A
Maximum field current	$I_{\mathrm{f.max}}$	7.854	A
Stator resistance @ 100℃	R_{s}	19.55	mΩ
Field resistance @ 100℃	R_{f}	54.71	Ω
D-axis self-inductance @ zero current	$l_{\mathrm{dd\cdot 0}}$	1.30	mH
Q-axis self-inductance @ zero current	$l_{\mathrm{qq\cdot 0}}$	1.30	mH
Field self-inductance @ zero current	$l_{\mathrm{ff\cdot 0}}$	20.29	H
DQ mutual-inductance @ zero current	$l_{\mathrm{dq\cdot 0}}$	0.00	mH
DF mutual -inductance @ zero current	$l_{\mathrm{df\cdot 0}}$	92.80	mH
QF mutual -inductance @ zero current	$l_{\mathrm{qf\cdot 0}}$	-3.58	μH

There are two power electronic converters in this study. One is a three-phase inverter which delivers power to the stator winding. Another one is a dc-dc H-bridge converter which delivers power to the field winding. These two converters share the same dc-link voltage source. Since the aspect of control is the focus of this study, the converters here are considered as ideal voltage sources without voltage drops across the switches or the transformer of the H-bridge converter. The parameters of the converters are listed in Table 4-2. The voltage limit of the three-phase inverter is decided by considering only the linear modulation range.

Table 4-2 Parameters of power electronics for driving an 800 V 250 kW EESM

Parameters	Symbol	Value	Unit
DC-link voltage	U_{dc}	800	V
Ratio of dc-link voltage usage		0.95	
Transformer turns ratio of H-bridge converter	α_{T}	1:1	
Three-phase voltage max	$U_{\mathrm{s.amp.max}}$	462	V
Field voltage max	$U_{\mathrm{f.max}}$	800	V
Field voltage min	$U_{\mathrm{f.min}}$	0	V

B. Operational Areas with Copper Loss Minimization

The iteration algorithm with copper loss minimization is applied. The obtained torque-speed maps of stator current, field current and stator voltage are presented in Figure 4-3, Figure 4-4 and Figure 4-5 respectively. Comparing Figure 4-3 and Figure 4-4, a torque-boosting area can be identified in the region close to 800 N·m. A field-weakening area can be noticed in Figure 4-5 at speed higher than 4000 rpm.

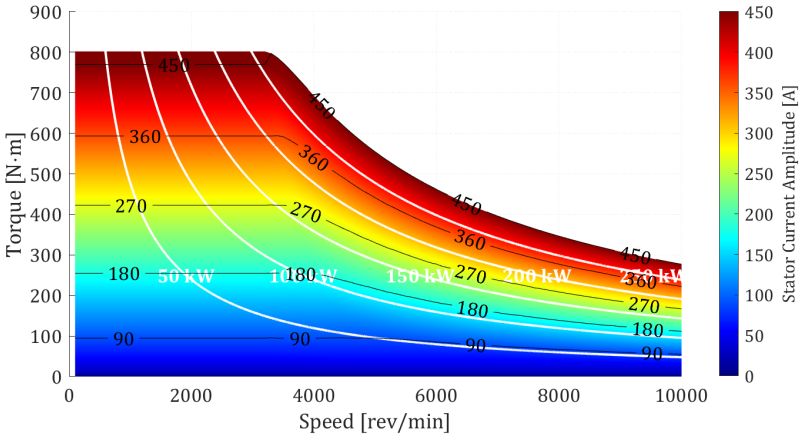

Figure 4-3 Stator current amplitude of an 800 V 250 kW EESM in copper loss minimization.

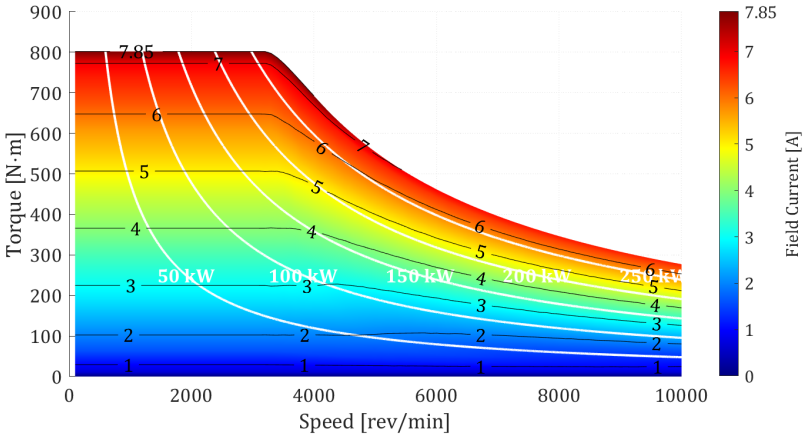

Figure 4-4 Field current of an 800 V 250 kW EESM in copper loss minimization.

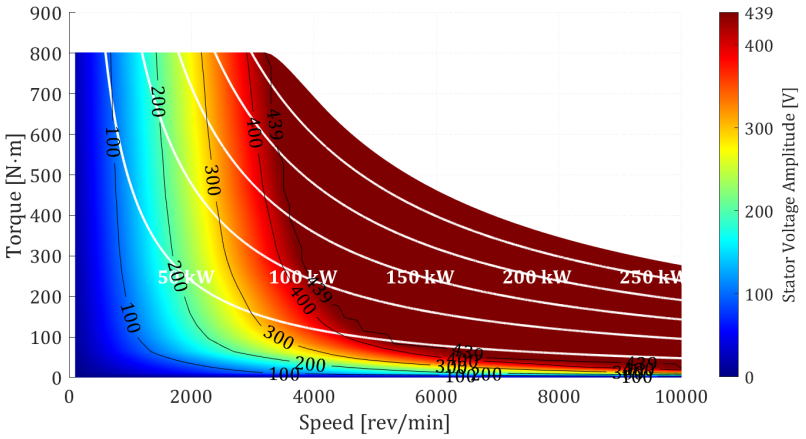

Figure 4-5 Voltage amplitude of an 800 V 250 kW EESM in copper loss minimization.

C. Step Responses of the Dynamic Current Reference Determination Algorithm

To evaluate the dynamic current reference determination algorithm, three points, one in normal operation area, one in torque-boosting area and one in field-weakening area, are selected as listed in Table 4-3. The solutions at 3 ms after the step of torque request are compared with those obtained from iteration.

Table 4-3 Verification of dynamic current reference determination algorithm

		Normal Operation	Torque-Boosting	Field-Weakening	Unit
Speed		3000	3000	6000	rev/min
T_{em}	**Target**	400	800	400	N·m
	Iteration	400.00	800.00	400.01	
	Dynamic	400.00	799.80	399.41	
I_d	**Iteration**	-42.72	-130.7	-326.59	A
	Dynamic	-43.51	-84.08	-356.78	
I_q	**Iteration**	254.25	430.6	215.03	A
	Dynamic	252	444.19	191.99	
I_f	**Iteration**	4.22	7.79	5.81	A
	Dynamic	4.3	7.86	6.95	
$P_{Cu.s}$	**Iteration**	1.95	5.94	4.48	kW
	Dynamic	1.92	6.01	4.83	
$P_{Cu.f}$	**Iteration**	0.97	3.32	1.85	kW
	Dynamic	1.01	3.38	2.64	
P_{Cu}	**Iteration**	2.92	9.26	6.33	kW
	Dynamic	2.93	9.39	7.47	

As can be noticed from Table 4-3, the solutions of currents in normal operation area agree with the iterative solutions. However, the solutions in torque-boosting area differ, but the value of total copper losses is similar to the one from iteration. This indicates that the solutions from dynamic algorithm are close to the optimum ones and the cost does not vary sharply when the solution is close to the optimum point. In field-weakening area, the current solutions of differ significantly. Consequently, the stator copper loss is 350 W higher and the field copper loss is 800 W higher than the iterative solutions. This means the algorithm in field weakening needs improvement.

The step responses in normal operation are presented in Figure 4-6. The speed is fixed at 3000 rpm, and a step of torque request of 400 N·m is given at 1 ms as shown in (a). The responses of current references can be seen in (b) and (c). The waveform of torque calculated from current references is marked as $T_{\mathrm{em.ref}}$ which is compared with the torque request $T_{\mathrm{em.req}}$ in (a). The sampling frequency is at 20 kHz which indicates a sampling period of 50 µs. As can be noticed, $T_{\mathrm{em.ref}}$ reaches 90% of the request $T_{\mathrm{em.req}}$ within 3 steps, i.e. 150 µs. The same response time can be seen in current reference waveforms. After $T_{\mathrm{em.ref}}$ reaches the request, the adjustment of current references continues until 1.8 ms to minimize the total copper loss.

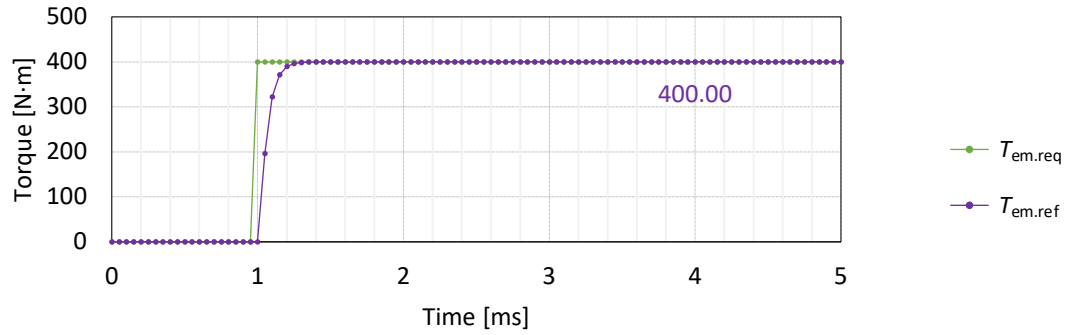

(a) Torque request and reference corresponding to current references.

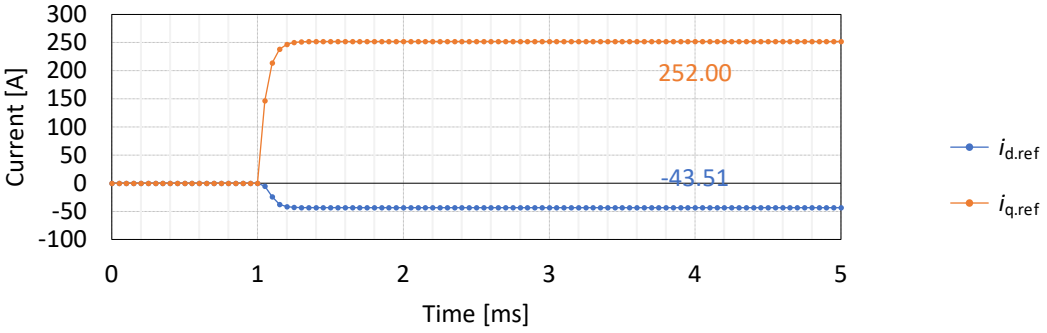

(b) Dynamic determination of d- and q-axis current references.

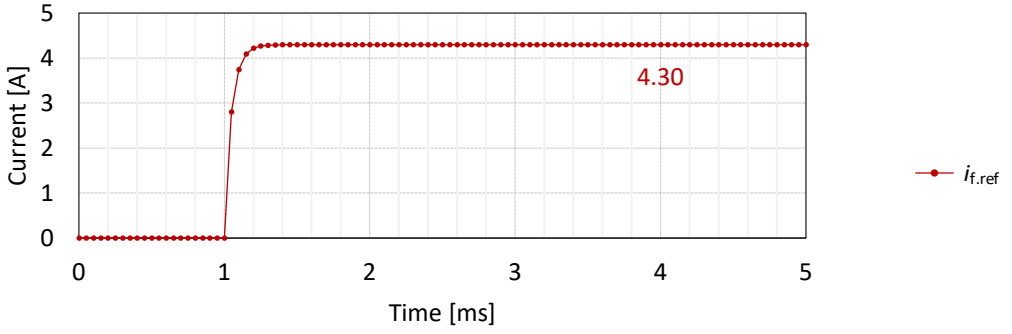

(c) Dynamic determination of field current reference.

Figure 4-6 Step responses of torque and current references in normal operation area using the dynamic current reference determination algorithm and the dynamic model of an 800 V 250 kW EESM.

The step responses in torque-boosting area are shown in Figure 4-7. The speed is fixed at 3000 rpm. A step of torque request of 800 N·m is given at 1 ms as shown in (a). As has been pointed out in Figure 4-3, the stator current amplitude reaches the maximum before field current while the torque approaches 800 N·m. Hence this is in the situation of torque-boosting following the definition in Section 3.4.2. As can be seen in (a), the response $T_{\mathrm{em.ref}}$ swiftly approaches the request $T_{\mathrm{em.req}}$ before 1.2 ms, but it takes more time to really catch 800 N·m around 2 ms. This can be explained with (b) and (c). Before 1.2 ms, the stator current amplitude and field current increase proportionally to realize copper loss minimization. At 1.2 ms, the stator current amplitude hits the limit, and the further increase of torque totally relies on the increase of field current. The angle of stator current also adjusts due to the saturation of the iron-core while field current is increasing. Finally, at 2 ms, $T_{\mathrm{em.ref}}$ reaches $T_{\mathrm{em.req}}$.

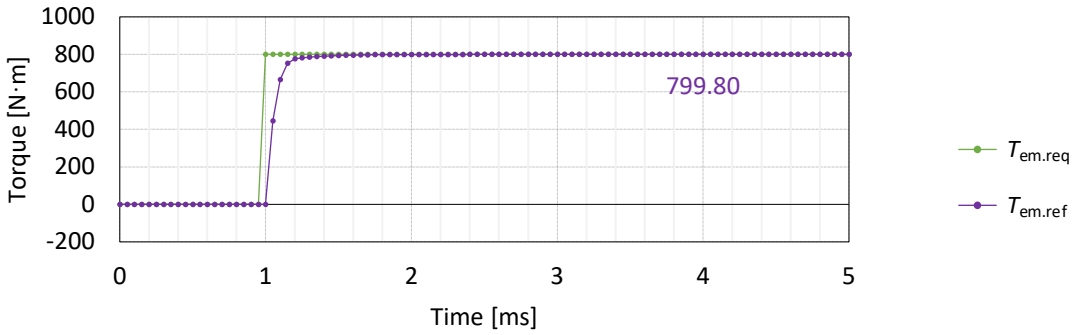

(a) Torque request and reference corresponding to current references.

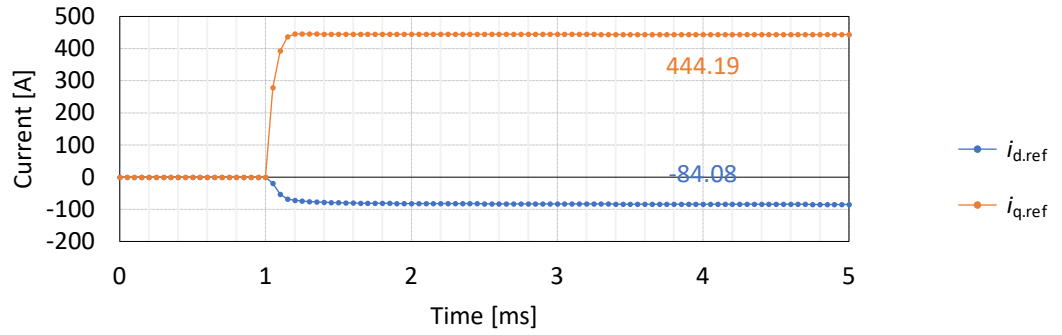

(b) Dynamic determination of d- and q-axis current references.

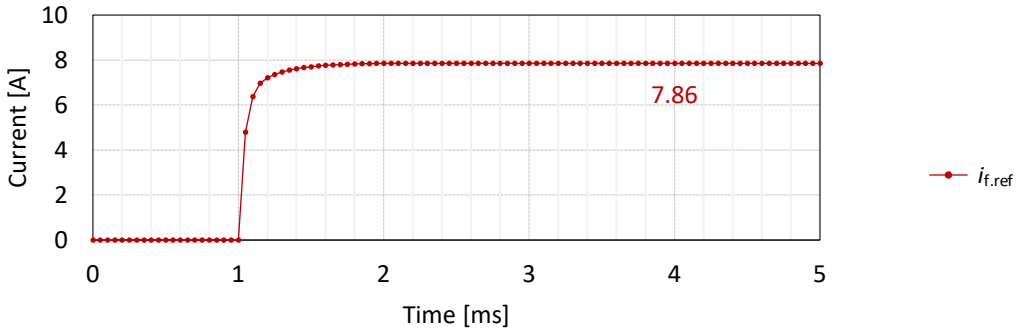

(c) Dynamic determination of field current reference.

Figure 4-7 Step responses of torque and current references in torque-boosting area using the dynamic current reference determination algorithm and the dynamic model of an 800 V 250 kW EESM.

The step responses in field-weakening area are shown in Figure 4-8. The speed is fixed at 6000 rpm. A step of torque request of 400 N·m is given at 1 ms as shown in (a). As has been pointed out in Figure 4-5, this is in the situation of field-weakening following the definition in Section 3.4.3. As can be noticed, the responses of all reference quantities here are slower than those in the normal operation area. This is due to the reason that the current vector cannot follow the direction of torque gradients while the voltage limit is reached. The cancelation vector in (4-30) slows down the grow of torque, which results in a longer response time in all reference quantities. The current vectors keep on being adjusted even after $T_{\mathrm{em.ref}}$ reaches $T_{\mathrm{em.req}}$. Hence the values in the field-weakening case presented in Table 4-3 and Figure 4-8 are not the steady state values.

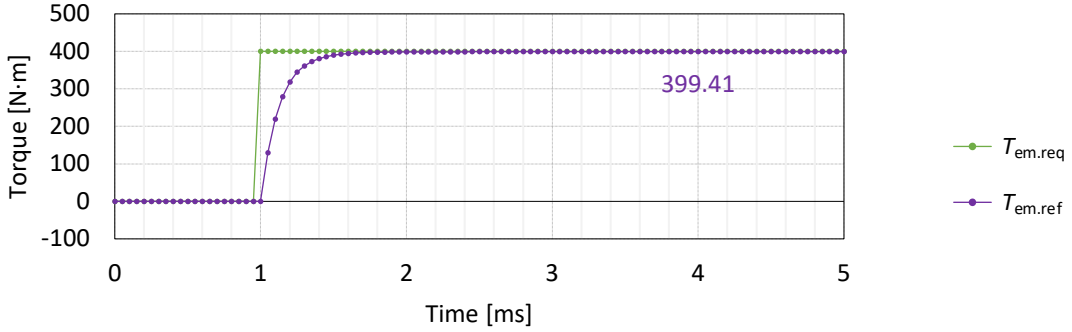

(a) Torque request and reference corresponding to current references.

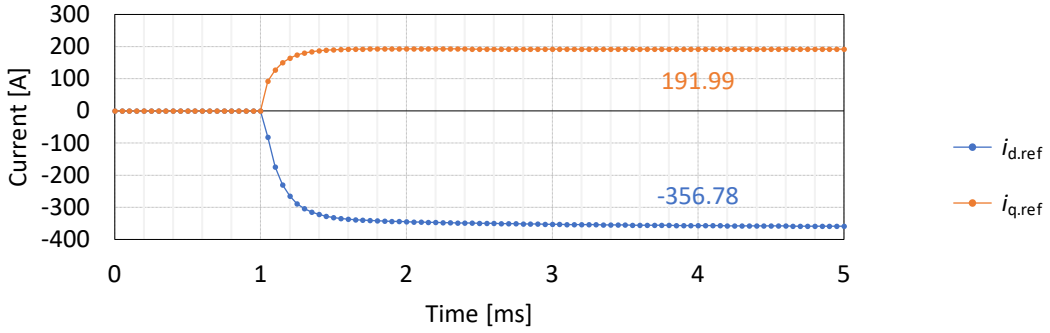

(b) Dynamic determination of d- and q-axis current references.

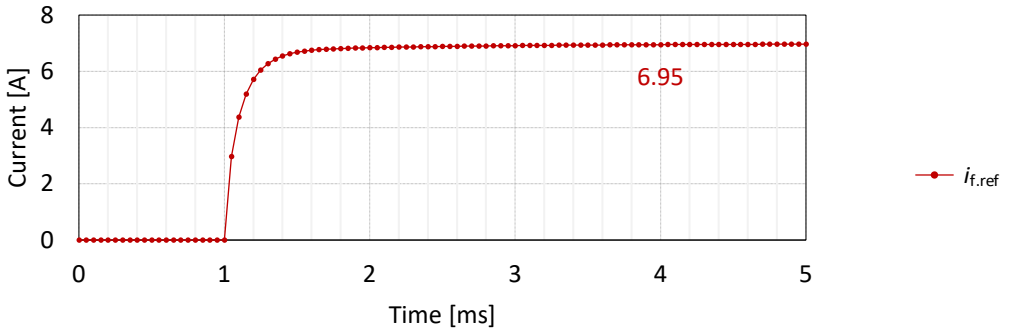

(c) Dynamic determination of field current reference.

Figure 4-8 Step responses of torque and current references in field-weakening area using the dynamic current reference determination algorithm and the dynamic model of an 800 V 250 kW EESM.

4.2 Dynamic Current Control

The aim of the dynamic current control is to form the step responses of current rises into the shape of first order. To achieve this, the controller is designed by taking care of three parts of the terminal voltage of the machine separately

$$\boldsymbol{u} = \boldsymbol{u}_{\mathrm{self}} + \boldsymbol{u}_{\mathrm{mutual}} + \boldsymbol{u}_{\mathrm{cross}} \tag{4-36}$$

where $\boldsymbol{u}_{\mathrm{self}}$ is the voltage across the resistances and self-inductances, i.e. in this part, the d-axis, q-axis and field circuits are independent, so it is actually a stacking of three single-input single-output (SISO) systems

$$\boldsymbol{u}_{\mathbf{self}} = \boldsymbol{R}\boldsymbol{i} + \boldsymbol{l}_{\mathrm{self}}\frac{d\boldsymbol{i}}{dt} \tag{4-37}$$

$\boldsymbol{u}_{\mathrm{mutual}}$ is the voltage across the mutual-inductances, i.e. in this part, the d-axis voltage is decided by the q-axis and field current derivatives, the q-axis voltage is decided by the d-axis and field current derivatives and the field voltage is decided by the d-axis and q-axis current derivatives

$$\boldsymbol{u}_{\mathrm{mutual}} = \boldsymbol{l}_{\mathrm{mutual}}\frac{d\boldsymbol{i}}{dt} \tag{4-38}$$

$\boldsymbol{u}_{\mathrm{cross}}$ is the cross-coupling part

$$\boldsymbol{u}_{\mathrm{cross}} = \boldsymbol{\omega}\boldsymbol{\psi} \tag{4-39}$$

In terms of controller design, these three parts can be taken care of separately

$$\boldsymbol{u}_{\mathrm{ctrl}} = \boldsymbol{u}_{\mathrm{ctrl.self}} + \boldsymbol{u}_{\mathrm{ctrl.mutual}} + \boldsymbol{u}_{\mathrm{ctrl.cross}} \tag{4-40}$$

where $\boldsymbol{u}_{\mathrm{ctrl}}$ is the total controller output, $\boldsymbol{u}_{\mathrm{ctrl.self}}$, $\boldsymbol{u}_{\mathrm{ctrl.mutual}}$ and $\boldsymbol{u}_{\mathrm{ctrl.cross}}$ are the controller outputs for the self-, mutual and cross-coupling parts respectively.

4.2.1 Feedforward for Cross-Coupling Part

The cross-coupling part is an addition part

$$\boldsymbol{u}_{\mathrm{ctrl.cross}} = \boldsymbol{u}_{\mathrm{cross}} = \boldsymbol{\omega}\boldsymbol{\psi} \tag{4-41}$$

With this cross-coupling term fed forwarded, the remaining parts are RL circuits including resistances, self-inductances and mutual inductances.

4.2.2 Loop Shaping PI Regulator for Self-Part

The self-part is a stack of three RL circuits. For each RL circuit, a PI regulator can be designed to shape the current response into first order with a bandwidth of α_{c}. The risetime is defined as the time interval for the current to rise from 10% to 90% of the steady state level. The relation between the bandwidth α_{c} in rad/s and risetime t_{r} in s follows

$$t_{\mathrm{r}} = \ln 9 \,/\alpha_{\mathrm{c}} \tag{4-42}$$

To have a first-order response, the PI coefficients are set as

$$k_{\mathrm{P}} = \alpha_{\mathrm{c}} \cdot L \quad , \quad k_{\mathrm{I}} = \alpha_{\mathrm{c}} \cdot R \tag{4-43}$$

Hence the voltage applied across the self-part is

$$\boldsymbol{u}_{\text{ctrl.self}} = \boldsymbol{K}_{\text{P}}\boldsymbol{i}_{\text{err}} + \boldsymbol{K}_{\text{I}}\int \boldsymbol{i}_{\text{err}}dt \tag{4-44}$$

in terms of all the three RL circuits together, where

$$\boldsymbol{i}_{\text{err}} = \boldsymbol{i}_{\text{ref}} - \boldsymbol{i}_{\text{msr}} \tag{4-45}$$

$\boldsymbol{i}_{\text{ref}}$ are current references, $\boldsymbol{i}_{\text{msr}}$ are current measurements, $\boldsymbol{K}_{\text{P}}$ and $\boldsymbol{K}_{\text{I}}$ are matrices of PI coefficients

$$\boldsymbol{K}_{\text{P}} = \boldsymbol{A}_{\text{c}}\boldsymbol{L} \quad , \quad \boldsymbol{K}_{\text{I}} = \boldsymbol{A}_{\text{c}}\boldsymbol{R} \tag{4-46}$$

$\boldsymbol{A}_{\text{c}}$ is the matrix of control bandwidth

$$\boldsymbol{A}_{\text{c}} = \begin{bmatrix} \alpha_{\text{c.d}} & 0 & 0 \\ 0 & \alpha_{\text{c.q}} & 0 \\ 0 & 0 & \alpha_{\text{c.f}} \end{bmatrix} \tag{4-47}$$

and $\alpha_{\text{c.d}}$, $\alpha_{\text{c.q}}$ and $\alpha_{\text{c.f}}$ are the bandwidths of d-axis, q-axis and field current control respectively.

4.2.3 Compensation for Mutual-Part

The vector of current derivatives to form the desired first-order responses with bandwidths in (4-47) can be determined as

$$\frac{d\boldsymbol{i}}{dt} = \boldsymbol{l}_{\text{self}}^{-1}(\boldsymbol{u}_{\text{ctrl.self}} - \boldsymbol{R}\boldsymbol{i}_{\text{msr}}) \tag{4-48}$$

The self-inductance matrix is diagonal as shown in (2-7). Therefore, it is inversible, which means the solution of $\boldsymbol{L}_{\text{self}}^{-1}$ always exists. The current derivatives here are the ones decided by the controller to form first-order responses instead of the derivatives of current samplings which are noisy.

Then to achieve the target current derivatives in (4-48), the vector of voltages that needs to be applied across the mutual inductances can be determined as

$$\boldsymbol{u}_{\text{ctrl.mutual}} = \boldsymbol{l}_{\text{mutual}}\frac{d\boldsymbol{i}}{dt} \tag{4-49}$$

Combining (4-48) and (4-49), the vector of voltages applied across the mutual inductances is

$$\boldsymbol{u}_{\text{ctrl.mutual}} = \boldsymbol{l}_{\text{mutual}}\boldsymbol{l}_{\text{self}}^{-1}(\boldsymbol{u}_{\text{ctrl.self}} - \boldsymbol{R}\boldsymbol{i}_{\text{msr}}) \tag{4-50}$$

This shows the mutual induced voltages to be compensated for to form the target first-order current rises.

4.2.4 Another Perspective of the Control

The controller output voltage introduced in (4-40) can be described in another format

$$\boldsymbol{u}_{\text{ctrl}} = \boldsymbol{u}_{\text{ctrl.R}} + \boldsymbol{u}_{\text{ctrl.L}} + \boldsymbol{u}_{\text{ctrl.cross}} \tag{4-51}$$

where $\boldsymbol{u}_{\mathrm{ctrl.R}}$ is the voltage vector applied across the resistances, $\boldsymbol{u}_{\mathrm{ctrl.L}}$ is the voltage vector applied across the inductances and $\boldsymbol{u}_{\mathrm{ctrl.cross}}$ is the feed forward of cross-coupling terms which is the same as described in (4-41). The voltage vector $\boldsymbol{u}_{\mathrm{ctrl.R}}$ follows the Ohm's Law

$$\boldsymbol{u}_{\mathrm{ctrl.R}} = \boldsymbol{R}\boldsymbol{i}_{\mathrm{msr}} \tag{4-52}$$

The voltage vector $\boldsymbol{u}_{\mathrm{ctrl.L}}$ is determined by the current derivatives to form first-order responses

$$\boldsymbol{u}_{\mathrm{ctrl.L}} = \boldsymbol{L}\frac{d\boldsymbol{i}}{dt} = \boldsymbol{l}\boldsymbol{l}_{\mathrm{self}}^{-1}(\boldsymbol{u}_{\mathrm{ctrl.self}} - \boldsymbol{R}\boldsymbol{i}_{\mathrm{msr}}) \tag{4-53}$$

The $\boldsymbol{u}_{\mathrm{ctrl.self}}$ here is determined in the same way as in (4-44). From this perspective, the PI regulator described in (4-46) is a tool to determine the current derivatives targeting the shape of first-order responses. Then the current derivatives are further used to determine the voltage vector that needs to be applied across the total inductances.

4.2.5 Anti-Windup

The voltages applied across the windings are limited to the converter output capabilities. In case the voltage reference exceeds the limit, the voltage output is saturated. In this situation, the controller needs to be aware of this to avoid the integrator from winding up. This is the anti-windup technique.

In this study, since the PI regulator is only used to take care of the self-part of the winding, the anti-windup technique only needs to be applied accordingly there to avoid the windup of the integrator. The input to the integrator is then modified from $\boldsymbol{i}_{\mathrm{err}}$ in (4-45) to

$$\boldsymbol{i}_{\mathrm{err}} + \boldsymbol{K}_{\mathrm{P}}^{-1}(\boldsymbol{u}_{\mathrm{ctrl.self.lim}} - \boldsymbol{u}_{\mathrm{ctrl.self}}) \tag{4-54}$$

Due to the limited voltage output capability during saturation, the feed forward of the d- and q-axis cross-coupling terms cannot function well even with the anti-windup technique implemented, so as the compensation for the induced voltages due to mutual coupling.

4.2.6 Evaluation

The same design of 800 V 250 kW EESM for electric trucks is used in this study.

A. Dynamic Current Control within Voltage Limit

The study is started with the simplest case in which the controller output voltages are within the converter output voltage limits. The bandwidths of the current control and the corresponding risetimes are listed in Table 4-4. The current reference steps are defined in Table 4-5. The current steps are small compared with the current limits. This is to avoid the voltages from exceeding the limits. In this study, for the sake of convenience, the control taking care of only the self-inductances is noted as "PI" which means the original case, whereas the proposed control algorithm taking care of both the self- and mutual inductances is noted as "PI&CMP".

Table 4-4 Parameters of current controller

Parameter	Bandwidth		Rise Time	
	Value	Unit	Value	Unit
D-axis current control	10	Hz	35	ms
Q-axis current control	10	Hz	35	ms
Field current control	5	Hz	70	ms

Table 4-5 Steps of current references

References	From		To		At	
	Value	Unit	Value	Unit	Value	Unit
D-axis current step	0	A	50	A	0.7	s
Q-axis current step	0	A	50	A	0.4	s
Field current step	0	A	1	A	0.1	s

As a brief comparison of the results, the risetimes of the currents are measured and the bandwidths are calculated, as presented in Table 4-6. The risetimes in Case "PI" deviate from the target values as presented in Table 4-5, whereas the risetimes in Case "PI&CMP" closely follow the targets. This indicates that with mutual induced voltages compensated, first-order responses can be achieved. In addition, the rise times of the d-axis and field currents deviate more than that of the q-axis current. This is due to the higher mutual inductance between the d-axis and field than that between the q-axis and field.

Table 4-6 Current responses

Case	Quantity	Bandwidth		Rise Time	
		Value	Unit	Value	Unit
PI	D-axis current	7.15	Hz	48.88	ms
	Q-axis current	9.96	Hz	35.12	ms
	Field current	4.18	Hz	83.60	ms
PI & CMP	D-axis current	10.20	Hz	34.27	ms
	Q-axis current	10.20	Hz	34.27	ms
	Field current	5.10	Hz	68.55	ms

The step responses of the currents with and without compensations for mutual induced voltages are compared in Figure 4-9 and Figure 4-10. As already compared in Table 4-6, the current responses in Case "PI&CMP", i.e. the waveforms of $i_{\mathrm{d.msr.1}}$, $i_{\mathrm{q.msr.1}}$ and $i_{\mathrm{f.msr.1}}$ can be considered as first order. Discrepancies between the two cases are then pointed out and explained.

A disturbance in $i_{\mathrm{d.msr.0}}$ starting from 0.1 s can be noticed in Figure 4-9 when the field current rises as shown in Figure 4-10. The disturbance here is due to the EMF across L_{df} induced by the field current rise. This amount of induced voltage should be compensated for by the controller to keep the d-axis current at zero, but it is not in Case "PI". Therefore, the d- and q-axis voltages deviate from how they should behave as shown in Figure 4-11. The disturbance in d-axis current then affects the field current in return through an induced voltage across L_{fd}. The influence can be firstly seen in the deviation of field voltage shown in Figure 4-12. Then it ends up with a discrepancy between $i_{\mathrm{f.msr.0}}$ and $i_{\mathrm{f.msr.1}}$ around 0.2 s shown in Figure 4-10.

At 0.7 s, the d-axis current rises, and a dip in $i_{\mathrm{f.msr.0}}$ can be noticed in Figure 4-10. The explanation for this is similar to the one for the disturbance at 0.1 s in d-axis current. An EMF across L_{fd} is induced by the rise of d-axis current. The controller in Case "PI" does not take this mutual induced voltage into account. Therefore, a dip appears in the field current. The field current controller detects the error and then gradually increases the voltage output as shown in Figure 4-12 to turn the field current back as shown in Figure 4-10. The disturbance in field current then induces an EMF in d-axis and affects the d-axis current in return as shown in Figure 4-9.

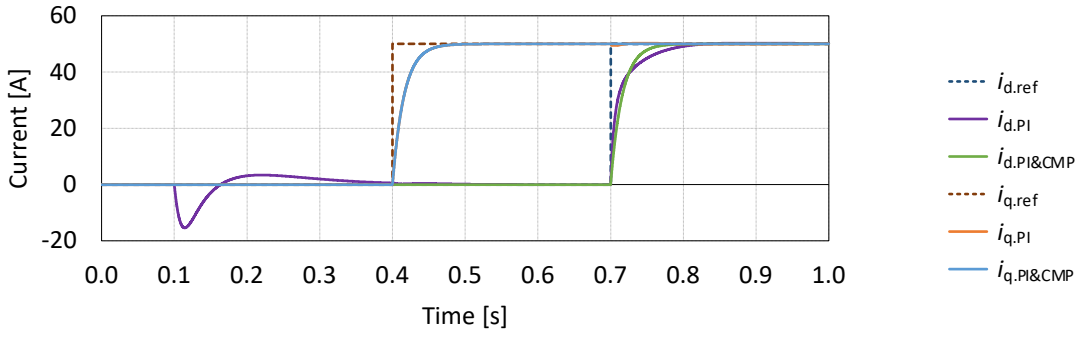

Figure 4-9 Step responses of d- and q-axis current.

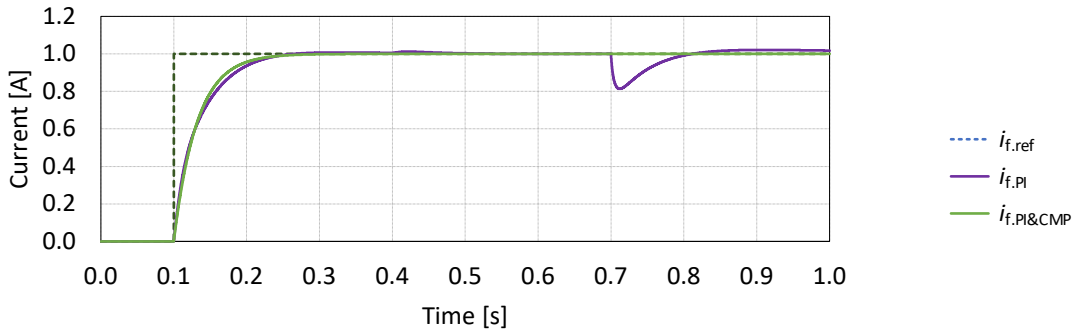

Figure 4-10 Step response of field current.

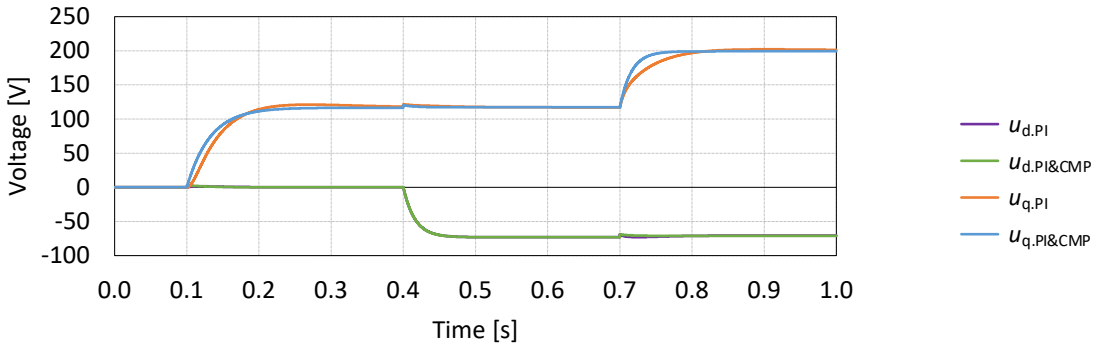

Figure 4-11 Waveforms of d- and q-axis voltages.

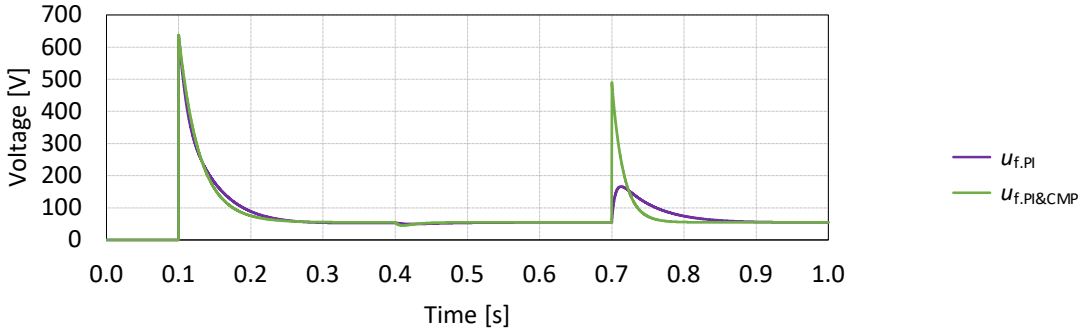

Figure 4-12 Waveforms of field voltage.

The waveform of the electromagnetic torque is presented in Figure 4-13. As can be noticed, the dip in field current shown in Figure 4-10 causes a dip in torque as shown in Figure 4-13. With mutual induced voltages compensated, the torque response becomes smooth.

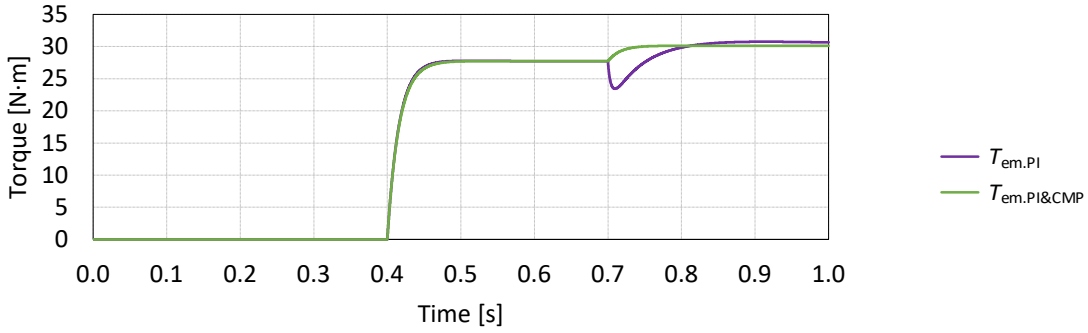

Figure 4-13 Waveforms of electromagnetic torque.

B. Dynamic Current Control with Voltage Limit Reached

In this section, the control bandwidths are given as 10 times of the previous ones as listed in Table 4-7. The current references are given as the ones with which the machine delivers peak torque. The steps of current references are defined in Table 4-8. With these setups, the voltage limits would be hit when the currents step up. Two cases are studied in this section. One case is with no anti-windup implemented, named as "PI&CMP", whereas the other case is with anti-windup implemented, named as "PI&CMP&AWP".

Table 4-7 Parameters of current controller

Parameter	Bandwidth		Rise Time	
	Value	Unit	Value	Unit
D-axis current control	100	Hz	3.5	ms
Q-axis current control	100	Hz	3.5	ms
Field current control	50	Hz	7.0	ms

Table 4-8 Steps of current references

References	From		To		At	
	Value	Unit	Value	Unit	Value	Unit
D-axis current step	0	A	-131.8	A	0.05	s
Q-axis current step	0	A	430.3	A	0.20	s
Field current step	0	A	7.854	A	0.35	s

The stator and field current responses are presented in Figure 4-14 and Figure 4-15. The stator and field voltages can be seen in Figure 4-16 and Figure 4-17. In Figure 4-14, the d-axis current in Case "PI&CMP" is disturbed at 0.05 s. This happens when the field voltage hits the limit as can be seen in Figure 4-17. In this situation, $\boldsymbol{u}_{\mathrm{ctrl.self}}$ calculated in the controller exceeds the voltage limit. By using this exceeded voltage level of $\boldsymbol{u}_{\mathrm{ctrl.self}}$, the current derivatives $\frac{d\boldsymbol{i}}{dt}$ are over-estimated, because the actual voltages applied across the self-inductances is limited but the controller is not aware of this. Consequently, unnecessarily higher voltages are applied across the stator windings as can be seen in Figure 4-16. This causes the disturbance in d-axis current at 0.05 s.

After the d-axis current comes back to zero, it then goes to negative instead of staying at zero. This is due to the mechanism of PI control. A PI controller integrates the error to eliminate

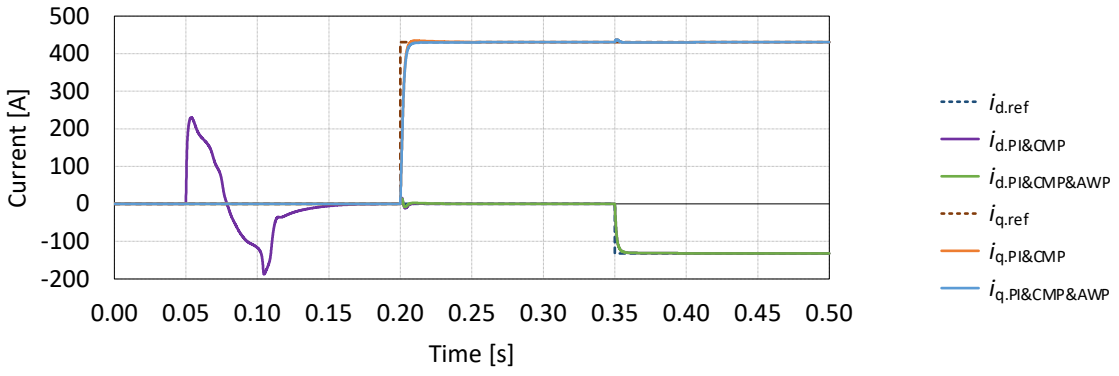

Figure 4-14 Step responses of d- and q-axis currents.

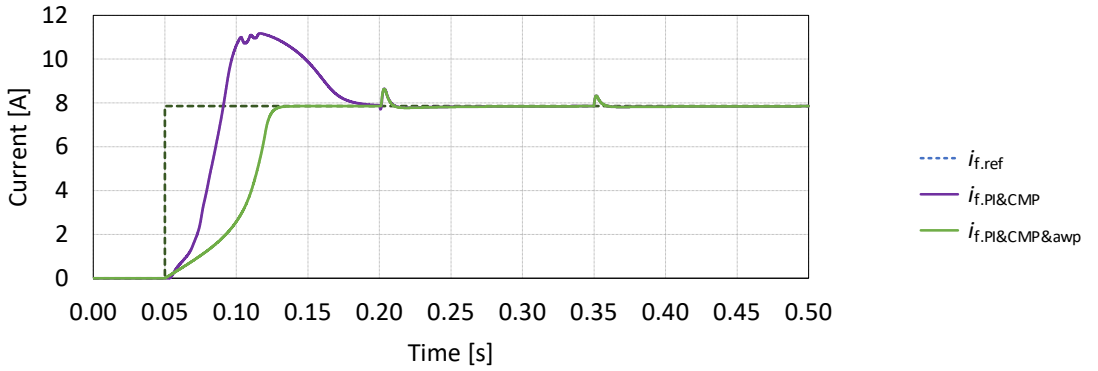

Figure 4-15 Step response of field current.

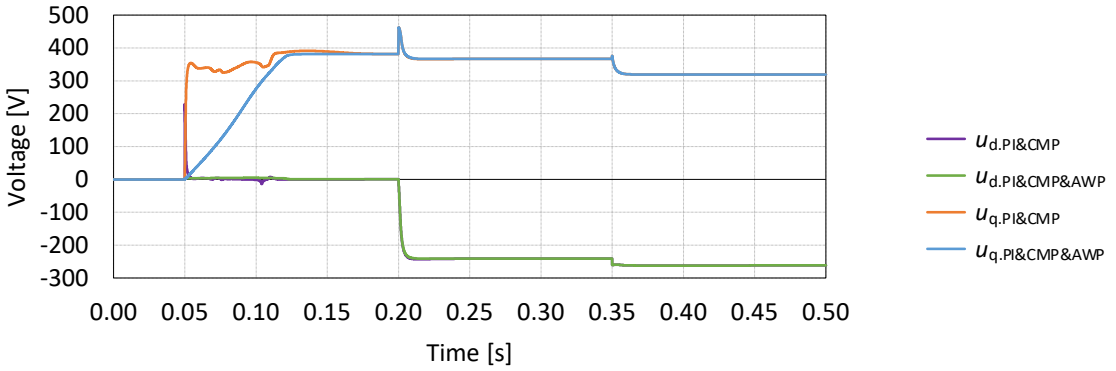

Figure 4-16 Waveforms of d- and q-axis voltages.

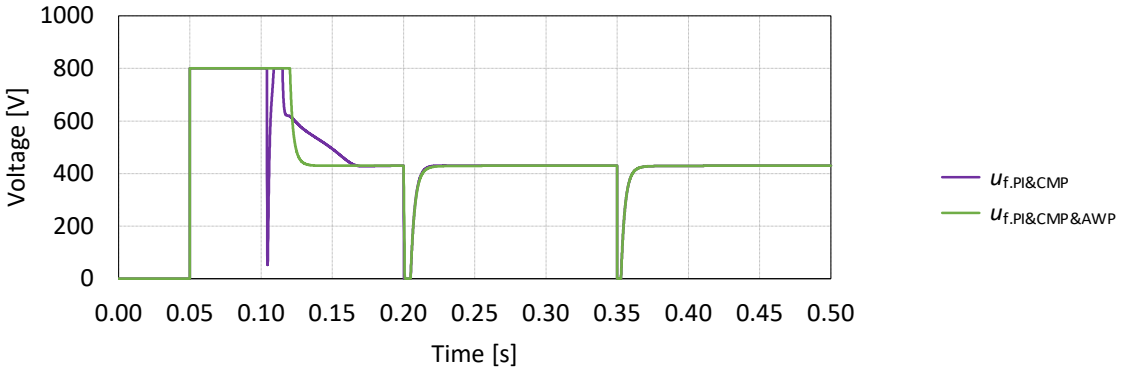

Figure 4-17 Waveforms of field voltage.

the error. A negative integral is established when the d-axis current goes to positive. To cancel this negative integral, the d-axis current needs to go negative for some time, and in the end, the negative area should be equal to the positive area enclosed by the current waveform and the time-axis.

The field current in Case “PI&CMP” rises faster than that in Case “PI&CMP&AWP” starting from 0.05 s. This is due to a negative EMF induced in the field winding by the decrease of the d-axis current. The induced negative EMF together with the applied field voltage at the terminal gives a higher voltage in total applied across the self-inductance in field winding. Consequently, the field current rises faster in Case “PI&CMP”.

A large over-shoot in field current can be observed in Case “PI&CMP”. This is due to two reasons. One reason is that, the PI regulator of the field current only takes care of the resistance and the self-inductance in the field winding. The EMFs across the mutual inductances are disturbances not considered in the PI regulator design. These EMFs cannot be canceled by the compensation algorithm either because the current derivatives are calculated based on $\boldsymbol{u}_{\mathrm{ctrl.self}}$ which is not the correct value when the voltage limit is hit. Another reason is that, anti-windup is not implemented in Case “PI&CMP”. Thus, the integrator keeps integrating the entire amount of error current even after the voltage limit is hit. This means the integrator winds up. Hence after the field voltage exits saturation, it takes time for the integrator to clear this extra amount of integral.

In contrast to Case “PI&CMP”, the current waveforms in Case “PI&CMP&AWP” are clean during the rise of field current. This is due to the anti-windup applied to $\boldsymbol{u}_{\mathrm{ctrl.self}}$. However, during the rises of d- and q-axis currents, the field current is disturbed even with anti-windup implemented as can be noticed in Figure 4-15. This is due to that the EMFs in the field winding induced by d- and q-axis currents are too high for the field voltage to compensate for though the field voltage in terminal already drops to zero. As has been described in the design section, the compensation for the induced voltage due to mutual coupling cannot function well when the voltage output capability is already exhausted. Hence in this situation, the same disturbances appear in field current in both Case “PI&CMP” and Case “PI&CMP&AWP”. In comparison, during the rise of field current, there is no disturbance in d- and q-axis currents. This is because the stator voltage output capability is not exhausted yet and the controller can still compensate for the induced voltages across the mutual inductances in the stator winding.

Chapter 5

Machine Design

Three types of electric vehicles are considered in this study, mild-hybrid cars, electric passenger cars, long-haul electric trucks. The machine design starts from the specifications. To achieve the specified performance, the machine characteristics need to be maximally used. This can be realized by following some design criteria formulated in this chapter. With these design criteria, a structural design procedure is concluded. In the end, a multi-objective optimization method is introduced to achieve the target while minimizing the cost.

5.1 Design Specifications

This section starts with the critical operation points are introduced as well as the automotive test cycles. Then the design specifications for electric machine are derived from the performance requirement of the EV using the vehicle model. From the maximum torque and power, mechanical and electrical dimensions are estimated.

5.1.1 Vehicle Model

A vehicle model is used to calculate the torque-speed profile for a traction motor from the speed profile of a vehicle. The machine speed can be formulated from the vehicle speed as

$$\Omega_{\mathrm{r}} = k_{\mathrm{gear}} \cdot \frac{v_{\mathrm{EV}}}{2\pi \cdot r_{\mathrm{tire}}} \tag{5-1}$$

where k_{gear} is the gear ratio, v_{EV} is the speed of the EV and r_{tire} is the tire radius. The torque requested from the machine to accelerate the vehicle can be formulated as

$$T_{\mathrm{EM}} = r_{\mathrm{tire}} \cdot \frac{m_{\mathrm{EV}} \cdot a_{\mathrm{EV}} + F_{\mathrm{road}}}{k_{\mathrm{gear}} \cdot \eta_{\mathrm{gear}}} \tag{5-2}$$

where r_{tire} is the radius of tires, m_{EV} is the weight of the vehicle, a_{EV} is the acceleration of the vehicle, and F_{road} is the total resistance which is the sum of air drag F_{air}, rolling resistance F_{roll} and grade force F_{grade}

$$F_{\mathrm{road}} = F_{\mathrm{air}} + F_{\mathrm{roll}} + F_{\mathrm{grade}} \tag{5-3}$$

These three forces can be formulated as

$$\begin{aligned} F_{\mathrm{air}} &= \frac{\rho_{\mathrm{air}} \cdot C_{\mathrm{drag}} \cdot A_{\mathrm{EV}}}{2} \cdot (v_{\mathrm{EV}} - v_{\mathrm{wind}})^2 \\ F_{\mathrm{roll}} &= C_{\mathrm{roll}} \cdot m_{\mathrm{EV}} \cdot g \cdot \cos \alpha_{\mathrm{EV}} \\ F_{\mathrm{grade}} &= m_{\mathrm{EV}} \cdot g \cdot \sin \alpha_{\mathrm{EV}} \end{aligned} \tag{5-4}$$

where ρ_{air} is the density of air, C_{drag} is the aerodynamic air drag coefficient, A_{EV} is the effective frontal area, v_{wind} is the speed of wind which is considered as zero in this study,

C_{roll} is the rolling resistance coefficient, g is the acceleration of gravity, α_{EV} is the angle of climbing slope.

The parameters of the passenger car considered in this study are shown in Table 5-1. The parameters are from a sport car presented in [57]. The specifications considered in this study are similar to the summaries from [58], e.g. Volkswagen e-up! (60 kW peak power, 210 N·m peak torque), supermini electric car Renault Zoe (65 kW peak power, 220 N·m peak torque), a medium sedan Renault Fluence (70 kW peak power, 226 N·m peak torque) and so forth.

Table 5-1 Parameters of the passenger car

Parameter	Symbol	Value	Unit
Weight	m_{EV}	1900	kg
Maximum vehicle speed	$v_{\mathrm{EV.max}}$	120	km/h
Effective frontal area	A_{EV}	2.2879	m^2
Aerodynamic drag coefficient	C_{drag}	0.35	
Rolling resistance coefficient	C_{roll}	0.012	
Coefficient of friction		0.8	
Gear ratio	k_{gear}	5.7	
Number of electric machines		1	
Number of tires		4	
Tire size		245/45 R19	

The parameters of a long-haul truck considered in this study are shown in Table 5-2. The weight of the truck considered in this study is around 40 tons and the totally power needed is around 500 kW. In this case, usually two motors are needed to drive the truck, which means each motor needs to deliver 250 kW. The specifications used in this study are based on the references from the LONGRUN Project [59], Volvo FE Electric (185 kW peak power, 850 N·m peak torque), Volvo FL Electric (185 kW peak power, 425 N·m peak torque) [60] and Mercedes eActros (126 kW peak power, 485 N·m peak torque) [61].

Table 5-2 Parameters of the long-haul truck

Parameter	Symbol	Value	Unit
Weight	m_{EV}	40 000	kg
Maximum vehicle speed		100	km/h
Effective frontal area	A_{EV}	9.7 · 0.86	m^2
Aerodynamic drag coefficient	C_{drag}	0.53	
Rolling resistance coefficient	C_{roll}	0.0051	
Coefficient of friction		0.8	
Gear ratio	k_{gear}	19	
Gear efficiency	η_{gear}	94	%
Number of electric machines		2	
Number of tires		12	
Tire size		315/70 R22.5	

5.1.2 Critical Operation Points

There are critical operating situations for a specific type of EV. For instance, during start-up, a high torque is demanded, whereas during cruising at high speed but low torque, a high efficiency is preferable. These critical operating situations can be described by a few parameters and need to be defined for each type of vehicle specifically.

In mild hybrid vehicles, the machine is mainly used for start-up and energy recovery. Therefore, the focus is to achieve as high torque as possible at low speed. The truck considered in this study is expected to be able to operate at three critical points: (1) starting up on a slope of 12%; (2) climbing on slope of 6% at 50 km/h; (3) cruising on flat road at 80 km/h. These critical operation points are shown in Table 5-3. Based on the vehicle model and the parameters mentioned in Table 5-2, the critical points defined for each machine can be derived from the critical points defined for the vehicle. In addition, since 8000 rev/min is the point that the machine should run for long time, a good efficiency should be achieved there.

Table 5-3 Critical operation points defined for the long-haul truck

	Duration	**Vehicle**		**Machine**	
Operation	**Time**	**Speed**	**Slope**	**Speed**	**Torque**
	[min]	**[km/h]**	**[%]**	**[rev/min]**	**[N·m]**
Peak torque	5	0 ~ 30	12	3000	800
Climbing	20	50	6	5000	350
Cruising	long time	80	0	8000	50

5.1.3 Automotive Test Cycles

To describe the behaviors of vehicles in in practical situations, automotive test cycles are introduced. The test cycles can be used to evaluate the overall performance of traction motors in practical activities. For light-duty vehicles, the worldwide harmonized light-duty vehicles test cycles (WLTC) are used in this study. WLTC consist of four sections, covering the speed range from low and medium to high and extra high. For heavy-duty vehicles, CHTC-TT are used in this study. CHTC-TT is one of the scenarios described in the China automotive testing cycles (CATC) [62]. CATC is concluded in 2019 from a research covering over 17 vehicle models, 2.5 million data inputs, 700 thousand car owners and 31 provinces in China. As can be seen from CHTC-TT, a truck does not need to accelerate and deaccelerate frequently as the cars. Instead, it needs to run continuously at high speed but low torque. In this study, WLTC is used for mild-hybrid cars and electric passenger cars, while CHTC-TT is used for electric trucks.

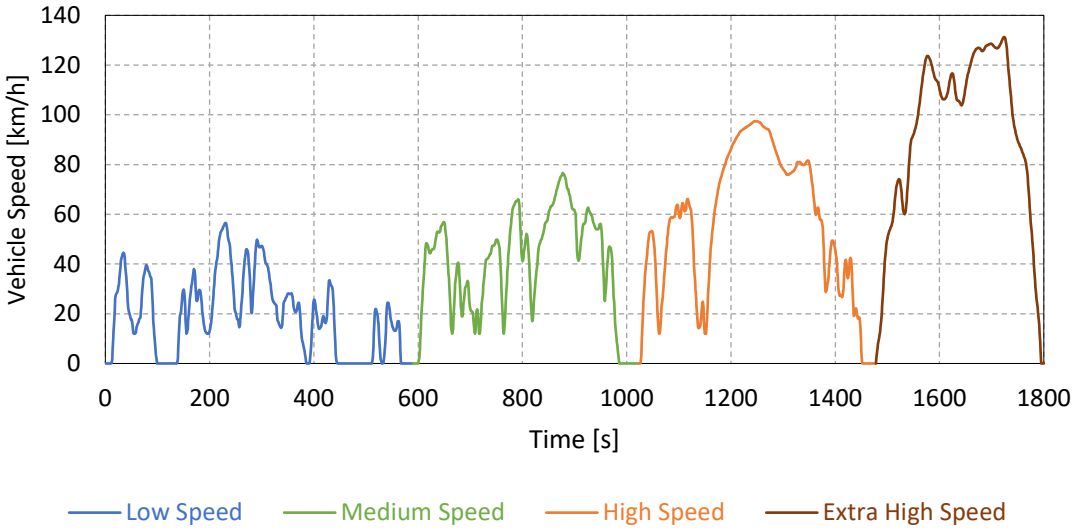

Figure 5-1 WLTC (worldwide harmonized light-duty vehicles test cycles).

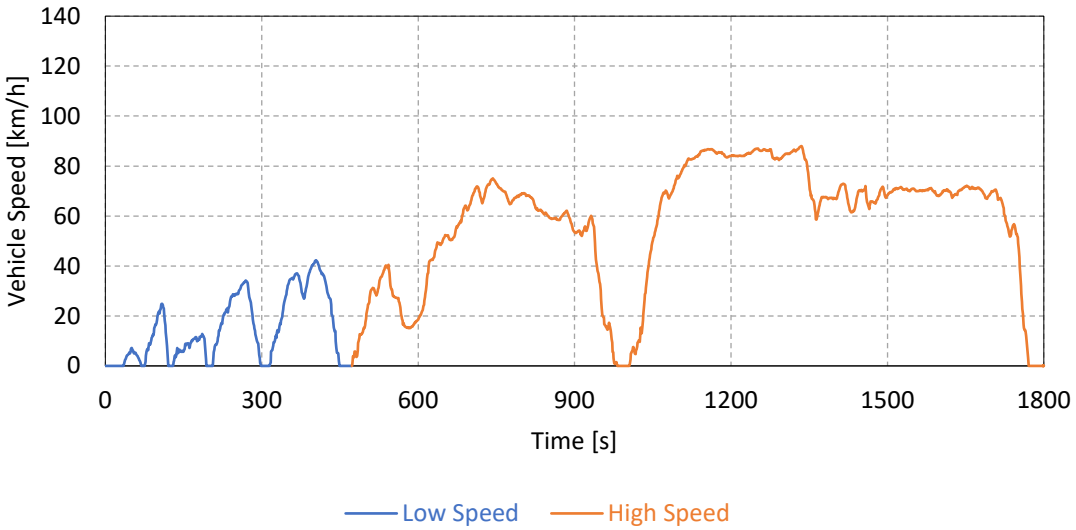

Figure 5-2 CHTC-TT (China heavy-duty test cycles for tractors and trailers).

5.1.4 Torque-Speed Profile

The torque-speed profile of the machine used for mild-hybrid cars is shown in Figure 5-3 [63] [64] [32] [40]. An algorithm to distribute torque request between the electric machine and the combustion engine is applied. Hence from the total torque request, the request of the electric machine is calculated. The torque-speed points following WLTC are presented. A peak torque of 40 N·m for starting up the vehicle is required for 1 s. A power of 10 kW is needed for 30 s to accelerate the car at high speed and to recovery energy during braking. A power of 5 kW is the continuous level, and it is needed for moving the car at low speed, e.g. parking.

The torque-speed profile of the machine used for electric passenger cars is shown in Figure 5-4. The torque-speed points following WLTC are presented. The operation for 30 s is around 60 kW while 30 kW is needed continuously.

The torque-speed profile of the machine used for electric trucks is shown in Figure 5-5. The torque-speed points following CHTC-TT are presented. The machine works for most time at high speed but low torque region.

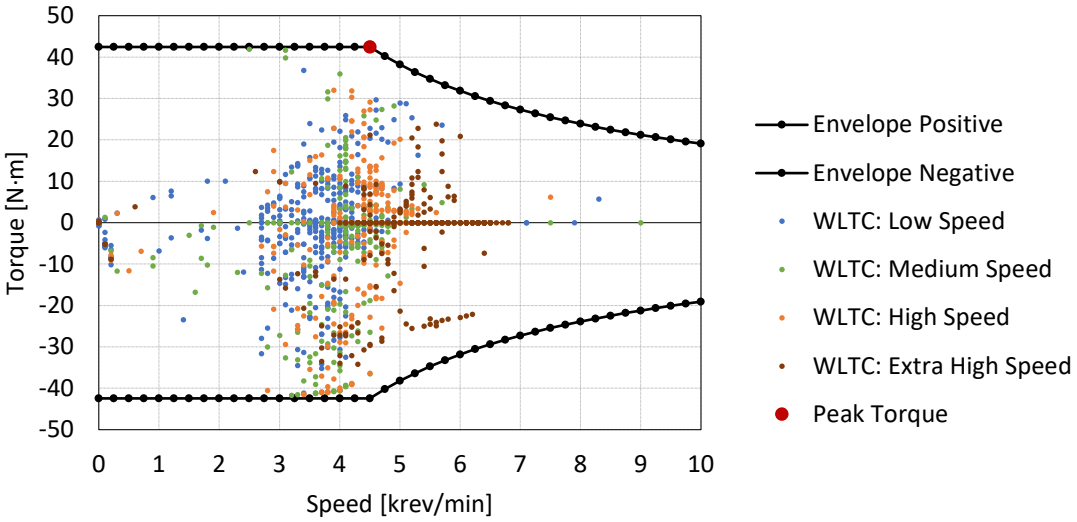

Figure 5-3 Torque-Speed profile of the machine for mild-hybrid cars.

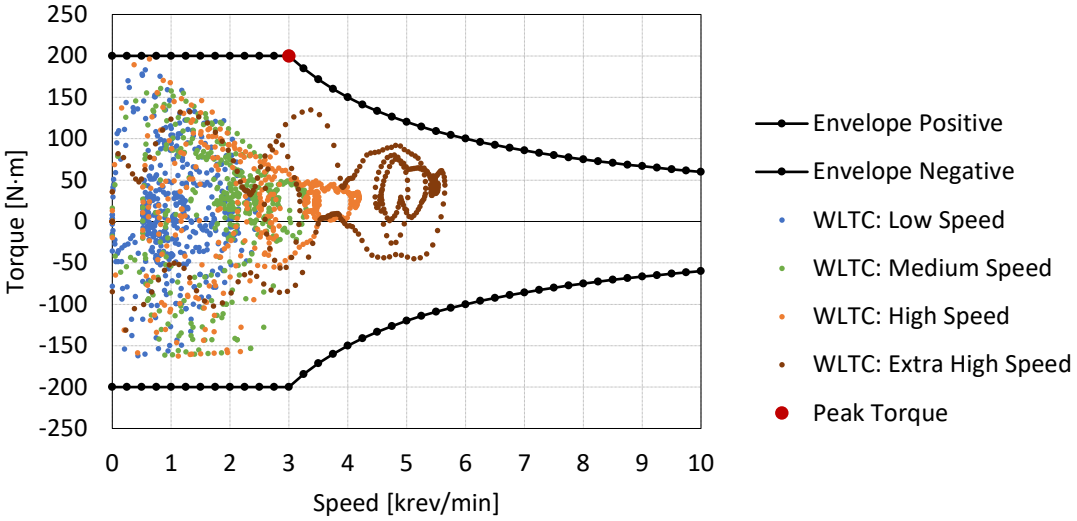

Figure 5-4 Torque-Speed profile of the machine for electric passenger cars.

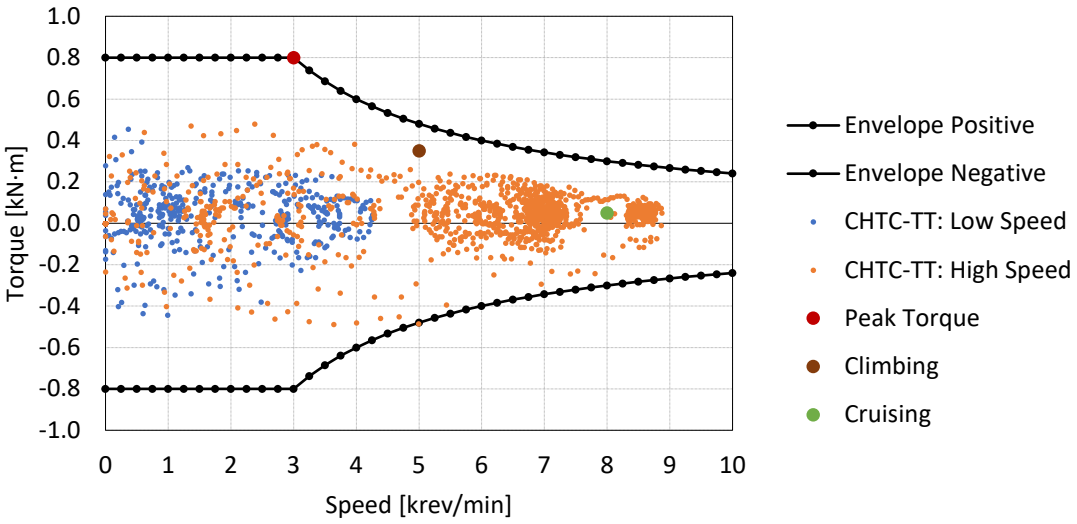

Figure 5-5 Torque-Speed profile of the machine for the electric trucks.

5.1.5 Mechanical and Electrical Dimensions

The machine needs to be mechanically dimensioned to fit the space on vehicles. The maximum torque of the machine is physically limited by the rotor volume V, electric load A in current per unit length and magnetic load B in flux density

$$T_{\mathrm{em}} = V \cdot A \cdot B \tag{5-5}$$

The electrical dimensions are based on the power needed to drive the vehicle and the output capacity of the inverters driving the machines. In mild-hybrid cars, a dc-link voltage of 48 V is the common level. In electric passenger cars, the dc-link voltage level is usually between 300 V and 400 V [58]. In this study, 360 V is considered as the nominal value. In electric trucks, the dc-link voltage is usually between 600 V and 850 V [60] [61]. In this study, the nominal in this study, 800 V is considered as the nominal value.

From the dc-link voltage, the maximum phase voltage amplitude can be decided

$$U_{\mathrm{s.amp}} = \frac{U_{\mathrm{dc}}}{\sqrt{3}} \cdot m_{\mathrm{a}} \tag{5-6}$$

where m_{a} is the amplitude modulation index, using space vector modulation (SVM). The maximum current can be estimated

$$I_{\mathrm{s.amp}} = \frac{2}{3} \cdot \frac{P_{\mathrm{em}}}{U_{\mathrm{s.amp}} \cdot \cos\varphi_{\mathrm{PF}}} \quad \Rightarrow \quad I_{\mathrm{s.rms}} = \frac{\sqrt{2}}{\sqrt{3}} \cdot \frac{P_{\mathrm{em}}}{U_{\mathrm{dc}} \cdot m_{\mathrm{a}} \cdot \cos\varphi_{\mathrm{PF}}} \tag{5-7}$$

In EESM design, it is possible to deliberately set the power factor to unity at peak power. Hence $\cos\varphi_{\mathrm{PF}} \approx 1$ can be considered in (5-7). The mechanical and electrical dimensions of the machines are given in Table 5-4.

Table 5-4 Mechanical and electrical dimension limits

Parameter	Symbol	Value			Unit
		Mild-Hybrid Car	Passenger Car	Truck	
Stacking length	L_{STK}	80	120	360	mm
Stator outer diameter	OD_{STA}	120	175	270	mm
Airgap thickness	g_{air}	1.0	0.7	1.5	mm
Rotor inner diameter	ID_{ROT}		42	50	mm
30 s peak power	P_{peak}	10	60	250	kW
Continuous power	P_{cont}	5	30	180	kW
Maximum speed	$n_{\mathrm{r.max}}$	9000	9000	9000	rev/min
Base speed	$n_{\mathrm{r.base}}$	4500	3000	4500	rev/min
Maximum torque	T_{peak}	40	200	800	N·m
DC-link voltage	U_{dc}	48	360	800	V
Maximum current amplitude	I_{max}	707	350	450	A

5.1.6 Hairpin Winding

Hairpin windings are becoming a trend of traction motors, e.g. Prius 2017, Chevrolet Volt (Gen 2) [65]. In this study, the EESM for electric passenger cars is developed by replacing the rotor of a 360 V 60 kW hairpin PMSM. The hairpin PMSM is with the outer diameter of 235 mm including cooling jacket and the length of 240 mm including front and rear end cap. The power density is 6 kW / L and torque density is 20 N·m / L. The measurement of hair-pin resistance at different frequencies is presented in Figure 5-6. Curve fitting of the resistance profile gives

$$R_{s@f@T} = \frac{a \cdot f^2 + b \cdot f + c}{1000} \cdot [1 + \alpha_{Cu} \cdot (T - T_0)] \text{, for } f \leq 1 \text{ kHz} \tag{5-8}$$

in Ω, where

$$a = 3.19 \times 10^{-5}, b = 3.17 \times 10^{-3}, c = 3.37 \times 10^{1} \tag{5-9}$$

and

$$\alpha_{Cu} = 0.00393, T_0 = 20 \tag{5-10}$$

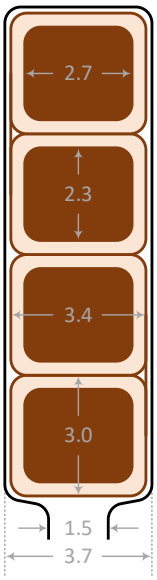

(a) Hair-Pin dimensions.

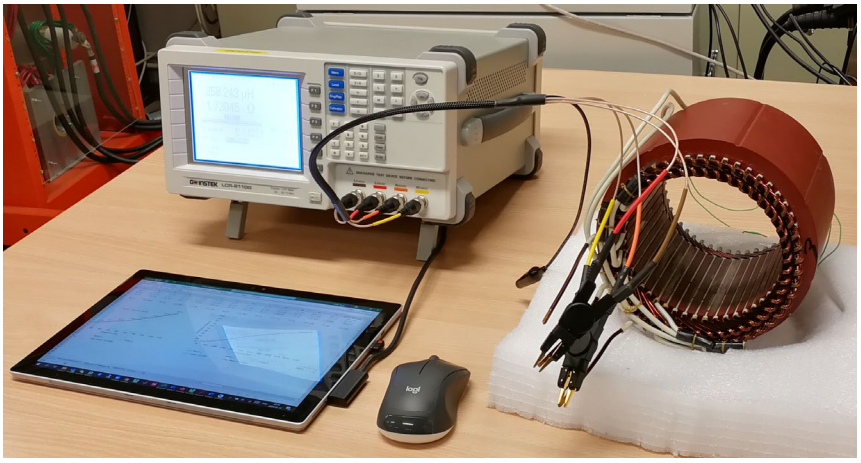

(b) Measuring setup.

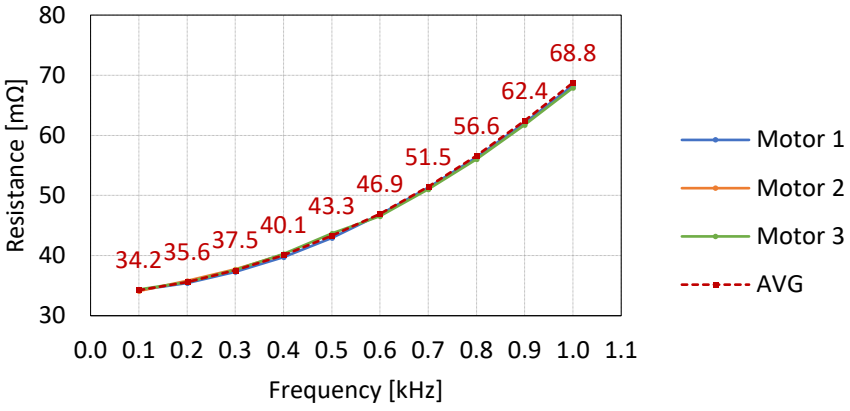

(c) Resistance profile.

Figure 5-6 Measurement of hair-pin resistance.

5.2 Machine Design Criteria

The field current employed in EESM indicates the possibility of adjusting power factor and achieving high torque. To maximally make use of these possibilities, machine design criteria are derived in this section: (1) to achieve unity power factor at peak torque, and (2) to minimize the zero torque-boosting area.

5.2.1 Unity Power Factor at Peak Power

By adjusting the field current of an EESM, high power factor, even unity power factor, can be achieved. This is an advantage of EESMs. Especially in heavy-duty applications, the vehicle runs on express ways at high speed for long time. The criterion to achieve unity power factor is derived in (3-22) and (3-23). Furthermore, in field weakening, the machine is working at the intersection between current limit circle and voltage limit ellipse. To guarantee unity power factor in this situation, the unity power factor ellipse needs to come across this intersection as well. To make sure that a solution in this situation is available, the center of the unity power factor ellipse described in (3-22) and (3-23) must locate outside of the current limit circle. This criterion can be formulated as

$$I_{\mathrm{s.max}} < \frac{L_{\mathrm{m}}}{L_{\mathrm{d}}} \cdot I_{\mathrm{f.max}} \tag{5-11}$$

The inductances L_{m} and L_{d} can be further formulated as

$$L_{\mathrm{m}} = \frac{N_{\mathrm{d.turn}} \cdot N_{\mathrm{f.turn}}}{\mathfrak{R}_{\mathrm{m}}} \cdot \frac{N_{\mathrm{s.ser}}}{N_{\mathrm{f.par}}} \quad , \quad L_{\mathrm{d}} = \frac{N_{\mathrm{d.turn}} \cdot N_{\mathrm{d.turn}}}{\mathfrak{R}_{\mathrm{d}}} \cdot \frac{N_{\mathrm{s.ser}}}{N_{\mathrm{s.par}}} \tag{5-12}$$

where N_{d} is the equivalent number of half-turns per pole in stator d-axis, N_{f} is the number of turns per pole in field winding, $\mathfrak{R}_{\mathrm{m}}$ is the reluctance of field winding flux path, $\mathfrak{R}_{\mathrm{d}}$ is the d-axis reluctance of stator winding flux path, $N_{\mathrm{s.ser}}$ and $N_{\mathrm{s.par}}$ are the numbers of series and parallel branches in stator winding respectively, and $N_{\mathrm{f.par}}$ is the number of parallel branches in field winding. N_{d} can be further formulated as

$$N_{\mathrm{d.turn}} = k_{\mathrm{w}} \cdot q \cdot r \cdot N_{\mathrm{s.turn}} \tag{5-13}$$

where k_{w} is the winding factor, q is the number of slots per pole per phase, r is the number of winding layers and N_{s} is the number of turns per coil in stator winding. Then the criterion can be concluded as

$$I_{\mathrm{f.max}} > k_{\mathrm{w}} \cdot q \cdot r \cdot \frac{N_{\mathrm{s.turn}}}{N_{\mathrm{f.turn}}} \cdot \frac{N_{\mathrm{f.par}}}{N_{\mathrm{s.par}}} \cdot \frac{\mathfrak{R}_{\mathrm{m}}}{\mathfrak{R}_{\mathrm{d}}} \cdot I_{\mathrm{s.max}} \tag{5-14}$$

In addition, $\mathfrak{R}_{\mathrm{d}}$ equals the mutual reluctance $\mathfrak{R}_{\mathrm{m}}$ in parallel with the leakage reluctance $\mathfrak{R}_{\sigma}$. Due to the large value of $\mathfrak{R}_{\sigma}$ compared with $\mathfrak{R}_{\mathrm{m}}$,

$$\mathfrak{R}_{\mathrm{d}} = \mathfrak{R}_{\mathrm{m}} // \mathfrak{R}_{\sigma} = \frac{\mathfrak{R}_{\mathrm{m}} \cdot \mathfrak{R}_{\sigma}}{\mathfrak{R}_{\mathrm{m}} + \mathfrak{R}_{\sigma}} \approx \mathfrak{R}_{\mathrm{m}} \tag{5-15}$$

With this approximation, (5-14) becomes

$$I_{\mathrm{f.max}} > k_{\mathrm{w}} \cdot q \cdot r \cdot \frac{N_{\mathrm{s.turn}}}{N_{\mathrm{f.turn}}} \cdot \frac{N_{\mathrm{f.par}}}{N_{\mathrm{s.par}}} \cdot I_{\mathrm{s.max}} \tag{5-16}$$

This is the criterion to decide the minimum field current level to guarantee unity power factor in field weakening.

5.2.2 Zero Torque-Boosting

Torque-boosting is the situation when either stator or field current reaches the maximum whereas the other does not. Hence the torque increases by increasing only one current. The torque-boosting area decreases the possibility to increase torque further. Hence it is preferred to be reduced as much as possible. This leads to

$$I_{\mathrm{f.max}} = \frac{I_{\mathrm{s.max}}}{\sqrt{c_{\mathrm{d}}^2 + c_{\mathrm{q}}^2}} \tag{5-17}$$

according to (3-77). Assuming that at maximum excitation level, the iron-core in d-axis is saturated so that L_{d} decreases to a similar level as L_{q}, then

$$P_{\mathrm{Cu.f}} = I_{\mathrm{f.max}}^2 \cdot R_{\mathrm{f}} \approx \frac{3}{2} \cdot I_{\mathrm{s.max}}^2 \cdot R_{\mathrm{s}} = P_{\mathrm{Cu.s}} \tag{5-18}$$

This means that, to eliminate the torque-boosting area, the copper losses in both stator and field winding need to be equal. As an approximation, taking active part into account, this criterion can be formulated as

$$\frac{I_{\mathrm{s.max}}}{I_{\mathrm{f.max}}} \approx \sqrt{\frac{2}{3}\frac{R_{\mathrm{f}}}{R_{\mathrm{s}}}} \tag{5-19}$$

5.3 Design Procedure

5.3.1 Pole Pairs and Slots

The stator winding arrangement includes the number of phases m, number of pole pairs p, number of slots per pole per phase q. The total number of slots Q therefore becomes

$$Q = 2 \cdot m \cdot p \cdot q \tag{5-20}$$

As for the selection of p, a higher value would shorten the length of end-winding which would further reduce copper losses. However, since the electrical speed ω_{r} is p times of the mechanical speed Ω_{r}

$$\omega_{\mathrm{r}} = p \cdot \Omega_{\mathrm{r}} = p \cdot \frac{\pi}{30} \cdot n_{\mathrm{r}} \tag{5-21}$$

where n_{r} is the speed in revolution per minute, a higher p requires a higher electrical speed ω_{r}, and consequently

- A higher iron-core loss, because the eddy current iron-core loss is proportional to ω_{r}^2 and the hysteresis iron-core loss is proportional to ω_{r}.
- A higher fundamental frequency f_1 from the inverter

$$f_1 = \frac{\omega_{\mathrm{r}}}{2 \cdot \pi} = \frac{p \cdot n_{\mathrm{r}}}{60} \tag{5-22}$$

And frequency modulation index m_{f} becomes lower at high speed of the machine

$$m_{\mathrm{f}} = f_{\mathrm{sw}}/f_1 \tag{5-23}$$

Then it becomes possible to calculate the maximum number of pole pairs allowed in consideration of switching

$$p_{\max} = \frac{2 \cdot \pi \cdot f_{\mathrm{sw}}}{m_{\mathrm{f.min}} \cdot \Omega_{\mathrm{r.max}}} = \frac{60 \cdot f_{\mathrm{sw}}}{m_{\mathrm{f.min}} \cdot n_{\mathrm{r.max}}} \tag{5-24}$$

The winding arrangement considered in this study is shown in Table 5-5.

Table 5-5 Winding arrangement

Parameters	Symbol	Value		
		Mild-Hybrid Car	Passenger Car	Truck
Number of phases	m	3	3	3
Number of pole pairs	p	4	4	4
Number of slots per pole per phase	q	1	2	2
Number of layers	r	1	2	2
Pole pitch	τ	3	6	6
Coil pitch	y	3	5	5
Number of slots	Q	24	48	48
Winding factor	k_{w}	1.000	0.933	0.933

5.3.2 Strands, Turns, Coils, Branches, and Phase

The relation between winding structures can be illustrated in Figure 5-7. The most basic element to form a winding is a copper strand. From manufacturing perspectives, a strand diameter between 0.7 mm and 1.0 mm would be practical. The strand area can be decided as

$$A_{\mathrm{strand}} = \pi \cdot r_{\mathrm{strand}}^2 \tag{5-25}$$

The copper area of a strand is quite limited. To conduct a higher current, several strands are placed in parallel to form a turn. Then several turns are winding around the teeth of the stator to increase the EMF. Obviously, these turns are in series. The series-connected turns form a coil, and several coils are connected in series to form a branch. Finally, several can be connected in parallel to form a phase winding.

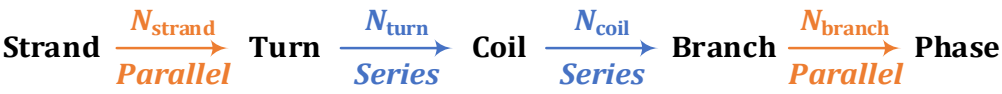

(a) Strands, Turns, Coils, Branches, and Phase.

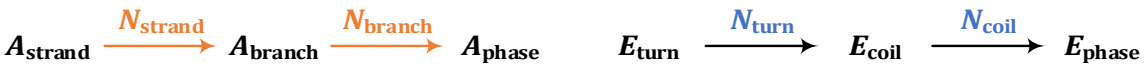

(b) Copper area. (c) EMF.

Figure 5-7 Illustration of strands, coils, branches and turns.

Therefore, all the parallel-connected elements are dividing the current

$$A_{\text{branch}} = A_{\text{strand}} \cdot N_{\text{strand}} \quad , \quad A_{\text{phase}} = A_{\text{branch}} \cdot N_{\text{branch}} \tag{5-26}$$

and all the series connected elements are dividing the EMF

$$E_{\text{branch}} = E_{\text{turn}} \cdot N_{\text{turn}} \quad , \quad E_{\text{phase}} = E_{\text{coil}} \cdot N_{\text{coil}} \tag{5-27}$$

Among the parameters, N_{coil} and N_{branch} are constrained by winding arrangement

$$N_{\text{coil}} \cdot N_{\text{branch}} = p \cdot q \cdot r \tag{5-28}$$

For the stator winding, the total copper area per phase able to conduct the maximum current can be estimated as

$$A_{\text{phase}} = \frac{I_{\text{rms.max}}}{J_{\text{rms.max}}} \tag{5-29}$$

The number of strands is therefore decided by taking of ceiling of the ratio

$$N_{\text{strand}} = \text{ceiling}\left\{\frac{A_{\text{branch}}}{A_{\text{strand}}}\right\} \tag{5-30}$$

In the end, the copper areas of each strand and the phase can be using (5-26) .

For the field winding, to guarantee the same amount of MMF generated from each pole, N_{branch} is set to 1. In addition, the field excitation is expected to be contactless through an H-bridge inverter, a rotating transformer and a diode rectifier. Therefore, a higher resistance of the field winding is preferred to minimize the voltage drop across the diodes in percentage. Hence N_{strand} is set to 1. The strand current is the same as the terminal current.

5.3.3 Airgap and Slot Geometry

The stator and rotor geometries are parameterized as shown in Figure 5-8. $Bs0$, $Bs1$ and $Bs2$ mean the widths of slot opening, slot top and slot bottom. $Hs0$, $Hs1$ and $Hs2$ mean the heights of slot opening, slot wedge and slot body. Rs means the fillet radius of slot corner.

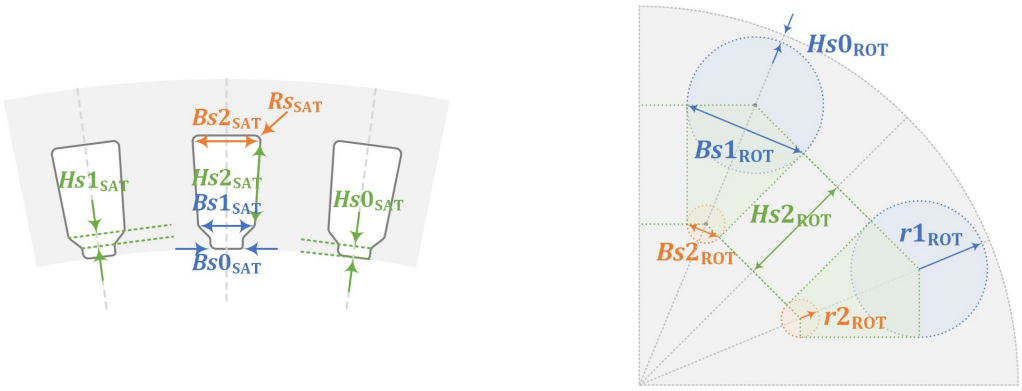

(a) Stator geometric parameters. (b) Rotor geometric parameters.

Figure 5-8 Parameters of the stator and rotor geometries.

Parametric sweeps are applied to decide the optimum geometries of stator and rotor slots. The slot width and height are swept while the stator and rotor slot areas are fixed in the sweep. Parallel tooth in stator and parallel pole in rotor are set as constraints as well, which means

$$Bs2_{\mathrm{STA}} = Bs1_{\mathrm{STA}} + 2 \cdot Hs2_{\mathrm{STA}} \cdot \tan \alpha_{\mathrm{STA}} \tag{5-31}$$

$$Bs2_{\mathrm{ROT}} = Bs1_{\mathrm{ROT}} - 2 \cdot Hs2_{\mathrm{ROT}} \cdot \tan \alpha_{\mathrm{ROT}} \tag{5-32}$$

where

$$\alpha_{\mathrm{STA}} = \pi/Q \quad , \quad \alpha_{\mathrm{ROT}} = \pi/2/p \tag{5-33}$$

The tooth width and yoke width can be formulated as

$$w_{\mathrm{STA.tooth}} = \left(\frac{ID_{\mathrm{STA}}}{2} + Hs0_{\mathrm{STA}} + Hs1_{\mathrm{STA}}\right) \cdot \frac{\sin 2\alpha_{\mathrm{STA}}}{\sin \beta_{\mathrm{STA}}} - Bs1_{\mathrm{STA}} \cdot \cos \alpha_{\mathrm{STA}} \tag{5-34}$$

$$w_{\mathrm{STA.yoke}} = \frac{OD_{\mathrm{STA}} - ID_{\mathrm{STA}}}{2} - Hs0_{\mathrm{STA}} - Hs1_{\mathrm{STA}} - Hs2_{\mathrm{STA}} - Rs_{\mathrm{STA}} \tag{5-35}$$

where

$$\beta_{\mathrm{STA}} = \pi/2 - \alpha_{\mathrm{STA}} \quad , \quad \beta_{\mathrm{ROT}} = \pi/2 - \alpha_{\mathrm{ROT}} \tag{5-36}$$

The stator and rotor slot areas can be formulated as

$$\begin{aligned} A_{\mathrm{slot.STA}} = {} & (Bs1_{\mathrm{STA}} + Bs2_{\mathrm{STA}}) \cdot Hs2_{\mathrm{STA}}/2 \\ & + Rs_{\mathrm{STA}}^2 \cdot (\pi/2 + \alpha_{\mathrm{STA}} + \sin \alpha_{\mathrm{STA}} \cdot \cos \alpha_{\mathrm{STA}}) \\ & + [Rs_{\mathrm{STA}} \cdot (1 + \sin \alpha_{\mathrm{STA}})] \cdot (Bs2_{\mathrm{STA}} - 2 \cdot Rs_{\mathrm{STA}} \cdot \cos \alpha_{\mathrm{STA}}) \end{aligned} \tag{5-37}$$

$$\begin{aligned} A_{\mathrm{slot.ROT}} = {} & (r1_{\mathrm{ROT}} + r2_{\mathrm{ROT}})/\cos \alpha_{\mathrm{ROT}} \cdot Hs2_{\mathrm{ROT}} \\ & + r1_{\mathrm{ROT}}^2 \cdot (\pi - \beta_{\mathrm{ROT}}) + r2_{\mathrm{ROT}}^2 \cdot \beta_{\mathrm{ROT}} \end{aligned} \tag{5-38}$$

where

$$r1_{\mathrm{ROT}} = \frac{Bs1_{\mathrm{ROT}}}{2 \cdot \cos \alpha_{\mathrm{ROT}}} \quad , \quad r2_{\mathrm{ROT}} = \frac{Bs2_{\mathrm{ROT}}}{2 \cdot \cos \alpha_{\mathrm{ROT}}} \tag{5-39}$$

5.4 Optimization for Maximum Peak Torque

Following the specifications introduced in Section 5.1, a 4-polepair 24-slot EESM for mild hybrid vehicle is designed. The target is to achieve the maximum torque within the fixed volume and current density. In order to push as much torque as possible out of the motor, the flux path needs to be made as wide as possible to avoid magnetic saturation. To achieve this, a parametric sweep is established. The sweep consists of airgap diameter, slot width, slot depth, pole width and pole height. The stator slot area and the rotor slot area are fixed according to a fixed current density. In the end, the optimum sizes of stator slot and rotor pole along with the optimum stator inner diameter are determined. The parameters of the final design are presented in Table 5-6.

The flux distributions of no-load operation and peak torque operation are calculated in FEM and presented in Figure 5-9. As can be noticed from the flux distributions, the flux density of the stator teeth, yoke and rotor pole body are around 1.6 T, which is slightly below the limit of saturation around 1.8 T. In peak torque operation, the flux distribution is asymmetric. Local saturation can be found on one tip of the pole shoe whereas the saturation on the other tip is eased. This is due to the fact that, the d- and q-axis flux are in the same direction on one tip whereas on the other tip, the flux flow in the opposite direction and therefore canceled [16].

Table 5-6 Parameters of a 4-polepair 24-slot EESM for mild hybrid vehicle

Parameter	Symbol	Value	Unit
Stator slot width	$Bs1$	5.56	mm
Stator slot depth	$Hs2$	4.5	mm
Rotor pole body width	w_{pole}	16.5	mm
Rotor pole body height	h_{pole}	14.5	mm
Number of turns in stator	$N_{\mathrm{STA.turn}}$	6	
Number of turns in rotor per pole	$N_{\mathrm{ROT.turn}}$	75	
Steel material		SURA M250-35A	

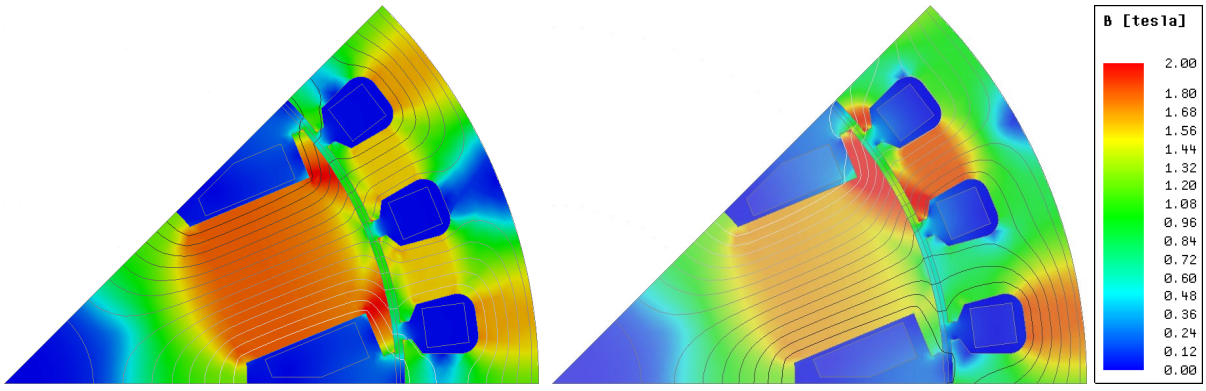

(a) No-load operation. (b) Peak torque operation.

Figure 5-9 Flux distribution in FEM of a 48 V EESM.

5.4.1 Prototyping

The prototyping of the 48 V 20 kW EESM and validation are presented in this section. The machine prototype is for mild hybrid vehicles, mainly used for vehicle starting up and cruising. The parameters of the machine are listed in Table 5-7. The resistances and inductances of the stator and field windings are identified experimentally. The mutual inductance between the stator and field windings is determined by measuring no-load EMF from the stator side. The d- and q-axis inductances are ascertained by injecting d- and q-axis currents separately.

Table 5-7 Parameters of a 4-polepair 24-slot EESM for mild hybrid vehicles

Parameter	Value	Unit	Parameter	Value	Unit
DC-link voltage	48	V	Maximum phase current amplitude	500	A
30 s peak power	10	kW	Continuous power	5	kW
Maximum torque (for 1 s)	30	N·m	Base speed	4500	rev/min
Stator outer diameter	120	mm	Stator inner diameter	90	mm
Active length	80	mm	Air gap	1	mm
Stator winding resistance (dc)	4	mΩ	Field winding resistance (dc)	5	Ω
Stator d-axis inductance (unsaturated)	24.4	μH	Stator q-axis inductance (unsaturated)	20.6	μH
Field winding inductance (unsaturated)	130	mH	Mutual inductance (unsaturated)	1.0	mH

The cross-section of the EESM in CAD drawing is illustrated in Figure 5-10 (a). The excitation of the machine is brushless. A rotating transformer is placed between the field winding and the end cap on the rear as pointed out in (a). The primary side is mounted on the stator frame whereas the secondary side is mounted on the rotor frame. An H-bridge inverter delivers power to the primary side, and through an airgap, the power reaches the secondary side. After a diode rectifier, dc current flows to the field winding. The diameter of the machine including the cooling jacket is 155 mm and the length between the front and the rear end caps is 172 mm. Considering a peak torque of 33.8 N·m, the torque density is over 10 N·m/L. Figure 5-10 (b) and (c) show the stator and rotor of the protype. Winding terminals come out from the rear of the machine. PT100 sensors are inserted into the winding to monitor temperatures. The rear of the shaft is hollow for the wires of the PT100 sensors to come out.

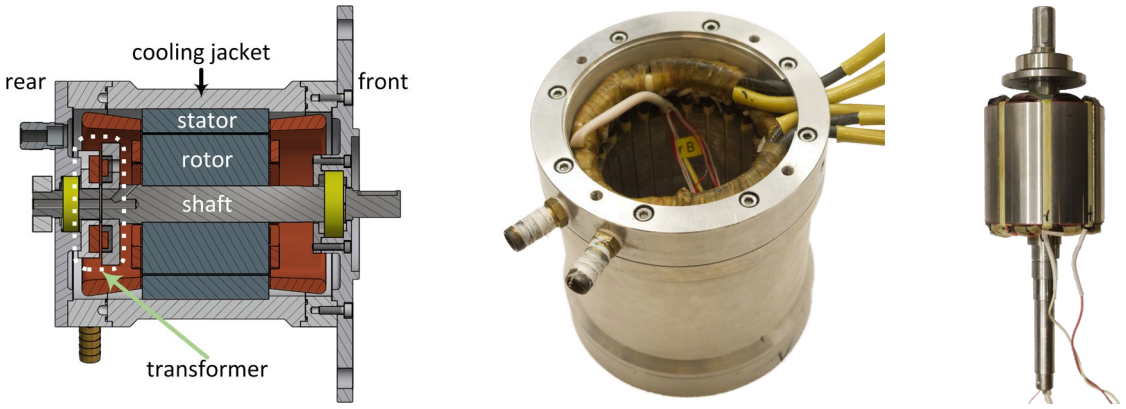

(a) Cross-section of the machine assembly. (b) Stator. (c) Rotor.

Figure 5-10 Cross-Section of a 48 V EESM.

5.4.2 Experimental Verification

The photos of the experimental setup are shown in Figure 5-11. Subplot (a) shows the power electronics and the measurements as well as the machine which have been described in the previous sections. Subplot (b) shows the control and monitor station. The details of the signal processing circuit and the control programme are described in Appendix C.

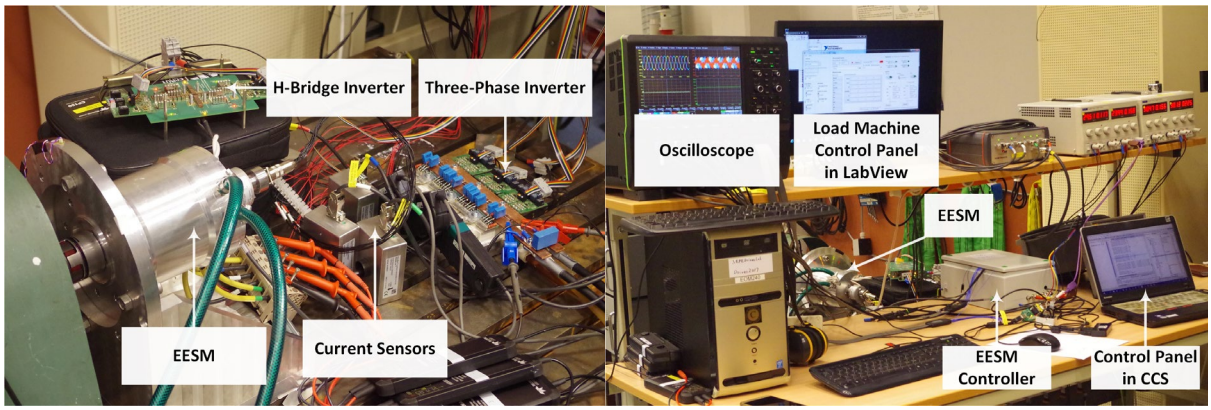

(a) Test bench. (b) Control station.

Figure 5-11 Experimental setup.

The torque measurements from torque transducer are presented in Figure 5-13 (a). The field current ranges from 5 A to 15 A in a step of 5 A, while the q-axis current ranges from 100 A to 500 A in a step of 100 A. The measurements are performed at a speed of 750 rpm, due to the fact that a higher speed consumes more power than the power source equipped in the laboratory. In addition, the application of this motor is for the start-up of a mild hybrid vehicle in which a sufficient output torque is more important than output power.

The measurements fit the FEM results quite well. The efficiency and displacement power factor are presented in Figure 5-13 (b) and (c). The displacement power factor (DPF) is defined as the power factor considering only the fundamental components of voltage and current. As can be noticed, the efficiency and DPF fit the FEM calculations quite well.

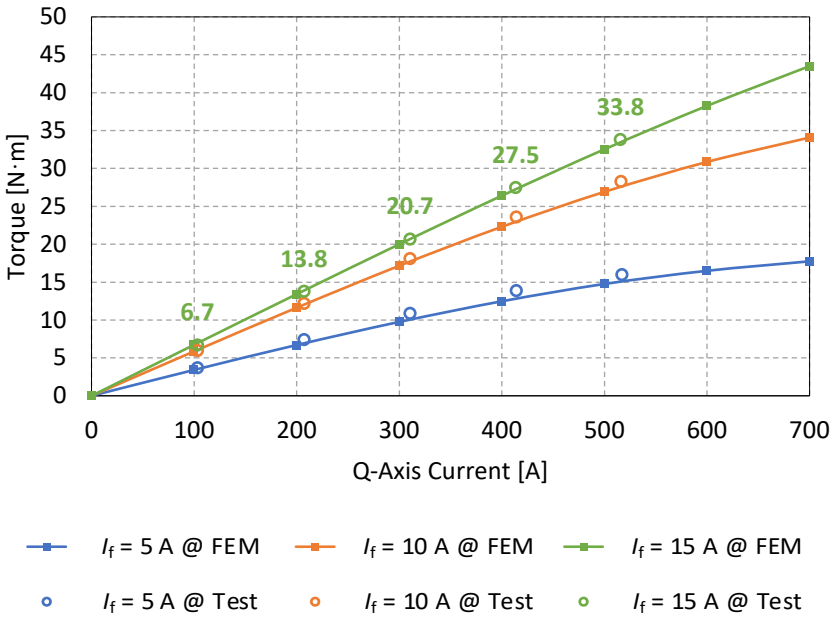

Figure 5-12 Torque measurement in verification of torque at 750 rpm.

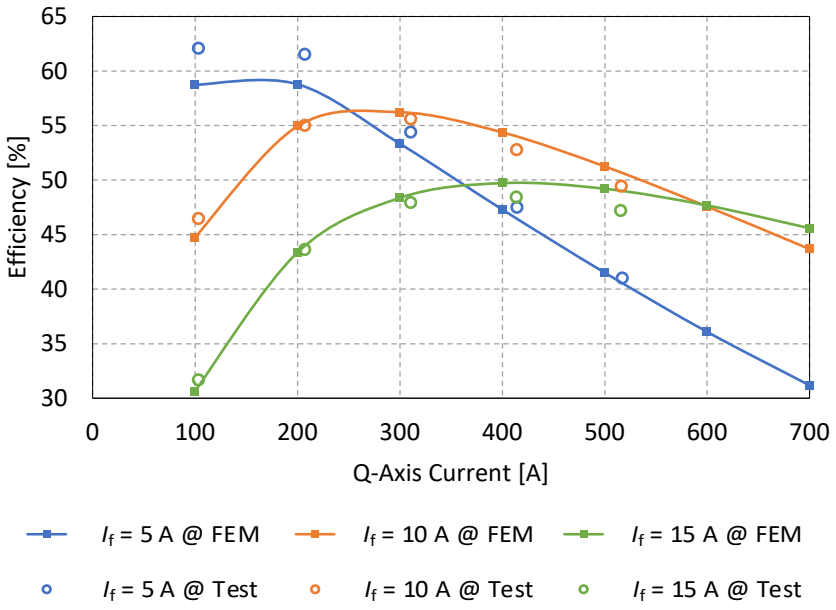

Figure 5-13 Efficiency measurement in verification of torque at 750 rpm.

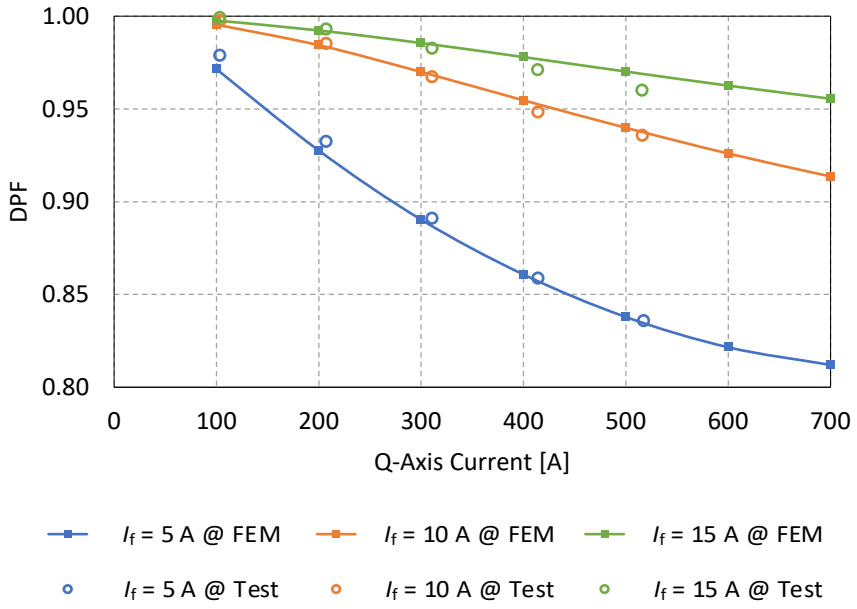

Figure 5-14 Displacement power factor in verification of torque at 750 rpm.

5.5 Optimization for Multi-Objectives

In this section, the multi-objective optimization is presented with the design of 800 V 250 kW EESM for electric trucks.

5.5.1 Cost Function and Constraints

In the design of EESM for electric trucks, the strand diameter is arbitrarily decided as 1.0 mm for both stator and field windings. Considering thermal issues, the current densities of stator and field windings are set as 15 and 10 A/mm^2 respectively. A few parameters are fixed in the analysis of slot geometries as listed in Table 5-8. The airgap thickness is set to 1.5 mm to avoid radial collisions. The values of other parameters in the table are believed to be practical choices in terms of manufacturing and would not significantly affect the machine performance. The rotor is decided as closed-slot to prevent the field windings from flying out at high speed.

Table 5-8 Fixed parameters before optimization

Parameter	Symbol	Value	Unit
Airgap thickness	t_{airgap}	1.5	mm
Stator	$Hs0_{\mathrm{STA}}$	1	mm
	$Hs1_{\mathrm{STA}}$	1	mm
	$Bs0_{\mathrm{STA}}$	2	mm
	Rs_{STA}	1	mm
Rotor	$Hs0_{\mathrm{ROT}}$	2	mm
	$Hs1_{\mathrm{ROT}}$	0	mm
	$Bs0_{\mathrm{ROT}}$	0	mm

5.5.2 Parametric Sweep and Prieto-Frontier

Parametric sweeps are applied in optimization to maximize the peak torque while minimize losses. As mentioned before, the air gap diameter, widths and heights of slots are varied while the slot areas are kept constant. The maximum torque versus core-loss of each geometrical design is presented in Figure 5-15. The copper losses are almost the same for all cases and therefore are not presented here. The geometries with the same air gap diameter are illustrated in the same color. The optimum points are expected to achieve high torque and low iron-core losses at the same time. The Pareto frontier regarding this target is illustrated in the graph. Additionally, there are only three candidates lay above 800 N·m. The differences of torque level between them are minor. Therefore, it is clear to select the one with the lowest core-loss among the three, which is marked by a circle in blue. The parameters of this finalized design are listed in Table 5-9 and Table 5-10.

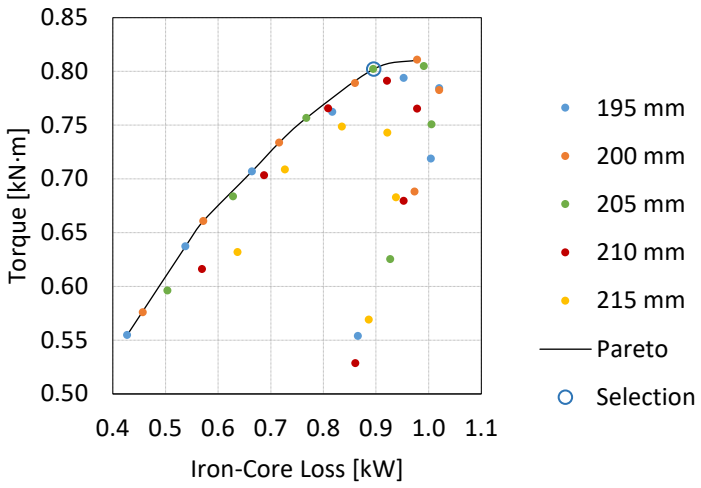

Figure 5-15 Peak torque versus iron-core losses of different geometries.

Table 5-9 Winding and geometrical parameters of the finalized design of the 800 V 250 kW EESM

Parameter	Stator		Rotor	
	Value	Unit	Value	Unit
d_{airgap}	205	mm	205	mm
N_{branch}	4		1	
N_{coil}	2		8	
N_{turn}	5		270	
N_{strand}	7		1	
$Hs2$	14.58	mm	26.62	mm
$Bs1$	7.79	mm	28.99	mm
$Bs2$	9.70	mm	6.94	mm

Table 5-10 Electrical parameters of the finalized design of the 800 V 250 kW EESM

Parameter	Symbol	Value	Unit
Stator resistance @ 100℃	R_{s}	19.55	mΩ
Field resistance @ 100℃	R_{f}	54.71	Ω
D-axis self-inductance @ zero current	L_{dd}	1.30	mH
Q-axis self-inductance @ zero current	l_{qq}	1.30	mH
Field self-inductance @ zero current	l_{ff}	20.29	H
Mutual inductance @ zero current	l_{df}	92.80	mH

5.5.3 Results

A. Flux Distributions

The flux distributions of the machine with the finalized geometry at no load and peak torque are presented in Figure 5-16. The maximum field current of 7.854 A is applied in both cases. The peak torque is achieved with the maximum stator current amplitude of 450 A and a current angle of 107°.

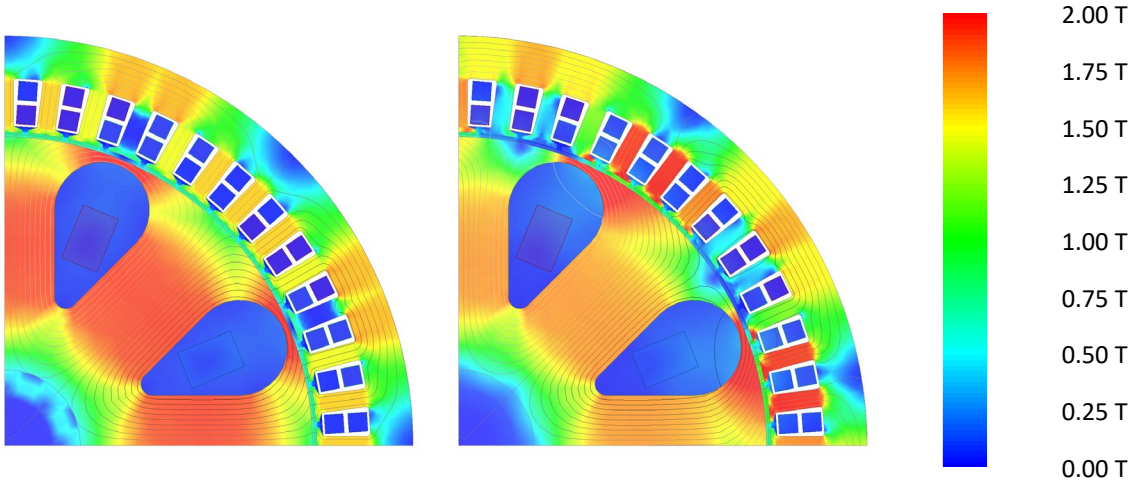

(a) No load operation. (b) Peak torque operation.

Figure 5-16 Flux density distribution of the 800 V 250 kW EESM.

At no load, the teeth and yoke of the stator are evenly saturated. Comparably, at peak torque, some of the stator teeth become more saturated due to armature reaction. This leads to a reverse of saliency from $L_{\mathrm{dd}} > L_{\mathrm{qq}}$ to $L_{\mathrm{dd}} < L_{\mathrm{qq}}$. Consequently, the peak torque is achieved at a current angle of 107° instead of being at first quadrant in dq-frame.

In addition, the saturation of rotor pole is eased at peak torque due to the amount of negative d-axis current applied from the stator winding. The flux generated from the negative d-axis current counteracts the flux generated from the field winding and eases the saturation in rotor pole body. Moreover, the saturation of the rotor pole shoes becomes uneven. This is due to the q-axis current applied from the stator winding. The flux generated from the q-axis current cancels the flux at one tip of the pole shoe while enhances the flux at the other tip.

B. Critical Operation Points

Flux linkage maps are generated by varying d-axis, q-axis and field currents in FEM parametric sweeps. Then the solutions of d-axis, q-axis and field currents at any specific torque-speed point can be obtained through iterations to minimize copper and iron-core losses. The solutions of the critical points are then verified in FEM. The results from iterations agree to the FEM results as shown in Table 5-11.

Table 5-11 Verification of critical operation points of the long-haul truck

		Peak Torque	Climbing	Cruising	Unit
Speed		3000	5000	8000	rev/min
Torque	**Iteration**	802.07	350.00	50.00	N·m
	FEM	802.02	350.46	50.14	
Power	**Iteration**	251.98	183.26	41.89	kW
	FEM	251.96	183.50	42.00	
η	**Iteration**	96.11	97.70	97.82	%
	FEM	96.11	97.70	97.92	
$\cos\varphi$	**Iteration**	0.93	0.98	0.93	
	FEM	0.90	0.97	0.93	
P_{Cu}		9.31	3.19	0.34	kW
P_{Fe}	**Iteration**	0.90	1.13	0.59	kW
	FEM	0.90	1.14	0.55	

C. Efficiency Map

The efficiency map of the machine can be achieved by extending the usage of the iteration algorithm to all points in the torque-speed map. Only copper and iron-core losses are considered in the efficiency calculation. The sum of copper and iron-core losses is set as the target for minimization in the iteration algorithm. Results are presented in Figure 5-17. The envelope at high speed is steadily at approximately 300 kW. This is due to the ability of the machine to keep unity power factor at high speed. This ability is achieved by following the field current criterion introduced in (5-16). The high efficiency area is successfully set at high speed but low torque region, which is the mostly used condition as described in Figure 5-5.

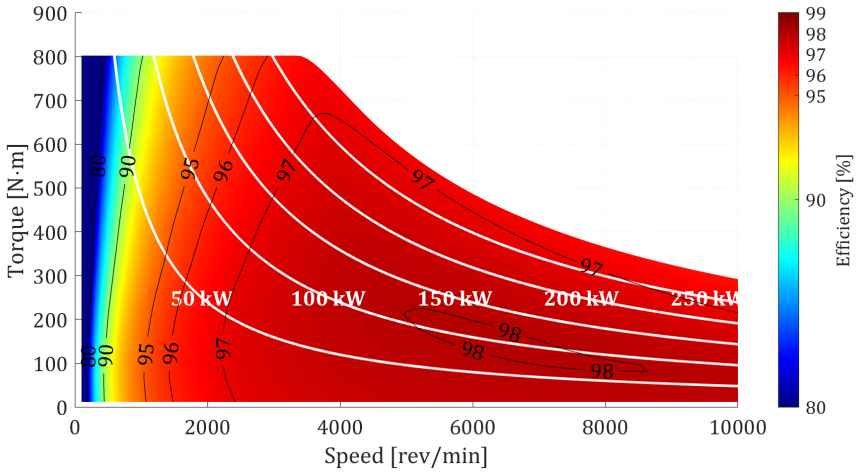

Figure 5-17 Efficiency map of the 800 V 250 kW EESM at torque-speed coordinates considering only copper losses and iron losses.

D. Performance in Test Cycles

The machine performance is evaluated in CHTC-TT. The results are presented in Figure 5-18. The difference between input and output power are minor. This is due to that, in CHTC-TT the truck mostly runs at high speed but low torque, which fits exactly the high efficiency area in Figure 5-17. The copper losses are generally higher than iron-core losses during acceleration and deceleration when high level of torque is demanded. In contrast, when the vehicle runs steadily at almost constant speed, the torque demand is low, and the copper losses are at a similar level of iron-core losses. Balance of the two is a well-known rule of thumb to achieve high efficiency of machine design, and this is how good efficiency is achieved here.

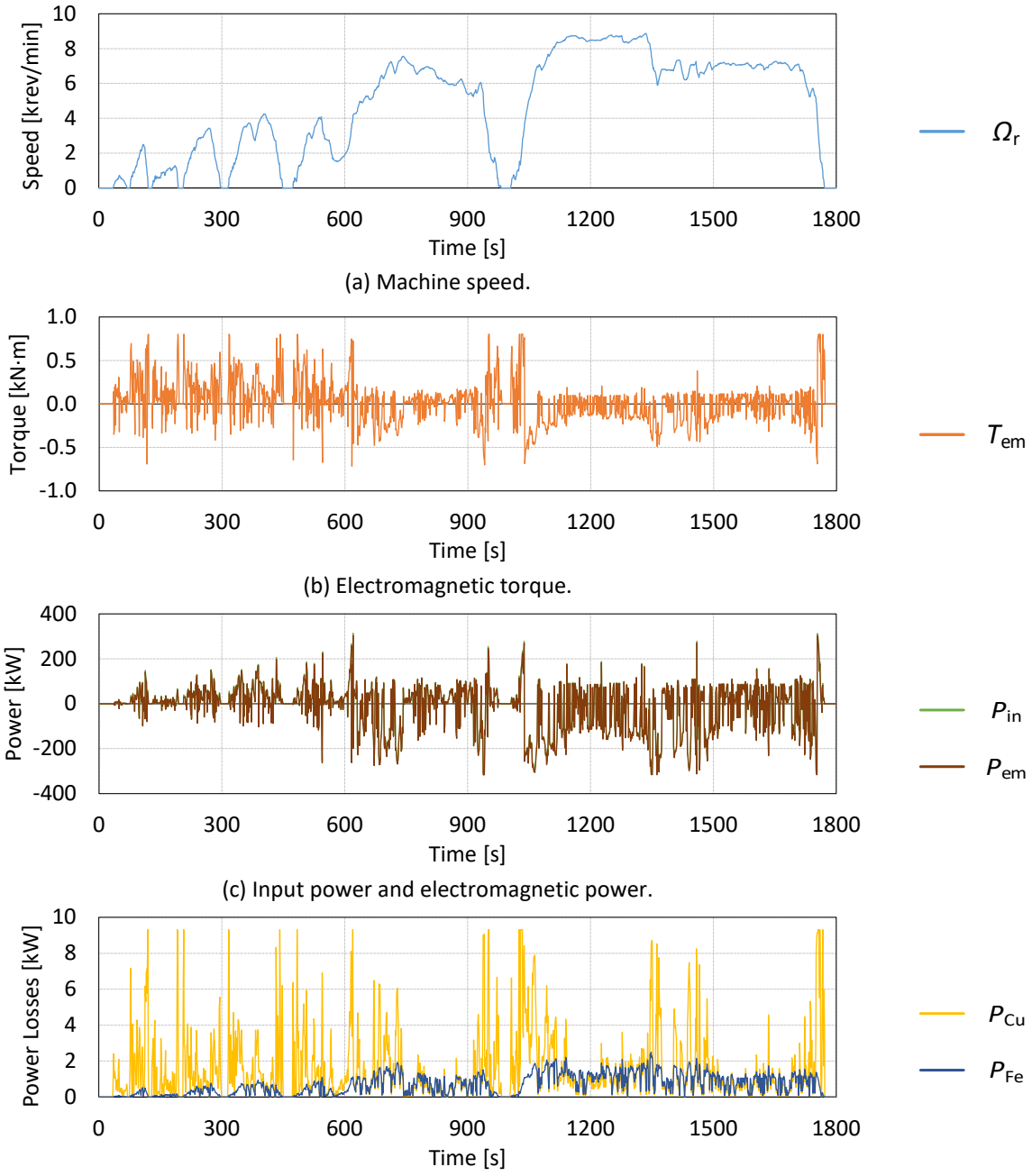

(a) Machine speed.

(b) Electromagnetic torque.

(c) Input power and electromagnetic power.

(d) Copper and iron-core losses.

Figure 5-18 Performance of the 800 V 250 kW EESM evaluated in CHTC-TT.

Chapter 6

High-Frequency Brushless Excitation

High-frequency brushless excitation is developed to avoid friction losses due to brushes and sliprings. The topology using an isolated H-bridge converter is discussed in Section 6.1, which consists of characteristics study, estimation of field current and closed-loop control. In Section 6.2, another topology using switching harmonics is introduced. The switching harmonics are extracted through a resonance circuit and used for field excitation.

6.1 Excitation Using Isolated H-Bridge Converter

The electrical quantities of the system are described in Figure 6-1. The reason to have a capacitor across the field winding is to avoid high-frequency oscillations between the transformer leakage inductance and the diode stray capacitance [64].

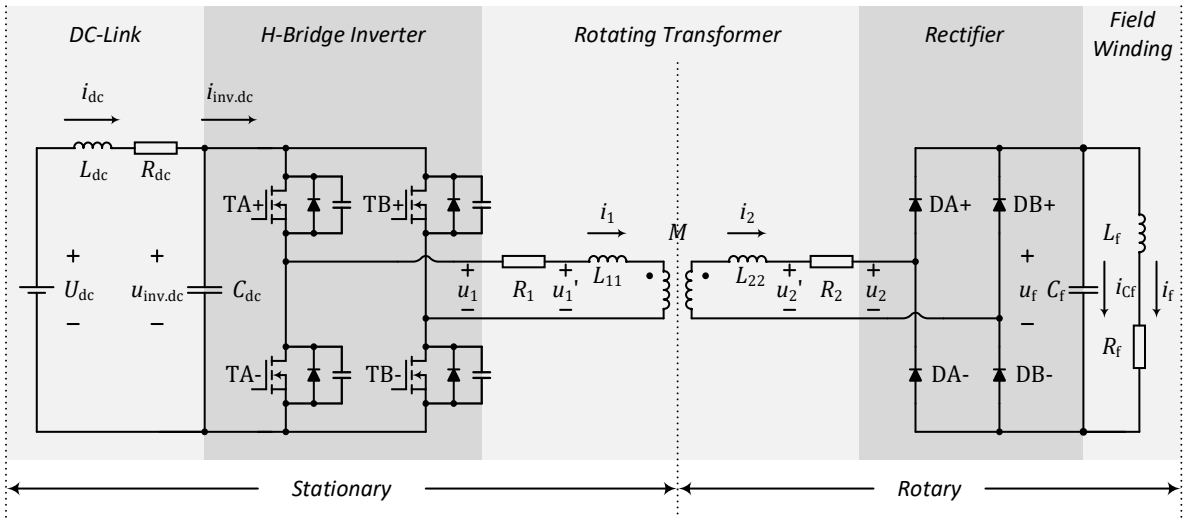

Figure 6-1 Schematic of wireless excitation system dynamic model.

6.1.1 Steady State Modeling

In steady state modeling, the relation between the input and output is characterized. The output power equals the input power times the efficiency

$$U_{\mathrm{dc}} \cdot I_{\mathrm{dc}} \cdot \eta_{\mathrm{tot}} = P_{\mathrm{dc}} \cdot \eta_{\mathrm{tot}} = P_{\mathrm{f}} = I_{\mathrm{f}}^2 \cdot R_{\mathrm{f}} \tag{6-1}$$

where U_{dc} is the dc-link voltage, I_{dc} is the dc-link current, η_{tot} is the total efficiency, P_{dc} is the dc-link input power and P_{f} is the field winding output power. Therefore, the dc-link current is proportional to the square of the field current, by assuming an almost constant efficiency

$$I_{\mathrm{dc}} = \frac{R_{\mathrm{f}}}{U_{\mathrm{dc}} \cdot \eta_{\mathrm{tot}}} \cdot I_{\mathrm{f}}^2 \tag{6-2}$$

Due to the limitation of space and the centrifugal force during the rotation, it is not possible to place a C_f high enough to keep the field voltage as a pure DC quantity. Hence the field winding is neither in a voltage-stiff case nor in a current-still case, but somewhere in the between. It is therefore not straight forward to derive the waveforms analytically. However, an analytical solution roughly showing the relationship between the duty cycle and the field current can still be derived by considering the fundamental component [66]. The amplitude of the fundamental component of the inverter output voltage is

$$U_{1\cdot\mathrm{amp}} = \frac{4}{\pi} \cdot U_\mathrm{dc} \cdot \sin\left(\frac{\pi}{2} d\right) \tag{6-3}$$

where d is the duty cycle of the H-bridge inverter. Assuming lossless, and considering only the fundamental component, the mean absolute value of the fundamental component on the secondary side of the transformer becomes the field voltage and the field current can therefore be calculated as

$$I_\mathrm{f} = \frac{U_\mathrm{f}}{R_\mathrm{f}} = \frac{2}{\pi} \cdot \frac{N_2}{N_1} \cdot \frac{U_{1\cdot\mathrm{amp}}}{R_\mathrm{f}} = \frac{8}{\pi^2} \cdot \frac{N_2}{N_1} \cdot \frac{U_\mathrm{dc}}{R_\mathrm{f}} \cdot \sin\left(\frac{\pi}{2} d\right) \tag{6-4}$$

where N_1 is the number of turns of the primary winding and N_2 is the number of turns of the secondary winding. This expression means the I_f curve is in the shape of $\sin\left(\frac{\pi}{2} d\right)$. And the dc-link current can therefore be calculated by substituting (6-4)(6-16) into (6-2)

$$I_\mathrm{dc} = \frac{32}{\pi^4} \cdot \frac{N_2^2}{N_1^2} \cdot \frac{U_\mathrm{dc}}{R_\mathrm{f}} \cdot \frac{1 - \cos(\pi d)}{\eta_\mathrm{tot}} \tag{6-5}$$

which means the I_dc curve is in the shape of $[1 - \cos(\pi d)]$. Define a characteristic current

$$I_\mathrm{char} = \frac{N_2^2}{N_1^2} \cdot \frac{U_\mathrm{dc}}{R_\mathrm{f}} \tag{6-6}$$

then the ratio of $\frac{I_\mathrm{dc}}{I_\mathrm{char}}$ and $\frac{I_\mathrm{f}}{I_\mathrm{char}}$ are plotted in Figure 6-2, assuming $N_1 = N_2$ and $\eta_\mathrm{tot} = 100\%$.

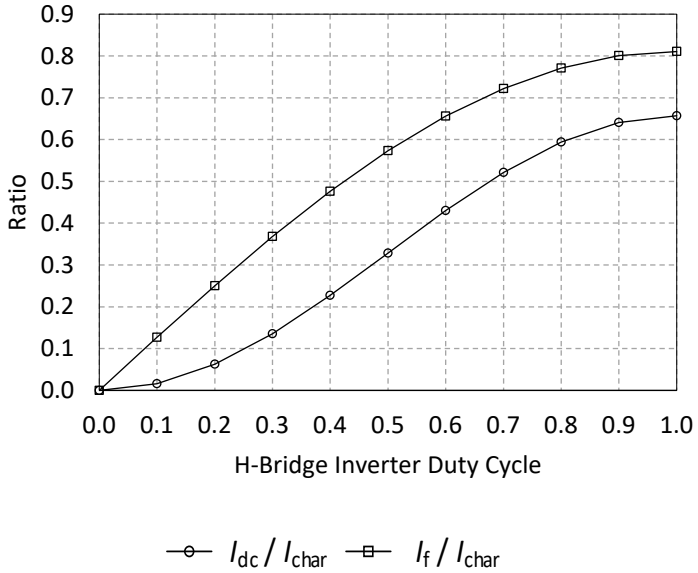

Figure 6-2 Ratios of $\frac{I_\mathrm{dc}}{I_\mathrm{char}}$ and $\frac{I_\mathrm{f}}{I_\mathrm{char}}$.

6.1.2 Dynamic Modeling

To develop a reliable and modular dynamic model of the excitation system, the system is decomposed into several modules, dc-link, H-bridge inverter, transformer, rectifier and field winding, as shown in Figure 6-1. Each part can be described by a few differential equations or arithmetic equations. Necessary simplifications are introduced without sacrificing the accuracy too much, e.g. the diodes are described by a threshold voltage and an equivalent resistance. In some parts of the system, the circuit is nonlinear, and a few criteria are needed to judge the operation modes of the circuit. The judgement of the circuit modes is developed based on the physical understanding of the circuit, similar as in [67]. This simplifies calculation and reduces computation time.

In Figure 6-1, U_{dc} and i_{dc} are the voltage and current of the dc power source; R_{dc}, L_{dc} and C_{dc} are the dc-link resistance, inductance and capacitance respectively; $u_{\mathrm{inv.dc}}$ is the dc-link capacitor bank voltage, $i_{\mathrm{inv.dc}}$ is the dc-link current going to the switches; u_1 and u_2 are the transformer primary and secondary side terminal voltages, i_1 and i_2 are the transformer primary and secondary side currents, u_1' and u_2' are the transformer primary and secondary side voltages without resistive voltage drop; R_1 and R_2 are primary and secondary side resistances, L_{11} and L_{22} are primary and secondary side self-inductance, M is the mutual-inductance; R_{f}, L_{f} and C_{f} are the field winding resistance, inductance and capacitance respectively.

A. DC-Link

The dc-link inductance L_{dc} together with the dc-link capacitance C_{dc} are energy storage components and therefore the dc-link current, i_{dc} together with voltage across the capacitor, $u_{\mathrm{inv.dc}}$, are counted as states. The states can be described as

$$\begin{cases} \dfrac{di_{\mathrm{dc}}}{dt} = \dfrac{U_{\mathrm{dc}} - u_{\mathrm{inv.dc}} - R_{\mathrm{dc}} \cdot i_{\mathrm{dc}}}{L_{\mathrm{dc}}} \\ \dfrac{du_{\mathrm{inv.dc}}}{dt} = \dfrac{i_{\mathrm{dc}} - i_{\mathrm{inv.dc}}}{C_{\mathrm{dc}}} \end{cases} \tag{6-7}$$

Hence the current going into the inverter is considered as input to the model and is described as

$$i_{\mathrm{inv.dc}} = i_1 \cdot (s_{\mathrm{TA+}} - s_{\mathrm{TB+}}) \tag{6-8}$$

where i_1 denotes the output current of the inverter, s denotes the switching signal of the MOSFETs: $s = 0$ means off and $s = 1$ means on. When the upper switch is on, then the bottom is off simultaneously and vice versa. Apart from that, blanking time is also implemented, when the two switches are off simultaneously for a short while to prevent any shoot-circuit of dc-link.

B. H-Bridge Inverter

The dc-link capacitor voltage and transformer current are the inputs, whereas the transformer input voltage is the output of this module. The inverter is composed by two phases, A and B, and the voltage of each leg $u_{\mathrm{inv.A}}$ and $u_{\mathrm{inv.B}}$ can be described as

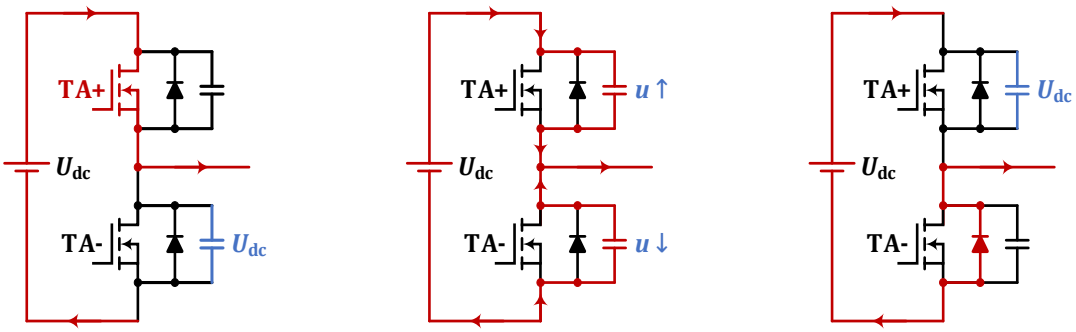

(a) Before charging. (b) During charging. (c) After charging.

Figure 6-3 Charging and discharging of drain-source capacitances during blanking time.

$$u_{\text{inv.A}} = \begin{cases} \frac{u_{\text{inv.dc}}}{2} - R_{\text{ds}} \cdot i_1 & s_{\text{TA+}} = 1 \quad s_{\text{TA-}} = 0 \\ R_{\text{ds}} \cdot i_1 - \frac{u_{\text{inv.dc}}}{2} & s_{\text{TA+}} = 0 \quad s_{\text{TA-}} = 1 \end{cases} \tag{6-9}$$

$$u_{\text{inv.B}} = \begin{cases} \frac{u_{\text{inv.dc}}}{2} - R_{\text{ds}} \cdot i_1 & s_{\text{TB+}} = 1 \quad s_{\text{TB-}} = 0 \\ R_{\text{ds}} \cdot i_1 - \frac{u_{\text{inv.dc}}}{2} & s_{\text{TB+}} = 0 \quad s_{\text{TB-}} = 1 \end{cases} \tag{6-10}$$

where R_{ds} is the drain-source resistance of the MOSFET. Then, the inverter output voltage u_1 is the difference between the outputs of Phase A and B

$$u_1 = u_{\text{inv.A}} - u_{\text{inv.B}} \tag{6-11}$$

During blanking time, the drain-source capacitance of each MOSFET, C_{ds}, charges and discharges, as illustrated in Figure 6-3. Before the blanking interval starts, as shown in (a), the upper leg conducts, and the lower leg capacitance is charged to U_{dc}. When the blanking interval starts, as shown in (b), both upper and lower switch are off, but the current needs to continue flowing due to the inductance of the transformer. The lower leg diode cannot conduct immediately since the voltage across it is at U_{dc}. Therefore, a discharging process of the lower leg capacitance voltage commences. The sum of the upper and lower leg capacitance voltage should be at U_{dc}, so the discharging of the lower leg capacitance happens together with the charging of the upper leg capacitance. This continues until the charging and discharging completes as shown in (c). Thereafter, the lower leg diode takes all the current. The charging and discharging process can be described as

$$\begin{aligned} C_{\text{ds}} \frac{du_{\text{A+}}}{dt} &= i_{\text{A+}} \quad , \quad C_{\text{ds}} \frac{du_{\text{B+}}}{dt} = i_{\text{B+}} \\ C_{\text{ds}} \frac{du_{\text{A-}}}{dt} &= i_{\text{A-}} \quad , \quad C_{\text{ds}} \frac{du_{\text{B-}}}{dt} = i_{\text{B-}} \end{aligned} \tag{6-12}$$

where C_{ds} is the drain-source capacitance of each MOSFET, $u_{\text{A+}}$, $u_{\text{A-}}$, $u_{\text{B+}}$ and $u_{\text{B-}}$ are the voltages across the upper leg of Phase A, lower leg of Phase A, upper leg of Phase B, lower leg of Phase B respectively, and $i_{\text{A+}}$, $i_{\text{A-}}$, $i_{\text{B+}}$ and $i_{\text{B-}}$ are the currents through the upper leg of Phase A, lower leg of Phase A, upper leg of Phase B, lower leg of Phase B respectively. The constraints during the charging and discharging process can be described as

$$u_{\text{A+}} + u_{\text{A-}} = u_{\text{inv.dc}} = u_{\text{B+}} + u_{\text{B-}} \tag{6-13}$$

Therefore, from (6-12) and (6-13),

$$i_{\mathrm{A+}} + i_{\mathrm{A-}} = C_{\mathrm{ds}} \frac{du_{\mathrm{A+}}}{dt} + C_{\mathrm{ds}} \frac{du_{\mathrm{A-}}}{dt} = C_{\mathrm{ds}} \frac{d(u_{\mathrm{A+}} + u_{\mathrm{A-}})}{dt} = C_{\mathrm{ds}} \frac{du_{\mathrm{inv.dc}}}{dt} \quad (6\text{-}14)$$

$$i_{\mathrm{B+}} + i_{\mathrm{B-}} = C_{\mathrm{ds}} \frac{du_{\mathrm{B+}}}{dt} + C_{\mathrm{ds}} \frac{du_{\mathrm{B-}}}{dt} = C_{\mathrm{ds}} \frac{d(u_{\mathrm{B+}} + u_{\mathrm{B-}})}{dt} = C_{\mathrm{ds}} \frac{du_{\mathrm{inv.dc}}}{dt} \quad (6\text{-}15)$$

Since,

$$i_{\mathrm{A+}} - i_{\mathrm{A-}} = i_1 = i_{\mathrm{B-}} - i_{\mathrm{B+}} \quad (6\text{-}16)$$

from (6-14), (6-15) and (6-16), it can be concluded that

$$i_{\mathrm{A+}} = i_{\mathrm{B-}} = \frac{C_{\mathrm{ds}} \frac{du_{\mathrm{inv.dc}}}{dt} + i_1}{2} \quad (6\text{-}17)$$

$$i_{\mathrm{B+}} = i_{\mathrm{A-}} = \frac{C_{\mathrm{ds}} \frac{du_{\mathrm{inv.dc}}}{dt} - i_1}{2} \quad (6\text{-}18)$$

The voltage derivatives can therefore be solved as

$$\frac{du_{\mathrm{inv.A}}}{dt} = \frac{du_{\mathrm{A-}}}{dt} = \frac{i_{\mathrm{A-}}}{C_{\mathrm{ds}}} = \frac{\frac{du_{\mathrm{inv.dc}}}{dt} - \frac{i_1}{C_{\mathrm{ds}}}}{2} \approx -\frac{1}{2}\frac{i_1}{C_{\mathrm{ds}}} \quad (6\text{-}19)$$

$$\frac{du_{\mathrm{inv.B}}}{dt} = \frac{du_{\mathrm{B-}}}{dt} = \frac{i_{\mathrm{B-}}}{C_{\mathrm{ds}}} = \frac{\frac{du_{\mathrm{inv.dc}}}{dt} + \frac{i_1}{C_{\mathrm{ds}}}}{2} \approx \frac{1}{2}\frac{i_1}{C_{\mathrm{ds}}} \quad (6\text{-}20)$$

The approximation "≈" is valid when the dc-link capacitance is big enough so that $u_{\mathrm{inv.dc}}$ is with almost no fluctuation. With (6-19) and (6-20), $u_{\mathrm{inv.A}}$ and $u_{\mathrm{inv.B}}$ can be obtained by take integrations of $-\frac{1}{2}\frac{i_1}{C_{\mathrm{ds}}}$ and $\frac{1}{2}\frac{i_1}{C_{\mathrm{ds}}}$ respectively. And this charging or discharging process continues until the anti-parallel diodes of the MOSFETs are forward-biased. Thereafter,

$$u_{\mathrm{inv.A}} = \begin{cases} -\frac{u_{\mathrm{inv.dc}}}{2} - V_{\mathrm{F.inv}} & i_1 > 0 \\ \frac{u_{\mathrm{inv.dc}}}{2} + V_{\mathrm{F.inv}} & i_1 < 0 \end{cases} \quad (6\text{-}21)$$

$$u_{\mathrm{inv.B}} = \begin{cases} \frac{u_{\mathrm{inv.dc}}}{2} + V_{\mathrm{F.inv}} & i_1 > 0 \\ -\frac{u_{\mathrm{inv.dc}}}{2} - V_{\mathrm{F.inv}} & i_1 < 0 \end{cases} \quad (6\text{-}22)$$

C. Rotating Transformer

The transformer terminal voltages are considered as the input whereas the transformer currents are considered as the outputs. The transformer can be described as

$$u_1' = L_{11} \cdot \frac{di_1}{dt} - M \cdot \frac{di_2}{dt} \quad , \quad u_2' = M \cdot \frac{di_1}{dt} - L_{22} \cdot \frac{di_2}{dt} \quad (6\text{-}23)$$

where u_1' and u_2' are the voltage drops across the transformer inductances only, i.e. they are equal to the terminal voltage u_1 and u_2 compensated by the voltage drops across the resistances $R_1 \cdot i_1$ and $R_2 \cdot i_2$

$$u_1' = (u_1 - R_1 \cdot i_1) \quad , \quad u_2' = (u_2 + R_2 \cdot i_2) \tag{6-24}$$

The current derivatives can therefore be described as

$$\frac{di_1}{dt} = -\frac{L_{22}}{M^2 - L_{11}L_{22}} u_1' + \frac{M}{M^2 - L_{11}L_{22}} u_2' \tag{6-25}$$

$$\frac{di_2}{dt} = -\frac{M}{M^2 - L_{22}L_{11}} u_1' + \frac{L_{11}}{M^2 - L_{22}L_{11}} u_2' \tag{6-26}$$

D. Rectifier

In this module, the transformer secondary current, field voltage and current are the inputs whereas rectifier capacitor current and transformer secondary voltage are the outputs. The rectifier has two operation modes, the power transferring mode when two diodes in diagonal positions conduct, as shown in Figure 6-4 (a) and (b), and the commutation mode when all the four diodes conduct, as shown in Figure 6-4 (c). The method to decide the mode of a circuit is given at the end of this section.

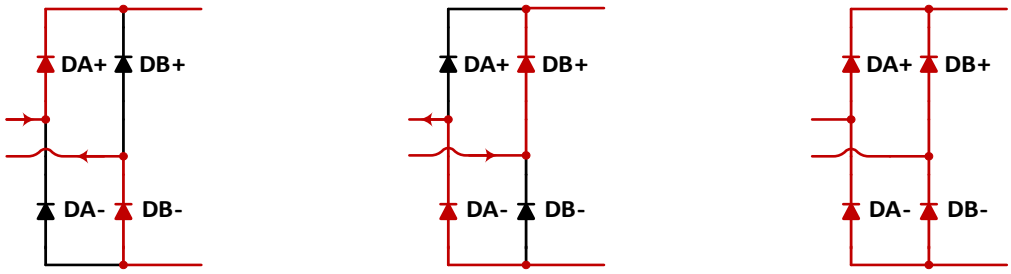

(a) Power transferring ($i_2 > 0$). (b) Power transferring ($i_2 < 0$). (c) Commutation.

Figure 6-4 Power transferring mode and commutation mode.

During power transferring mode, there are two cases depending on the direction of the transformer current. In case $i_2 > 0$, as shown in subplot (a), i_2 is divided into the rectifier output capacitor current and the field current

$$i_{C_f} + i_f - i_2 = 0 \tag{6-27}$$

whereas in case $i_2 < 0$, as shown in subplot (b), the transformer current i_2, the rectifier output capacitor and the field current add up to be zero

$$i_{C_f} + i_f + i_2 = 0 \tag{6-28}$$

To sum up, (6-27) and (6-28) can be expressed as

$$i_{C_f} = |i_2| - i_f \tag{6-29}$$

In addition, the transformer secondary voltage u_2 is decided by the field voltage and the diode forward voltage drop

$$u_2 = \text{sign}(i_2) \cdot (u_f + 2 \cdot u_D) = \text{sign}(i_2) \cdot [u_f + 2 \cdot (V_{F0} + R_d \cdot |i_2|)] \tag{6-30}$$

where

$$u_{\mathrm{D}} = V_{\mathrm{F0}} + R_{\mathrm{d}} \cdot |i_2| \tag{6-31}$$

And, in case the capacitance is quite small, the field voltage will drop to a value that all the four diodes are forward-biased. Then it comes to the commutation mode, as shown in subplot (c), during which, the current through Leg A can be described as

$$i_{\mathrm{DA+}} - i_{\mathrm{DA-}} = i_2 \tag{6-32}$$

And the voltage can be described as

$$0 = u_{\mathrm{f}} + u_{\mathrm{DA+}} + u_{\mathrm{DA-}} \tag{6-33}$$

where $u_{\mathrm{DA+}}$ and $u_{\mathrm{DA-}}$ can be described by the approximated model of diodes

$$u_{\mathrm{DA+}} = V_{\mathrm{F0}} + R_{\mathrm{s}} \cdot i_{\mathrm{DA+}} \tag{6-34}$$

$$u_{\mathrm{DA-}} = V_{\mathrm{F0}} + R_{\mathrm{s}} \cdot i_{\mathrm{DA-}} \tag{6-35}$$

Then from (6-33), (6-34) and (6-35), it yields

$$i_{\mathrm{DA+}} + i_{\mathrm{DA-}} = -\frac{u_{\mathrm{f}} + 2 \cdot V_{\mathrm{F0}}}{R_{\mathrm{s}}} \tag{6-36}$$

Thereafter, from (6-32) and (6-36), $i_{\mathrm{DA+}}$ and $i_{\mathrm{DA-}}$ can be solved

$$i_{\mathrm{DA+}} = \frac{-\frac{u_{\mathrm{f}} + 2 \cdot V_{\mathrm{F0}}}{R_{\mathrm{d}}} + i_2}{2} \tag{6-37}$$

$$i_{\mathrm{DA-}} = \frac{-\frac{u_{\mathrm{f}} + 2 \cdot V_{\mathrm{F0}}}{R_{\mathrm{d}}} - i_2}{2} \tag{6-38}$$

The voltage drop across each diode can therefore be decided by the diode current

$$u_{\mathrm{DA+}} = V_{\mathrm{F0}} + R_{\mathrm{d}} \cdot i_{\mathrm{DA+}} \tag{6-39}$$

$$u_{\mathrm{DA-}} = V_{\mathrm{F0}} + R_{\mathrm{d}} \cdot i_{\mathrm{DA-}} \tag{6-40}$$

Similarly, $i_{\mathrm{DB+}}$, $i_{\mathrm{DB-}}$, $u_{\mathrm{DB+}}$ and $u_{\mathrm{DB-}}$ can be solved

$$i_{\mathrm{DB+}} = \frac{-\frac{u_{\mathrm{f}} + 2 \cdot V_{\mathrm{F0}}}{R_{\mathrm{d}}} - i_2}{2} = i_{\mathrm{DA-}} \tag{6-41}$$

$$i_{\mathrm{DB-}} = \frac{-\frac{u_{\mathrm{f}} + 2 \cdot V_{\mathrm{F0}}}{R_{\mathrm{d}}} + i_2}{2} = i_{\mathrm{DA+}} \tag{6-42}$$

$$u_{\mathrm{DB+}} = V_{\mathrm{F0}} + R_{\mathrm{d}} \cdot i_{\mathrm{DB+}} = u_{\mathrm{DA-}} \tag{6-43}$$

$$u_{\mathrm{DB-}} = V_{\mathrm{F0}} + R_{\mathrm{d}} \cdot i_{\mathrm{DB-}} = u_{\mathrm{DA+}} \tag{6-44}$$

In the end, the transformer secondary voltage and the capacitor current can be decided

$$u_2 = u_{\mathrm{DA-}} - u_{\mathrm{DB-}} = u_{\mathrm{DA-}} - u_{\mathrm{DA+}} \tag{6-45}$$

$$i_{C_\mathrm{f}} = i_{\mathrm{DA+}} + i_{\mathrm{DB+}} - i_\mathrm{f} = i_{\mathrm{DA+}} + i_{\mathrm{DA-}} - i_\mathrm{f} \tag{6-46}$$

As for the transition between the two modes, it can be firstly assumed that the circuit is in commutation mode, in which, $i_{\mathrm{DA+}}$ and $i_{\mathrm{DA-}}$ can be calculated using (6-37) and (6-38). If both $i_{\mathrm{DA+}}$ and $i_{\mathrm{DA-}}$ are positive, then the circuit is really in commutation mode. Otherwise, the circuit is in the power transferring mode.

E. Field Winding

The field winding is modeled by field winding resistance R_f, inductance L_f, as well as filter output capacitance C_f. The input is the capacitor current i_{C_f} and the outputs are the field voltage u_f and current i_{L_f}

$$\frac{du_\mathrm{f}}{dt} = \frac{i_{C_\mathrm{f}}}{C_\mathrm{f}} \quad , \quad \frac{di_{L_\mathrm{f}}}{dt} = \frac{u_\mathrm{f} - R_{\mathrm{f.T}} \cdot i_{L_\mathrm{f}}}{L_\mathrm{f}} \tag{6-47}$$

where $R_{\mathrm{f.T}}$ is the temperature corrected field resistance. The field resistance at temperature T is scaled from the resistance at temperature 20℃

$$R_{\mathrm{f.T}} = R_{\mathrm{f.20℃}} \cdot [1 + \alpha_{\mathrm{Cu}} \cdot (T - 20)] \tag{6-48}$$

where α_{Cu} is the temperature coefficient of resistivity of copper.

6.1.3 Phase-Shift Control

In phase-shift control, each phase is 50% pull-up and 50% pull-down. And it is the phase-shift between the two phases that decides the output voltage. In case of an inductive load, the current waveform becomes trapezoid. The waveforms are illustrated in Figure 6-5. u_A and u_B are the output voltage from Leg A and B respectively, u_AB is the voltage difference in the between, i is the output current and U_dc is the dc-link voltage. As can be noticed, by changing the phase-shift between u_A and u_B, the output voltage can be adjusted as well as the output current.

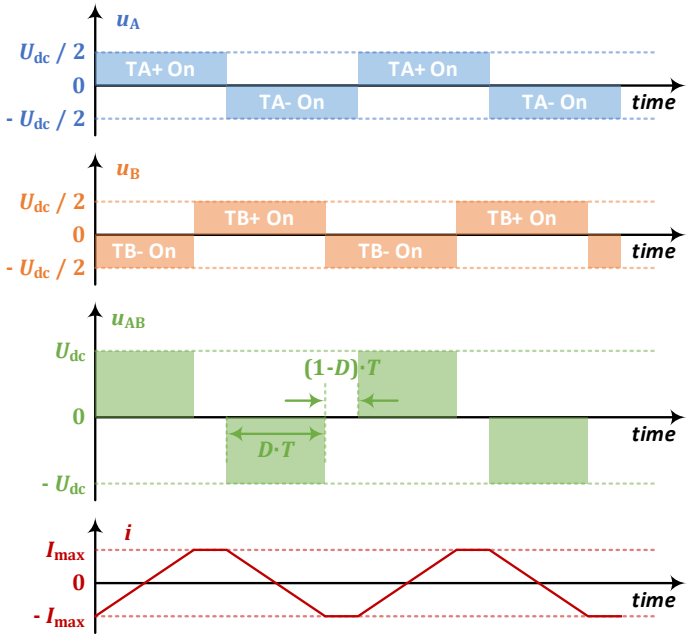

Figure 6-5 Phase-Shift control of H-bridge inverter.

The harmonics of the voltage waveform u_{AB} can be calculated by Fourier transform, from which

$$\frac{U_{h\cdot\mathrm{amp}}}{U_{\mathrm{dc}}} = \frac{4}{\pi \cdot h} \cdot \sin\left(h \cdot \frac{D \cdot \pi}{2}\right) \tag{6-49}$$

where h means the harmonic order and D means the duty cycle. The total rms of all harmonic contents can be formulated as

$$V_{\mathrm{tot\cdot rms}} = \sqrt{\frac{2}{T} \cdot V_{\mathrm{d}}^2 \cdot D\frac{T}{2}} = \sqrt{D}V_{\mathrm{d}} \tag{6-50}$$

The total THD can be formulated as

$$THD_{\mathrm{v}} = \frac{\sqrt{V_{\mathrm{rms}}^2 - V_{1\cdot\mathrm{rms}}^2}}{V_{1\cdot\mathrm{rms}}} \tag{6-51}$$

And this gives the lowest voltage THD of 0.290 at the duty cycle of 0.742. This can be noticed in Figure 6-6 where the harmonic distribution, the sum of all the harmonics as well as the voltage THD with respect to duty cycle are shown.

For the trapezoid current waveform, the rms value can be calculated by combining the triangular part and the flat part:

$$I_{\mathrm{rms}} = \sqrt{\frac{1}{T} \cdot \int_0^T i(t)^2 \mathrm{d}t} = \sqrt{\frac{2}{T} \cdot \int_0^{\frac{T}{2}} i(t)^2 \mathrm{d}t} = I_{\mathrm{max}}\sqrt{1 - \frac{2D}{3}} \tag{6-52}$$

And at $D = 0.742$

$$I_{\mathrm{rms}} = 0.711 \cdot I_{\mathrm{max}} \tag{6-53}$$

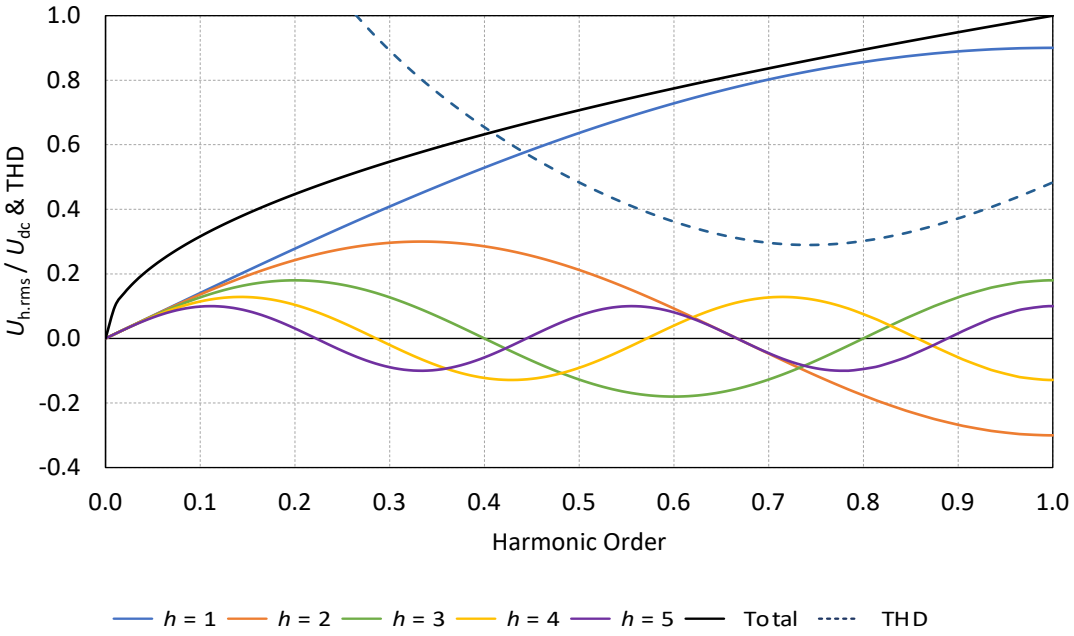

Figure 6-6 Harmonic distribution of phase-shift control.

6.1.4 Zero Voltage Switching

The phase-shift modulation technique is applied to generate the switching signals to achieve zero voltage switching (ZVS). The schematic to illustrate the idea of ZVS is shown in Figure 6-7. In plot (a), TA+ and TB- are on, and the output voltage from the inverter is U_{dc}. After a time interval of DT, the inverter is going to turn off TB- and turn on TB+ as shown in Figure 6-5. In plot (b), it shows the blanking time when TB- is turned off but TB+ is not turned on yet. During this time, the transformer inductance tries to keep current flowing. This current charges the drain-source capacitance of TB- and discharges the drain-source capacitance of TB+. After the charging and discharging complete, the drain-source voltage of TB+ goes to zero and the diode of TB+ conducts, as shown in plot (c). In the end, the TB+ is turned on as shown in (d), and during the turn-on process, the drain-source voltage is always zero and this gives no switching loss.

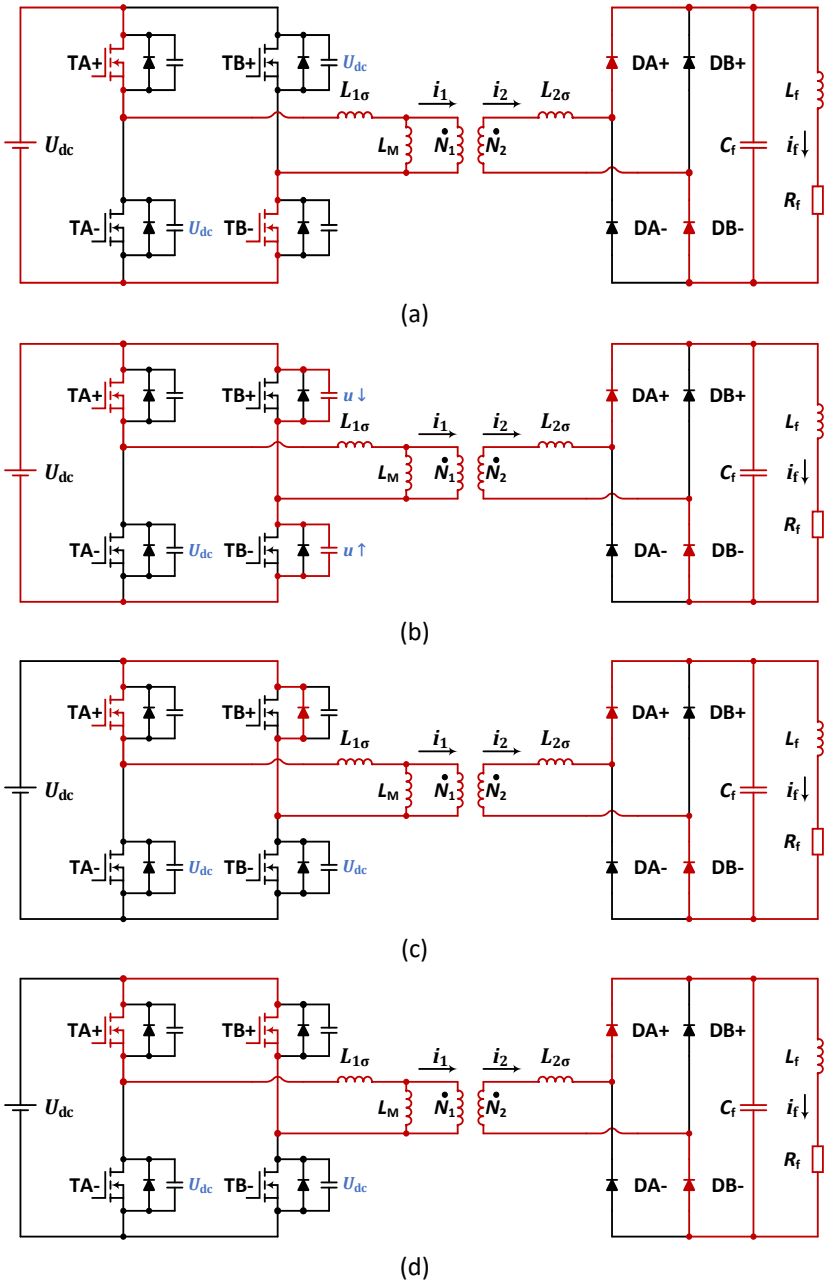

Figure 6-7 Schematic of ZVS in the H-bridge converter for field excitation.

Based on the mechanism of ZVS described above, two criteria can be concluded to determine ZVS. Firstly, the inductive energy storage in the transformer is larger than the capacitive energy storage in the parasitic capacitance of the switches, i.e.

$$\frac{1}{2} \cdot L_\sigma \cdot I^2 > \frac{1}{2} \cdot C_{\mathrm{ds.eq}} \cdot {U_{\mathrm{dc}}}^2 \tag{6-54}$$

where $C_{\mathrm{ds.eq}}$ is the equivalent drain-source capacitance, formulated as

$$C_{\mathrm{ds.eq}} = 2 \cdot \frac{4}{3} \cdot C_{\mathrm{oss}} = \frac{8}{3} \cdot C_{\mathrm{oss}} \tag{6-55}$$

The parameter C_{oss} can be found in the datasheet of the semiconductor switch. Since there are two drain-source capacitance in the loop, there comes the factor of 2, and $\frac{4}{3}$ is to estimate the C_{oss} at higher voltage than the condition mentioned in the datasheet [68].

The second criterion is that the blanking time is long enough for the energy to transfer from the inductance to the capacitance. The capacitance $C_{\mathrm{ds.eq}}$ and the inductance L_σ forms an LC circuit which gives a resonance frequency as

$$\omega_{\mathrm{ZVS}} = \frac{1}{\sqrt{L_\sigma \cdot C_{\mathrm{ds.eq}}}} \tag{6-56}$$

And in order to guarantee the discharging of TB+ is complete, the blanking time should be at least 1/4 of the resonance period, i.e.

$$T_{\mathrm{blank}} \geq \frac{T_{\mathrm{ZVS}}}{4} = \frac{\pi}{2} \frac{1}{\omega_{\mathrm{ZVS}}} = \frac{\pi}{2} \cdot \sqrt{L_\sigma \cdot C_{\mathrm{ds.eq}}} \tag{6-57}$$

6.1.5 Commutation

Duty cycle loss due to commutation can be observed in H-bridge converter, where the duty cycle at the input of the rectifier is lower than the duty cycle at the output of the inverter. The explanation is given as illustrated in Figure 6-8. After TA+ and TB+ have been conducting as shown in Figure 6-7, TA+ turns off and TA- turns on. As a negative voltage is applied across the transformer, the current going through the transformer decreases. However, since the field current is kept constant by the field inductance, when the transformer current becomes lower than the field current, i.e. $|i_2| < i_{\mathrm{f}}$, the output capacitor C_{f} discharges to feed current into the field winding. In case C_{f} discharges completely, the sum of $i_{\mathrm{DA+}}$ and $i_{\mathrm{DB+}}$ must be equal to the field current, i.e. $i_{\mathrm{DA+}} + i_{\mathrm{DB+}} = i_{\mathrm{f}}$. Then the decrease of the transformer current to lower than i_{f}, i.e. $i_{\mathrm{DA+}} < i_{\mathrm{f}}$, must be compensated by introducing $i_{\mathrm{DB+}}$, which means that both DA+ and DB+ must conduct current at the same time as shown in (b). This further indicates that a short circuit of the secondary side of the transformer is introduced. Therefore, the output voltage of the transformer is clamped to zero by the short-circuit of the rectifier. The short-circuit remains until the transformer current reverses and reaches the field current level in (c). After that, the DB+ and DA- path can feed enough current to the field winding and that is when DA+ and DB- shut down and the short circuit disappears.

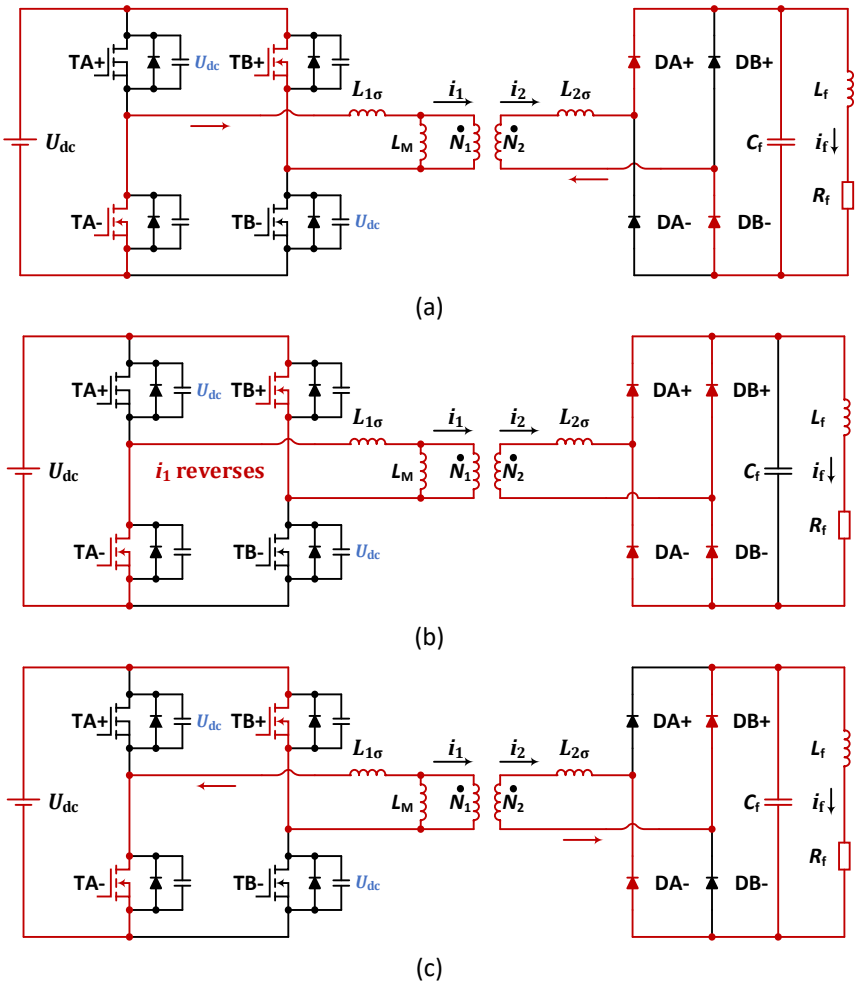

Figure 6-8 Duty cycle loss due to commutation in the H-bridge converter for field excitation.

The duty cycle loss reduces the power transfer from the primary side to the secondary side and is therefore definitely not preferable. The duration of the duty cycle loss depends on how fast the transformer current can be reversed. And during short circuit of the rectifier in (b),

$$\frac{di_1}{dt} = u_{\mathrm{dc}} / \left[L_{1\sigma} + L_{\mathrm{M}} // \left(\frac{N_1^2}{N_2^2} L_{2\sigma} \right) \right] \tag{6-58}$$

Hence a higher dc-link voltage and a lower leakage-inductance can give a quicker current reverse and therefore a shorter loss of duty cycle. However, a lower leakage-inductance means a lower energy storage in the inductance and due to the criteria of ZVS, a lower leakage-inductance will reduce the range of ZVS, i.e. ZVS cannot be achieved at a higher current level than in a higher self-inductance case. Hence one important issue to consider is the trade-off between the loss of duty cycle on the secondary side and the ZVS range [64].

6.1.6 Experimental Verification of Excitation System

A. Prototype

The H-bridge inverter and rectifier to excite the field are shown in Figure 6-9. In the H-bridge inverter prototype, switches in the same leg are placed close to each other to minimize the loop inductance. dc-link capacitors are placed close to the switches as well to damp the switching ringing. As for the driver circuit, a universal MOSFET driver PCB is designed. This circuit is suitable for both MOSFET power modules and discrete switches.

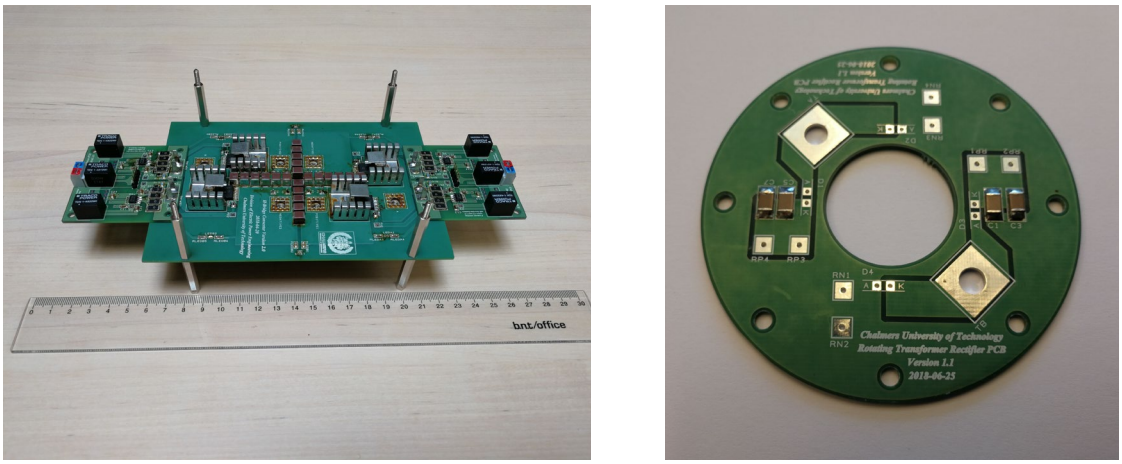

(a) H-bridge inverter. (b) Rectifier PCB.

Figure 6-9 Protype of the power electronic inverters for a 48 V EESM.

A protype of the rotating transformer is shown in Figure 6-10. The primary and secondary pot cores are identical. The inner side of the pot cores are covered with Kapton tape which provides galvanic isolation and dissipates heat from the copper winding. The windings are then molded with epoxy so that the windings, pot cores are together with aluminum case. The diodes of the rectifier are fixed to the back of the aluminum case. The legs of the diodes are bended 90^{o} and connected to the rectifier PCB. The rectifier PCB is attached to the back of the aluminum case.

The inductances of the transformer are dependent on the airgap and the relationship is shown in Figure 6-11. The coupling factor is defined as

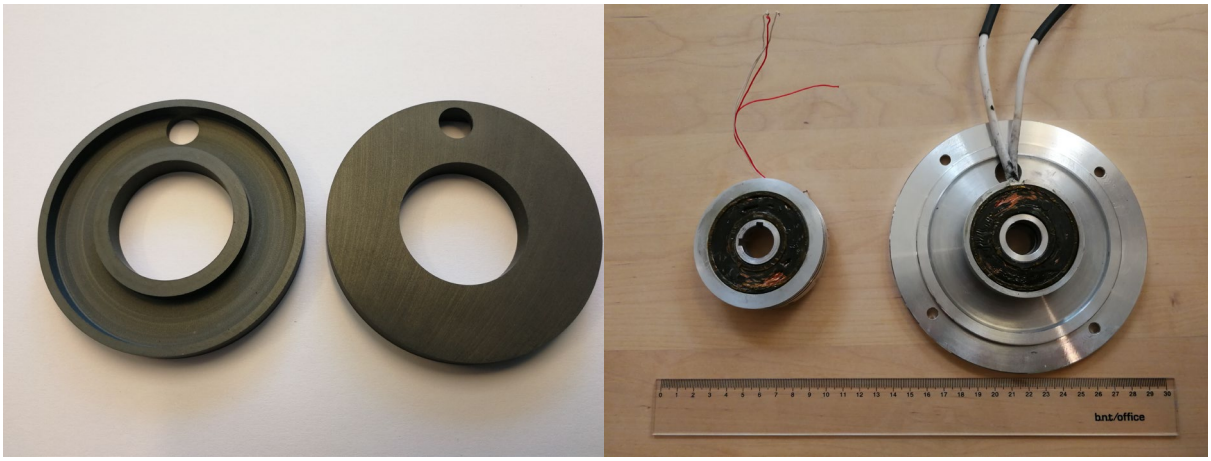

(a) Ferrite pot cores. (b) Rotating transformer.

Figure 6-10 Protype of the rotating transformer for a 48 V EESM.

$$k_{\text{coupling}} = \frac{M}{\sqrt{L_{11} \cdot L_{22}}} \tag{6-59}$$

The mutual inductances measured from both sides show some differences, and with a higher airgap, the difference becomes smaller. This is due to the difficulty of keeping the exact relative position of both transformer sides in different measurements. The total flux consists of mutual flux and leakage flux. For small airgaps, the mutual flux is the major part of the total flux. A minor change of relative position influences the mutual flux significantly. In contrast, for large airgaps, the mutual flux occupies a smaller portion of the total flux, which becomes not so sensitive to relative position change. Therefore, the difference in the mutual inductance measured from both sides becomes small. In the verification, the mean values of the measurements from both sides are used as the inputs of the simulations.

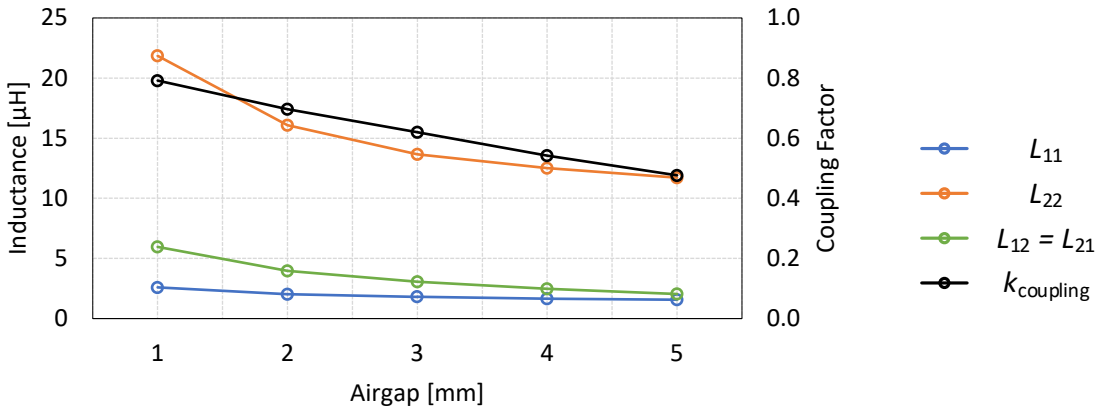

Figure 6-11 Inductances and coupling factor of the transformer with 1, 2, 3, 4 and 5 mm airgap.

With the protype manufactured, the modeling of the brushless excitation system is verified experimentally. The verifications include variations of four parameters, the dc-link voltage, the airgap, the rectifier output capacitance and the field winding resistance. The variations are introduced to make sure that model is commonly valid for this topology instead of being only valid for a special set of parameters. The verification towards field winding resistance is done by conducting experiments at different temperatures.

B. Transformer Airgap

The field current with respect to duty cycles in experiments and simulations with different airgaps are compared in Figure 6-12. The abbreviation “Sim” indicates “Simulation” while the abbreviation “Exp” indicates “Experiment”. The tests are carried out with 188 nF rectifier output capacitance, 60 V dc-link voltage and approximately 30°C winding temperature. The airgap varies from 1 to 5 mm with a step size of 1 mm. As can be noticed, the simulated results in general fit the experimental results, especially in the 3, 4 and 5 mm airgap cases. However, in the 1 and 2 mm cases, the measured field currents are slightly higher than the simulated ones, probably due to the measurement of mutual inductances. There are probably small differences in the coil alignment between the inductance measurement test and the power transferring test as explained before. As will be shown later in the parameter sensitivity study section, this difference may be due to a measurement error of mutual inductance of around 1.25%.

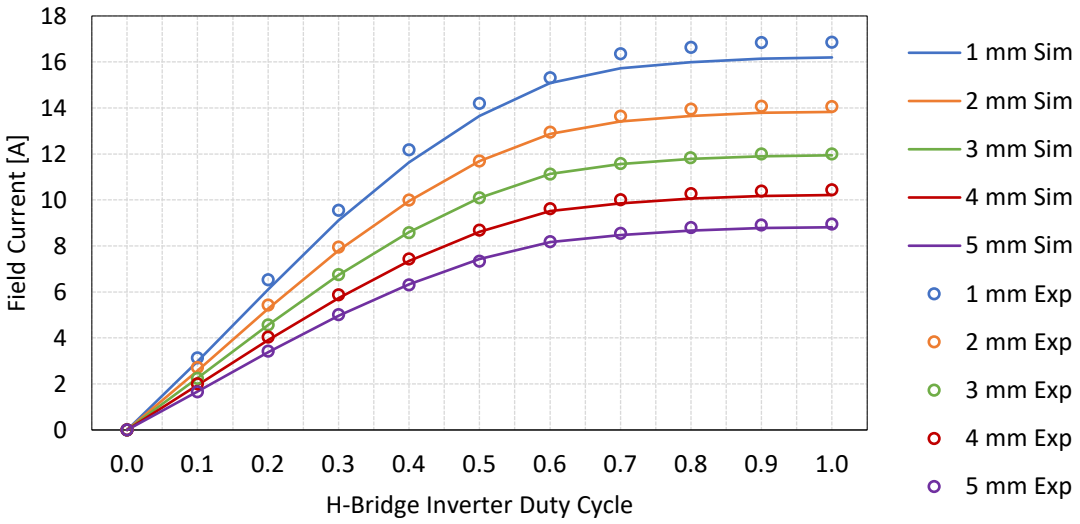

Figure 6-12 Field current against duty cycle with 1, 2, 3, 4 and 5 mm airgap, $C_{\mathrm{f}} = 188$ nF, $U_{\mathrm{dc}} = 60$ V, $T_{\mathrm{f}} = 30$°C.

C. DC-Link Voltage

The field current and dc-link current with respect to duty cycle in experiments and simulations with different dc-link voltages are compared in Figure 6-13 and Figure 6-14 respectively. The tests are carried out with 188 nF rectifier output capacitance, 1 mm airgap and around 30°C winding temperature. The dc-link voltage varies from 36 V to 60 V with a step size of 12 V. The simulated results in general fit the experimental results. The field current and the dc-link current are proportional to the dc-link voltage for all duty cycles. Apart from that, the dc-link current also shows a different profile than the field current, and the relationship between the two can be described by the power balance of the system. In steady state, the output power equals the input power times the efficiency. Assuming an almost constant efficiency, the dc-link current is proportional to the square of the field current as shown in (6-2). This explains why the field current curves between duty cycle 0.0 and 0.5 in Figure 6-12 are almost linear whereas the dc-link current curves seem to be parabolas in Figure 6-14.

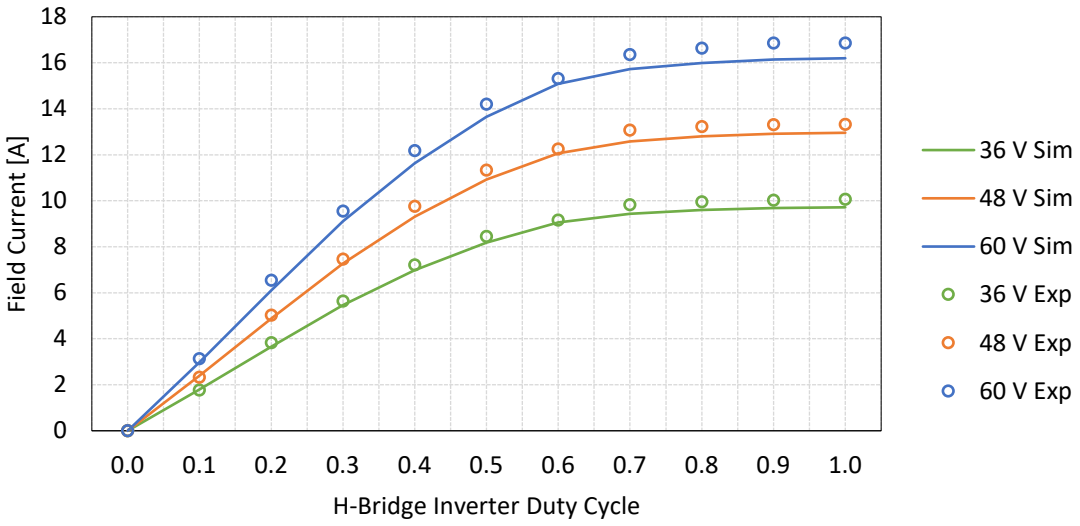

Figure 6-13 Field current against duty cycle with $U_{\mathrm{dc}} = 36, 48, 60$ V, 1 mm airgap, $C_{\mathrm{f}} = 188$ nF, $T_{\mathrm{f}} = 30$°C.

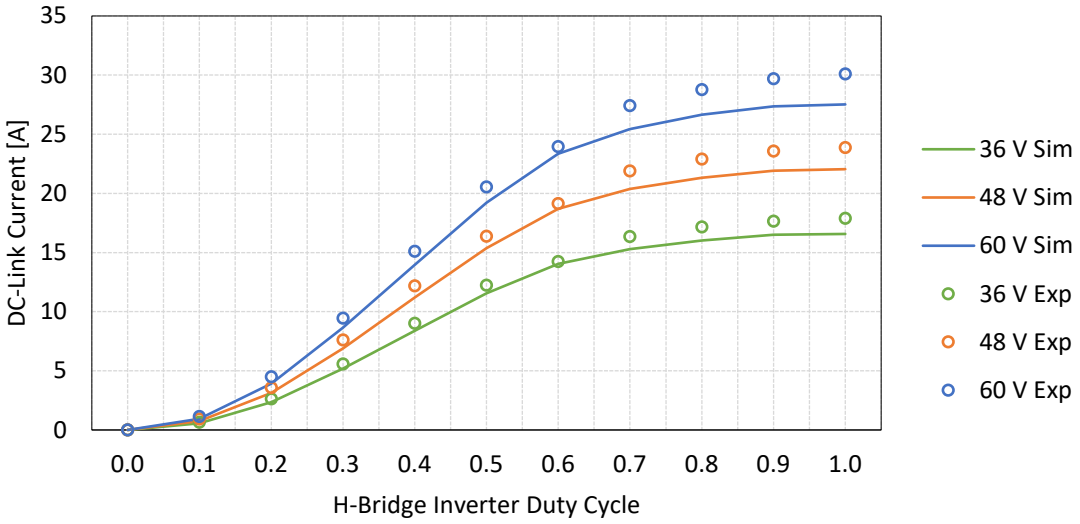

Figure 6-14 DC-link current against duty cycle with $U_{\mathrm{dc}} = 36, 48, 60$ V, 1 mm airgap, $C_{\mathrm{f}} = 188$ nF, $T_{\mathrm{f}} = 30$°C.

D. Field Winding Capacitance

The waveforms given by the circuit with different rectifier output capacitance from experiments and simulations are compared in Figure 6-15. Plots (a) – (e) are with $C_{\mathrm{f}} = 47$ nF whereas Plots (f) – (j) are with $C_{\mathrm{f}} = 188$ nF. The tests are carried out with 48 V dc-link voltage, 1 mm airgap and around 30°C winding temperature. The start time instants of the waveforms are adjusted so that the primary side voltage waveforms are aligned in phase. As can be noticed, in all the subplots from (a) to (j), the simulated waveforms fit the experimental ones quite well.

In (d), with 47 nF capacitor, the field voltage drops to and stays at zero for some time interval. This indicates the commutation mode operation, when the four diodes conduct simultaneously. In comparison, in (i), a higher field winding capacitance of 188 nF keeps the field voltage always above zero. This is due to the larger capacitance which keeps the voltage relatively stable. In this case, there is no commutation time interval. Consequently, the secondary side voltage shown in (c) stays at zero for a time interval before changing the polarity, whereas in (h), the secondary side voltage changes polarity immediately.

Apart from that, in both (a) and (f), switching voltage spikes at the primary side can be observed in experiments, whereas the model does not show any spike in simulations. This is due to the fact that the model simplifies the MOSFET characteristics and does not describe the parasitic inductance on the PCB. Hence this model is suitable to analyze the system level performance instead of details during switching transients.

At the output of the excitation system, two quantities are of interest, the maximum field current and the maximum field voltage peak. The field voltage peak is the peak value in the field winding voltage waveform. For instance, the field voltage peak is 209 V in the 47 nF case shown in Figure 6-15 (d), and 132 V in the 181 nF case shown in Figure 6-15 (i). In general, a high field current with a low voltage peak is preferable, which means a high capability of power delivery and a low stress applied across the rectifier diodes. The field voltage peak and the field current are compared in Figure 6-16. The measurements and simulations are performed with 48 V dc-link voltage, 1 mm airgap, around 30°C winding temperature and at

0.99 duty cycle. The maximum field current as well as the maximum field voltage peak appear at the maximum duty cycle, and this is why the case at 0.99 duty cycle is presented. The capacitance varies from 47 nF to 188 nF with 47 nF as the step size. As can be noticed, the simulated results generally fit the experimental results. By adding capacitance, the field

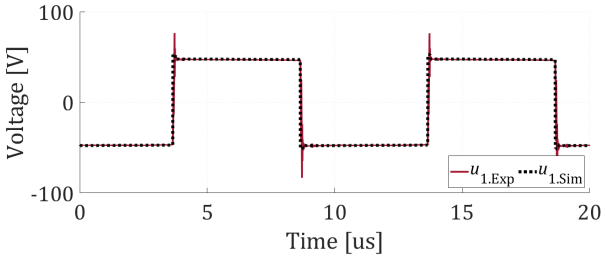

(a) Primary side voltage ($C_f = 47$ nF).

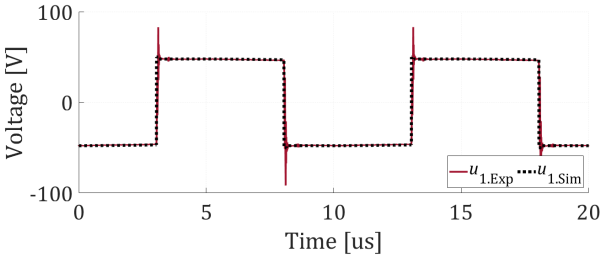

(f) Primary side voltage ($C_f = 188$ nF).

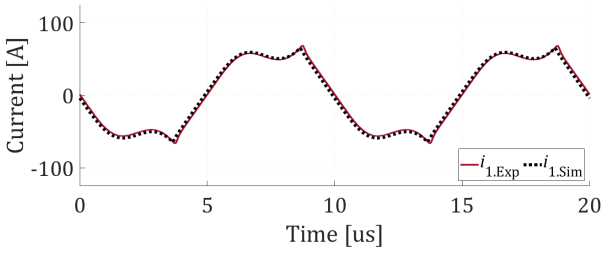

(b) Primary side current ($C_f = 47$ nF).

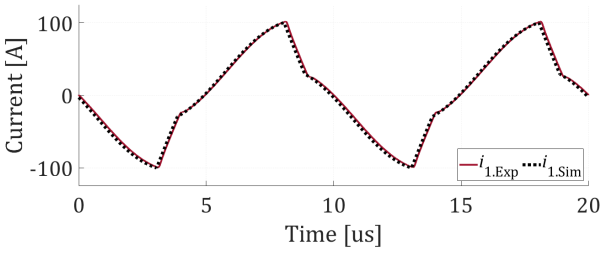

(g) Primary side current ($C_f = 188$ nF).

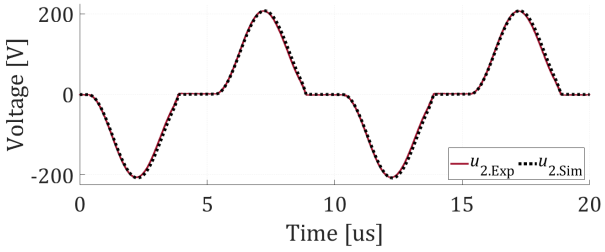

(c) Secondary side voltage ($C_f = 47$ nF).

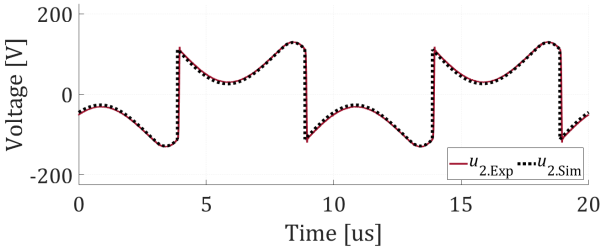

(h) Secondary side voltage ($C_f = 188$ nF).

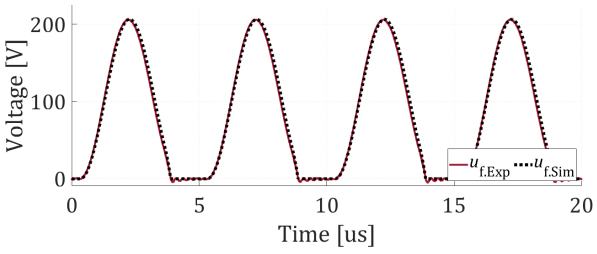

(d) Field voltage ($C_f = 47$ nF).

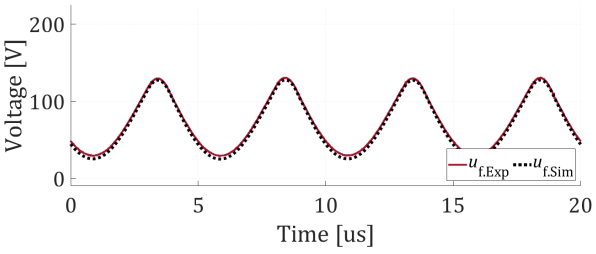

(i) Field voltage ($C_f = 188$ nF).

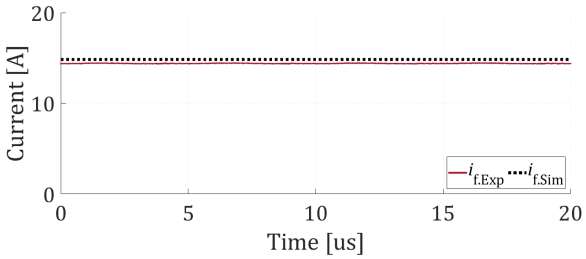

(e) Field current ($C_f = 47$ nF).

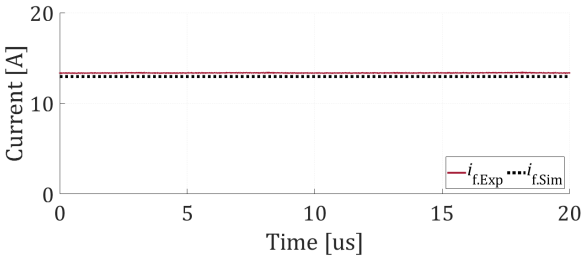

(j) Field current ($C_f = 188$ nF).

Figure 6-15 Voltage and current waveforms with 1 mm airgap, $U_{dc} = 48$ V, $T_f = 30$°C, 0.99 duty cycle.

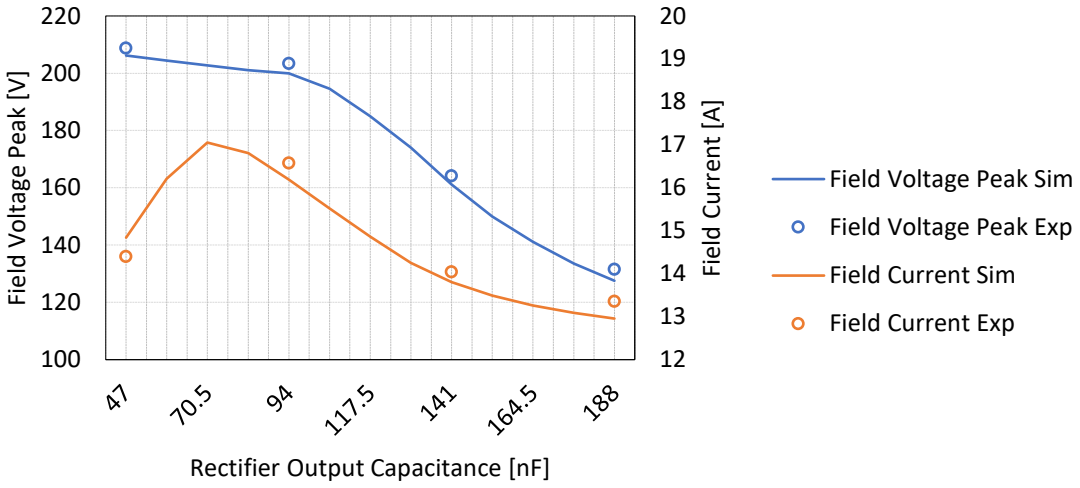

Figure 6-16 Field voltage peak and field current with $C_{\mathrm{f}} = 47, 96, 141, 188$ nF, 1 mm airgap, $U_{\mathrm{dc}} = 48$ V, $T_{\mathrm{f}} = 30$°C, 0.99 duty cycle.

voltage peak decreases, whereas the field current increases in the beginning but decreases as more capacitance is added. Investigations show that this non-monotonous profile is due to the resonance between the rectifier output capacitance and the transformer inductances when the rectifier diodes conduct. Considering the transformer parameters shown in Figure 6-11, to get a resonance frequency at around 100 kHz, 66.5 nF is needed which is close to where the maximum field current appears in the curve.

E. Field Winding Resistance

During EESM operation, the field winding can be heated up by the copper loss. The temperature rise then increases the resistance of the winding leading to further decrease in the field current, as shown in Figure 6-17. The measurements and simulations are done with 60 V dc-link voltage, 1 mm airgap and 188 nF rectifier output capacitance. The presented curves are with the field winding temperature from 40°C to 100°C with 20°C as the step size. As can be noticed, the field current decreases linearly with respect to the temperature increase both in simulation and experiment. The mismatch between the simulated and

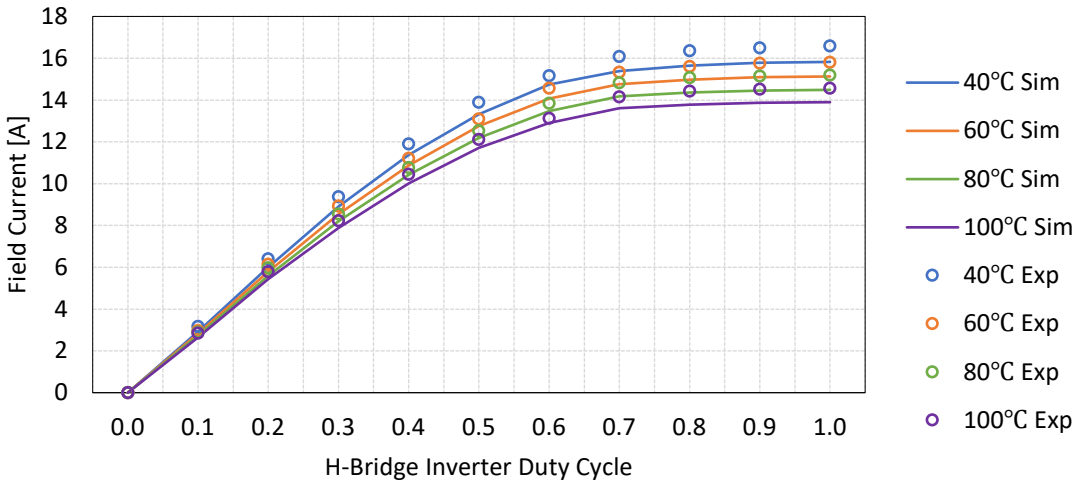

Figure 6-17 Field current against duty cycle with $T_{\mathrm{f}} = 40, 60, 80, 100$°C, 1 mm airgap, $C_{\mathrm{f}} = 188$ nF, $U_{\mathrm{dc}} = 60$ V.

experimental results is due to the limited accuracy of the measurement of mutual inductance. However, the shape of the curves and the gaps in between are consistent between the simulated and experimental results. These curves also indicate that an open-loop control of field current is very sensitive to temperature variations. As a solution, an observer needs to be developed to estimate the field current, so that the effects of the temperature variations can be compensated for.

F. System Analysis and Optimization with the Model

Further analysis of the excitation system can be done with the help of the model to derive design guidelines for the purpose of optimization. First, a parameter sensitivity study is performed to identify the most sensitive parameters, followed by a selection of rectifier output capacitance and finally, loss analysis is performed to identify the component requiring specific attention.

G. Sensitivity Study of Parameters in the Excitation System

Parameter sensitivity study is essential in understanding the characteristics of the system. The sensitive parameters need to be detected, so that sufficient attention will be paid to these parameters during the design. In addition, if necessary, trade-offs can be made to guarantee the key parameters whereas to sacrifice the parameters with less importance.

Figure 6-18 shows the sensitivity study of the mutual inductance. Mutual inductance variations of ±2.5%, ±5.0% are introduced and the profile of field current against duty cycle is presented. As can be noticed, a variation of mutual inductance by +5.0% increases the field current by 15%, which means the mutual inductance is a key parameter which influences the field current effectively. In addition, the experimental results lay within the +0.0% case and the +2.5% case, and this indicates that probably a +1.25% measurement error of mutual inductance causes the error between the simulations and the experiments as observed earlier. Therefore, specific attention should be paid in estimation and measurement of mutual inductance.

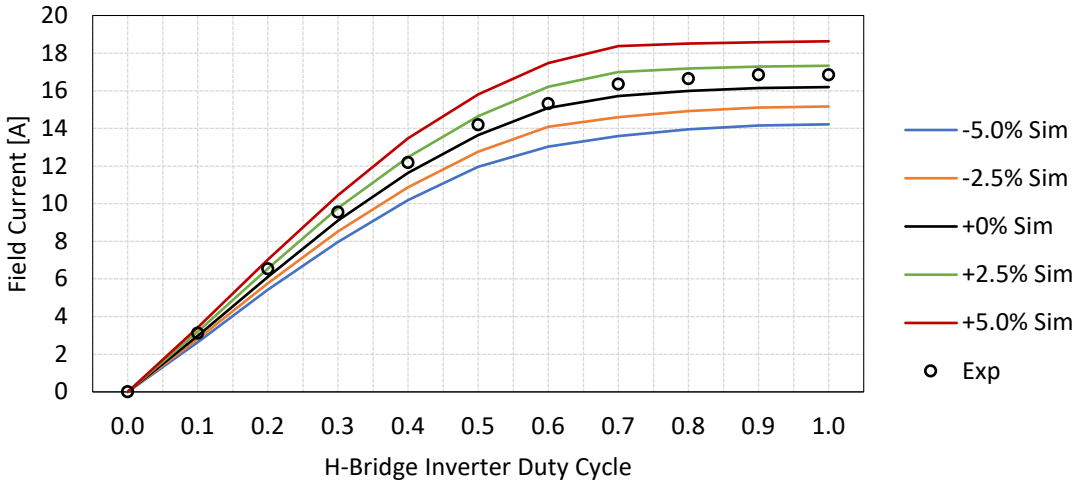

Figure 6-18 Field current against duty cycle with ±2.5%, ±5.0% mutual inductance variations, $T_{\mathrm{f}} = 30℃$, 1 mm airgap, $C_{\mathrm{f}} = 188\ \mathrm{nF}$, $U_{\mathrm{dc}} = 60\ \mathrm{V}$.

H. Selection of Rectifier Output Capacitance

The rectifier rotates together with the rotor and therefore components in the rectifier circuit should be as few as possible. However, capacitors are needed to guarantee the performance of the circuit, e.g. a high field current is needed to guarantee a certain power transfer capability, and a low field voltage peak is preferable to limit the stress of the diodes. The field current and the field voltage peak are therefore checked with a parametric sweep of rectifier output capacitance, as shown in Figure 6-19.

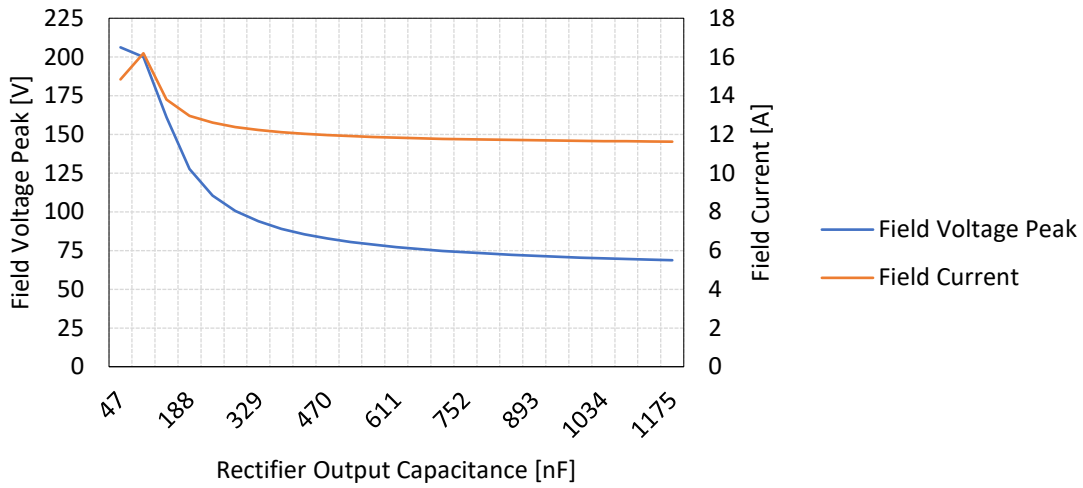

Figure 6-19 Simulated field peak voltage and field current with variations of rectifier output capacitance, $T_{\mathrm{f}} = 30°\mathrm{C}$, 1 mm airgap, $U_{\mathrm{dc}} = 48\ \mathrm{V}$.

An optimal selection depends on the target. In case the peak voltage is not of concern, then the capacitance gives the highest field current is the optimal solution, which is 94 nF. However, in case the maximum field current is already higher than required, then attention mostly needs to be paid to the voltage peak. As can be noticed, the voltage peak decreases fast in the beginning. The most significant drop of both quantities occurs at around 141 nF. If more capacitance than 329 nF is added, the voltage peak does not vary so much. A roughly good choice can be made with capacitance between 141 nF and 329 nF.

I. Loss Analysis

The fundamental frequency of the excitation system is 100 kHz, and due to the bandwidth limitation of the measurement devices, the loss of each component in the excitation system cannot be measured accurately. Fortunately, with the help of the model, it becomes possible to figure out roughly how the losses are distributed among different parts of the system. Thereafter, the component contributing to the major loss of the system can be detected, and the efficiency can be improved accordingly in the next design iteration.

Figure 6-21 shows the total efficiency from dc-link to field winding with $T_{\mathrm{f}} = 30°\mathrm{C}$, 1 mm airgap, $C_{\mathrm{f}} = 188\ \mathrm{nF}$. Admittedly, the simulated values are different from the experimental values, probably due to the limited accuracy of the measurements as well as the simplification of the modeling, but the tendencies of the curves are consistent. The efficiency increases when the duty cycle increases from 0.1 to 0.6 or 0.7, and thereafter, the efficiency starts to decrease. This may be because the lowest harmonic contents appear at around 0.7 duty cycle, where a low percentage of reactive current is consumed.

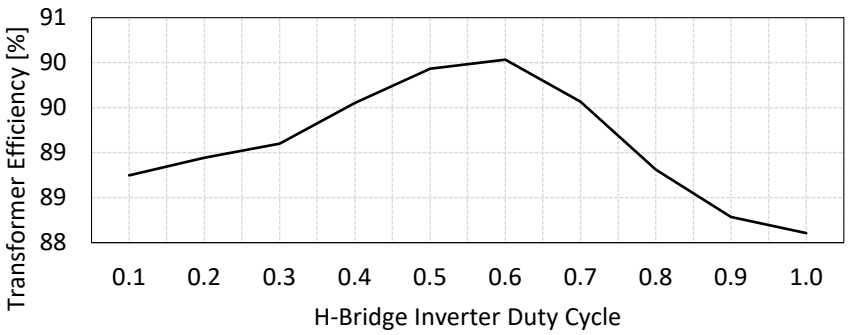

Figure 6-20 Efficiency of the transformer with $U_{\mathrm{dc}} = 60$ V, $T_{\mathrm{f}} = 30$°C, 1 mm airgap, $C_{\mathrm{f}} = 188$ nF. The $U_{\mathrm{dc}} = 36, 48$ V cases look very similar.

The efficiency of each component is compared, and the transformer gives the lowest efficiency. Figure 6-20 shows the efficiency curve of the transformer, and the shape of the curve is similar to the overall efficiency curve as shown in Figure 6-21. It can therefore be concluded that it is mostly the efficiency of the transformer that decides the shape of the overall system efficiency curve.

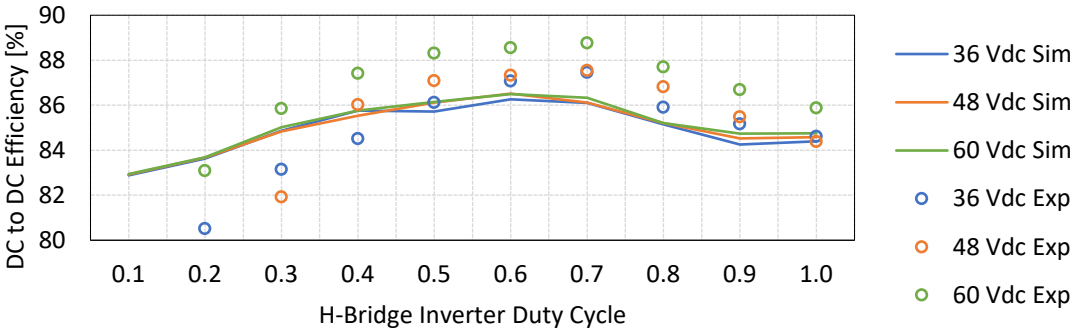

Figure 6-21 Efficiency from dc-link to field winding with $U_{\mathrm{dc}} = 36, 48, 60$ V, $T_{\mathrm{f}} = 30$°C, 1 mm airgap, $C_{\mathrm{f}} = 188$ nF.

Figure 6-22 shows how each component contributes to the overall loss, from the model. The transformer loss is the major loss among all components. This indicates that in this excitation system, a better design of the transformer would probably improve the efficiency of the entire system significantly.

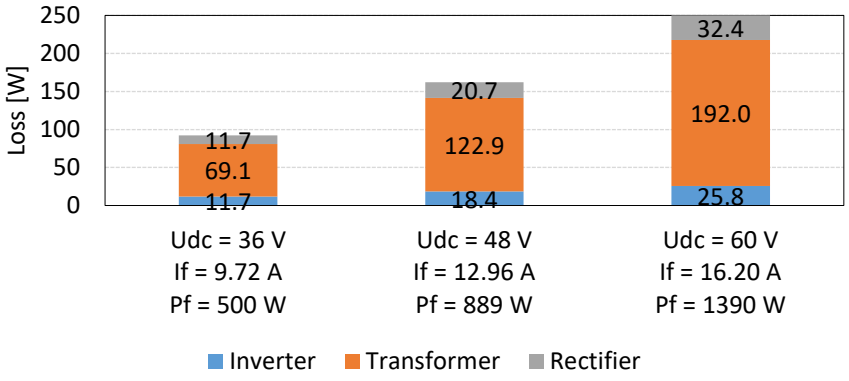

Figure 6-22 Distribution of the loss among components in the circuit with $U_{\mathrm{dc}} = 36, 48, 60$ V, $T_{\mathrm{f}} = 30$°C, 1 mm airgap, $C_{\mathrm{f}} = 188$ nF, 0.99 duty cycle.

6.1.7 Estimation of Current and Temperature of Field Windings

Introducing a rotating transformer reduces the friction losses and efforts of maintenance, but also brings challenges to the prevalence of EESM. The field winding is physically inaccessible after assembly. This makes field current not possible to be measured directly. Nevertheless, to implement a closed-loop field current control, a feedback of instantaneous field current is needed. In addition, the heat generated by the field winding copper loss is a well-known challenge. Hence, estimating field winding temperature to protect the winding from over temperature becomes necessary. The aim of the study in this section is therefore to develop an online algorithm to estimate the current and temperature of the field winding, so that a closed-loop field current control and an over-temperature protection of field winding can be possibly implemented.

A. Schematic and Principle of the Algorithm

The schematic of the estimation algorithm is shown in Figure 6-23. The inputs to the algorithm are the duty cycle decided by the current controller, which adjusts the excitation level of the machine, as well as the dc-link input current of the H-Bridge inverter, which is the feedback of the algorithm and corrects the estimation. The outputs of the algorithm are the estimations of field current and field winding temperature.

The algorithm contains two datasets, one for field current and one for dc-link current, with the duty cycle and temperature as the inputs. The datasets in this algorithm can be either look-up tables or formulas. And the formulas can be derived analytically or developed by applying curve-fitting to the simulated or experimental data.

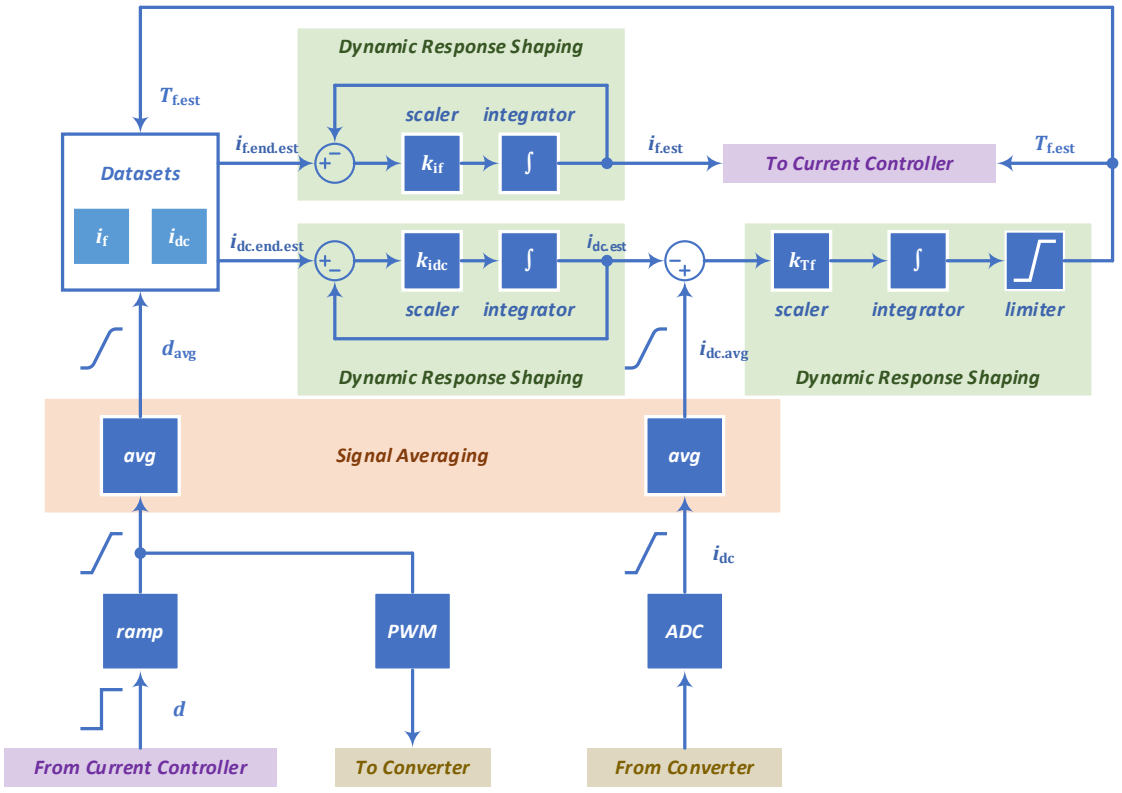

Figure 6-23 Schematic of the estimation algorithm.

As the start, the algorithm firstly assumes a winding temperature, and the current controller gives a duty cycle. The duty cycle and the assumed winding temperature are fed into the datasets. Then the estimated steady-state field current and dc-link current are generated. Through dynamic response shaping processes, the steady-state estimations are shaped into instantaneous values. The estimated field current is fed into the current controller for field current control while the estimated dc-link current is compared with the measured dc-link current. The error in the between is then used to correct the temperature estimation. Thereafter, with the updated temperature estimation, the field current and dc-link current estimations are updated as well. Hence the datasets together with the dc-link current and field winding temperature dynamic response shaping processes forms the temperature correction loop. The updates will continue until the error between the estimation and measurement of the dc-link current goes to zero.

B. Signal Filtering and Ramping

The algorithm requires a stable measurement of dc-link current. To achieve this, a moving average of the dc-link current measurement is implemented so that high frequency noise can be filtered out. In this study, an average of 100 samples is applied. However, this filtering will introduce a time delay. And since the measured dc-link current is compared with the estimated dc-link current which is calculated from the duty cycle, the duty cycle needs to be delayed by the same time duration so that the two signals in comparison can be synchronized. To realize this, the same moving average filter is added in the path through which the duty cycle signal is fed into the algorithm. In addition, the duty cycle is ramped in the machine control in practical situation, so that the back-EMF increases gradually, and the stator current controller has enough time to react.

C. Datasets

Datasets can be described by look-up tables, analytical or formulas generated by curve fitting of experimental data. Analytical solution can be derived if the rectifier output capacitance is high enough to keep the field voltage constant [66]. The results have been presented in (6-3) and (6-4). If the criterion does not fit, then curve fitting of the experimental data can be applied.

D. Dynamic Response Shaping

The datasets give steady state estimations of the dc-link current and the field current. In order to shape a transient curve of current rising, an integrator is utilized to gradually eliminate the error between the instantaneous value and the steady state value of the estimation

$$i_{\mathrm{dc.est}} = k_{i_{\mathrm{dc}}} \cdot \int (i_{\mathrm{dc.end.est}} - i_{\mathrm{dc.est}}) \cdot dt \tag{6-60}$$

$$i_{\mathrm{f.est}} = k_{i_{\mathrm{f}}} \cdot \int (i_{\mathrm{f.end.est}} - i_{\mathrm{f.est}}) \cdot dt \tag{6-61}$$

where $i_{\mathrm{dc.est}}$ is the instantaneous dc-link current estimation, $i_{\mathrm{dc.end.est}}$ is the steady state dc-link current estimation, $k_{i_{\mathrm{dc}}}$ is the gain of the dc-link current shaping integration, $i_{\mathrm{f.est}}$ is the instantaneous field current estimation, $i_{\mathrm{f.end.est}}$ is the steady state field current estimation, $k_{i_{\mathrm{f}}}$ is the gain of the field current shaping integration. Then, the field winding temperature can be estimated

$$T_{\mathrm{f.est}} = k_{T_\mathrm{f}} \cdot \int \left(i_{\mathrm{dc.avg}} - i_{\mathrm{dc.est}}\right) \cdot dt \tag{6-62}$$

where k_{T_f} is the gain of the field winding shaping integration. The gains in (6-60), (6-61) and (6-62) are initially calculated from the time constant and the thermal capacity of the field winding, and then tuned in experiments. In order to avoid possible error, $T_{\mathrm{f.est}}$ is clamped within 0 and 200°C.

E. Validation in Simulations

An H-bridge inverter is used in the excitation system as shown in Figure 1-5. Figure 6-24 shows the sequence of the duty cycle applied to the inverter, which is to test the developed algorithm for field current estimation. The duty cycle ramps from 0 up to 1.0 at 0.5 s and ramps down to 0.5 s at 2.5 s. At 4.5 s, it ramps to 1.0 and at 6.5 s ramps down to 0.5 again.

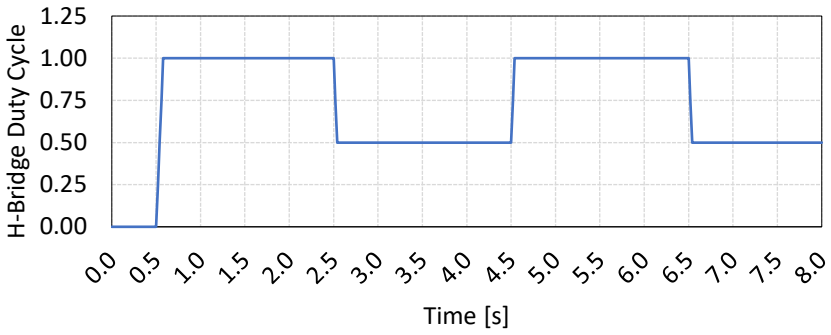

Figure 6-24 Sequence test of duty cycle.

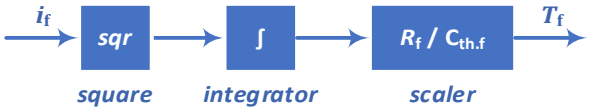

Figure 6-25 Thermal model of the field winding.

A simplified thermal model is implemented to describe the temperature rise of the field winding as shown in Figure 6-25. The copper loss of the field winding can be calculated as

$$p_\mathrm{f} = {i_\mathrm{f}}^2 \cdot R_\mathrm{f} \tag{6-63}$$

where p_f is the instantaneous field copper loss and i_f is the instantaneous field current. With a thermal capacitance $C_{\mathrm{th.f}}$ of 360 J/K which is obtained from copper losses during machine test, the field winding temperature can be calculated by integration of the copper loss

$$T_\mathrm{f} = \int \frac{p_\mathrm{f}}{C_{\mathrm{th.f}}} \cdot dt = \frac{R_\mathrm{f}}{C_{\mathrm{th.f}}} \cdot \int {i_\mathrm{f}}^2 \cdot dt \tag{6-64}$$

where T_f is the field winding temperature. This is not a delicate thermal modeling of the machine winding. Instead, it is to introduce temperature variations and to evaluate the tracking performance of the estimation algorithm with such temperature variations.

To verify the dynamic tracking capability of the estimation algorithm, cases with different starting temperatures are simulated and the case with temperature starting at 30°C is shown in Figure 6-26. The initial value of the temperature estimation is 40°C and after the algorithm is activated at 0.5 s, the algorithm starts to eliminate the temperature estimation error. As

can be noticed in (c), the dc-link current estimation, as the feedback of the algorithm, follows the real dc-link current well. This verifies the functionality of the integrator in the dynamic response shaping process.

The temperature estimation in (b) shows that the tendency of the estimated temperature follows the real temperature quite well. Error exists due to the accuracy of linear interpolation (look-up table, denoted TAB) and curve fitting (denoted CF). The tracking by using curve fitting gives slightly larger error than linear interpolation since curve fitting is an approximation of the curve. Spikes can be seen when the duty cycle steps, this is due to the error between the estimated and the real dc-link currents during the transients. And the dynamic response shaping process helps to reduce the spikes. Due to the successful estimations of the dc-link

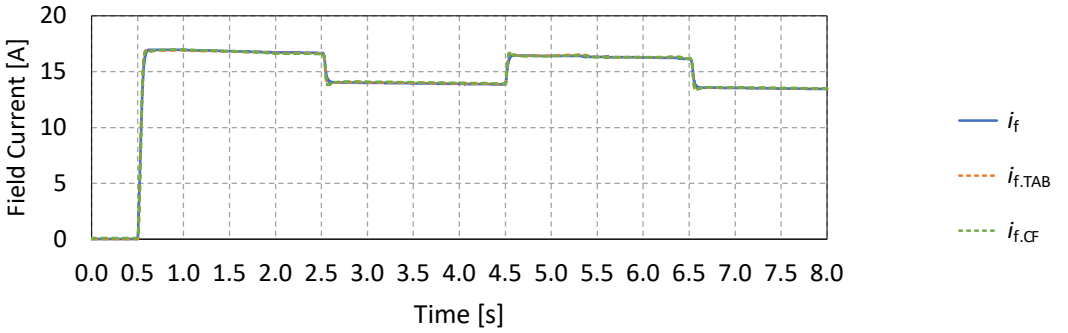

(a) Field current from 0 to 8 s.

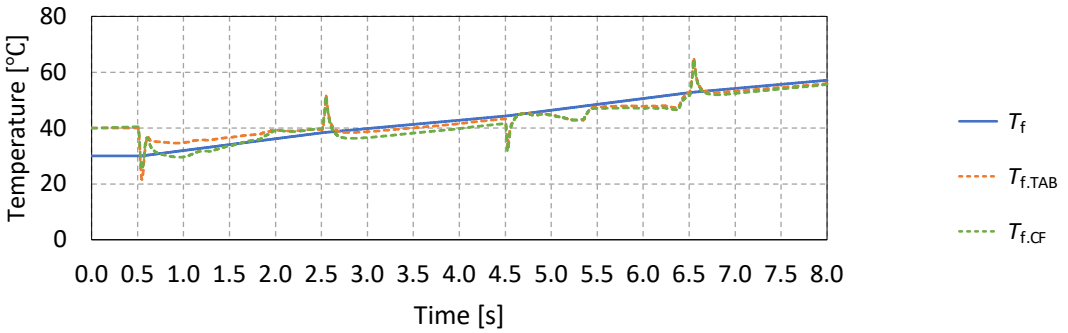

(b) Field winding temperature from 0 to 8 s.

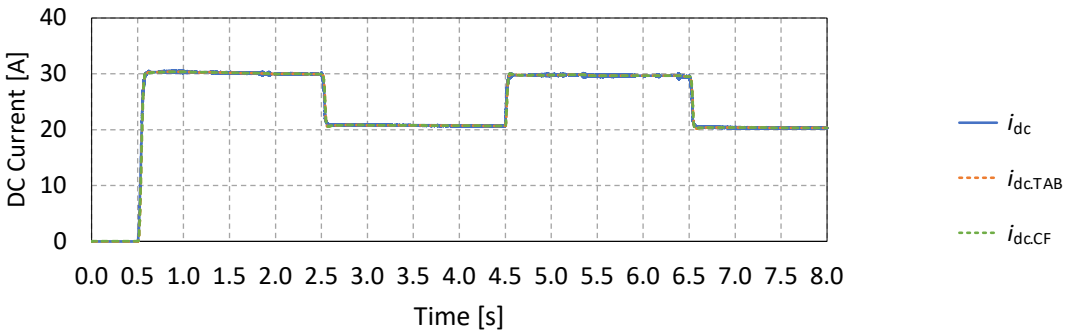

(c) DC-link current from 0 to 8 s.

Figure 6-26 Duty cycle sequence simulation at 30℃. TAB means look-up table and CF means curve fitting.

current and field winding temperature, the field current estimation follows the real value consequently as shown in (a).

The zoomed-in details of the field current estimation during the step are shown in Figure 6-27. Generally, the differences between the estimated and the real curves are quite minor during both the rising and falling of the field current. Validation in Experiments

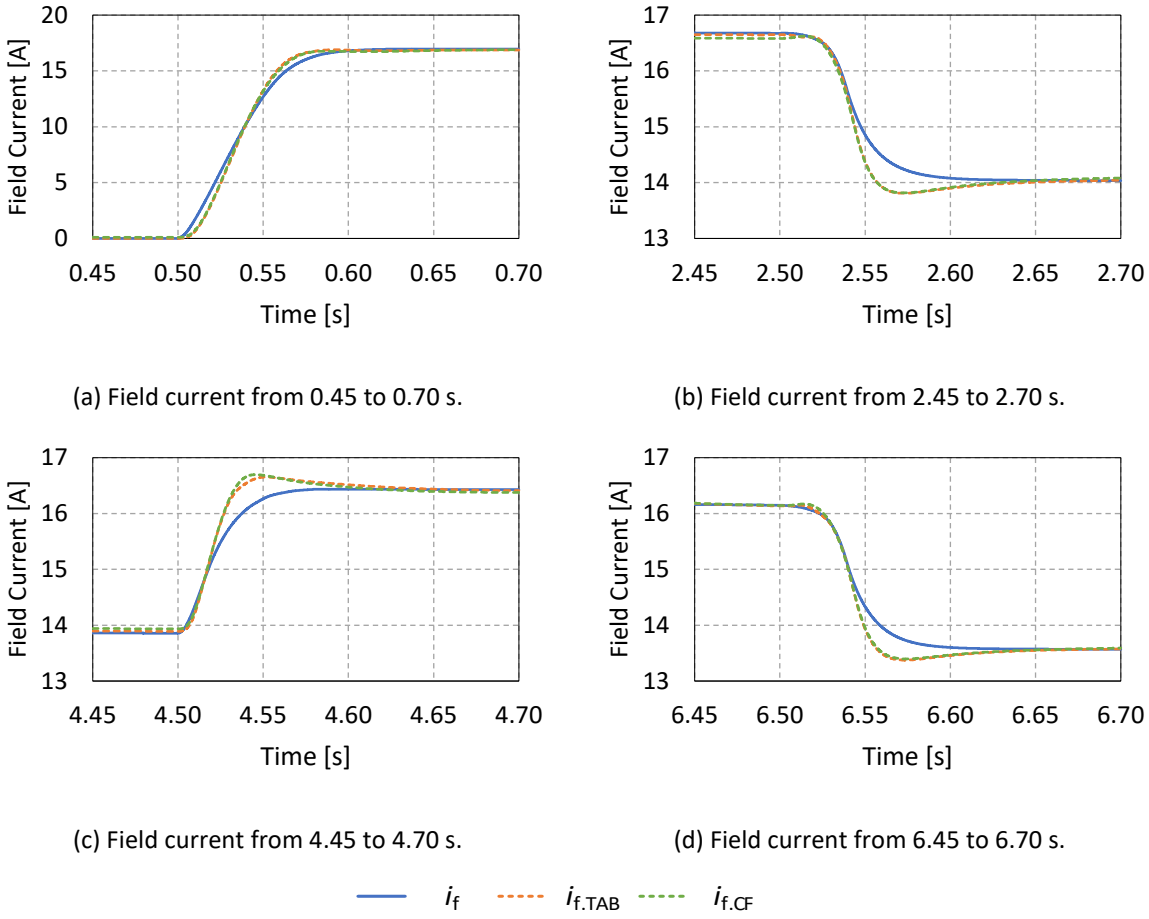

(a) Field current from 0.45 to 0.70 s.

(b) Field current from 2.45 to 2.70 s.

(c) Field current from 4.45 to 4.70 s.

(d) Field current from 6.45 to 6.70 s.

Figure 6-27 Duty cycle sequence simulation at 30℃. TAB means look-up table and CF means curve fitting.

F. Validation in Experiments

The same sequence of duty cycle as shown in Figure 6-24 is performed to verify the algorithm experimentally. The winding temperature starts at 30℃ in (6-14) and at 100℃ in (6-15) respectively. Due to a limited number of DAC channels of the DSP, only field current and field winding temperature estimation curves are extracted. Similarly, as in the simulation, the initial temperature estimation is set at 40℃ and the algorithm starts after the algorithm is activated at 0.5 s. The temperature is measured by two PT100 sensors and is also calculated roughly by using the ratio between the field voltage and field current.

The estimated field current and the real field current are compared in (a) and the zoomed-in curves are shown in (c)-(f). The estimation generally follows the real current quite well. In the 100℃ case, an overshoot of field current estimation occurs at 0.5 s in (a), due to the huge gap between the initial temperature assumption and real temperature. The current estimation error is then eliminated as the temperature estimation tracks the real one as shown in (b).

As can also be noticed that, the estimation error is higher at 0.5 duty cycle than at 1.0 duty cycle. This can be explained by Figure 6-14. At a lower duty cycle, the differences between

the curves are smaller. Since the algorithm utilizes the difference between dc-link currents at different temperatures as the feedback to correct the temperature estimation, a smaller difference of dc-link currents makes the temperature estimation more difficult. Analytically, an increase of temperature gives an increase of R_{f}, and from the analytical solution shown in (6-5), the difference in dc-link current can be expressed as

$$\Delta I_{\mathrm{dc}} \propto \frac{1-\cos(\pi d)}{R_{\mathrm{f.1}} R_{\mathrm{f.2}}} (R_{\mathrm{f.2}} - R_{\mathrm{f.1}}) \tag{6-65}$$

where $R_{\mathrm{f.1}}$ and $R_{\mathrm{f.2}}$ are the resistances at different temperatures. The part $\frac{1-\cos(\pi d)}{R_{\mathrm{f.1}} R_{\mathrm{f.2}}}$ can be regarded as an amplification factor of the resistance difference $(R_{\mathrm{f.2}} - R_{\mathrm{f.1}})$. A higher duty cycle therefore gives a higher amplification factor $\frac{1-\cos(\pi d)}{R_{\mathrm{f.1}} R_{\mathrm{f.2}}}$ and therefore a higher ΔI_{dc}. This is the reason why a higher duty cycle shows a better resolution of temperature estimation.

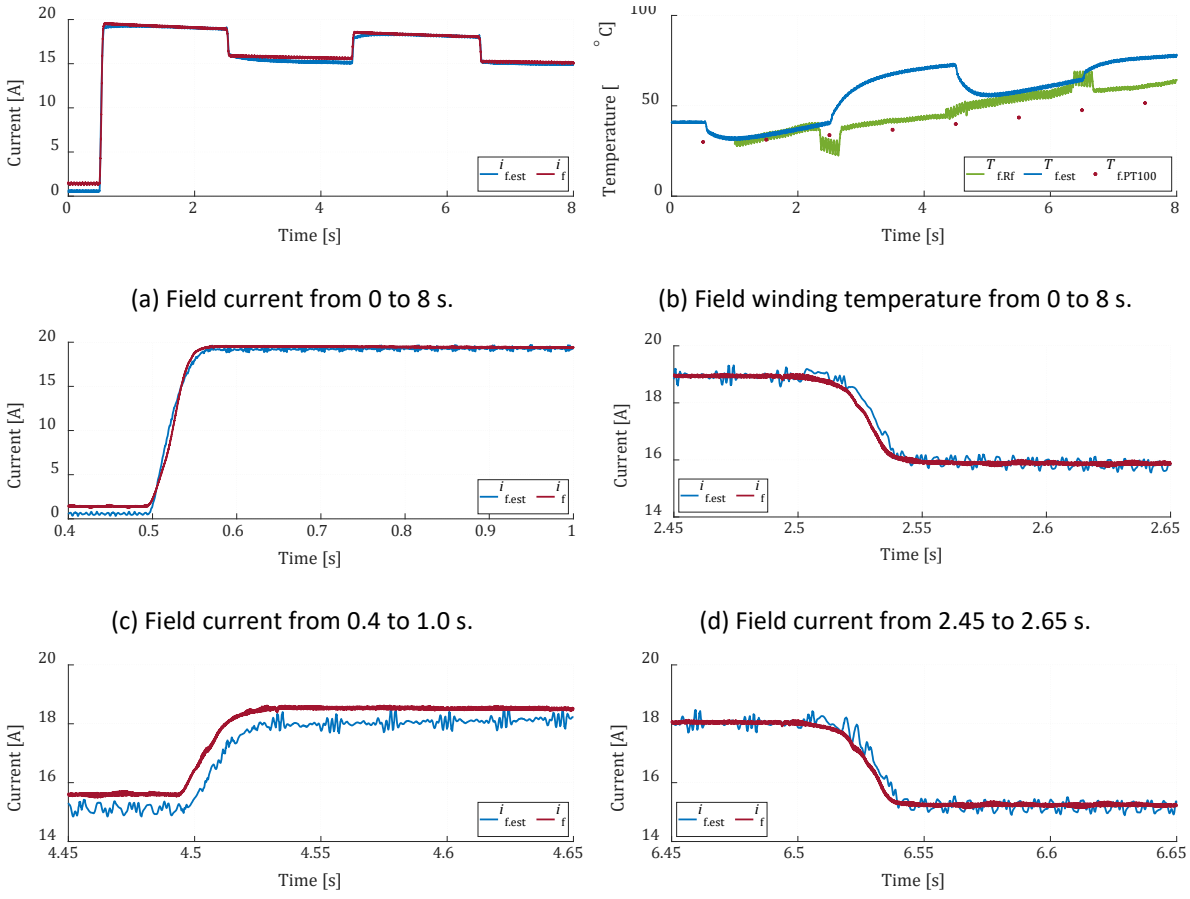

(a) Field current from 0 to 8 s.

(b) Field winding temperature from 0 to 8 s.

(c) Field current from 0.4 to 1.0 s.

(d) Field current from 2.45 to 2.65 s.

(e) Field current from 4.45 to 4.65 s.

(f) Field current from 6.45 to 6.65 s.

Figure 6-28 Duty cycle sequence test at 30℃.

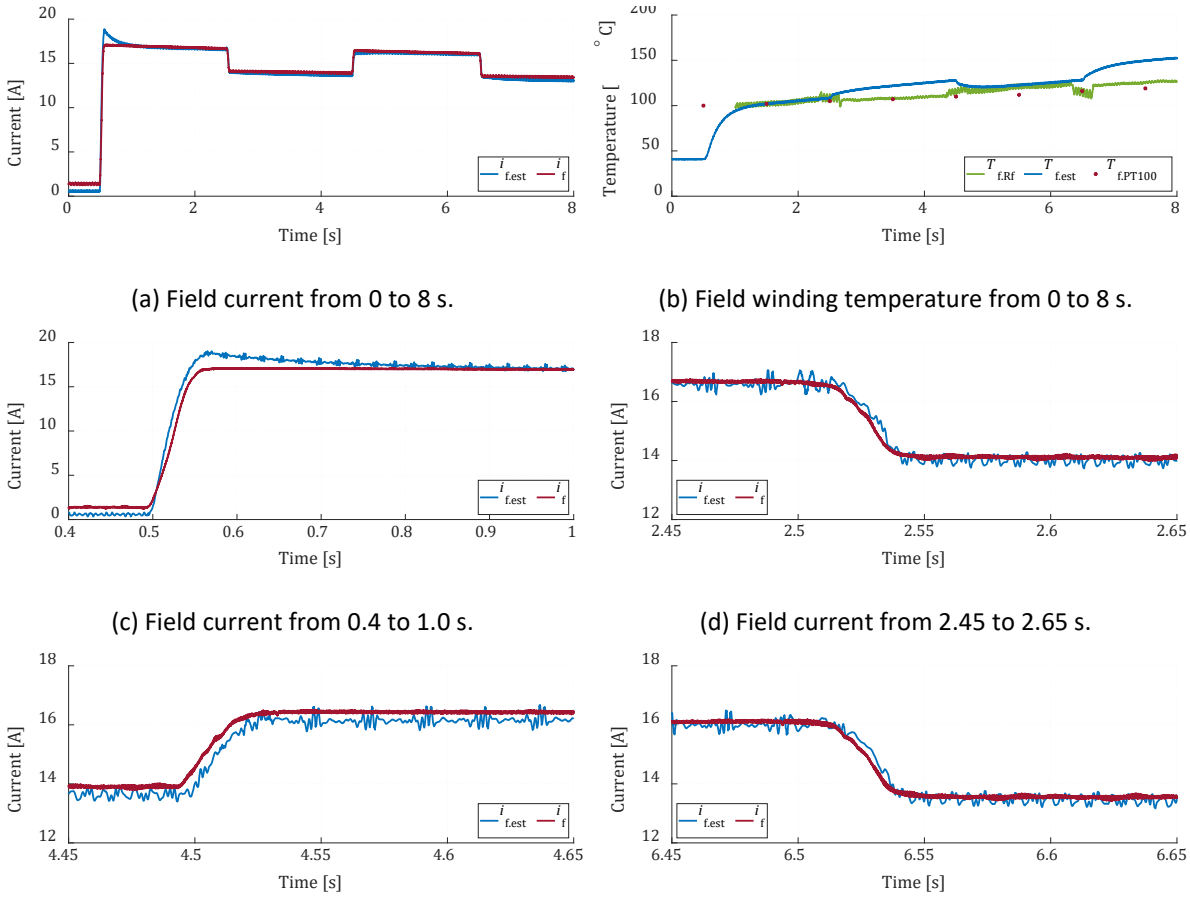

(a) Field current from 0 to 8 s.

(b) Field winding temperature from 0 to 8 s.

(c) Field current from 0.4 to 1.0 s.

(d) Field current from 2.45 to 2.65 s.

(e) Field current from 4.45 to 4.65 s.

(f) Field current from 6.45 to 6.65 s.

Figure 6-29 Duty cycle sequence test at 100℃.

6.1.8 Field Current Control

A. Algorithm

With the estimated field current, it becomes possible to apply closed-loop control to field current. The schematic of the algorithm is shown in Figure 6-30.

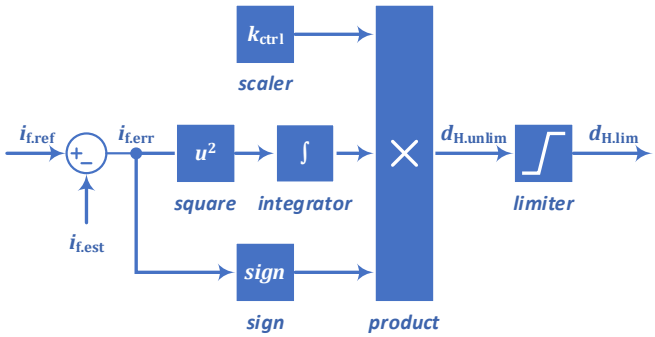

Figure 6-30 Schematic of closed-loop field current control.

Firstly, the field current error $i_{\mathrm{f.err}}$ is calculated by comparing the reference value $i_{\mathrm{f.ref}}$ and the estimated value $i_{\mathrm{f.est}}$

$$i_{\mathrm{f.err}} = i_{\mathrm{f.ref}} - i_{\mathrm{f.est}} \tag{6-66}$$

Then, the error is squared and amplified by a scaler k_{ctrl}

$$d_{\mathrm{H.unlim}} = k_{\mathrm{ctrl}} \cdot \mathrm{sign}(i_{\mathrm{f.err}}) \cdot \int {i_{\mathrm{f.err}}}^2 \cdot dt \tag{6-67}$$

where $d_{\mathrm{H.unlim}}$ is the unlimited duty cycle and it is then clamped between 0 and 1 to be $d_{\mathrm{H.lim}}$. The reason to take the square is that, it is preferred to adjust the duty cycle in a big step when the error is large, whereas when the error becomes smaller, the duty cycle needs to be fine-tuned to avoid overshoot.

B. Validation in Simulations

A sequence of field current reference is applied as shown in Figure 6-24. The field current reference ramps from 0 up to 18 A at 0.5 s and ramps down to 12 A at 2.5 s. At 4.5 A, it ramps

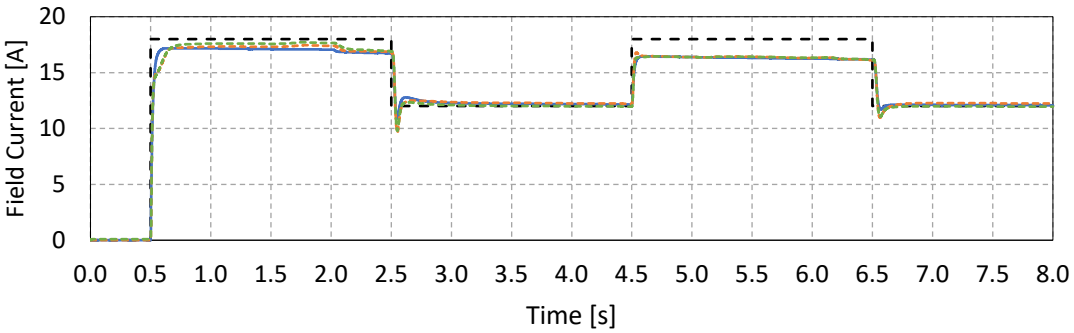

(a) Field current from 0 to 8 s.

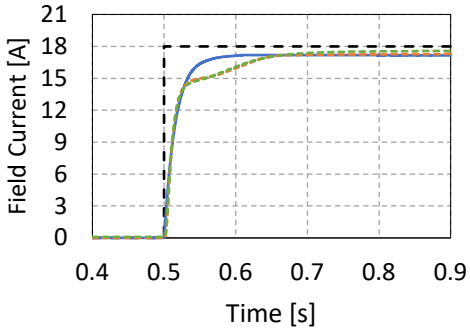

(b) Field current from 0.4 to 0.9 s.

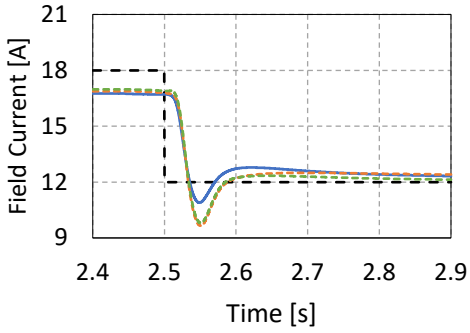

(c) Field current from 2.4 to 2.9 s.

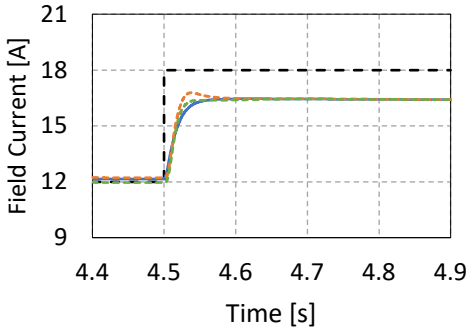

(d) Field current from 4.4 to 4.9 s.

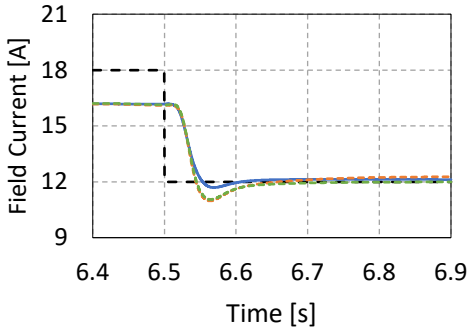

(e) Field current from 6.4 to 6.9 s.

Figure 6-31 Closed-loop field current control at 30°C. TAB means look-up table and CF means curve fitting.

to 18 A and at 6.5 s it ramps down to 12 A again. The overall performance is illustrated in (a). As can be seen, the reference exceeds the maximum current output capability with reference of 18 A. The gap between the reference and the real current enlarges as time passes due to the increase of temperature. In comparison, the current follows the reference of 12 A quite well.

C. Validation in Experiments

Figure 6-32 presents the experimental result which starts at 30℃. The current reference $i_{\mathrm{f.ref}}$ and current estimation $i_{\mathrm{f.est}}$, are output from the DAC of the DSP, whereas the real current i_{f} is measured by a current probe. As can be noticed, the real current follows the reference well. The real current lags the reference by less than 10 ms and it rises from 0 A to 18 A within 50 ms.

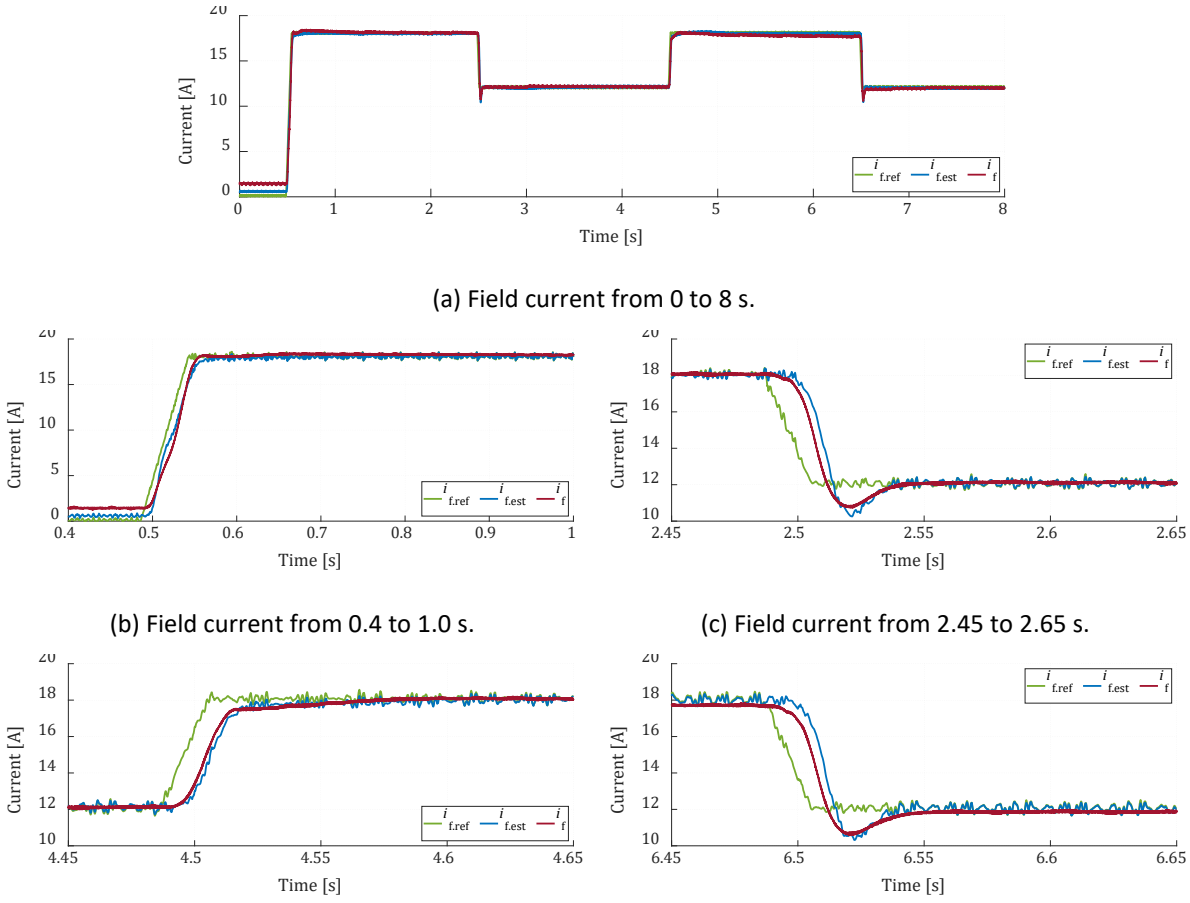

(a) Field current from 0 to 8 s.

(b) Field current from 0.4 to 1.0 s.

(c) Field current from 2.45 to 2.65 s.

(d) Field current from 4.45 to 4.65 s.

(e) Field current from 6.45 to 6.65 s.

Figure 6-32 Closed-loop field current control at 30℃.

Figure 6-33 presents the experimental result which starts at 100℃. The same sequence is applied. As can be noticed, starting at 100℃, due to the increase of resistance, the field current cannot reach 18 A even with duty cycle 1.0. Hence a gap always exists between the real field current and the 18 A reference. The gap enlarges gradually since the temperature increases during the test. During the transients around 0.5 s, the field current is temporarily over-estimated because estimator needs time to catch up with the real temperature. The temperature estimation adjusts until around 1.0 s, the current estimation comes back to the real value.

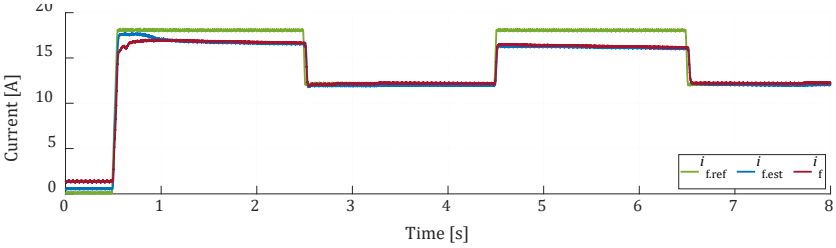

(a) Field current from 0 to 8 s.

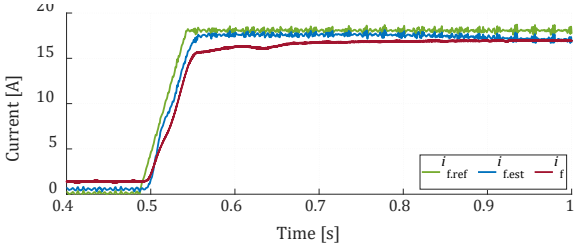

(b) Field current from 0.4 to 1.0 s.

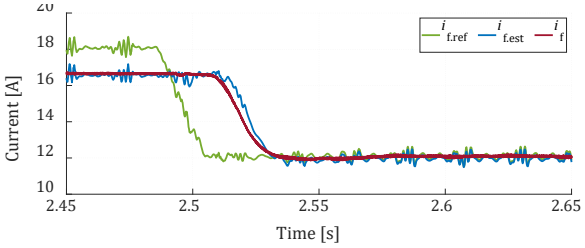

(c) Field current from 2.45 to 2.65 s.

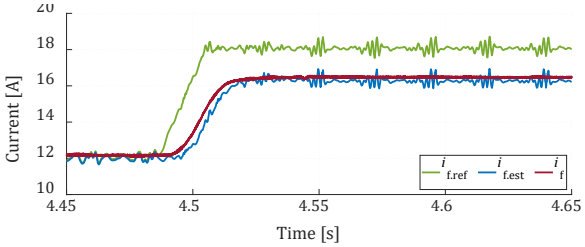

(d) Field current from 4.45 to 4.65 s.

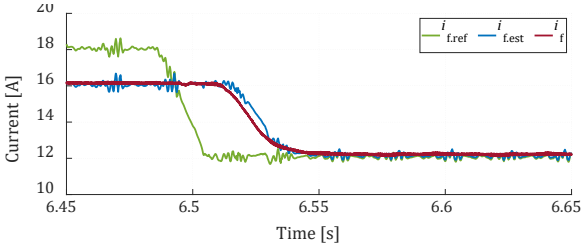

(e) Field current from 6.45 to 6.65 s.

Figure 6-33 Closed-loop field current control at 100°C.

6.2 Excitation Using Common Mode Switching Harmonics

To drive an EESM, in addition to the three-phase inverter used for powering the stator windings, another dc-dc converter is needed to power the field winding in rotor. This increases the cost and reduces reliability of the drive system. In this study, a novel technique is proposed to utilize the Common Mode (CM) switching harmonics of the three-phase inverter to obtain an additional dc output for field excitation. With the proposed technique, CM switching harmonics can be regulated independently from the Differential Mode (DM) power flow to the stator winding.

This technique can be applied universally if a main ac load and an auxiliar dc load need to be powered simultaneously. For instance, in an EV, a low voltage (LV) battery may need to be charged from a high voltage (HV) battery while a PMSM is operating. In this case, the PMSM is the main ac load while the LV battery is the auxiliar dc load. In this section, to indicate that the technique can be applied universally, the EESM stator winding is regarded as the main ac load, while the EESM field winding is regarded as the auxiliar dc load.

The circuit topology employed in the technique is shown in Figure 6-34. As can be noticed, to physically implement the CM power flow to the auxiliary dc load, a harmonic extraction circuit is designed and placed in parallel with the ac load. The circuit and control are verified in simulations and experiments. Finally, the impact on inverter efficiency is investigated.

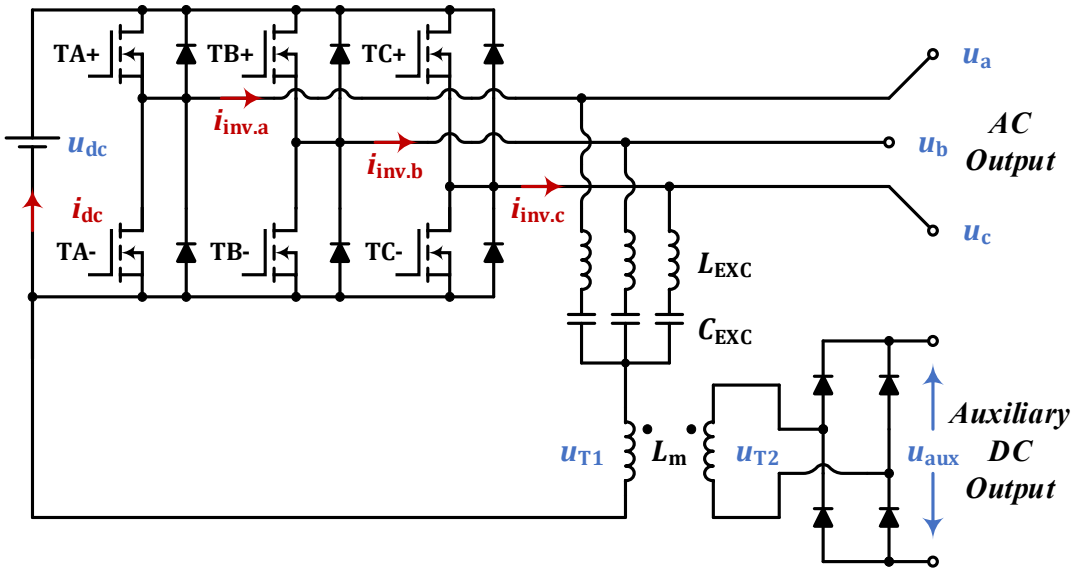

Figure 6-34 Schematic diagram of the proposed circuit which utilizes common mode switching harmonics for auxiliary power output.

6.2.1 Control of CM SVM Switching Harmonics

The switching harmonics in SVM patterns consist of both CM and DM components [69]. In this section, the SVM switching harmonics, especially the CM contents, are analyzed. As shown in Figure 6-35 (a), a two-level three-phase inverter with u_{dc} as the dc-link voltage is considered in this study. However, the analysis can be extended to converters with multi-level and multi-phase. The SVM hexagon on αβ-plane is shown in Figure 6-35 (b), where the entire hexagon is divided into six sectors [70].

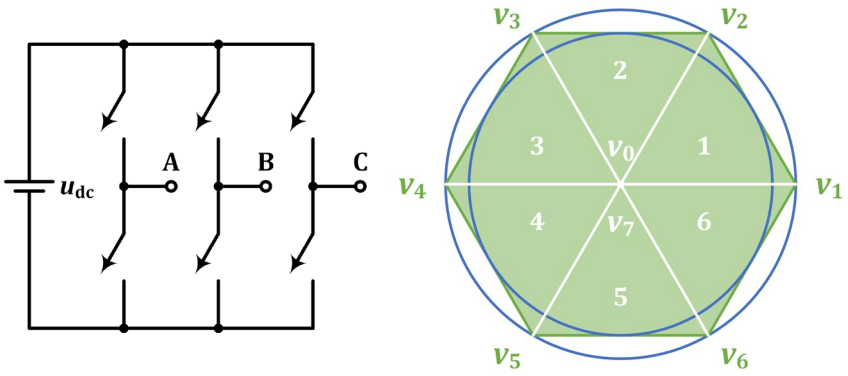

(a) Three-phase inverter. (b) SVM hexagon on αβ-plane.

Figure 6-35 Three-phase inverter with SVM.

A. Common- and Differential-Mode Contents of SVM States

The vectors of SVM states can be defined as

$$\boldsymbol{V}_{\mathbf{SVM}} = [v_0 \quad v_1 \quad v_2 \quad v_3 \quad v_4 \quad v_5 \quad v_6 \quad v_7] = \begin{bmatrix} 0 & 1 & 1 & 0 & 0 & 0 & 1 & 1 \\ 0 & 0 & 1 & 1 & 1 & 0 & 0 & 1 \\ 0 & 0 & 0 & 0 & 1 & 1 & 1 & 1 \end{bmatrix} \tag{6-68}$$

A duty cycle vector can be defined correspondingly

$$\boldsymbol{d}_{\mathbf{SVM}} = [d_0 \quad d_1 \quad d_2 \quad d_3 \quad d_4 \quad d_5 \quad d_6 \quad d_7]^{\mathrm{T}} \tag{6-69}$$

The duty cycle vector for the three phases are

$$\boldsymbol{d}_{\mathbf{abc}} = \begin{bmatrix} d_{\mathrm{a}} \\ d_{\mathrm{b}} \\ d_{\mathrm{c}} \end{bmatrix} = \boldsymbol{V}_{\mathbf{SVM}}\, \boldsymbol{d}_{\mathbf{SVM}} \tag{6-70}$$

Hence the three-phase output voltages can be described as

$$\boldsymbol{u}_{\mathbf{abc}} = \begin{bmatrix} u_{\mathrm{a}} \\ u_{\mathrm{b}} \\ u_{\mathrm{c}} \end{bmatrix} = u_{\mathrm{dc}}\, \boldsymbol{d}_{\mathbf{abc}} \tag{6-71}$$

With amplitude-invariant Clarke transform [71], the voltage vector can be transformed from abc-frame to αβγ-frame

$$\boldsymbol{u}_{\boldsymbol{\alpha\beta\gamma}} = \begin{bmatrix} u_{\alpha} \\ u_{\beta} \\ u_{\gamma} \end{bmatrix} = \boldsymbol{T}_{\mathbf{abc}\rightarrow\boldsymbol{\alpha\beta\gamma}}\, \boldsymbol{u}_{\mathbf{abc}} \tag{6-72}$$

where $\boldsymbol{T}_{\mathbf{abc}\rightarrow\boldsymbol{\alpha\beta\gamma}}$ is the transform matrix. In αβγ-frame, the DM and CM components can be clearly identified. The DM components are described as u_{α} and u_{β}, whereas the CM component is described as u_{γ}.

If the mid-point of the inverter dc-link is regarded as the reference ground, then by using (6-72), the eight SVM state vectors in both abc- and αβγ-frame can be summarized in Table 6-1. The states are illustrated as green circles in three-dimensional (3D) αβγ-frame in Figure 6-36. As can be noticed, none of the states is located on the αβ-plane. The projection of the state vectors from the 3D space to the αβ-plane form a hexagon in green, which is actually the SVM hexagon in Figure 6-36 (b). The state vectors form a hexahedron in 3D space. All six faces are rhombi. The upper three rhombi are in yellow while the lower three are in blue.

From the table and the figure, the following statements can be concluded.

- For all the eight states, $u_\gamma \neq 0$ is valid. This means there is no state that gives purely DM components.
- Only for v_0 and v_7, $\|u_{\alpha\beta}\| = 0$ is valid, whereas for all the six other states, $\|u_{\alpha\beta}\| \neq 0$ is valid.

Usually, v_0 and v_7 are classified as zero states, since they only give CM components, while the other six states can be classified as active states since they are the ones that can give DM components. Furthermore, among all the active states, v_1, v_3, v_5 are with odd number of 1 and hence can be classified as odd states, while v_2, v_4, v_6 can be classified as even states. This categorization is proposed in [72] and it is used here for the convenience of analysis later.

Table 6-1 SVM switching states in abc and αβγ coordinates

State Vector			$\frac{u_a}{u_{dc}}$	$\frac{u_b}{u_{dc}}$	$\frac{u_c}{u_{dc}}$	$\frac{u_\alpha}{u_{dc}}$	$\frac{u_\beta}{u_{dc}}$	$\frac{u_\gamma}{u_{dc}}$
CM		v_0	$-1/2$	$-1/2$	$-1/2$	0	0	$-1/2$
DM	Odd	v_1	$1/2$	$-1/2$	$-1/2$	$2/3$	0	$-1/6$
	Even	v_2	$1/2$	$1/2$	$-1/2$	$1/3$	$1/\sqrt{3}$	$1/6$
	Odd	v_3	$-1/2$	$1/2$	$-1/2$	$-1/3$	$1/\sqrt{3}$	$-1/6$
	Even	v_4	$-1/2$	$1/2$	$1/2$	$2/3$	0	$1/6$
	Odd	v_5	$-1/2$	$-1/2$	$1/2$	$-1/3$	$-1/\sqrt{3}$	$-1/6$
	Even	v_6	$1/2$	$-1/2$	$1/2$	$1/3$	$-1/\sqrt{3}$	$1/6$
CM		v_7	$1/2$	$1/2$	$1/2$	0	0	$1/2$

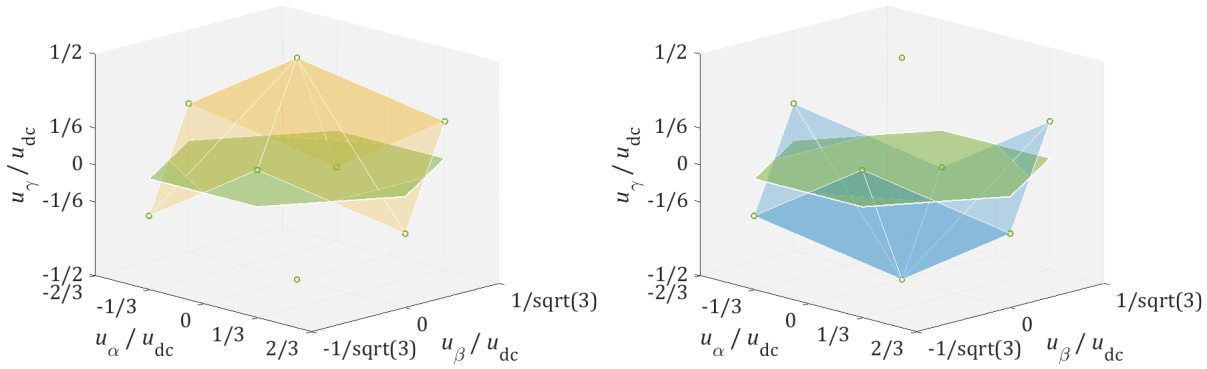

(a) Upper three rhombi & SVM hexagon. (b) Lower three rhombi & SVM hexagon.

Figure 6-36 αβγ components of SVM switching states.

B. Determination of Duty Cycles in SVM

The duty cycles of three phases, d_{a}, d_{b} and d_{c}, can be determined from the duty cycles of the switching states, d_0, d_1, d_2 until d_7, as summarized in Table 6-2. To obtain d_0 until d_7, firstly the sector where the vector is located needs to be identified. Thereafter, an angle θ_{60° can be defined to describe the location of the vector within each 60° hexagon sector. The calculation of θ_{60° is illustrated in Figure 6-37. The voltage vectors in each sector are marked in blue while the corresponding θ_{60° is marked in purple. In programing, the calculation can be formulated by using θ_{360°, the absolute angle in 2π

$$\theta_{60^\circ} = \begin{cases} \theta_{360^\circ} & sector\ 1 \\ 2\pi/3 - \theta_{360^\circ} & sector\ 2 \\ \theta_{360^\circ} - 2\pi/3 & sector\ 3 \\ 4\pi/3 - \theta_{360^\circ} & sector\ 4 \\ \theta_{360^\circ} - 4\pi/3 & sector\ 5 \\ 2\pi - \theta_{360^\circ} & sector\ 6 \end{cases} \tag{6-73}$$

Then the duty cycles of odd and even states can be formulated

$$d_{\mathrm{odd}} = m_{\mathrm{a}} \cos(\theta_{60^\circ} + \pi/6)\ , d_{\mathrm{even}} = m_{\mathrm{a}} \sin\theta_{60^\circ} \tag{6-74}$$

The sum of duty cycles of all active states can be defined as d_{DM}

$$d_{\mathrm{DM}} = \sum_{i=1}^{6} d_i = d_{\mathrm{odd}} + d_{\mathrm{even}} = m_{\mathrm{a}} \cos(\theta_{60^\circ} - \pi/6) \tag{6-75}$$

while the remaining can be defined as d_{CM}

Table 6-2 Duty cycles of three phases

Sector	$\boldsymbol{d_{\mathrm{a}}}$	$\boldsymbol{d_{\mathrm{b}}}$	$\boldsymbol{d_{\mathrm{c}}}$
1	$d_1 + d_2 + d_7$	$d_2 + d_7$	d_7
2	$d_2 + d_7$	$d_2 + d_3 + d_7$	d_7
3	d_7	$d_3 + d_4 + d_7$	$d_4 + d_7$
4	d_7	$d_4 + d_7$	$d_4 + d_5 + d_7$
5	$d_6 + d_7$	d_7	$d_5 + d_6 + d_7$
6	$d_6 + d_1 + d_7$	d_7	$d_6 + d_7$

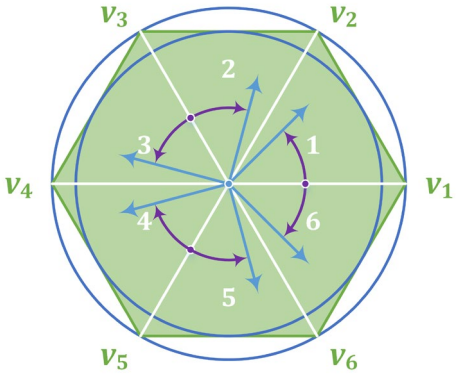

Figure 6-37 Determination of θ_{60°.

$$d_{\mathrm{CM}} = 1 - d_{\mathrm{DM}} = 1 - m_{\mathrm{a}} \cos(\theta_{60^\circ} - \pi/6) \tag{6-76}$$

which is shared between v_0 and v_7

$$d_{\mathrm{CM}} = d_0 + d_7 \tag{6-77}$$

In default SVM scheme, d_{CM} is evenly shared between v_0 and v_7. However, there are other possibilities, which will be described in the next section.

C. Parameters to Determine SVM Switching Patterns

In this study, two disciplines are respected to determine the SVM switching pattern: (1) the line voltages implemented by the SVM pattern in average of a switching cycle should follow the request, and (2) maximally one turn-on switching action and one turn-off switching action of each half-bridge branch are allowed within each switching cycle. The first discipline is the basic requirement for the inverter to drive a three-phase load, whereas the second is to avoid unnecessary switching losses.

When both disciplines are fulfilled, a specific SVM switching pattern can be determined by three parameters: amplitude modulation index m_{a}, distribution of CM state vector k_7 and interleave shift α_{shift}.

- **Amplitude Modulation Index m_a**

To form a continuous rotation of the projected voltage vector on αβ-plane $u_{\alpha\beta}$, the maximum possible length of the vector is the radius of the inscribed circle of the SVM hexagon

$$u_{\max} = \max\{\|u_{\alpha\beta}\|\} = u_{\mathrm{dc}} / \sqrt{3} \tag{6-78}$$

The amplitude modulation index describes the length of the voltage vector, and it can be defined as the radius in per unit by taking $u_{\max}$ as the base

$$m_{\mathrm{a}} = \|u_{\alpha\beta}\| / u_{\max} = \sqrt{3} \cdot \|u_{\alpha\beta}\| / u_{\mathrm{dc}} \tag{6-79}$$

A certain value of m_{a} indicates a certain level of line voltages. The line voltage rms can be determined as

$$U_{\mathrm{line.rms}} = m_{\mathrm{a}} \cdot u_{\mathrm{dc}} / \sqrt{2} \tag{6-80}$$

- **Distribution of CM State Vector k_7**

Assuming all phases share the same triangular carrier wave, based on SVM, d_1, d_2, d_3 until d_6 are decided by m_{a}. Hence if m_{a} is fixed, according to (6-76) and (6-77), d_{DM} and d_{CM} are fixed consequently.

However, as for how d_{CM} is shared between v_0 and v_7, there are many possibilities. This is described by a distribution factor k_7 in this study

$$k_7 = d_7 / d_{\mathrm{CM}} \in [\,0\,,1\,] \tag{6-81}$$

which means the share of d_7 over d_{CM}. A higher k_7 means to shift all phase voltage references up by the same amount while the line voltage references are kept constant. In conventional SVM, d_0 and d_7 share d_{CM} equally, which means $k_7 = 0.5$. In this study, k_7 is allowed to vary between 0 and 1.

- **Interleave Shift α**

Interleave shift in this study means to introduce phase difference between triangular carrier waves in SVM. An interleave shift will not change the average voltage in each phase but will change the time instant when the switching actions occur. Thus, the line voltages will be the same and this will not violate the SVM disciplines.

D. Control of Switching Harmonic Contents

Fourier analysis can be performed to quantify the harmonic contents for each switching cycle. For one single phase leg, considering a waveform centered at zero time instant, then the amplitude of the cosine component at harmonic order h is

$$a_h = \frac{2 \cdot \sin(h\pi d) - \sin(h\pi)}{\pi \cdot h} \tag{6-82}$$

while the amplitude of the sine component b_h is zero due to half-wave symmetric. The complex form is therefore

$$c_h = a_h + jb_h = \frac{2 \cdot \sin(h\pi d) - \sin(h\pi)}{\pi \cdot h} \tag{6-83}$$

When an interleave shift α is introduced, the complex Fourier component of this phase becomes

$$c_h = \frac{2}{\pi}\frac{\sin(h\pi d) - \sin(h\pi)}{h} e^{j\alpha} \tag{6-84}$$

Considering the waveform of Phase B as centered at zero and let Phase A leads B by α while Phase C lags B by α, then the CM content can be formulated as

$$\frac{u_{\gamma.\mathrm{sw}}}{u_{\mathrm{dc}}} = \frac{2}{\pi}\frac{\sin(\pi d_{\mathrm{a}})\cos\alpha + \sin(\pi d_{\mathrm{b}}) + \sin(\pi d_{\mathrm{c}})\cos\alpha}{3} \tag{6-85}$$

The time-domain waveforms of the switching frequency component with $k_7 = 0$ and $\alpha = 0°$ are shown in Figure 6-38. 360 points are calculated in each fundamental cycle, i.e. 1 point per degree. As can be noticed, with a lower value of m_{a}, the average over one fundamental cycle is higher and the ripple is lower.

The average values of the switching frequency component over one fundamental cycle with $\alpha = 0°$, $30°$, $60°$, $90°$ and $120°$ are shown in Figure 6-38. The average value of the component is not linear with respect to m_{a}. An increasing α leads to a decreasing average value. At $\alpha = 30°$, $60°$, $90°$ and $120°$, all the average values in the map decrease to 91.1%, 73.2%, 33.3% and 0% of that at $\alpha = 0°$. This can be explained analytically. The average value of the switching harmonic content over one fundamental cycle can be calculated as

$$\frac{U_{\gamma.\mathrm{sw}}}{U_{\mathrm{dc}}} = \frac{1}{2\pi}\int_0^{2\pi} \frac{u_{\gamma.\mathrm{sw}}}{u_{\mathrm{dc}}} d\theta \tag{6-86}$$

Due to three-phase symmetry,

$$\int_0^{2\pi} \sin(\pi d_{\mathrm{a}})\, d\theta = \int_0^{2\pi} \sin(\pi d_{\mathrm{b}})\, d\theta = \int_0^{2\pi} \sin(\pi d_{\mathrm{c}})\, d\theta \tag{6-87}$$

Hence the average can be calculated by considering only one phase and using a scaling factor $\frac{1+2\cdot\cos\alpha}{3}$

$$\int_0^{2\pi}\frac{u_{\gamma.\mathrm{sw}}}{u_{\mathrm{dc}}}d\theta=\frac{1+2\cdot\cos\alpha}{3}\frac{2}{\pi}\int_0^{2\pi}\sin(\pi d_{\mathrm{a}})\,d\theta \tag{6-88}$$

With $\alpha = 30°, 60°, 90°$ and $120°$, the scaling factor $\frac{1+2\cdot\cos\alpha}{3}$ gives 0.911, 0.732, 0.333 and 0 which are consistent with Figure 6-38. In addition, due to symmetry, the integrations of $\sin(\pi d_{\mathrm{a}})$ in sectors 1, 2 and 3 are equal to those in sector 6, 5 and 4 respectively. Therefore, (6-68) can be simplified as

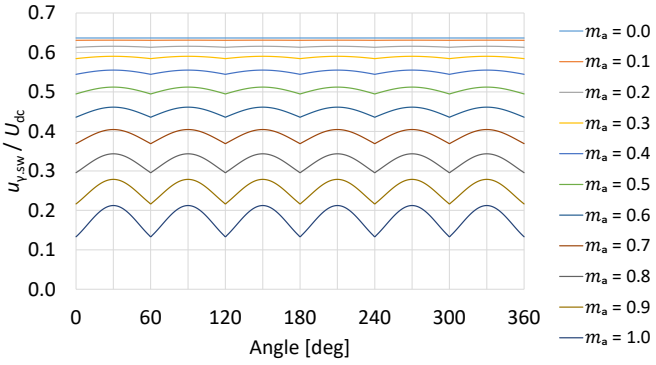

Figure 6-38 Switching harmonics in each switching cycle (k_7 = 0, $\alpha = 0°$).

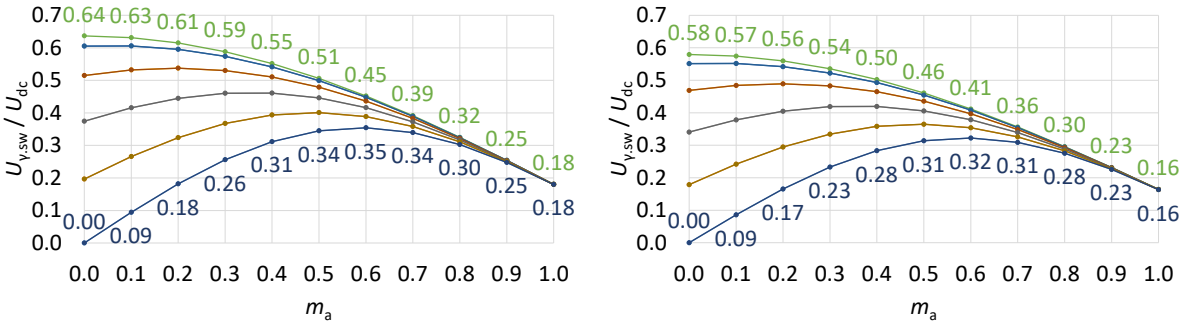

(a) $\alpha = 0°$.

(b) $\alpha = 30°$.

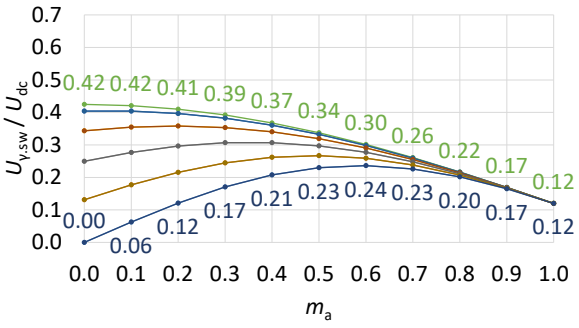

(c) $\alpha = 60°$.

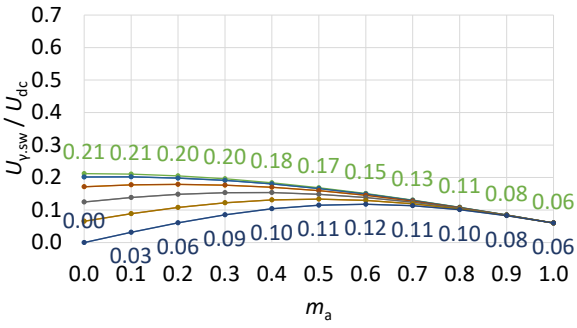

(d) $\alpha = 90°$.

k_7 = 0.0 k_7 = 0.1 k_7 = 0.2 k_7 = 0.3 k_7 = 0.4
k_7 = 0.5 k_7 = 0.6 k_7 = 0.7 k_7 = 0.8 k_7 = 0.9 k_7 = 1.0

Figure 6-39 Switching harmonics in average (m_a = 0.0 - 1.0, k_7 = 0.0 - 1.0).

$$\int_0^{2\pi} \sin(\pi d_{\mathrm{a}})\, d\theta = 2\int_0^{\pi/3} \{\sin(\pi d_0) + \sin(\pi d_7) + \sin[\pi(d_2 + d_7)]\} d\theta \quad (6\text{-}89)$$

6.2.2 Extraction of CM SVM Switching Harmonics

In this section, the principle of harmonic extraction is explained and then a model of the circuit is established. The validation of the circuit is presented in the next section.

A. Topology

The output of the inverter is split into two branches. One branch goes to the main ac load, which can be an electrical machine or a grid for example. The other branch goes to a harmonic extraction circuit which blocks DM harmonics while lets CM harmonics pass. After the extraction circuit is a transformer. The transformer is used for galvanic isolation and is not necessary for the functionality of the extraction circuit. The secondary side of the transformer is connected to a full-bridge rectifier, and then to the auxiliary dc load. The auxiliary dc load can be a battery or compressor for example. The harmonic extraction circuit and the transformer form a resonance circuit. The resonance frequency is tuned to the switching frequency. Hence the CM switching harmonics are extracted and delivered to the auxiliary dc load.

B. Harmonic Extraction Circuit

The extraction circuit is built to only let the CM switching harmonics pass through. To realize this, the circuit consists of a CM-passing coil which only lets CM components pass through, and capacitors connected in series which resonate with the coil. The resonance is tuned at the switching frequency, so that only the CM switching harmonics are able to pass through.

- **CM-Passing Coil**

With the positive direction of coil currents defined in Figure 6-40 (a), three-phase currents can be decomposed into CM and DM components. The CM part is the average of the three currents

$$i_{\mathrm{CM}} = (i_{\mathrm{a}} + i_{\mathrm{b}} + i_{\mathrm{c}})/3 \quad (6\text{-}90)$$

where i_{a}, i_{b}, i_{c} are the three-phase currents in the extraction circuit and i_{CM} is the CM component of them. The remaining part is the DM components

$$\boldsymbol{i}_{\mathrm{DM}} = \boldsymbol{i}_{\mathrm{abc}} - \boldsymbol{i}_{\mathrm{CM}} \quad (6\text{-}91)$$

where

$$\boldsymbol{i}_{\mathrm{DM}} = \begin{bmatrix} i_{\mathrm{DM.a}} \\ i_{\mathrm{DM.b}} \\ i_{\mathrm{DM.c}} \end{bmatrix}, \boldsymbol{i}_{\mathrm{abc}} = \begin{bmatrix} i_{\mathrm{a}} \\ i_{\mathrm{b}} \\ i_{\mathrm{c}} \end{bmatrix}, \boldsymbol{i}_{\mathrm{CM}} = \begin{bmatrix} i_{\mathrm{CM}} \\ i_{\mathrm{CM}} \\ i_{\mathrm{CM}} \end{bmatrix} \quad (6\text{-}92)$$

and $i_{\mathrm{DM.a}}$, $i_{\mathrm{DM.b}}$, $i_{\mathrm{DM.c}}$ are the three-phase DM component currents in the extraction circuit. Hence from (6-90) and (6-92), the sum of DM currents is zero

$$i_{\mathrm{DM.a}} + i_{\mathrm{DM.b}} + i_{\mathrm{DM.c}} = 0 \quad (6\text{-}93)$$

There are two ways to wind three-phase coils symmetrically as shown in Figure 6-40 (b) and (c). The flux linkages generated by the three-phase coils can be formulated as

$$\boldsymbol{\psi}_{\mathrm{abc}} = \boldsymbol{L}_{\mathrm{abc}} \boldsymbol{i}_{\mathrm{abc}} \tag{6-94}$$

where $\boldsymbol{\psi}_{\mathrm{abc}}$ is the flux linkage vector, $\boldsymbol{L}_{\mathrm{abc}}$ is the inductance matrix and $\boldsymbol{i}_{\mathrm{abc}}$ is the current vector

$$\boldsymbol{\psi}_{\mathrm{abc}} = \begin{bmatrix} \psi_{\mathrm{a}} \\ \psi_{\mathrm{b}} \\ \psi_{\mathrm{c}} \end{bmatrix}, \boldsymbol{L}_{\mathrm{abc}} = \begin{bmatrix} L_{\mathrm{s}} & L_{\mathrm{m}} & L_{\mathrm{m}} \\ L_{\mathrm{m}} & L_{\mathrm{s}} & L_{\mathrm{m}} \\ L_{\mathrm{m}} & L_{\mathrm{m}} & L_{\mathrm{s}} \end{bmatrix}, \boldsymbol{i}_{\mathrm{abc}} = \begin{bmatrix} i_{\mathrm{a}} \\ i_{\mathrm{b}} \\ i_{\mathrm{c}} \end{bmatrix} \tag{6-95}$$

Due to symmetry, all the self-inductances L_{s} are equal, so are the mutual inductances L_{m}. The self-inductances are the sum of the magnetizing inductance L_{M} and the leakage inductance L_{σ}

$$L_{\mathrm{s}} = L_{\mathrm{M}} + L_{\sigma} \tag{6-96}$$

The magnetizing inductance L_{M} indicates the ability of a coil for generating flux that links all other coils. The generated flux can be shared by other coils in series, as shown in Figure 6-40 (b), or in parallel, as shown Figure 6-40 (c). The link between different coils is indicated by mutual inductances L_{m}.

In the case of CM current component,

$$\boldsymbol{\psi}_{\mathrm{CM}} = \boldsymbol{L}_{\mathrm{abc}}\, \boldsymbol{i}_{\mathrm{CM}} = (L_{\mathrm{s}} + 2L_{\mathrm{m}})\, \boldsymbol{i}_{\mathrm{CM}} \tag{6-97}$$

Thus, the CM inductance is

$$L_{\mathrm{CM}} = L_{\mathrm{s}} + 2L_{\mathrm{m}} \tag{6-98}$$

In case of DM current component,

$$\boldsymbol{\psi}_{\mathrm{DM}} = \boldsymbol{L}_{\mathrm{abc}}\, \boldsymbol{i}_{\mathrm{DM}} = (L_{\mathrm{s}} - L_{\mathrm{m}})\, \boldsymbol{i}_{\mathrm{DM}} \tag{6-99}$$

Thus, the DM inductance is

$$L_{\mathrm{DM}} = L_{\mathrm{s}} - L_{\mathrm{m}} \tag{6-100}$$

As for the arrangement in Figure 6-40 (b), the main flux from one coil is shared by the other two in series. Thus, the mutual inductance equals magnetizing inductance

$$L_{\mathrm{m}} = L_{\mathrm{M}} \tag{6-101}$$

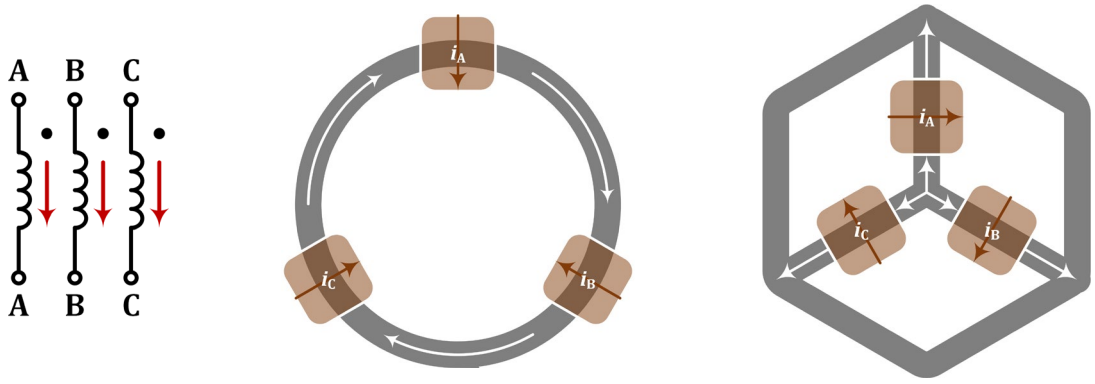

(a) Coil currents. (b) DM-Passing coil. (c) CM-Passing coil.

Figure 6-40 DM- and CM-passing coils.

In this case,

$$L_{\mathrm{CM}} = L_{\sigma} + 3L_{\mathrm{M}}\,, L_{\mathrm{DM}} = L_{\sigma} \tag{6-102}$$

As for the arrangement in Figure 6-40 (c), the main flux is shared by the other two in parallel. Besides, the flux generated by each coil counteracts each other. Thus, the mutual inductance should be half of the magnetizing inductance with a minus sign

$$L_{\mathrm{m}} = -L_{\mathrm{M}}/2 \tag{6-103}$$

In this case,

$$L_{\mathrm{CM}} = L_{\sigma}\,, L_{\mathrm{DM}} = L_{\sigma} + 3L_{\mathrm{M}}/2 \tag{6-104}$$

A Summary of these two winding arrangements is concluded in Table 6-3. As can be noticed, by increasing L_{M} while minimizing L_{σ}, in case of Figure 6-40 (b), CM components are blocked while DM components can pass. Hence it is a DM-passing coil. In case of Figure 6-40 (c), the situation is exactly the opposite, which means it is a CM-passing coil. With these two types of coils, CM and DM components can be separated as shown in Figure 6-41. In this study, the focus is to make use of the CM switching component. Thus, only a CM-passing coil is present in this study.

Table 6-3 DM- and CM-passing coils

	DM-Passing Coil	**CM-Passing Coil**
L_{m}	L_{M}	$-\frac{L_{\mathrm{M}}}{2}$
$\boldsymbol{L}_{\mathrm{abc}}$	$\begin{bmatrix} L_{\mathrm{M}}+L_{\sigma} & L_{\mathrm{M}} & L_{\mathrm{M}} \\ L_{\mathrm{M}} & L_{\mathrm{M}}+L_{\sigma} & L_{\mathrm{M}} \\ L_{\mathrm{M}} & L_{\mathrm{M}} & L_{\mathrm{M}}+L_{\sigma} \end{bmatrix}$	$\begin{bmatrix} L_{\mathrm{M}}+L_{\sigma} & -\frac{L_{\mathrm{M}}}{2} & -\frac{L_{\mathrm{M}}}{2} \\ -\frac{L_{\mathrm{M}}}{2} & L_{\mathrm{M}}+L_{\sigma} & -\frac{L_{\mathrm{M}}}{2} \\ -\frac{L_{\mathrm{M}}}{2} & -\frac{L_{\mathrm{M}}}{2} & L_{\mathrm{M}}+L_{\sigma} \end{bmatrix}$
L_{CM}	$L_{\sigma} + 3L_{\mathrm{M}}$	L_{σ}
L_{DM}	L_{σ}	$L_{\sigma} + \frac{3}{2}L_{\mathrm{M}}$

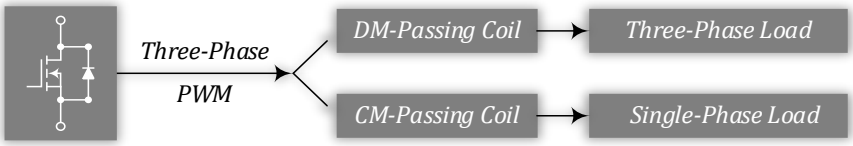

Figure 6-41 DM- and CM-passing coils.

- **Resonance Circuit**

A resonance can be formed by the CM-passing coil and the capacitance in series. The series-resonance is designed to extract the component at the switching frequency. The equivalence of the circuit from three-phase to single-phase in terms of the CM switching harmonic is illustrated in Figure 6-42. The resistance in three-phase can be regarded as being placed in parallel and becomes 1/3 in single-phase. The same applies for capacitance and inductance. The equivalent inductance in the CM circuit is the leakage inductance of the CM passing coil according to (6-104).

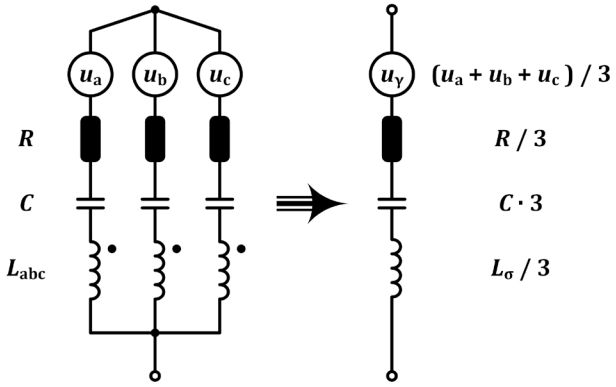

Figure 6-42 Resonance circuit formed by the extraction circuit.

C. *Rectifier and DC Load*

The transformer is connected to a rectifier. At the output of the rectifier is there a dc load. The dc load can be capacitive or inductive as shown in Figure 6-43. Assuming a sinusoidal voltage or current input, the rectifier load can be represented as an equivalent resistance at the sinusoidal frequency [66].

In case of a capacitive dc load, the voltage U_{C} is kept constant in steady state as shown in (a). The equivalent resistance can be calculated as

$$R_{\mathrm{eq.C}} = \frac{U_{\mathrm{rec.ac.amp}}}{I_{\mathrm{rec.ac.amp}}} = \frac{4/\pi \cdot U_{\mathrm{C}}}{\pi/2 \cdot I_{\mathrm{R}}} = \frac{8}{\pi^2} \cdot \frac{U_{\mathrm{C}}}{I_{\mathrm{R}}} = \frac{8}{\pi^2} \cdot R. \tag{6-105}$$

In case of an inductive dc load, the current I_{L} is kept constant in steady state as shown in (b). The equivalent resistance can be calculated as

$$R_{\mathrm{eq.L}} = \frac{U_{\mathrm{rec.ac.amp}}}{I_{\mathrm{rec.ac.amp}}} = \frac{\pi/2 \cdot U_{\mathrm{R}}}{4/\pi \cdot I_{\mathrm{L}}} = \frac{\pi^2}{8} \cdot \frac{U_{\mathrm{R}}}{I_{\mathrm{L}}} = \frac{\pi^2}{8} \cdot R. \tag{6-106}$$

In this study, since a capacitor is placed at the output of the rectifier, it is considered as the capacitive case shown in (a).

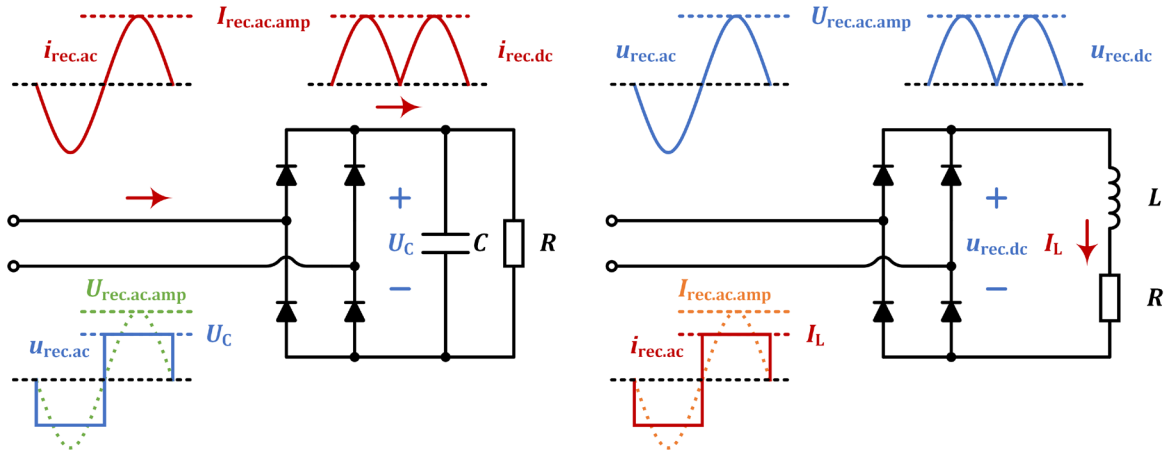

(a) Rectifier and capacitive load. (b) Rectifier and inductive load.

Figure 6-43 Rectifier connected with capacitive or inductive load.

6.2.3 Experimental Verification

An experimental setup is constructed to verify the control and circuit. Analytical results are calculated based on the modeling in Section 6.2.2 and compared with the experimental results. In the end, the impact on the inverter efficiency is investigated.

A. System Setup

The experimental setup is shown in Figure 6-44. Code Composer Studio is used to program a TMS320F28379 chip for controlling the inverter. The three-phase outputs of the inverter are split into two branches. One branch goes to the three-phase RL load whereas the other goes to the extraction circuit. 3C90 ferrite toroidal cores and litz wires are used to make the CM passing coil. The cross-section area of each core is 172 mm^2. Three layers of cores are stacked on top of each other to avoid saturation. The capacitors used here are from the C-CAP series in CELEM with coaxial technology. The three capacitors are placed in one row and clamped between a copper plate on top and an aluminum plate on bottom. The currents passing through the three capacitors join at the copper plate, and the joint current goes to the transformer.

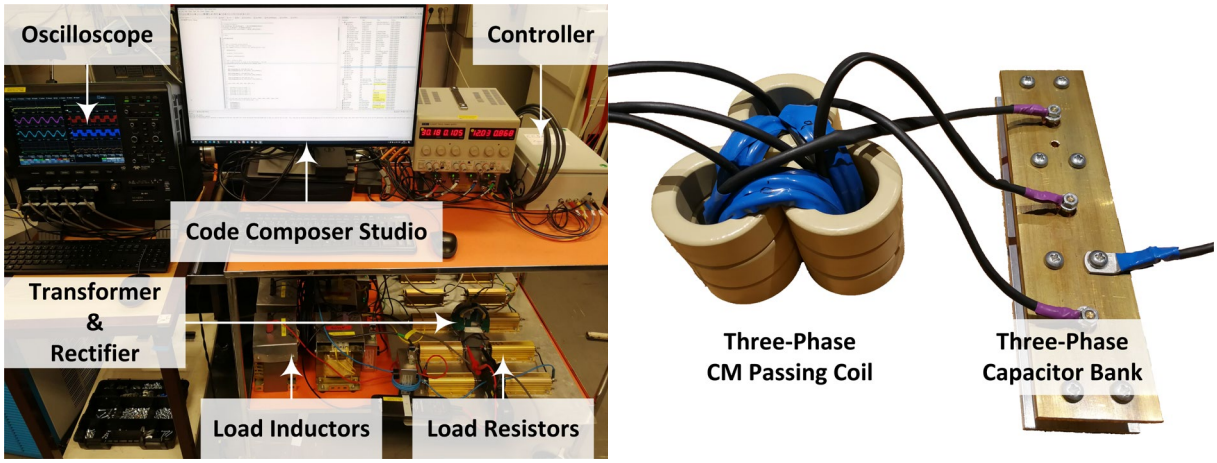

(a) Control panel, transformer, resistors and inductors. (b) Extraction circuit.

Figure 6-44 Experimental setup.

In this study, the inverter is constructed by three SiC power modules CAB450M12XM3. The parameters and operating condition of the inverter are concluded in Table 6-4. The parameters of the extraction circuit are concluded in Table 6-5. The transformer used in this study is the one designed for brushless excitation [23]. Litz wires with diameter 0.1 mm are used to form the windings on both sides. Pot cores with an airgap in between form the main flux path. The resistance and inductance of the three-phase RL load are listed in Table 6-5. The values are measured by powering the load from the inverter and applying FFT to the voltages and currents. The parameters of the diode rectifier and the field load in this study are listed in Table 6-8.

Table 6-4 SiC power electronic inverter parameters

Parameter	Symbol	Value	Unit
DC-link voltage	U_{dc}	200	V
Sine fundamental frequency	f_{sin}	100	Hz
Switching frequency	f_{sw}	30	kHz
Drain-source resistance	$R_{\mathrm{ds.on}}$	2.6	mΩ
Anti-parallel diode voltage drop	V_{F}	4.7	V
Blanking time	T_{b}	250	ns

Table 6-5 Extraction circuit parameters

Parameter	Symbol	Value	Unit
Resistance	R_{EXT}	47.73	mΩ
Number of turns	N_{EXT}	6	
Phase A self-inductance	$L_{\mathrm{EXT.A}}$	965.20	μH
Phase B self-inductance	$L_{\mathrm{EXT.B}}$	963.62	μH
Phase C self-inductance	$L_{\mathrm{EXT.C}}$	960.23	μH
Mutual-inductance	M_{EXT}	959.19	μH
Capacitance	C_{EXT}	85	nF

Table 6-6 Parameters of the transformer

Parameter	Symbol	Value	Unit
Airgap thickness	g_{T}	1	mm
Primary side number of turns	$N_{\mathrm{T.1}}$	20	
Secondary side number of turns	$N_{\mathrm{T.2}}$	7	
Primary side resistance	$R_{\mathrm{T.1}}$	138.00	mΩ
Secondary side resistance	$R_{\mathrm{T.2}}$	33.05	mΩ
Primary side self-inductance	$L_{\mathrm{T.1}}$	107.57	μH
Secondary side self-inductance	$L_{\mathrm{T.2}}$	16.66	μH
Mutual-inductance	$L_{\mathrm{T.m}}$	35.57	μH

Table 6-7 Parameters of the three-phase load

Parameter	Symbol	Value	Unit
AC load phase resistance	R_{RL}	22.45	Ω
AC load phase inductance	L_{RL}	32.38	mH

Table 6-8 Parameters of the diode rectifier and the field load

Parameter	Symbol	Value	Unit
Diode forward voltage drop	V_{F}	0.84	V
DC load capacitance	C_{f}	40	μF
DC load resistance	R_{f}	10.80	Ω
DC load inductance	L_{f}	83.05	mH

B. Resonance Profile

The diagram of resonance circuit is shown in Figure 6-45 (a). The extraction circuit and the transformer primary side form the resonance circuit in no-load condition. In load condition, the transformer secondary side and the equivalent resistance of the rectifier with the dc load are in parallel with the transformer magnetizing inductance. The circuit parameters are referred to the primary side of the transformer. The total admittance is firstly calculated based on the circuit parameters, and then measured with an RLC meter. The results are shown in Figure 6-46. The vertical axis shows the admittances in logarithm. The resonance points are indicated in tabs, and the resonance frequencies are around 30 kHz. In load condition, the admittance curves become damped due to the load resistance.

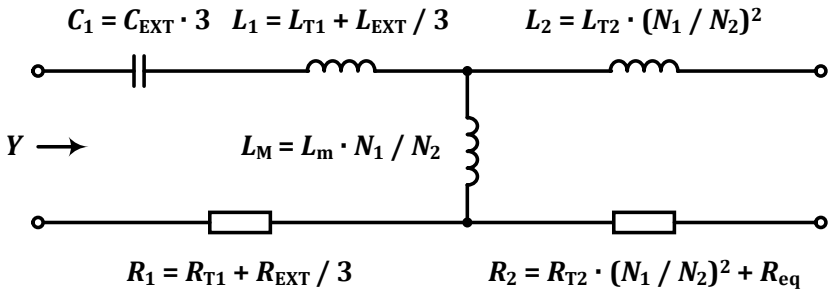

(a) Diagram of resonance circuit.

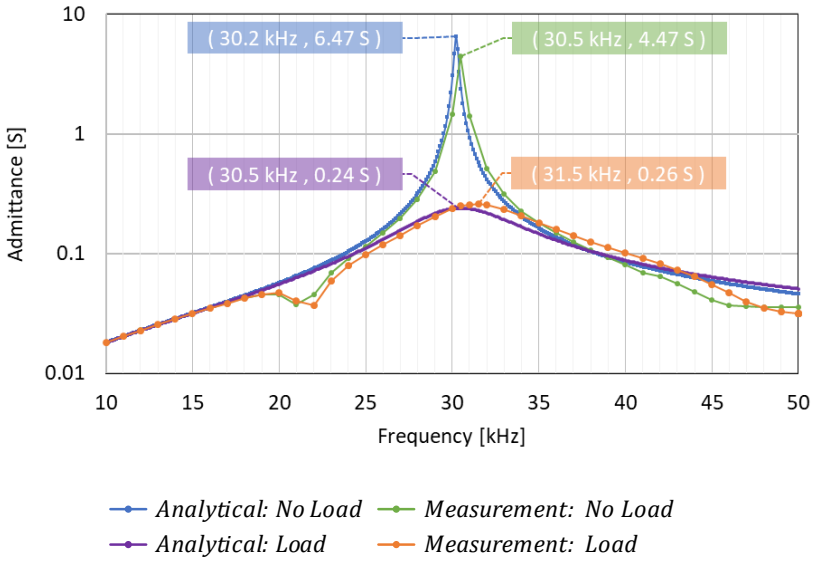

(b) Admittance of the resonance circuit.

Figure 6-45 Resonance analysis.

C. Analytical Results

Assuming that (1) the inverter and the rectifier are lossless; (2) purely the CM harmonic component at switching frequency passes the extraction circuit; (3) purely the fundamental frequency component goes to the RL load, then the three-phase power and the dc load power are calculated. Theoretically, the three-phase power should only be dependent on the amplitude modulation index. To calculate the power that goes to the dc load, the profile of CM contents illustrated in Figure 6-38 are utilized. Based on the circuit shown in Figure 6-45 (a), the overall admittance of the CM branch at 30 kHz is calculated to be 0.1975 S, including the CM extraction circuit, the transformer and the equivalent resistance of the dc load. 21%

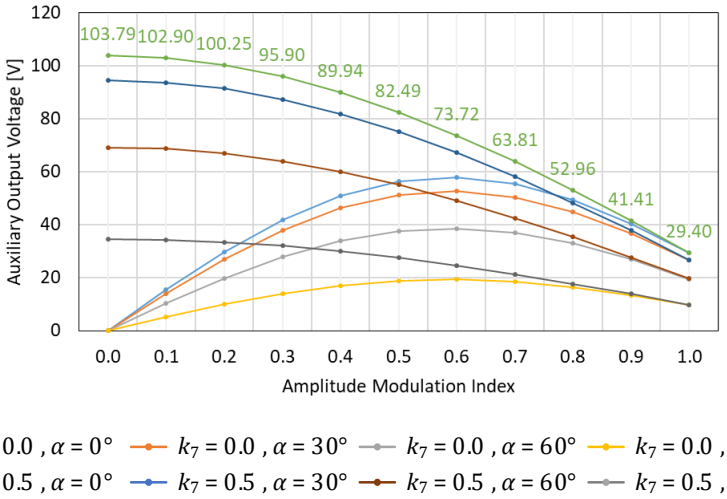

Figure 6-46 Auxiliary voltage output in from theoretical calculations.

of the CM branch current goes to the dc-load whereas the remaining goes to the magnetizing branch of the transformer. From there, the power delivered to the dc load is calculated. The profile of the dc load power is illustrated in Figure 6-46. The power delivery reaches the maximum in case of $k_7 = 0.5$ and $\alpha = 0°$. The solutions with other k_7 values are in different shapes compared with the case $k_7 = 0.5$. The curves are also symmetric with respect to $k_7 = 0.5$, i.e. the curve with $k_7 = 0.4$ is the same as that with $k_7 = 0.6$ and so forth. Adding shift α does not change the shape of the profile but scales down the curves evenly which is consistent to (6-88).

D. Simulation Results

To verify the analytical results, the SVM algorithm is programmed in Simulink while the circuit topology is built by PLECS blocks. The simulation results are presented in Figure 6-47. The shape of the profiles here closely follows the analytical curves shown in Figure 6-46. In analytical calculations, the side-band CM harmonics are neglected, while in simulations, the side-band CM harmonics contribute to the auxiliary output. Hence, the curves in simulation results are slightly higher than those in analytical results.

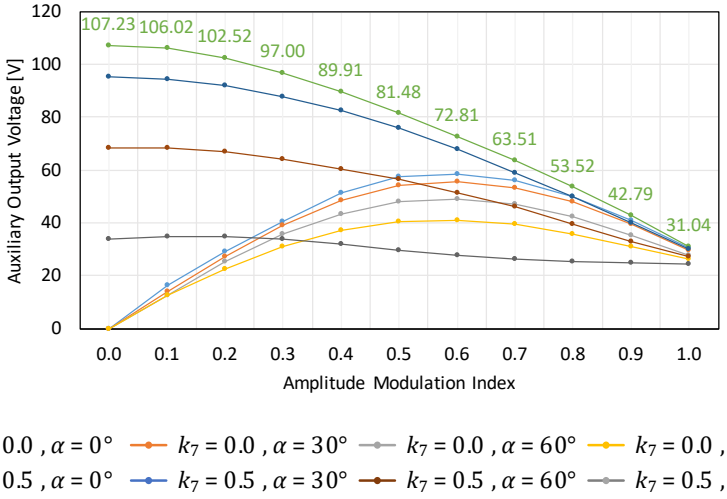

Figure 6-47 Auxiliary voltage output in circuit simulations.

E. Experimental Results

Experimental results are shown in Figure 6-48. The curves here closely follow the analytical results shown in Figure 6-46. In analytical calculations, converter losses are neglected. Due to this, the auxiliary dc output voltage is overestimated. However, at the same time, the side-band CM harmonics contribute to the auxiliary output in experiments but not in analytical calculations. In the end, the discrepancies due to these two factors are more or less canceled. Hence the overall results in Figure 6-48 closely follow the profiles in Figure 6-46. As can be noticed, the auxiliary voltage output varies with all three parameters, m_{a}, k_7 and α. This further indicates the possibility to independently control the auxiliary voltage output utilizing CM switching harmonics by tuning k_7 and α without violating the control of three-phase power. In the plots of auxiliary dc output, the curves cover a wide voltage range at low levels of m_{a}. However, as m_{a} increases, all curves start to converge. At $m_{\mathrm{a}} = 1.0$, there are minor differences between different curves. Besides, at this point, the voltage across the auxiliary dc load becomes very limited despite of whichever k_7 and α is chosen

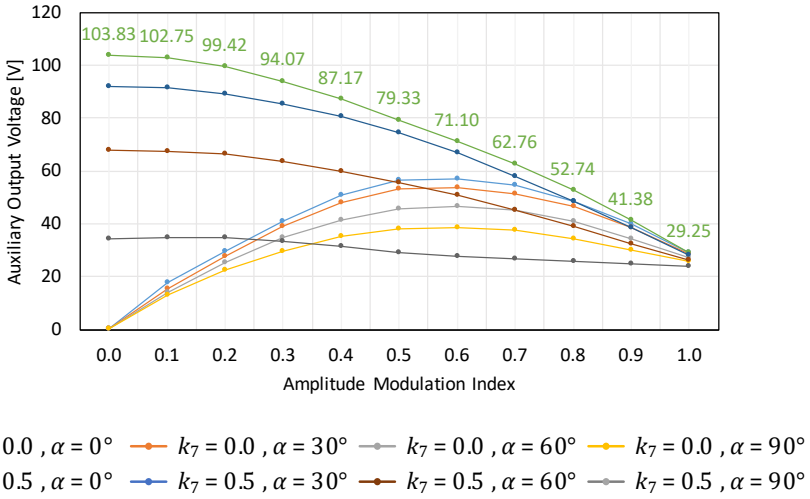

Figure 6-48 Auxiliary voltage output in experiments.

F. Experimental Waveforms

- **Original Case: $m_a = 0.5$ & $k_7 = 0.5$ & $\alpha = 0°$**

With $k_7 = 0.5$ and $\alpha = 0°$, the inverter is operating with conventional SVM technique which gives the maximum amount of CM switching harmonics. The time domain waveforms in this case are measured in experiments. Waveforms in one electrical fundamental cycle are presented in Figure 6-49. The inverter output currents $i_{\mathrm{INV.abc}}$ shown in (a) are split into the three-phase load currents $i_{\mathrm{RL.abc}}$ and the harmonic extraction currents $i_{\mathrm{EXT.abc}}$, as shown in (b). $i_{\mathrm{RL.abc}}$ are sinusoidal at 100 Hz while $i_{\mathrm{EXT.abc}}$ contain switching harmonics. The harmonic currents going through the harmonic extraction circuit are all in phase. This indicates that the CM passing coil successfully blocks the DM components. The currents from three-phase harmonic extraction circuit join together and the sum goes to the transformer as shown in (c). After the rectifier, the current becomes a dc quantity and goes to the dc load. The dc load current is 7.40 A.

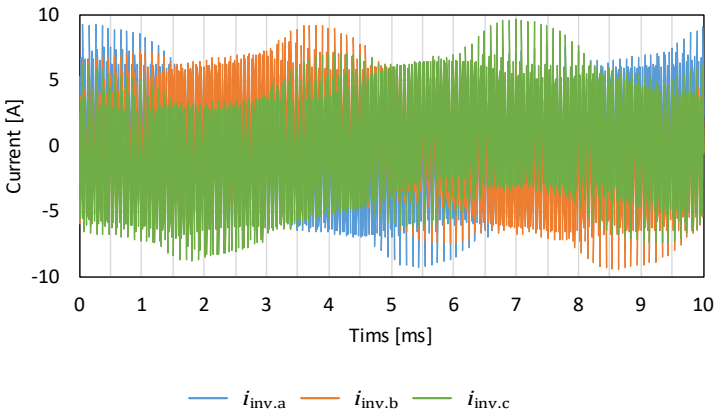

(a) Inverter currents.

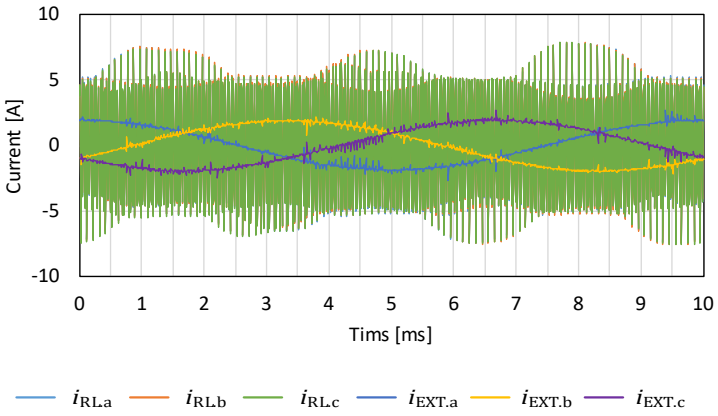

(b) Three-phase load & extraction circuit currents.

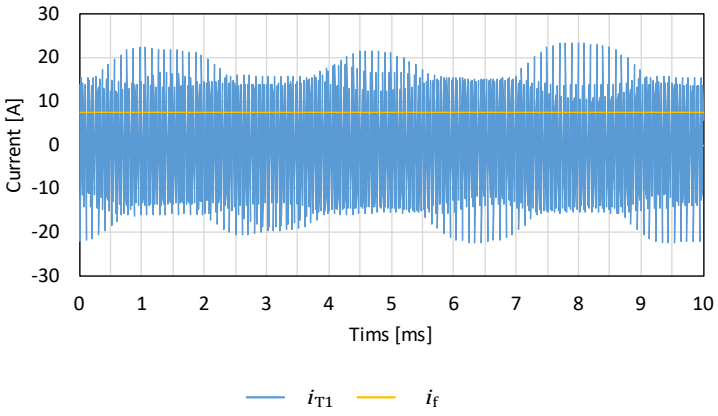

(c) Transformer primary side current & dc-load current.

Figure 6-49 Time-domain waveforms $m_a = 0.5$, $k_7 = 0.5$, $\alpha = 0°$.

- **Variation of k_7: $m_a = 0.5$ & $k_7 = 0.0$ & $\alpha = 0°$**

With $k_7 = 0.0$ and $\alpha = 0°$, the CM switching harmonics are reduced by placing 100% inactive duty cycle to state vector v_7. The waveforms are shown in Figure 6-50. As can be noticed, the three-phase RL currents in Figure 6-50 (b) are the same as those Figure 6-49 (b). this indicates that the adjustment of CM switching contents does not affect the power going to the three-phase load at fundamental frequency. At the same time, the harmonic contents going through the extraction circuit reduce. This leads to cleaner waveforms of inverter output currents and lower amplitude of transformer current. Consequently, the current reaches the dc load reduces. The dc load current is 5.26 A.

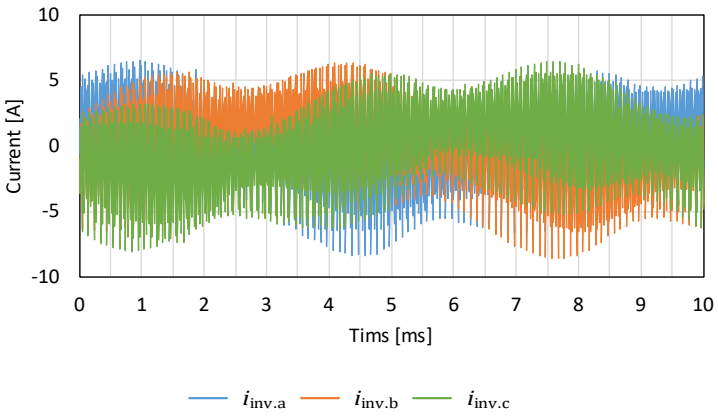

(a) Inverter currents.

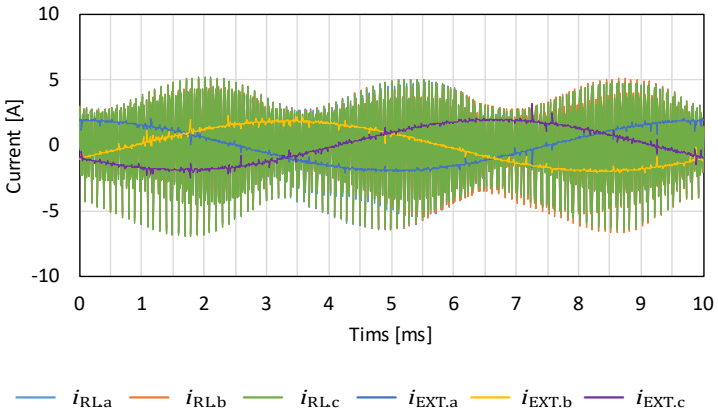

(b) Three-phase load & extraction circuit currents.

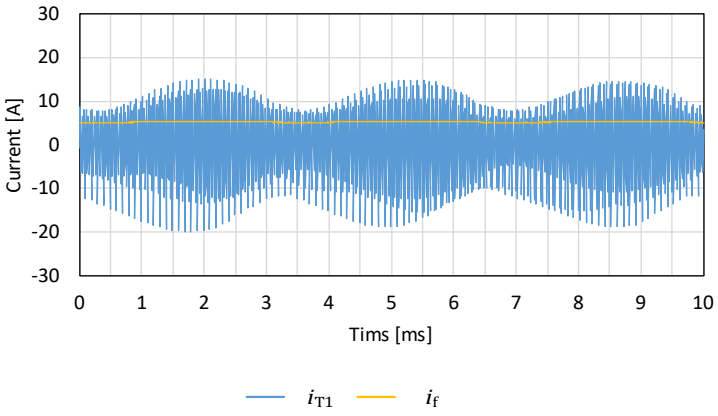

(c) Transformer primary side current & dc-load current.

Figure 6-50 Time-domain waveforms $m_a = 0.5$, $k_7 = 0.5$, $\alpha = 90°$.

- **Variation of α: $m_a = 0.5$ & $k_7 = 0.5$ & $\alpha = 90°$**

With $k_7 = 0.0$ and $\alpha = 0°$, the CM switching harmonics are reduced by introducing interleave phase shift of carrier waves. The waveforms are shown in Figure 6-51. The three-phase currents going to the RL load in this case are not affected either. Comparing with the case of $k_7 = 0.0$ and $\alpha = 0°$, the harmonic currents are reduced more significantly. As a consequence, the current reaches the dc load reduces to 2.75 A, 37% of the case with maximum CM switching harmonics. From analytical analysis, the CM harmonic at the switching frequency in this case are 33% of the maximum. These two values are similar, which

means the variation of power transfer can be roughly calculated by comparing CM switching harmonic contents.

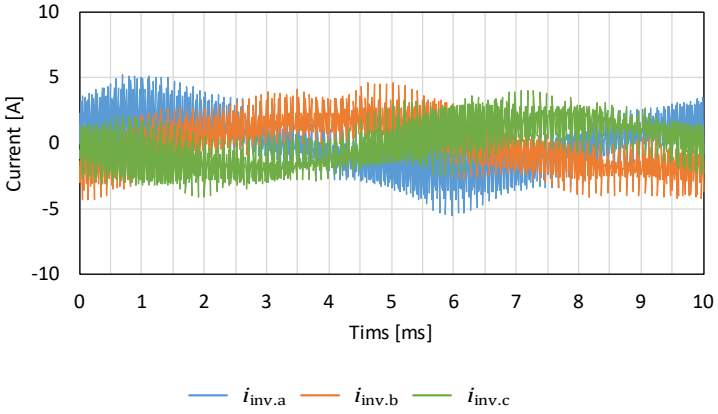

(a) Inverter currents.

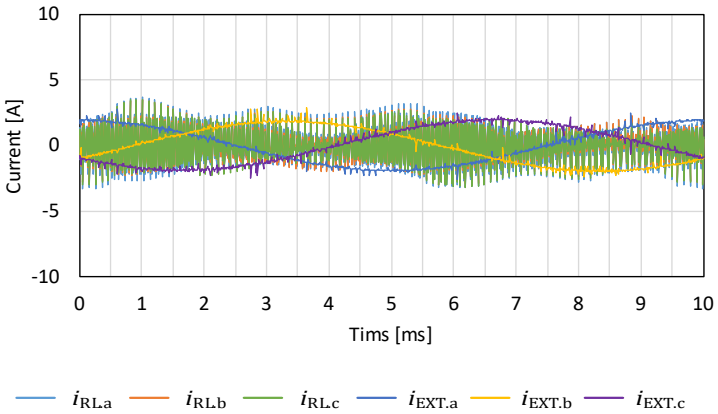

(b) Three-phase load & extraction circuit currents.

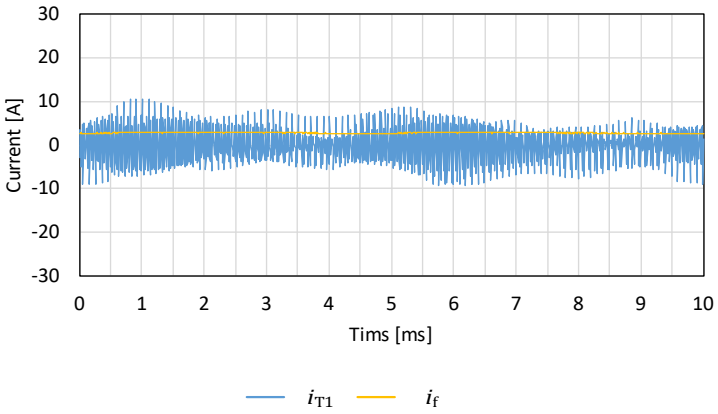

(c) Transformer primary side current & dc-load current.

Figure 6-51 Time-domain waveforms $m_{\mathrm{a}} = 0.5$, $k_7 = 0.0$, $\alpha = 0°$.

G. Impact on Inverter Efficiency

From the results presented in this section, it can be concluded that it is possible to extract the CM switching harmonics and use them to power an auxiliary dc load. To investigate whether the harmonic extraction would have an impact on the efficiency of the inverter, two tests are conducted. Firstly, the inverter is only connected to a three-phase RL load. In each phase, the resistance is 2.21 Ω and the inductance is 219 µH. Thereafter, the CM harmonic extraction branch and the auxiliary dc load are connected in parallel with the original three-phase RL

load. In both cases, the dc-link voltage is 200 V and the switching frequency is 30 kHz. The SVM is fixed to $k_7 = 0.5$ and $\alpha = 0°$, while m_a is swept from 0 to 0.9 with step of 0.1 and an additional point of 0.95. The inverter efficiency in both cases is calculated as

$$\eta = \frac{P_\mathrm{inv.out}}{P_\mathrm{inv.in}} \times 100\% = \frac{\sum_{i=1}^{N_\mathrm{sin}} p_\mathrm{inv.out}}{\sum_{i=1}^{N_\mathrm{sin}} p_\mathrm{inv.in}} \times 100\% \tag{6-107}$$

using the voltage and current measurements, where

$$\begin{aligned} p_\mathrm{inv.out} &= u_\mathrm{inv.a} \cdot i_\mathrm{inv.a} + u_\mathrm{inv.b} \cdot i_\mathrm{inv.b} + u_\mathrm{inv.c} \cdot i_\mathrm{inv.c} \\ p_\mathrm{inv.in} &= u_\mathrm{inv.dc} \cdot i_\mathrm{inv.dc} \end{aligned} \tag{6-108}$$

and N_sin is the number of samples taken over an integer number of fundamental cycles. The results are shown in Figure 6-52. The maximum inverter input power reaches 7.15 kW. The percentage of auxiliary load power consumption with respect to the total power consumption on both loads is shown in green. As can be seen, the curve decreases as m_a increases. The efficiency difference at different inverter input power levels and different percentages of auxiliary load power consumption is generally below 0.5%. Hence the influence of the extraction circuit on the inverter efficiency is minor.

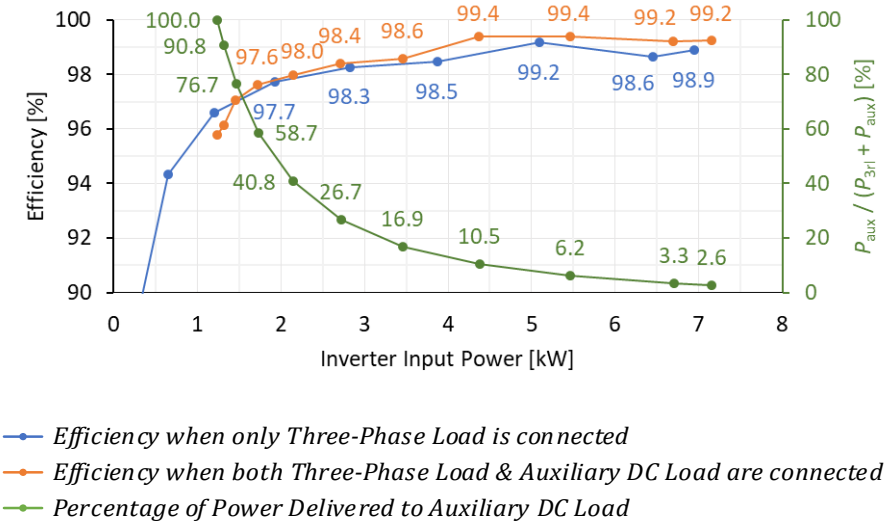

Figure 6-52 Experimental comparison of inverter efficiency between the cases with and without the auxiliary dc load.

6.3 Design of Rotating Transformers

6.3.1 Geometry Type

There are mainly two geometry types of rotating transformer design as shown in Figure 6-53. The axial excitation design shown in (a) provides identical pot cores on both primary and secondary sides. This is a benefit in case of replacement and mass production. However, due to the limitation of axial tolerance, the airgap after assembly may differ from the design. The radial excitation design shown in (b) provides the opposite characteristics. Radial tolerance is easier to guarantee whereas the primary and secondary sides have different shapes.

(a) Axial excitation. (b) Radial excitation.

Figure 6-53 Axial and radial excitation.

6.3.2 Electromagnetic Design

Neglecting leakage flux, the optimal solution is to avoid bottleneck in the flux path, in other words, to have equal cross-section along the flux path. As a simplification of the geometry, the cross-section at three points are designed to be equal, one mid-point at each tooth and the mid-point at the yoke. The selections of points are as shown in Figure 6-54, taking axial excitation design as an example.

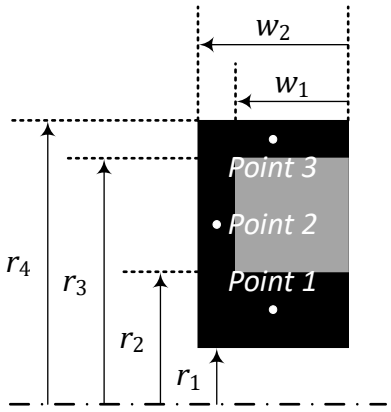

Figure 6-54 Parameters of axial excitation design.

Illustrated in parameters, it becomes

$$\pi \cdot (r_2^2 - r_1^2) = 2\pi \cdot \frac{(r_2 + r_3) \cdot (w_2 - w_1)}{2} = \pi \cdot (r_4^2 - r_3^2)$$
$$\Rightarrow \quad r_2^2 - r_1^2 = (r_2 + r_3) \cdot (w_2 - w_1) = r_4^2 - r_3^2 \tag{6-109}$$

With the assistance of FEA, the flux density at the three points are to be checked as verification.

6.3.3 Number of Turns

As for the selection of number of turns, firstly, the turns ratio needs to be decided. Neglecting leakage inductance, the field voltage should be equal to the dc-link voltage in case 1.0 duty cycle is applied. And in order to guarantee the maximum field current under minimum dc-link voltage at the highest temperature

$$\frac{N_2}{N_1} \approx \frac{U_{\mathrm{f.max}}}{U_{\mathrm{dc.min}}} = \frac{I_{\mathrm{f.max}} \cdot R_{\mathrm{f.max}}}{U_{\mathrm{dc.min}}} \tag{6-110}$$

Secondly, a higher number of turns reduces the flux density but increases the current density providing a fixed geometry. Following this relationship, the number of turns is adjusted simultaneously on both sides of the winding, to achieve a balance of the flux density and the current density.

6.3.4 Transformer Design for A 48 V EESM

A transformer for the excitation of a 48 EESM is designed by following the considerations introduced in this section. The ferrite material used in the pot core is PC40 from TDK with a saturation flux density of 400 mT and a suitable frequency range between 100 and 400 kHz. The axial excitation design is with identical pot cores on both primary and secondary sides. As mentioned in Section 6.3.1, this gives benefits in case of replacement and mass production. In this design, both electromagnetic performance and mechanical strength are considered. In terms of electromagnetics, the flux density along the flux path iron core is tuned to be as uniform as possible, whereas considering mechanical strength and manufacturing, the minimum thickness is set to 2 mm.

The flux distributions are shown in Figure 6-55. The Points 1, 2 and 3 are defined on both primary (stationary) side and secondary (rotary) side according to Figure 6-54. The flux densities of these points are illustrated in Figure 6-56. As can be noticed, the flux densities are far below 400 mT. The pot cores are over dimensioned to guarantee mechanical strength. In addition, the flux densities among all the three points on the same side are similar. This verifies the proposed design strategy. Furthermore, the peak flux density of the primary side is higher than the peak of the secondary side. This is due to the flux leakage on the primary side, i.e. some flux lines only link with the primary side. This is unavoidable if identical pot cores are used on both sides of the transformer. Otherwise, the size of the secondary side pot core can be reduced.

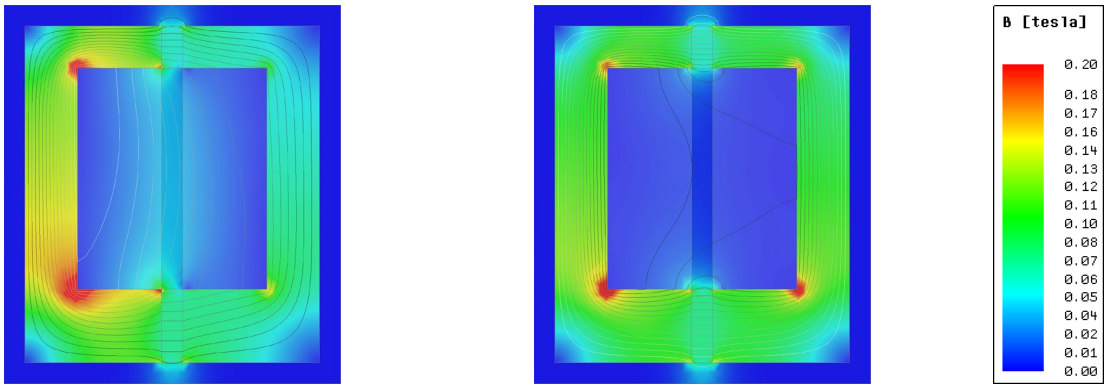

(a) Maximum flux density on primary side. (b) Maximum flux density on secondary side.

Figure 6-55 Flux distribution in the ferrite pot core.

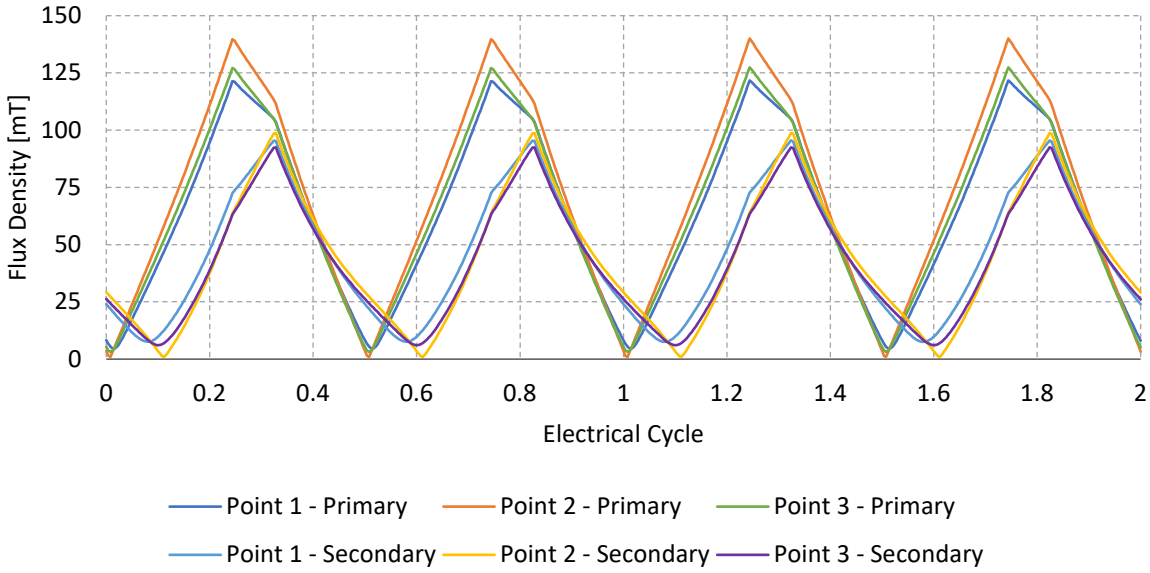

Figure 6-56 Flux density variations in FEM.

Due to the low flux density compared with the saturation level, the frequency for power transfer is selected as 100 kHz, i.e. the lowest value within the frequency range. This frequency selection minimizes iron-core loss as well as switching losses of the H-Bridge inverter. The experimental verifications of the transformer design are presented in Section 6.1.6

Chapter 7

Conclusions and Future Work

7.1 Conclusions

The purpose of this study is to investigate the potential of EESM application with high frequency brushless excitation in EVs. To achieve this aim, the focus is to confront the challenges and to tackle the problems. The following conclusions can be drawn from the study.

- Power factor flexibility is one key advantage provided by EESMs due to the freedom of adjusting field current. Hence it is essential to figure out in which condition can high power factor be achieved. To comprehend this, power factor contours in the dq-plane are proposed where high power factor area is identified. Among these contours, the one that defines unity power factor can be used to determine whether the maximum electromagnetic power can be achieved along the torque-speed envelope.
- The control strategies of EESMs become more complicated than those of PMSMs due to the additional control freedom introduced by the field current. Therefore, the dq-plane as the visualization method for PMSM analysis is insufficient for EESM analysis. The solution proposed in this study is to place the field current axis perpendicular to the dq-plane. Then the 2D contours in the dq-plane are extended to 3D isosurfaces. With the help of 3D isosurfaces, copper loss minimization can be illustrated as the copper loss isosurface and the torque isosurface pushing against each other.
- To achieve different targets of machine performance, control strategies are studied to find the most proper combination of stator and field currents. To minimize copper losses, the d-, q- and field currents are proportional to each other, in case of no saturation. Considering saturation of the iron-core, an iterative method is proposed to find the optimum solution in torque-speed map. The shape of the torque-speed envelope is unique whereas inside the envelope, the distributions of efficiency, power factor and terminal voltage are decided by different control strategies. Higher efficiency can be provided by EESMs at high speed range compared with PMSMs, due to the lower iron-core and copper losses in EESM field weakening.
- In dynamic current control with an FOC structure, the determination of current references becomes complicated due to the third degree of control freedom introduced by the field current. To tackle this problem, a current reference determination algorithm is proposed based on torque gradients. The gradients are defined in a coordinate system where the length of a current vector indicates the sum of stator and field copper losses. The move of current reference vector follows the direction of torque gradients so that the torque built by the current references catches the torque request swiftly. When the current limit or voltage limit is reached, extra constraints are introduced, and the move of the current reference vector is redirected. Consequently, the algorithm works for all conditions, including normal operation, torque-boosting and field weakening.

- Due to the magnetic mutual coupling between the stator and field windings, a current rise in the field winding would induce an EMF in the stator winding and vice versa. This introduces disturbances to the current responses. To deal with the disturbances, a compensation technique is proposed. An extra voltage component is added to the output of the controller which cancels the induced EMF due to the coupling. With this technique, the responses of current and electromagnetic torque become smooth.
- Compared with PMSMs, tradeoff is not needed in machine design between high starting torque and effective field weakening in EESMs, due to the flexible field current. The challenge is to maximumly make use of this advantage provided by EESMs. To realize this, two design criteria are derived: (1) to achieve unity power factor at peak power, the maximum flux generated by field winding needs to be able to cancel that generated by the stator winding, assuming no leakage flux, and (2) to maximize the starting torque under copper loss minimization, the copper losses in field winding and stator winding shall be almost equal. These criteria are integrated into the design procedure with multi-objective optimization where parametric sweep and Prieto Frontier are introduced. A 48 V EESM is prototyped during the study. In experimental verification, a torque density of 10 N·m/L is achieved including cooling jacket.
- Due to the inaccessibility of the field winding using HF brushless excitation, to have feedback control of field current in a closed loop, a dynamic estimation method is proposed. In this algorithm, the dc-link current is utilized as a feedback to correct the estimation. The current and temperature variations are tracked quite well. Based on the estimation, a closed-loop field current control is established. The field current reference is tracked within an error of 2% in experimental verifications. This closed-loop field current control enables a complete dynamic closed-loop control of the EESM.
- To drive an EESM, apart from the three-phase inverter that powers the machine stator, an additional dc-dc converter is needed to power the field winding. This increases the cost and becomes a disadvantage of the EESM drive system. To solve this problem, a topology is proposed to make use of the common mode switching harmonics of the stator inverter for field excitation. Switching harmonics are extracted, transferred through the transformer and used to power the field winding. With this topology, both the stator and field winding of the machine can be powered using only one inverter.

From all the challenges tackled in this study, it can be concluded that the application of EESMs in EVs is feasible.

7.2 On-Going and Future Work

Experimental verification of dynamic control will be conducted in a 360 V 60 kW EESM, including current reference determination and dynamic current control. The temperature rise in rotor is a challenge for EESMs due to copper losses in the field winding. To understand the heat transfer during machine operation, a lumped parameter model will be built. The key parameters of the model are obtained with the assistance of empirical method from literature and computational fluid dynamics (CFD) analysis. The focus is to characterize the heat dissipation and temperature rise of the field winding. One step further, cooling strategies will be searched. An integrated design of resolver, rotating transformer and telemetry is an interesting idea. In this case, the rotating transformer does three tasks in one unit: to power the field winding, to indicate the angle and to transfer field current measurements to the controller in stationary.

References

[1] Y. L. Petit, "Electric Vehicle Life Cycle Analysis and Raw Material Availability," Transport & Environment, 2017.

[2] A. Nordelöf, M. Messagie, A.-M. Tillman, M. L. Söderman and J. V. Mierlo, "Environmental impacts of hybrid, plug-in hybrid, and battery electric vehicles—what can we learn from life cycle assessment?," *The International Journal of Life Cycle Assessment,* vol. 19, no. 11, p. 1866–1890, 2014.

[3] International Energy Agency, "Global EV Outlook 2020," International Energy Agency, 2020.

[4] International Energy Agency, "Global EV Outlook 2017," International Energy Agency, 2017.

[5] J. D. Widmer, R. Martin and M. Kimiabeigi, "Electric Vehicle Traction Motors without Rare Earth Magnets," *Sustainable Materials and Technologies,* vol. 3, pp. 7-13, 2015.

[6] Macmill Magnets Co., Ltd., "Permanent Magnets," Macmill Magnets Co., Ltd., [Online]. Available: http://www.macmillmagnet.com/Permanentmagnets.html.

[7] Webcraft GmbH, "Physical Magnet Data," Webcraft GmbH, [Online]. Available: https://www.supermagnete.de/eng/data_table.php.

[8] H. R. Kirchmayr, "Permanent Magnets and Hard Magnetic Materials," *Journal of Physics D: Applied Physics,* vol. 29, no. 11, pp. 2763 - 2778, 1996.

[9] N. L. Guo, N. Bo, X. H. Wang, M. Li and P. Sun, "Simplified Calculation of the Maximum Energy Product for the Hard/Soft/Hard Trilayers," *Journal of Superconductivity and Novel Magnetism,* vol. 30, no. 10, pp. 2835 - 2840, 2017.

[10] D. G. Dorrell, A. M. Knight, M. Popescu, L. Evans and D. A. Staton, "Comparison of Different Motor Design Drives for Hybrid Electric Vehicles," in *2010 IEEE Energy Conversion Congress and Exposition*, Atlanta, 2010.

[11] C. C. Pavel, C. Thiel, S. Degreif, D. Blagoeva, M. Buchert, D. Schüler and E. Tzimas, "Role of substitution in mitigating the supply pressure of rare earths in electric road transport applications," *Sustainable Materials and Technologies,* vol. 12, pp. 62 - 72, 2017.

[12] Y. Yang, A. Walton, R. Sheridan, K. Güth, R. Gauß, O. Gutfleisch, M. Buchert, B.-M. Steenari, T. V. Gerven, P. T. Jones and K. Binnemans, "REE Recovery from End-of-Life NdFeB Permanent MagnetScrap: A Critical Review," *Journal of Sustainable Metallurgy,* vol. 3, no. 1, pp. 3 - 30, 2017.

[13] K. Binnemans, P. T. Jones, B. Blanpain, T. V. Gerven, Y. Yang, A. Walton and M. Buchert, "Recycling of Rare Earths: A Critical Review," *Journal of Cleaner Production,* vol. 51, pp. 1-22, 2013.

[14] E. M. Illiano, "Design of a Highly Efficient Brushless Current Excited Synchronouos Motor for Automotive Purposes," Swiss Federal Institute of Technology in Zurich (ETH Zurich), Zurich, 2014.

[15] E. M. Illiano, "Design of a Brushless Separately Excited Synchronous Motor," BRUSA Elektronik AG, Sennwald, 2014.

[16] L. Huang, Z. Zhu and W. Chu, "Optimization of Electrically Excited Synchronous Machine for Electrical Vehicle Applications," in *Machines and Drives (PEMD 2016), 8th IET International Conference on Power Electronics*, Glasgow, UK, 2016.

[17] A. D. Gioia, I. P. Brown, Y. Nie, R. Knippel, D. C. Ludois, J. Dai, S. Hagen and C. Alteheld, "Design and Demonstration of a Wound Field Synchronous Machine for Electric Vehicle Traction With Brushless Capacitive Field Excitation," *IEEE Transactions on Industry Applications,* vol. 54, no. 2, pp. 1390 - 1403, 2018.

[18] M. Tosi, "Rotary Transformer Design for Brushless Electrically Excited Synchronous Machines," University of Padua, Padua, 2014.

[19] T. Raminosoa and R. Wiles, "Contactless Rotor Excitation for Traction Motors," in *2018 IEEE Energy Conversion Congress and Exposition (ECCE)*, Portland, 2018.

[20] C. Stancu, T. Ward, K. M. Rahman, R. Dawsey and P. Savagian, "Separately Excited Synchronous Motor With Rotary Transformer for Hybrid Vehicle Application," *IEEE Transactions on Industry Applications,* vol. 54, no. 1, pp. 223-232, 2018.

[21] H. Krupp and A. Mertens, "Rotary Transformer Design for Brushless Electrically Excited Synchronous Machines," in *2015 IEEE Vehicle Power and Propulsion Conference (VPPC)*, Montreal, 2015.

[22] Y. Luan, B. Lin, X. Ma and X. Zhu, "Innovative Contactless Energy Transfer Accessory for Rotary Ultrasonic Machining and Its Circuit Compensation Based on Coil Turns," *IEEE Transactions on Industrial Electronics,* vol. 64, no. 10, pp. 7810 - 7818, 2017.

[23] Y. Liu, D. Pehrman, O. Lykartsis, J. Tang and T. Liu, "High frequency exciter of electrically excited synchronous motors for vehicle applications," in *2016 XXII International Conference on Electrical Machines (ICEM)*, Lausanne, Switzerland, 2016.

[24] R. Wang, S. Pekarek and M. Bash, "Alternative excitation strategies for a wound rotor synchronous machine drive," in *2012 IEEE Energy Conversion Congress and Exposition (ECCE)*, Raleigh, NC, USA, 2012.

[25] K. Liang, W. Xuhui and F. Tao, "A new method to plan the optimal field excitation current trajectory in a hybrid excitation machine," in *2011 International Conference on Electrical Machines and Systems (ICEMS)*, Beijing, China, 2011.

[26] O. Haala, B. Wagner, M. Hofmann and M. März, "Optimal current control of externally excited synchronous machines in automotive traction drive applications," *International Journal of Electrical, Computer, Energetic, Electronic and Communication Engineering,* vol. 7, no. 9, pp. 1133-1139, 2013.

[27] Y. Kim and K. Nam, "Copper-Loss-Minimizing Field Current Control Scheme for Wound Synchronous Machines," *IEEE Transactions on Power Electronics,* vol. 32, no. 2, pp. 1335 - 1345, 2017.

[28] J. Choi, I. Jeong, K. Nam and S. Jung, "Sensorless control for electrically energized synchronous motor based on signal injection to field winding," in *IECON 2013 - 39th Annual Conference of the IEEE Industrial Electronics Society*, Vienna, Austria, 2013.

[29] Y. Zhou and S. Long, "Sensorless Direct Torque Control for Electrically Excited Synchronous Motor Based on Injecting High-Frequency Ripple Current Into Rotor Winding," *IEEE Transactions on Energy Conversion,* vol. 30, no. 1, pp. 246 - 253, 2014.

[30] S. Choe, E. Jung and S.-K. Sul, "Sensorless Control of Synchronous Machine With an Inverter Integrated Rotor," *IEEE Transactions on Industry Applications,* vol. 50, no. 4, pp. 2584 - 2591, 2013.

[31] S. Feuersänger and M. Pacas, "Rotor position identification in synchronous machines by using the excitation machine as a sensor," in *2016 IEEE Symposium on Sensorless Control for Electrical Drives (SLED)*, Nadi, Fiji, 2016.

[32] J. Tang, Y. Liu and S. Nimananda, "Modeling and Experimental Verification of High-Frequency Inductive Brushless Exciter for Electrically Excited Synchronous Machines," *IEEE Transactions on Industry Applications,* vol. 55, no. 5, pp. 4613 - 4623, 2019.

[33] J. Tang, D. Pehrman, G. Mademlis and Y. Liu, "Common Mode Power Control of Three-Phase Inverter for Auxiliary Load without Access to Neutral Point (Submitted on 2021-02-20)," *IEEE Transactions on Power Electronics.*

[34] G. Mademlis, N. Sharma, Y. Liu and J. Tang, "Zero-Sequence Current Reduction Technique for Electrical Machine Emulators with DC-Coupling by Regulating the SVM Zero States (Submitted on 2021-02-23)," *IEEE Transactions on Industrial Electronics.*

[35] R. H. Park, "Two-Reaction Theory of Synchronous Machines Generalized Method of Analysis - Part I," *Transactions of the American Institute of Electrical Engineers,* pp. 716 - 727, 1929.

[36] W. C. Duesterhoeft, M. W. Schulz and E. Clarke, "Determination of Instantaneous Currents and Voltages by Means of Alpha, Beta, and Zero Components," *Transactions of the American Institute of Electrical Engineers,* pp. 1248 - 1255, 1951.

[37] H. Akagi, E. H. Watanabe and M. Aredes, "The Instantaneous Power Theory," in *Instantaneous Power Theory and Applications to Power Conditioning*, Tokyo / Rio de Janeiro, Wiley-IEEE Press, 2007, pp. 41 - 107.

[38] G. Bertotti, "Physical interpretation of eddy current losses in ferromagnetic materials. I. Theoretical considerations," *Journal of Applied Physics,* vol. 57, no. 6, pp. 2110 - 2117, 1985.

[39] Y. Liu, S. K. Kashif and A. M. Sohail, "Engineering Considerations on Additional Iron Losses due to Rotational Fields and Sheet Cutting," in *2008 18th International Conference on Electrical Machines*, Vilamoura, Portugal, 2008.

[40] J. Tang and Y. Liu, "Comparison of Copper Loss Minimization and Field Current Minimization for Electrically Excited Synchronous Motor in Mild Hybrid Drives," in *19th European Conference on Power Electronics and Applications (EPE'17 ECCE Europe)*, Warsaw, Poland, 2017.

[41] A. Boglietti, A. Cavagnino, M. Lazzari and M. Pastorelli, "A Simplified Thermal Model for Variable-Speed Self-Cooled Industrial Induction Motor," *IEEE TRANSACTIONS ON INDUSTRY APPLICATIONS,* vol. 39, no. 4, pp. 945 - 952, 2003.

[42] A. Boglietti, A. Cavagnino, M. Popescu and D. Staton, "Thermal Model and Analysis of Wound-Rotor Induction Machine," *IEEE Transactions on Industry Applications,* vol. 49, no. 5, pp. 2078 - 2085, 2013.

[43] D. Annaratone, "Steady Conduction," in *Engineering Heat Transfer*, Milano, Springer, 2010, pp. 13 - 28.

[44] J. Pyrhönen, T. Jokinen and V. Hrabovcová, "Insulation of Electrical Machines," in *Design of Rotating Electrical Machines*, Wiley, 2014, pp. 495 - 522.

[45] D. Staton, A. Boglietti and A. Cavagnino, "Solving the More Difficult Aspects of Electric Motor Thermal Analysis in Small and Medium Size Industrial Induction Motors," *IEEE Transactions on Energy Conversion,* vol. 20, no. 3, pp. 620 - 628, 2005.

[46] A. Boglietti, A. Cavagnino and D. Staton, "Determination of Critical Parameters in Electrical Machine Thermal Models," *IEEE Transactions on Industry Applications,* vol. 44, no. 4, pp. 1150 - 1159, 2008.

[47] D. Annaratone, "Convection," in *Engineering Heat Transfer*, Milano, Springer, 2010, pp. 63 - 138.

[48] D. A. Howey, P. R. N. Childs and A. S. Holmes, "Air-Gap Convection in Rotating Electrical Machines," *IEEE Transactions on Industrial Electronics,* vol. 59, no. 3, pp. 1367 - 1375, 2010.

[49] J. Fan, C. Zhang, Z. Wang and E. G. Strangas, "Thermal Analysis of Water Cooled Surface Mount Permanent Magnet Electric Motor for Electric Vehicle," in *2010 International Conference on Electrical Machines and Systems (ICEMS)*, Incheon, 2010.

[50] I. S. Bjorklund and W. M. Kays, "Heat Transfer Between Concentric Rotating Cylinders," *Journal of Heat Transfer,* vol. 81, no. 3, pp. 175 - 183, 1959.

[51] K. M. Becker and J. Kaye, "Measurements of Diabatic Flow in an Annulus With an Inner Rotating Cylinder," *Journal of Heat Transfer,* vol. 84, no. 2, pp. 97 - 104, 1962.

[52] K. M. Becker and J. Kaye, "The Influence of a Radial Temperature Gradient on the Instability of Fluid Flow in an Annulus With an Inner Rotating Cylinder," *Journal of Heat Transfer,* vol. 84, no. 2, pp. 106 - 110, 1962.

[53] *Drive motor system for electric vehicles—Part 2: Test methods,* The Standardization Administration of the People's Republic of China, 2015.

[54] H. Ge, J. W. Jiang, J. Ye and A. Emadi, "Behavior Study of Permanent Magnet Synchronous Machines Based on a New Normalized Model," *IEEE Transactions on Industrial Electronics,* vol. 66, no. 10, pp. 7539 - 7550, 2019.

[55] G. Choi and T. M. Jahns, "Investigation of Key Factors Influencing the Response of Permanent Magnet Synchronous Machines to Three-Phase Symmetrical Short-Circuit Faults," *IEEE Transactions on Energy Conversion,* vol. 31, no. 4, pp. 1488 - 1497, 2016.

[56] O. Haala, B. Wagner, M. Hofmann and M. März, "Optimal current control of externally excited synchronous machines in automotive traction drive applications," *International Journal of Electrical, Computer, Energetic, Electronic and Communication Engineering,* vol. 7, no. 9, pp. 1133 - 1139, 2013.

[57] G. Mademlis, R. Orbay, Y. Liu, N. Sharma, R. Arvidsson and T. Thiringer, "Multidisciplinary Cooling Design Tool for Electric Vehicle SiC Inverters Utilizing Transient 3D-CFD Computations," *eTransportation,* 2020.

[58] E. A. Grunditz, "Design, material and mass of machine parts," in *Design and Assessment of Battery Electric Vehicle Powertrain, with Respect to Performance, Energy Consumption and Electric Motor Thermal Capability*, Gothenburg, Chalmers Univrsity of Technology, 2016, pp. 100-102.

[59] European Commission, "LONGRUN Project Home Page," [Online]. Available: https://h2020-longrun.eu/. [Accessed 07 March 2021].

[60] V. G. Press, "Volvo Trucks presents second electric truck model in three weeks," Volvo Group Press, 05 August 2018. [Online]. Available: https://www.volvogroup.com/en-en/news/2018/may/news-2912374.html. [Accessed 28 September 2019].

[61] Mercedes Benz, "eActros: Heavy-duty electric truck," Mercedes Benz, [Online]. Available: https://www.mercedes-benz.com/en/vehicles/trucks/eactros-heavy-duty-electric-truck/. [Accessed 25 September 2019].

[62] Standardization Administration of P.R.C, GB/T 38146.2-2019 China Automotive Test Cycle Part 2: Heavy-Duty Vehicle, Standardization Administration of P.R.C, 2019.

[63] J. Tang and Y. Liu, "Design and Experimental Verification of a 48 V 20 kW Electrically Excited Synchronous Machine for Mild Hybrid Vehicles," in *2018 XIII International Conference on Electrical Machines (ICEM)*, Alexandroupoli, 2018.

[64] J. Tang and Y. Liu, "Study of Voltage Spikes and Temperature Rise in Power Module Based Integrated Converter for 48 V 20 kW Electrically Excited Synchronous Machines," in *APEC 2018*, San Antonio, Taxes, USA, 2018.

[65] D. Staton and J. Goss, "Open Source Electric Motor Models," Motor Design Ltd, Berlin, 2017.

[66] R. L. Steigerwald, "A Comparison of Half-Bridge Resonant Converter Topologies," *IEEE Transactions on Power Electronics,* vol. 3, no. 2, pp. 174 - 182, 1988.

[67] V. Ruuskanen, M. Niemela, J. Pyrhonen, S. Kanerva and J. Kaukonen, "Modelling the brushless excitation system for a synchronous machine," *IET Electric Power Applications,* vol. 3, no. 3, pp. 231 - 239, 2009.

[68] Texas Instruments, "Phase-Shifted Full-Bridge, Zero-Voltage Transition Design Considerations Application Report," Texas Instruments, Dallas, 2011.

[69] D. G. Holmes and T. A. Lipo, "Zero Space Vector Placement Modulation Strategies," in *Pulse Width Modulation for Power Converters: Principles and Practice*, Wiley-IEEE Press, 2003, pp. 259 - 336.

[70] G. V. Stanke, H. W. v. d. Broeck and H.-C. Skudelny, "Analysis and Realization of a Pulsewidth Modulator Based on Voltage Space Vectors," *IEEE Transactions on Industry Applications,* vol. 24, no. 1, pp. 142 - 150, 1988.

[71] W. C. Duesterhoeft, M. W. Schulz and E. Clarke, "Determination of Instantaneous Currents and Voltages by Means of Alpha, Beta, and Zero Components," *Transactions of the American Institute of Electrical Engineers,* vol. 70, no. 2, pp. 1248 - 1255, 1951.

[72] L. Rovere, A. Formentini, G. L. Calzo, P. Zanchetta and T. Cox, "Zero-Sequence Voltage Elimination for Dual-Fed Common DC-Link Open-End Winding PMSM High-Speed Starter–Generator—Part I: Modulation," *IEEE Transactions on Industry Applications,* vol. 55, no. 6, pp. 7804 - 7812, 2019.

[73] R. Grune, "Verlustoptimaler Betrieb einer elektrisch erregten Synchronmaschine für den Einsatz in Elektrofahrzeugen," Technische Universität Berlin, Berlin, 2012.

[74] C. L. Fortescue, "Method of Symmetrical Co-Ordinates Applied to the Solution of Polyphase Networks," *AIEE Transactions,* vol. 37, p. 1027–1140, 1918.

[75] D. A. Staton, T. J. Miller and S. E. Wood, "Maximising the Saliency Ratio of the Synchronous Reluctance Motor," *IEE Proceedings B - Electric Power Applications,* vol. 140, no. 4, pp. 249 - 259, 1993.

[76] D. A. Staton and A. Cavagnino, "Convection Heat Transfer and Flow Calculations Suitable for Electric Machines Thermal Models," *IEEE Transactions on Industrial Electronics,* vol. 55, no. 10, pp. 3509 - 3516, 2008.

[77] C. Nordling and J. Österman, "T - 1 Mechanics and Thermal Physics," in *Physics Handbook for Science and Engineering*, Uppsala, Studentlitteratur AB, 2006, pp. 27 - 42.

[78] D. Annaratone, "Radiation," in *Engineering Heat Transfer*, Milano, Springer, 2010, pp. 139 - 190.

[79] M. Hinkkanen, H. A. A. Awan, Z. Qu, T. Tuovinen and F. Briz, "Current Control for Synchronous Motor Drives: Direct Discrete-Time Pole-Placement Design," *IEEE Transactions on Industry Applications,* vol. 52, no. 2, pp. 1530 - 1541, 2015.

[80] N. Mohan, T. M. Undeland and W. P. Robbins, "Three-Phase Inverter," in *Power Electronics: Converters, Applications, and Design*, John Wiley & Sons, Inc, 2003, pp. 225 - 236.

[81] L. Harnefors, "Current Control," in *Control of Variable-Speed Drives*, Applied Signal Processing and Control, Department of Electronics, Mälardalen University, 2002, pp. 19 - 29.

[82] International Energy Agency, "Global EV Outlook 2019," International Energy Agency, 2019.

[83] S. Skoog, "Experimental and model based evaluation of mild hybrid fuel consumption gains and electric machine utilization for personal vehicle application," in *2017 IEEE Transportation Electrification Conference and Expo, Asia-Pacific (ITEC Asia-Pacific)*, Harbin, 2017.

[84] Y. Tang, "AC Machinery Fundamentals," in *Electrical Machinery (Chinese)*, Beijing, China Machine Press, 2014, pp. 135 - 176.

[85] Cogent Power, "Typical Data for SURA M235-35A," Cogent Power, Surahammar, 2008.

[86] Cogent Power, "Typical Data for SURA M250-35A," Cogent Power, Surahammar, 2006.

[87] J. Tang and Y. Liu, "Dynamic Current Control to Compensate for Magnetic Mutual Coupling in Electrically Excited Synchronous Machines," in *2020 International Conference on Electrical Machines (ICEM)*, Gothenburg, Sweden, 2020.

[88] J. Tang and Y. Liu, "Design of Electrically Excited Synchronous Machines to Achieve Unity Power Factor in Field Weakening for Long-Haul Electric Trucks," in *2020 International Conference on Electrical Machines (ICEM)*, Gothenburg, Sweden, 2020.

[89] J. Tang, Y. Liu and S. Lundberg, "Estimation Algorithm for Current and Temperature of Field Winding in Electrically Excited Synchronous Machines With High-Frequency Brushless Exciters," *IEEE Transactions on Power Electronics,* vol. 36, no. 3, pp. 3512 - 3523, 2021.

[90] Standardization Administration of P.R.C, GB/T 38146.1-2019 China Automotive Test Cycle Part 1: Light-Duty Vehicle, Standardization Administration of P.R.C, 2019.

[91] Y. Kim and K. Nam, "Copper-Loss-Minimizing Field Current Control Scheme for Wound Synchronous Machines," *IEEE Transactions on Power Electronics,* vol. 32, no. 2, pp. 1335 - 1345, 2017.

Appendix A

Machine Model Transformation

In this appendix, the modeling of EESMs is firstly established in stational frame. Then it is transformed into αβ-frame and dq-frame.

A.1 Modeling in ABC-Frame

The stator voltages are composed by resistive voltage drops and electromotive forces (EMF) due to the derivative of magnetic flux linkages

$$\begin{bmatrix} u_\mathrm{a} \\ u_\mathrm{b} \\ u_\mathrm{c} \\ u_\mathrm{f} \end{bmatrix} = \begin{bmatrix} R_\mathrm{a} & 0 & 0 & 0 \\ 0 & R_\mathrm{b} & 0 & 0 \\ 0 & 0 & R_\mathrm{c} & 0 \\ 0 & 0 & 0 & R_\mathrm{f} \end{bmatrix} \begin{bmatrix} i_\mathrm{a} \\ i_\mathrm{b} \\ i_\mathrm{c} \\ i_\mathrm{f} \end{bmatrix} + \frac{\mathrm{d}}{\mathrm{d}t} \begin{bmatrix} \psi_\mathrm{a} \\ \psi_\mathrm{b} \\ \psi_\mathrm{c} \\ \psi_\mathrm{f} \end{bmatrix} \tag{A-1}$$

where u denotes voltages, R denotes resistances, i denotes currents, ψ denotes flux linkages, t denotes time and a, b, c and f denote Phases A, B, C and field windings respectively. If the machine is operating in the linear region of the BH curve, the flux linkages can be further expressed as [73]

$$\begin{bmatrix} \psi_\mathrm{a} \\ \psi_\mathrm{b} \\ \psi_\mathrm{c} \\ \psi_\mathrm{f} \end{bmatrix} = L_\mathrm{abcf} \begin{bmatrix} i_\mathrm{a} \\ i_\mathrm{b} \\ i_\mathrm{c} \\ i_\mathrm{f} \end{bmatrix} = \begin{bmatrix} L_\mathrm{a}(\theta_\mathrm{r}) & M_\mathrm{ab}(\theta_\mathrm{r}) & M_\mathrm{ac}(\theta_\mathrm{r}) & M_\mathrm{af}(\theta_\mathrm{r}) \\ M_\mathrm{ba}(\theta_\mathrm{r}) & L_\mathrm{b}(\theta_\mathrm{r}) & M_\mathrm{bc}(\theta_\mathrm{r}) & M_\mathrm{bf}(\theta_\mathrm{r}) \\ M_\mathrm{ca}(\theta_\mathrm{r}) & M_\mathrm{cb}(\theta_\mathrm{r}) & L_\mathrm{c}(\theta_\mathrm{r}) & M_\mathrm{cf}(\theta_\mathrm{r}) \\ M_\mathrm{fa}(\theta_\mathrm{r}) & M_\mathrm{fb}(\theta_\mathrm{r}) & M_\mathrm{fc}(\theta_\mathrm{r}) & L_\mathrm{f} \end{bmatrix} \begin{bmatrix} i_\mathrm{a} \\ i_\mathrm{b} \\ i_\mathrm{c} \\ i_\mathrm{f} \end{bmatrix} \tag{A-2}$$

where L denotes self-inductances, M denotes mutual-inductances, θ_r denotes rotor angle with respect to the axis of Phase A (a-axis). In the L_abcf matrix, L_f is the rotor self-inductance which is a constant, whereas other inductances are variables dependent on rotor position θ_r. With the help of Figure A-1, the tendency of these rotor-position-dependent inductances can be figured out.

When $\theta_\mathrm{r} = 0$, the rotor is aligned with the a-axis:

- The reluctance of Phase A reaches the minimum and therefore, the $L_\mathrm{a}(\theta_\mathrm{r})$ achieves the maximum.
- The b- and c-axis share the magnetic path maximally, which means Phase B and C share the flux maximally and therefore, the mutual-inductances of Phase B and C, $M_\mathrm{bc}(\theta_\mathrm{r})$ and $M_\mathrm{cb}(\theta_\mathrm{r})$, achieve the maximum.
- The excitation flux generated by i_f enhances the a-axis flux maximally and therefore, the $M_\mathrm{af}(\theta_\mathrm{r})$ and $M_\mathrm{fa}(\theta_\mathrm{r})$ achieve the maximum.

When $\theta_\mathrm{r} = \pi$, the rotor is anti-aligned with the a-axis:

- $L_\mathrm{a}(\theta_\mathrm{r})$, $M_\mathrm{bc}(\theta_\mathrm{r})$ and $M_\mathrm{cb}(\theta_\mathrm{r})$ still achieve the maximum since they are independent from i_f.

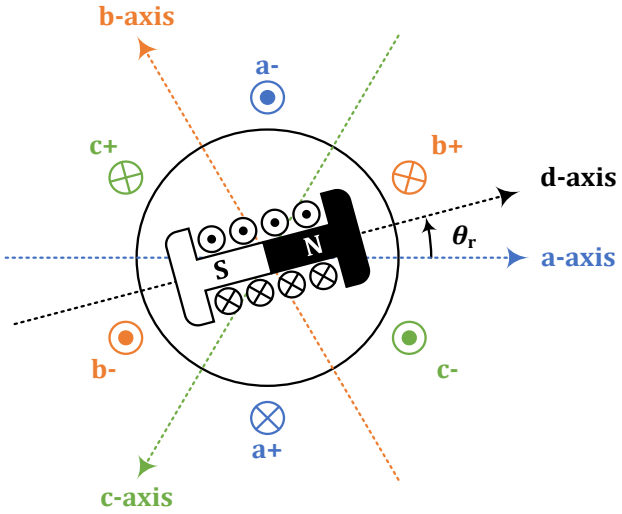

Figure A-1 Schematic of EESM windings in space.

- The excitation flux generated by i_{f} suppresses the a-axis flux maximally and therefore, the $M_{\mathrm{af}}(\theta_{\mathrm{r}})$ and $M_{\mathrm{fa}}(\theta_{\mathrm{r}})$ achieve the minimum.

The expressions of the inductances when the rotor is aligned with other axes can be addressed similarly. Assuming that the inductance dependent on the angle is sinusoidal, as shown in Figure A-2, then the *wave model* can be established as [73]

$$\begin{aligned} L_{\mathrm{a}}(\theta_{\mathrm{r}}) &= L_{\mathrm{s\cdot\Sigma}} + L_{\mathrm{s\cdot\Delta}} \cdot \cos(2\theta_{\mathrm{r}}) \\ L_{\mathrm{b}}(\theta_{\mathrm{r}}) &= L_{\mathrm{s\cdot\Sigma}} + L_{\mathrm{s\cdot\Delta}} \cdot \cos\left(2\theta_{\mathrm{r}} + \frac{2\pi}{3}\right) \\ L_{\mathrm{c}}(\theta_{\mathrm{r}}) &= L_{\mathrm{s\cdot\Sigma}} + L_{\mathrm{s\cdot\Delta}} \cdot \cos\left(2\theta_{\mathrm{r}} - \frac{2\pi}{3}\right) \end{aligned} \tag{A-3}$$

$$\begin{aligned} M_{\mathrm{ab}}(\theta_{\mathrm{r}}) = M_{\mathrm{ba}}(\theta_{\mathrm{r}}) &= M_{\mathrm{s\cdot\Sigma}} + L_{\mathrm{s\cdot\Delta}} \cdot \cos\left(2\theta_{\mathrm{r}} - \frac{2\pi}{3}\right) \\ M_{\mathrm{bc}}(\theta_{\mathrm{r}}) = M_{\mathrm{cb}}(\theta_{\mathrm{r}}) &= M_{\mathrm{s\cdot\Sigma}} + L_{\mathrm{s\cdot\Delta}} \cdot \cos(2\theta_{\mathrm{r}}) \\ M_{\mathrm{ca}}(\theta_{\mathrm{r}}) = M_{\mathrm{ac}}(\theta_{\mathrm{r}}) &= M_{\mathrm{s\cdot\Sigma}} + L_{\mathrm{s\cdot\Delta}} \cdot \cos\left(2\theta_{\mathrm{r}} + \frac{2\pi}{3}\right) \end{aligned} \tag{A-4}$$

$$\begin{aligned} M_{\mathrm{af}}(\theta_{\mathrm{r}}) = M_{\mathrm{fa}}(\theta_{\mathrm{r}}) &= L_{\mathrm{m}} \cdot \cos(\theta_{\mathrm{r}}) \\ M_{\mathrm{bf}}(\theta_{\mathrm{r}}) = M_{\mathrm{fb}}(\theta_{\mathrm{r}}) &= L_{\mathrm{m}} \cdot \cos\left(\theta_{\mathrm{r}} - \frac{2\pi}{3}\right) \\ M_{\mathrm{cf}}(\theta_{\mathrm{r}}) = M_{\mathrm{fc}}(\theta_{\mathrm{r}}) &= L_{\mathrm{m}} \cdot \cos\left(\theta_{\mathrm{r}} + \frac{2\pi}{3}\right) \end{aligned} \tag{A-5}$$

where $L_{\mathrm{s\cdot\Sigma}}$ and $M_{\mathrm{s\cdot\Sigma}}$ are the average of the stator self-inductance and the stator mutual-inductance over one electric period respectively, $L_{\mathrm{s\cdot\Delta}}$ is the peak-to-average inductance variation of the stator, L_{m} is the amplitude of the stator-rotor mutual-inductance variation. It should be pointed out that, $M_{\mathrm{s\cdot\Sigma}}$ is negative, since the flux generated by the Phase A coil goes oppositely to the Phase B coil.

A.2 ABC-DQO Coordinate Transformation

As can be noticed in (A-2), the modeling of the EESM in abc-frame is complicated since the inductance matrix L_{abcf} is dependent on the rotor position. In machine design, it is common to analyze the direct-axis (d-axis) and quadrature-axis (q-axis) flux paths separately. The d-

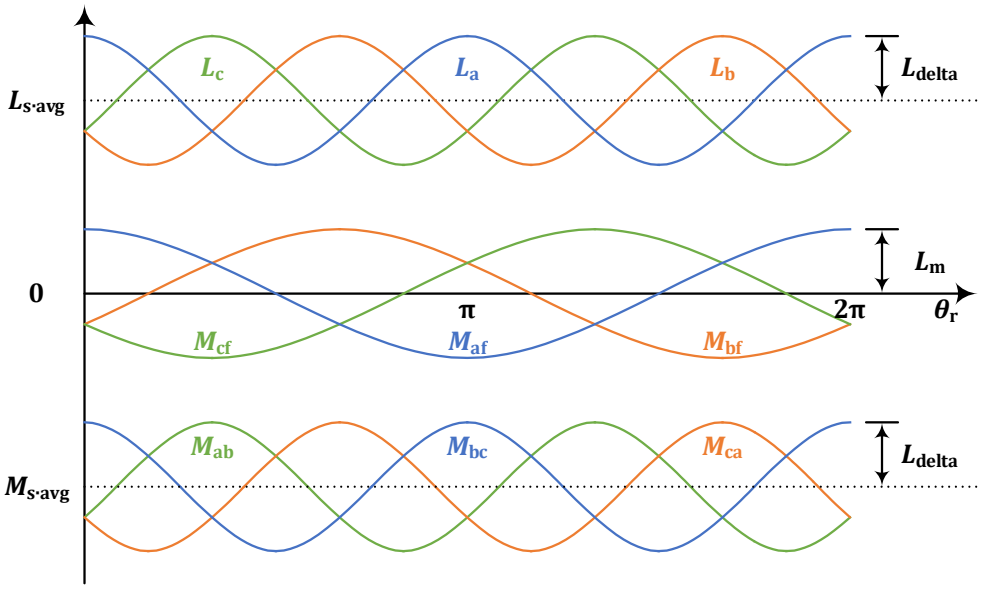

Figure A-2 Inductance wave model of EESM.
The waveforms are an example for illustration and the amplitudes are not to scale.

and q-axis flux paths of the EESM are shown in Figure A-3, where the d-axis is defined as the rotor main flux path and the q-axis is defined as 90°, electrical angle, leading the d-axis. The basic adjustment of rotor geometry is performed based on the flux distribution in dq-frame. Besides, in machine control, it is a mature technology to control DC quantities in dq-frame instead of AC quantities in abc-frame. These are the major reasons why abc → dq transformation is performed.

The abc ↔ αβγ transformation was proposed in [36] while the αβγ ↔ dqo transformation was proposed in [35]. With a combination of these two transformations, the three-phase electrical quantities, e.g. flux linkages, voltages and currents, can be presented in the dq-frame, and vice versa

$$\begin{bmatrix} x_{\mathrm{d}} \\ x_{\mathrm{q}} \\ x_{\mathrm{o}} \end{bmatrix} = T_{\mathrm{abc}\to\mathrm{dqo}} \begin{bmatrix} x_{\mathrm{a}} \\ x_{\mathrm{b}} \\ x_{\mathrm{c}} \end{bmatrix} \qquad \begin{bmatrix} x_{\mathrm{a}} \\ x_{\mathrm{b}} \\ x_{\mathrm{c}} \end{bmatrix} = T_{\mathrm{dqo}\to\mathrm{abc}} \begin{bmatrix} x_{\mathrm{d}} \\ x_{\mathrm{q}} \\ x_{\mathrm{o}} \end{bmatrix} \tag{A-6}$$

where x denotes any electrical quantity, d denotes d-axis, q denotes q-axis, o denotes zero-sequence, $T_{\mathrm{abc}\to\mathrm{dqo}}$ denotes the abc → dqo transformation matrix and $T_{\mathrm{dqo}\to\mathrm{abc}}$ denotes the dqo → abc transformation matrix. The transformation matrices are

$$T_{\mathrm{abc}\to\mathrm{dqo}} = k_1 \begin{bmatrix} \cos(\phi_{\mathrm{r}}) & \cos\left(\phi_{\mathrm{r}} - \frac{2}{3}\pi\right) & \cos\left(\phi_{\mathrm{r}} + \frac{2}{3}\pi\right) \\ -\sin(\phi_{\mathrm{r}}) & -\sin\left(\phi_{\mathrm{r}} - \frac{2}{3}\pi\right) & -\sin\left(\phi_{\mathrm{r}} + \frac{2}{3}\pi\right) \\ k_0 & k_0 & k_0 \end{bmatrix} \tag{A-7}$$

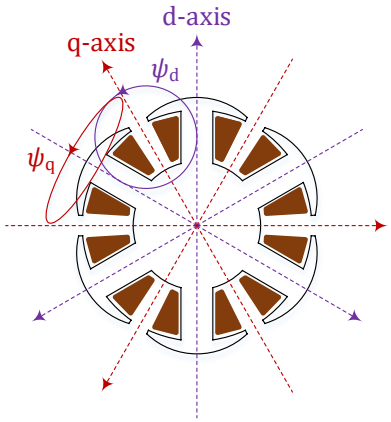

Figure A-3 The d- and q-axis of an EESM.

$$T_{\mathrm{dqo}\to\mathrm{abc}} = \frac{2}{3k_1}\begin{bmatrix} \cos(\phi_r) & -\sin(\phi_r) & \frac{1}{2k_0} \\ \cos\left(\phi_r - \frac{2}{3}\pi\right) & -\sin\left(\phi_r - \frac{2}{3}\pi\right) & \frac{1}{2k_0} \\ \cos\left(\phi_r + \frac{2}{3}\pi\right) & -\sin\left(\phi_r + \frac{2}{3}\pi\right) & \frac{1}{2k_0} \end{bmatrix} \tag{A-8}$$

where ϕ_r is the angle of the rotor flux with respect to a-axis, and in synchronous machines, the rotor angle equals the rotor flux angle

$$\theta_r = \phi_r \tag{A-9}$$

The scaling factors k_1 and k_0 in (A-7) and (A-8) are added to the transformation in order to fit different preferences. The *amplitude-invariant transformation* and *power-invariant transformation* are the two popular ones.

The idea of *amplitude-invariant transformation* is to match the amplitude of the dqo quantities to the amplitude of the abc quantities

$$\sqrt{{x_d}^2 + {x_q}^2} = \left|\vec{x}_{dq}\right| = \hat{x}_a = \hat{x}_b = \hat{x}_c \tag{A-10}$$

where $\left|\vec{x}_{dq}\right|$ means the amplitude of the vector in dq-frame, $\hat{x}_a$, $\hat{x}_b$ and $\hat{x}_c$ are the amplitudes of the a, b and c quantities. To achieve this, the scaling factors are

$$k_1 = \frac{2}{3} \quad , \quad k_0 = \frac{1}{2} \tag{A-11}$$

but other scaling factors must be applied in the instantaneous power calculation in dq-frame

$$u_a \cdot i_a + u_b \cdot i_b + u_c \cdot i_c = p = \frac{3}{2} \cdot u_d \cdot i_d + \frac{3}{2} \cdot u_q \cdot i_q + 3 \cdot u_o \cdot i_o \tag{A-12}$$

where p means instantaneous power. This is because $T_{\mathrm{abc}\to\mathrm{dqo}}$ is not unitary in *amplitude-invariant transformation*. Please note that the zero sequence is the same as the one in the symmetrical component transformation [74].

The idea of *power-invariant transformation* is to make sure that the instantaneous power calculated through inner-product of voltage and current vectors in the dqo-frame is consistent with that calculated in the abc-frame, i.e.

$$u_{\mathrm{a}} \cdot i_{\mathrm{a}} + u_{\mathrm{b}} \cdot i_{\mathrm{b}} + u_{\mathrm{c}} \cdot i_{\mathrm{c}} = p = u_{\mathrm{d}} \cdot i_{\mathrm{d}} + u_{\mathrm{q}} \cdot i_{\mathrm{q}} + u_{\mathrm{o}} \cdot i_{\mathrm{o}} \tag{A-13}$$

And in order to achieve this, $T_{\mathrm{abc}\to\mathrm{dqo}}$ and $T_{\mathrm{dqo}\to\mathrm{abc}}$ need to be unitary, which yields the scaling factors as

$$k_1 = \frac{\sqrt{2}}{\sqrt{3}} \quad , \quad k_0 = \frac{\sqrt{2}}{2} \tag{A-14}$$

The unitarity of $T_{\mathrm{abc}\to\mathrm{dqo}}$ and $T_{\mathrm{dqo}\to\mathrm{abc}}$ in *power-invariant transformation* means that they are the transpose and inverse of each other.

A.3 Coordinate Transformation in EESM

Usually the mid-point of the motor is not grounded, and therefore, the zero-sequence component in the current cannot appear. Then the $\mathrm{abc} \to \mathrm{dq}$ and $\mathrm{dq} \to \mathrm{abc}$ transformations can be formulated as

$$T_{\mathrm{abc}\to\mathrm{dq}} = k_1 \begin{bmatrix} \cos(\theta_{\mathrm{r}}) & \cos\left(\theta_{\mathrm{r}} - \frac{2}{3}\pi\right) & \cos\left(\theta_{\mathrm{r}} + \frac{2}{3}\pi\right) \\ -\sin(\theta_{\mathrm{r}}) & -\sin\left(\theta_{\mathrm{r}} - \frac{2}{3}\pi\right) & -\sin\left(\theta_{\mathrm{r}} + \frac{2}{3}\pi\right) \end{bmatrix} \tag{A-15}$$

$$T_{\mathrm{dq}\to\mathrm{abc}} = \frac{2}{3k_1} \begin{bmatrix} \cos(\theta_{\mathrm{r}}) & -\sin(\theta_{\mathrm{r}}) \\ \cos\left(\theta_{\mathrm{r}} - \frac{2}{3}\pi\right) & -\sin\left(\theta_{\mathrm{r}} - \frac{2}{3}\pi\right) \\ \cos\left(\theta_{\mathrm{r}} + \frac{2}{3}\pi\right) & -\sin\left(\theta_{\mathrm{r}} + \frac{2}{3}\pi\right) \end{bmatrix} \tag{A-16}$$

where $T_{\mathrm{abc}\to\mathrm{dq}}$ is the $\mathrm{abc} \to \mathrm{dq}$ transformation matrix and $T_{\mathrm{dq}\to\mathrm{abc}}$ is the $\mathrm{dq} \to \mathrm{abc}$ transformation matrix. Taking the field winding into consideration, the complete transformation in EESM becomes

$$\begin{bmatrix} x_{\mathrm{d}} \\ x_{\mathrm{q}} \\ x_{\mathrm{f}} \end{bmatrix} = \begin{bmatrix} T_{\mathrm{abc}\to\mathrm{dq}} & 0 \\ 0 & 1 \end{bmatrix} \begin{bmatrix} x_{\mathrm{a}} \\ x_{\mathrm{b}} \\ x_{\mathrm{c}} \\ x_{\mathrm{f}} \end{bmatrix} \quad , \quad \begin{bmatrix} x_{\mathrm{a}} \\ x_{\mathrm{b}} \\ x_{\mathrm{c}} \\ x_{\mathrm{f}} \end{bmatrix} = \begin{bmatrix} T_{\mathrm{dq}\to\mathrm{abc}} & 0 \\ 0 & 1 \end{bmatrix} \begin{bmatrix} x_{\mathrm{d}} \\ x_{\mathrm{q}} \\ x_{\mathrm{f}} \end{bmatrix} \tag{A-17}$$

A.4 Modeling in DQ-Current Frame

With the abc-dq transformation, the machine can be modeled in the dq-frame.

The flux linkage equation in the dq-frame can be derived from the flux linkage equation (A-2) in the abc-frame

$$\begin{bmatrix} \psi_{\mathrm{d}} \\ \psi_{\mathrm{q}} \\ \psi_{\mathrm{f}} \end{bmatrix} = L_{\mathrm{dqf}} \begin{bmatrix} i_{\mathrm{d}} \\ i_{\mathrm{q}} \\ i_{\mathrm{f}} \end{bmatrix} = \begin{bmatrix} T_{\mathrm{abc}\to\mathrm{dq}} & 0 \\ 0 & 1 \end{bmatrix} L_{\mathrm{abcf}} \begin{bmatrix} T_{\mathrm{dq}\to\mathrm{abc}} & 0 \\ 0 & 1 \end{bmatrix} \begin{bmatrix} i_{\mathrm{d}} \\ i_{\mathrm{q}} \\ i_{\mathrm{f}} \end{bmatrix} \tag{A-18}$$

Then, the inductance matrix L_{dqf} can be derived from L_{abcf}, as indicated in (A-17)

$$L_{\mathrm{dqf}} = \begin{bmatrix} T_{\mathrm{abc}\to\mathrm{dq}} & 0 \\ 0 & 1 \end{bmatrix} L_{\mathrm{abc}} \begin{bmatrix} T_{\mathrm{dq}\to\mathrm{abc}} & 0 \\ 0 & 1 \end{bmatrix} = \begin{bmatrix} L_{\mathrm{d}} & 0 & \frac{3}{2}k_1 L_{\mathrm{m}} \\ 0 & L_{\mathrm{q}} & 0 \\ \frac{1}{k_1}L_{\mathrm{m}} & 0 & L_{\mathrm{f}} \end{bmatrix} \tag{A-19}$$

where L_{d} is the d-axis inductance and L_{q} is the q-axis inductance

$$\begin{aligned} L_{\mathrm{d}} &= L_{\mathrm{s}\cdot\Sigma} - M_{\mathrm{s}\cdot\Sigma} + \frac{3}{2}L_{\mathrm{s}\cdot\Delta} \\ L_{\mathrm{q}} &= L_{\mathrm{s}\cdot\Sigma} - M_{\mathrm{s}\cdot\Sigma} - \frac{3}{2}L_{\mathrm{s}\cdot\Delta} \end{aligned} \tag{A-20}$$

In case *power-invariant transformation* is applied, then

$$L_{\mathrm{dqf}} = \begin{bmatrix} L_{\mathrm{d}} & 0 & \frac{\sqrt{3}}{\sqrt{2}}L_{\mathrm{m}} \\ 0 & L_{\mathrm{q}} & 0 \\ \frac{\sqrt{3}}{\sqrt{2}}L_{\mathrm{m}} & 0 & L_{\mathrm{f}} \end{bmatrix} \tag{A-21}$$

which is symmetric. However, if *amplitude-invariant transformation* is applied, then

$$L_{\mathrm{dqf}} = \begin{bmatrix} L_{\mathrm{d}} & 0 & L_{\mathrm{m}} \\ 0 & L_{\mathrm{q}} & 0 \\ \frac{3}{2}L_{\mathrm{m}} & 0 & L_{\mathrm{f}} \end{bmatrix} \tag{A-22}$$

which is not symmetric, and to express the flux linkages separately in this case

$$\begin{aligned} \psi_{\mathrm{d}} &= L_{\mathrm{d}} \cdot i_{\mathrm{d}} + L_{\mathrm{m}} \cdot i_{\mathrm{f}} \\ \psi_{\mathrm{q}} &= L_{\mathrm{q}} \cdot i_{\mathrm{q}} \\ \psi_{\mathrm{f}} &= L_{\mathrm{f}} \cdot i_{\mathrm{f}} + \frac{3}{2} \cdot L_{\mathrm{m}} \cdot i_{\mathrm{d}} \end{aligned} \tag{A-23}$$

In this work, *amplitude-invariant transformation* ($k_1 = \frac{2}{3}$) is selected due to the simple expressions in flux linkage equations.

The dynamic stator voltage equation of the machine can be derived in vector form

$$\begin{aligned} & \vec{u}_{\mathrm{s}}^{\mathrm{s}} = R_{\mathrm{s}} \cdot \vec{i}_{\mathrm{s}}^{\mathrm{s}} + \frac{\mathrm{d}\vec{\psi}_{\mathrm{s}}^{\mathrm{s}}}{\mathrm{d}t} \\ \Rightarrow \quad & \vec{u}_{\mathrm{s}} = R_{\mathrm{s}} \cdot \vec{i}_{\mathrm{s}} + \frac{\mathrm{d}\vec{\psi}_{\mathrm{s}}}{\mathrm{d}t} + \mathrm{j}\omega_{\mathrm{r}} \cdot \vec{\psi}_{\mathrm{s}} \\ \Rightarrow \quad & u_{\mathrm{d}} + \mathrm{j}u_{\mathrm{q}} = R_{\mathrm{s}} \cdot \left(i_{\mathrm{d}} + \mathrm{j}i_{\mathrm{q}}\right) + \frac{\mathrm{d}\left(\psi_{\mathrm{d}} + \mathrm{j}\psi_{\mathrm{q}}\right)}{\mathrm{d}t} + \mathrm{j}\omega_{\mathrm{r}} \cdot \left(\psi_{\mathrm{d}} + \mathrm{j}\psi_{\mathrm{q}}\right) \end{aligned} \tag{A-24}$$

where $\vec{u}_{\mathrm{s}}^{\mathrm{s}}$, $\vec{i}_{\mathrm{s}}^{\mathrm{s}}$ and $\vec{\psi}_{\mathrm{s}}^{\mathrm{s}}$ mean the stator voltage, current and flux linkage in the αβ-frame; $\vec{u}_{\mathrm{s}}^{\mathrm{s}}$, $\vec{i}_{\mathrm{s}}^{\mathrm{s}}$ and $\vec{\psi}_{\mathrm{s}}^{\mathrm{s}}$ mean the stator voltage, current and flux linkage in the dq-frame. Then, in matrix format, the stator along with the field equations can be summarized as

$$\begin{bmatrix} u_\mathrm{d} \\ u_\mathrm{q} \\ u_\mathrm{f} \end{bmatrix} = \begin{bmatrix} R_\mathrm{s} & 0 & 0 \\ 0 & R_\mathrm{s} & 0 \\ 0 & 0 & R_\mathrm{f} \end{bmatrix} \begin{bmatrix} i_\mathrm{d} \\ i_\mathrm{q} \\ i_\mathrm{f} \end{bmatrix} + \begin{bmatrix} 0 & -\omega_\mathrm{r} & 0 \\ \omega_\mathrm{r} & 0 & 0 \\ 0 & 0 & 0 \end{bmatrix} \begin{bmatrix} \psi_\mathrm{d} \\ \psi_\mathrm{q} \\ \psi_\mathrm{f} \end{bmatrix} + \frac{\mathrm{d}}{\mathrm{d}t} \begin{bmatrix} \psi_\mathrm{d} \\ \psi_\mathrm{q} \\ \psi_\mathrm{f} \end{bmatrix} \tag{A-25}$$

And assuming constant inductances, (A-25) becomes

$$\begin{bmatrix} u_\mathrm{d} \\ u_\mathrm{q} \\ u_\mathrm{f} \end{bmatrix} = \begin{bmatrix} R_\mathrm{s} & -\omega_\mathrm{r} L_\mathrm{q} & 0 \\ \omega_\mathrm{r} L_\mathrm{d} & R_\mathrm{s} & \omega_\mathrm{r} L_\mathrm{m} \\ 0 & 0 & R_\mathrm{f} \end{bmatrix} \begin{bmatrix} i_\mathrm{d} \\ i_\mathrm{q} \\ i_\mathrm{f} \end{bmatrix} + \begin{bmatrix} L_\mathrm{d} & 0 & L_\mathrm{m} \\ 0 & L_\mathrm{q} & 0 \\ \frac{3}{2} L_\mathrm{m} & 0 & L_\mathrm{f} \end{bmatrix} \begin{bmatrix} \frac{di_\mathrm{d}}{dt} \\ \frac{di_\mathrm{q}}{dt} \\ \frac{di_\mathrm{f}}{dt} \end{bmatrix} \tag{A-26}$$

Please notice that coupling terms $-\omega_\mathrm{r} L_\mathrm{q} i_\mathrm{q}$, $\omega_\mathrm{r} L_\mathrm{d} i_\mathrm{d}$ and $\omega_\mathrm{r} L_\mathrm{m} i_\mathrm{f}$ appear in the d- and q-axis equations. The term $\omega_\mathrm{r} L_\mathrm{m} i_\mathrm{f}$ is usually regarded as the back-EMF term

$$e_\mathrm{m} = \omega_\mathrm{r} \cdot L_\mathrm{m} \cdot i_\mathrm{f} \tag{A-27}$$

and the EMF along d- and q-axis can be defined as well

$$e_\mathrm{d} = -\omega_\mathrm{r} \cdot L_\mathrm{q} \cdot i_\mathrm{q} = -x_\mathrm{q} \cdot i_\mathrm{q} \tag{A-28}$$

$$e_\mathrm{q} = \omega_\mathrm{r} \cdot L_\mathrm{d} \cdot i_\mathrm{d} + \omega_\mathrm{r} \cdot L_\mathrm{m} \cdot i_\mathrm{f} = x_\mathrm{d} \cdot i_\mathrm{d} + e_\mathrm{m} \tag{A-29}$$

where x denotes reactances, e denotes EMF and m means mutual. In steady state, the current derivatives in dq-frame become zero, which means

$$\begin{bmatrix} U_\mathrm{d} \\ U_\mathrm{q} \\ U_\mathrm{f} \end{bmatrix} = \begin{bmatrix} R_\mathrm{s} & -\omega_\mathrm{r} L_\mathrm{q} & 0 \\ \omega_\mathrm{r} L_\mathrm{d} & R_\mathrm{s} & \omega_\mathrm{r} L_\mathrm{m} \\ 0 & 0 & R_\mathrm{f} \end{bmatrix} \begin{bmatrix} I_\mathrm{d} \\ I_\mathrm{q} \\ I_\mathrm{f} \end{bmatrix} \tag{A-30}$$

The ratio between d- and q-axis inductances is defined as saliency ratio [75]

$$k_\mathrm{dq} = \frac{L_\mathrm{d}}{L_\mathrm{q}} \tag{A-31}$$

In case $k_\mathrm{dq} = 1$, then the machine is defined as “non-salient”, whereas in case $k_\mathrm{dq} \neq 1$, then the machine is defined as “salient”. The difference between L_d and L_q is defined as L_Δ

$$L_\Delta = L_\mathrm{d} - L_\mathrm{q} = 3 \cdot L_{\mathrm{s \cdot delta}} \tag{A-32}$$

Appendix B

Instantaneous Power Basics

From the instantaneous voltage and current values, the instantaneous power can be calculated [37]. In αβ-frame, the complex power can be formulated as

$$\begin{aligned}\vec{s} = p + \mathrm{j}q &= \frac{3}{2K^2} \cdot \vec{u}^{(\alpha\beta)} \cdot \vec{i}^{(\alpha\beta)^*} \\ &= \frac{3}{2K^2} \cdot \left(u_\alpha + \mathrm{j}u_\beta\right) \cdot \left(i_\alpha - \mathrm{j}i_\beta\right) \\ &= \frac{3}{2K^2}\left(u_\alpha \cdot i_\alpha + u_\beta \cdot i_\beta\right) + \mathrm{j}\frac{3}{2K^2}\left(u_\beta \cdot i_\alpha - u_\alpha \cdot i_\beta\right)\end{aligned} \tag{B-1}$$

Transformed into dq-frame, the complex power can be expressed as

$$\begin{aligned}\vec{s} = p + \mathrm{j}q &= \frac{3}{2K^2} \cdot \vec{u}^{(\alpha\beta)} \cdot \vec{i}^{(\alpha\beta)^*} = \frac{3}{2K^2} \cdot \left[\vec{u}^{(\mathrm{dq})} \cdot \mathrm{e}^{\mathrm{j}\theta}\right] \cdot \left[\vec{i}^{(\mathrm{dq})} \cdot \mathrm{e}^{\mathrm{j}\theta}\right]^* \\ &= \frac{3}{2K^2} \cdot \left[\vec{u}^{(\mathrm{dq})} \cdot \vec{i}^{(\mathrm{dq})^*}\right] \cdot \left[\mathrm{e}^{\mathrm{j}\theta} \cdot \mathrm{e}^{-\mathrm{j}\theta}\right] \\ &= \frac{3}{2K^2}\left(u_\mathrm{d} \cdot i_\mathrm{d} + u_\mathrm{q} \cdot i_\mathrm{q}\right) + \mathrm{j}\frac{3}{2K^2}\left(u_\mathrm{q} \cdot i_\mathrm{d} - u_\mathrm{d} \cdot i_\mathrm{q}\right)\end{aligned} \tag{B-2}$$

With amplitude-invariant transformation ($K = 1$), the active power, reactive power, apparent power as well as power factor can be formulated as

$$p = \frac{3}{2}\left(u_\mathrm{d} \cdot i_\mathrm{d} + u_\mathrm{q} \cdot i_\mathrm{q}\right) \qquad q = \frac{3}{2}\left(u_\mathrm{q} \cdot i_\mathrm{d} - u_\mathrm{d} \cdot i_\mathrm{q}\right) \tag{B-3}$$

$$\begin{aligned}s &= \sqrt{p^2 + q^2} \\ &= \frac{3}{2}\sqrt{\left(u_\mathrm{d} \cdot i_\mathrm{d} + u_\mathrm{q} \cdot i_\mathrm{q}\right)^2 + \left(u_\mathrm{q} \cdot i_\mathrm{d} - u_\mathrm{d} \cdot i_\mathrm{q}\right)^2} \\ &= \frac{3}{2}\sqrt{(u_\mathrm{d} \cdot i_\mathrm{d})^2 + \left(u_\mathrm{q} \cdot i_\mathrm{q}\right)^2 + \left(u_\mathrm{q} \cdot i_\mathrm{d}\right)^2 + \left(u_\mathrm{d} \cdot i_\mathrm{q}\right)^2}\end{aligned} \tag{B-4}$$

$$\cos\varphi = \frac{p}{s} = \frac{p}{\sqrt{p^2 + q^2}} = \frac{1}{\sqrt{1 + \left(\frac{q}{p}\right)^2}} = \frac{1}{\sqrt{1 + \left(\frac{u_\mathrm{q} \cdot i_\mathrm{d} - u_\mathrm{d} \cdot i_\mathrm{q}}{u_\mathrm{d} \cdot i_\mathrm{d} + u_\mathrm{q} \cdot i_\mathrm{q}}\right)^2}} \tag{B-5}$$

Appendix C

Experimental Setup for 48 V EESM

The connection and measurement points of the system are illustrated in Figure C-1. A dc power source supplies power to a three-phase inverter and an H-Bridge inverter. The three-phase inverter delivers power to the three phases A, B and C in the stator, while the H-Bridge inverter delivers power to the rotating transformer for field excitation. The neutral point of the three phases are not connected. The machine is connected to a load machine through a torque sensor. An incremental encoder is installed on the shaft. In order to do field-oriented

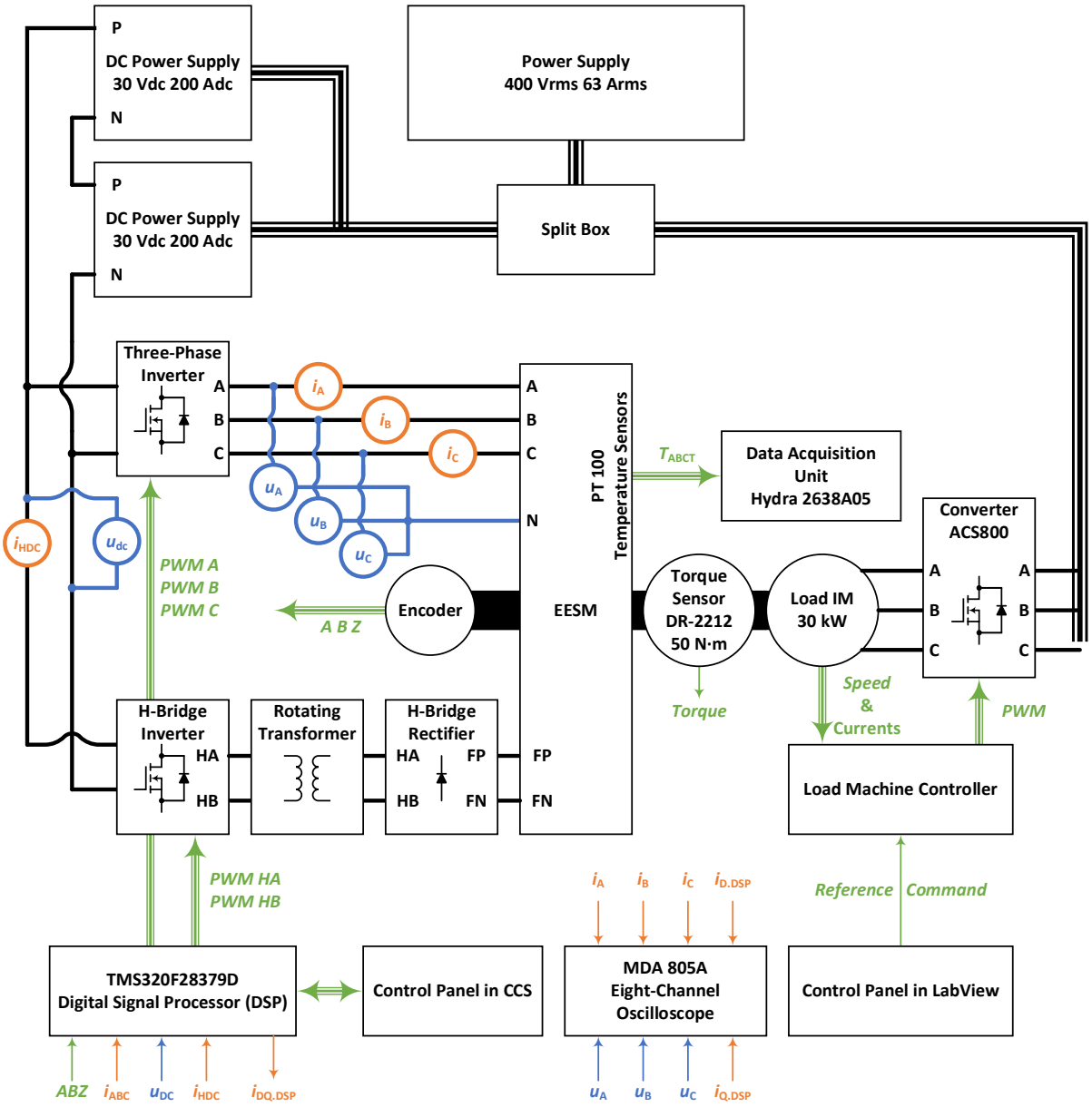

Figure C-1 Diagram of 48 V EESM experimental setup.

control of the machine, the three-phase currents are measured and the pulses from the incremental encoder are fed into a DSP. The DSP used in this study is TMS320F28379D from Texas Instrument. The three-phase voltages are measured with an oscilloscope, not for control but for power calculation. The dc-link voltage is measured for calculation of pulse width modulation (PWM) duty cycles. The dc-link current going to the H-bridge inverter is measured for field current estimation. In addition, PT100 temperature sensors are inserted into the windings to monitor the temperature.

Each current sensor provides a voltage signal between ±10 V. Through a processing circuit shown in Figure C-2, the signal is scaled to between 0 and 3 V and fed into the ADC of DSP. OPAMP 1 is a voltage follower which provides high input impedance and low output impedance. This avoids the current sensor from being overloaded. Then, a resistive voltage divider scales the signal from ±10 V to ±1.5 V. A capacitor of 100 nF is added here to filter out noise. Thereafter, OPAMP 2 is used to shift the voltage signal from ±1.5 V to between 0 and -3 V, by adding 1.5 V from a voltage reference chip. In the end, the signal is inverted by OPAMP 3 to between 0 and 3 V.

The voltage measurement utilizes a Hall sensor, as shown in Figure C-3. A resistor is added in parallel with the voltage to measure and a current goes through the resistor into the Hall sensor which is proportional to the voltage level. Since Hall effect is utilized, the output is galvanically isolated from the power circuit. The Hall sensor outputs a secondary side current which is proportional to the primary side current. And by adding a proper value of resistance at the output of the Hall sensor, the voltage across the resistor becomes within the range of between 0 and 3 V and is proportional to the voltage on the primary side. This voltage then can be fed into the ADC of the DSP.

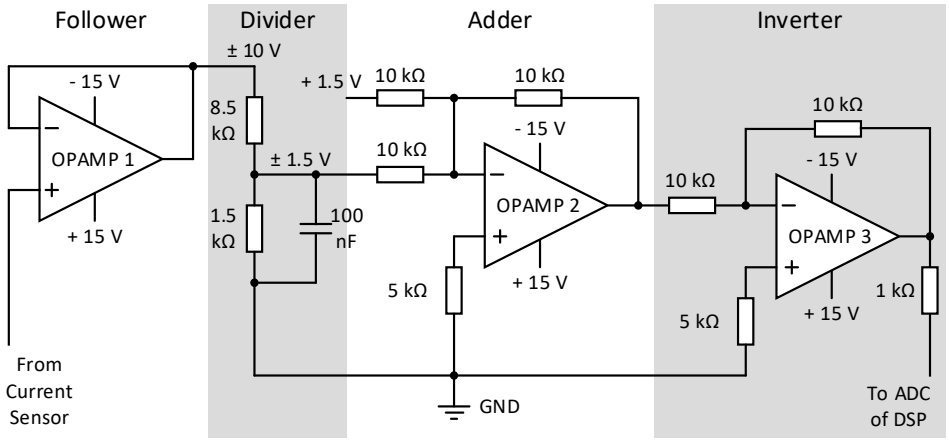

Figure C-2 Current measurement signal processing circuit of each channel (totally four channels).

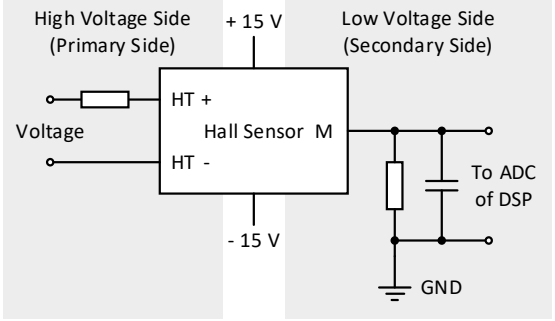

Figure C-3 Voltage measurement circuit.

The encoder provides TTL signal, which needs to be scaled into the range between 0 and 3.3 V before going to the EQEP of the DSP. The signal processing circuit is as shown in Figure C-4. Firstly, the pulses in pairs are fed into a differential line receiver which compares the positive and negative signals and outputs differential mode. This is used to reject common mode noise. Then a transceiver scales the voltage level from 5 V to 3.3 V. Thereafter, the signal is safe to go to the EQEP module of the DSP.

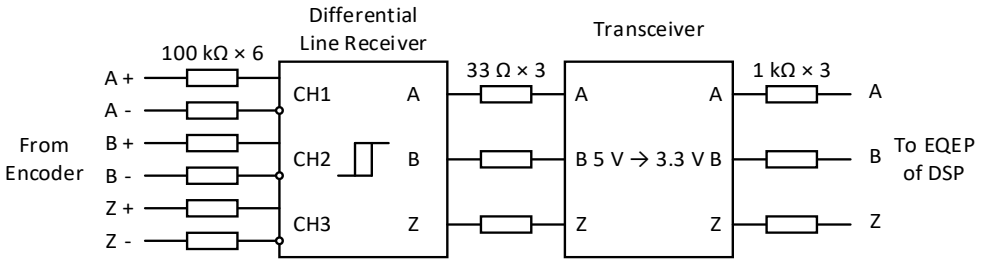

Figure C-4 Encoder signal processing circuit.

The current, voltage and encoder signal processing circuits are implemented on a signal processing PCB. A photo of the PCB was taken as shown in Figure C-5. The current measurement signals come to the PCB through the BNC connectors on the northwest corner. The power supply, encoder signals and voltage signals are placed from north to south along the right side. A TMS320F28379D launchpad was stacked on the top on the southwest. The PWM output pins are placed along the southwest edges close to the launchpad. The controller including the signal PCB and the launchpad is sealed in an iron box to avoid electromagnetic interference (EMI).

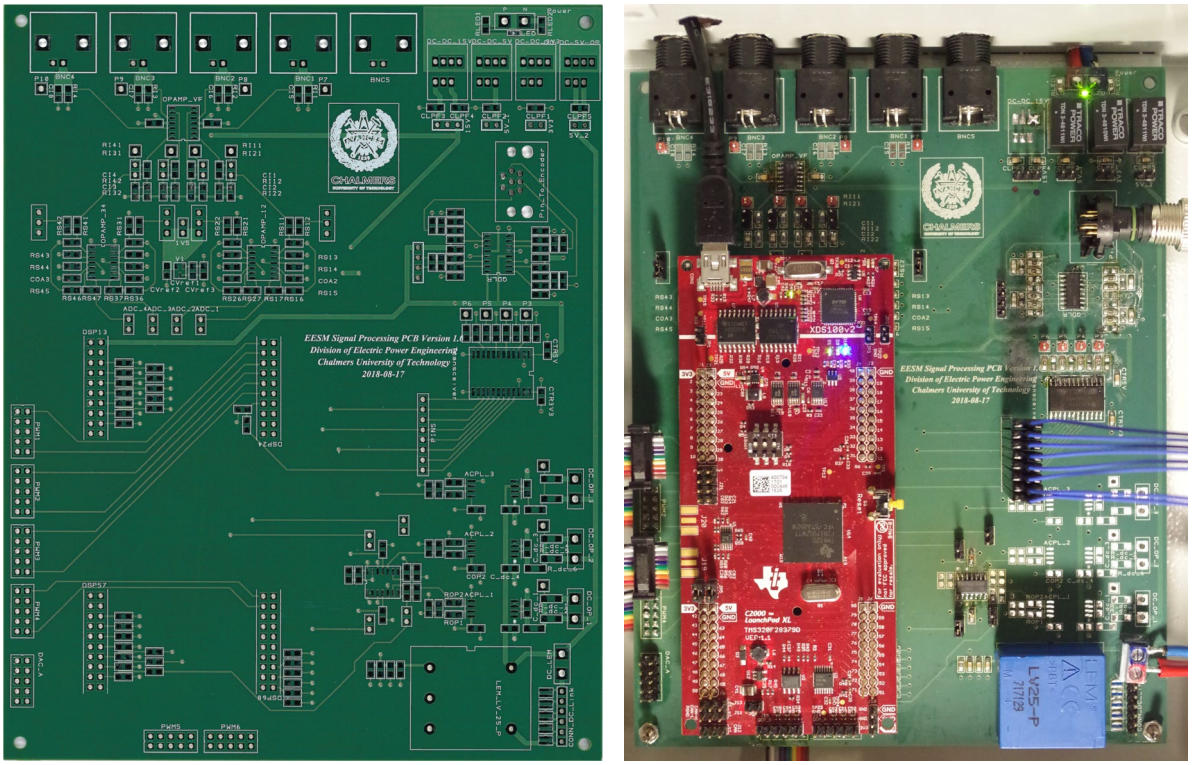

(a) Signal processing PCB (b) Controller hardware sealed in a steel box

Figure C-5 Hardware of controller.

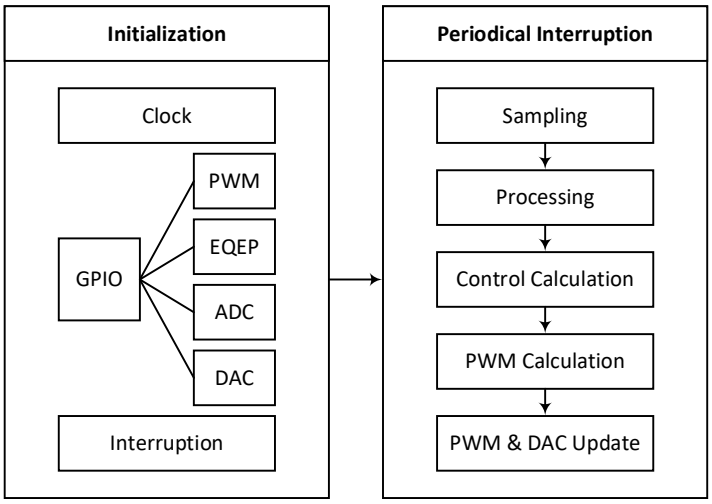

Figure C-6 Sequence in controller.

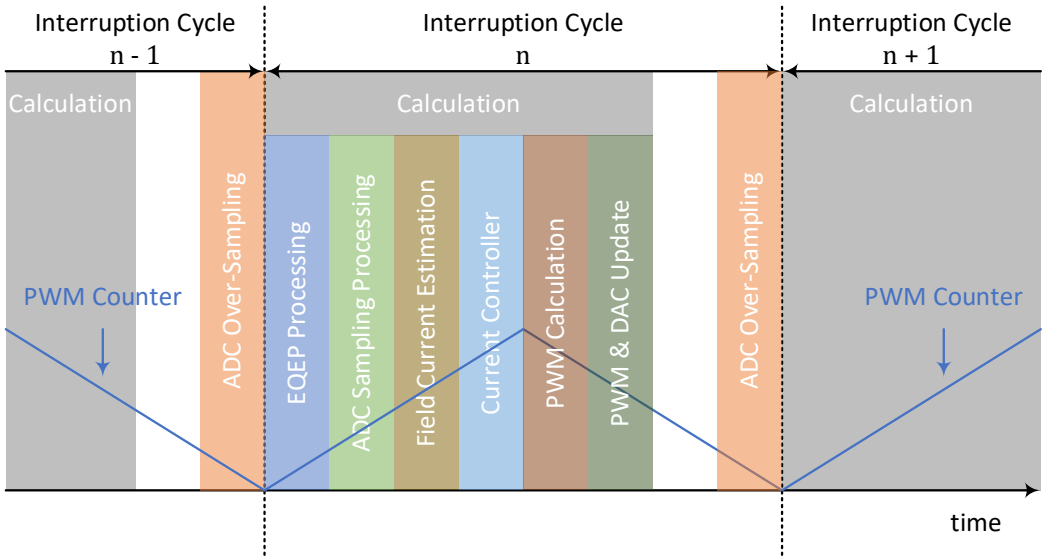

Figure C-7 Process during interruption.

Figure C-6 shows the sequence of the DSP programme. Initialization is performed in the beginning, which includes the initializations of the clock and the GPIO ports, as well as the configuration of periodical interruptions. The interruption period is set as the same as the period of switching cycle. Then the periodical interruptions start. In each interruption, sampling, processing of the sampling, control calculation, PWM calculation and PWM as well as DAC update are performed in a sequence.

The time allocation of each periodical interruption is illustrated in a schematic shown in Figure C-7. Over-sampling is a technique that takes four samples of each signal successively, and then takes the average of the medium two values as the measured value for processing. This technique is applied to reject EMI and get stable measurement values. Over sampling is performed before each interruption. Thereafter, the values in EQEP registers are processed to calculate the rotor speed and position. This is to make sure that the rotor position is taken at the beginning of the interruption so that the rotor angle at the end of the interruption can be compensated as accurate as possible by

$$\theta_{\mathrm{r.2}} = \theta_{\mathrm{r.1}} + \omega_{\mathrm{r.1}} \cdot T_{\mathrm{sw}} \qquad \text{(C-1)}$$

where $\theta_{\mathrm{r.1}}$ and $\omega_{\mathrm{r.1}}$ are the angle and speed measured by the EQEP module at the beginning of the interruption respectively, T_{sw} is the period of switching cycle and $\theta_{\mathrm{r.2}}$ is the estimated angle at the end of the interruption. Thereafter, ADC sampling is processed and field current is estimated. In current control, $\theta_{\mathrm{r.1}}$ is the one used for abc-dq transformation, whereas $\theta_{\mathrm{r.2}}$ is the one used for dq-abc transformation. In the end, PWM duty cycles are calculated and the outputs are updated.